Spring 1-1-2016

Determining Global Ionospheric Conductivity in the Satellite and Data Assimilation Age and Assessing its Influence on the Magnetosphere-Ionosphere-Thermosphere System

Ryan Michael McGranaghan
University of Colorado Boulder, ryan.mcgranaghan@gmail.com

Determining global ionospheric conductivity in the satellite and data assimilation age and assessing its influence on the Magnetosphere-Ionosphere-Thermosphere system

by

R. M. McGranaghan

B.A., University of Tennessee, 2011

M.S., University of Colorado, 2013

A thesis submitted to the

Faculty of the Graduate School of the

University of Colorado in partial fulfillment

of the requirements for the degree of

Doctor of Philosophy

Department of Aerospace Engineering Sciences

2016

This thesis entitled:
Determining global ionospheric conductivity in the satellite and data assimilation age and assessing its influence on the Magnetosphere-Ionosphere-Thermosphere system
written by R. M. McGranaghan
has been approved for the Department of Aerospace Engineering Sciences

_____

Prof. Delores J. Knipp

_____

Prof. Tomoko Matsuo

_____

Prof. Jeffrey Thayer

_____

Prof. Jeffrey Parker

_____

Prof. Doug Nychka

Date _____

The final copy of this thesis has been examined by the signatories, and we find that both the content and the form meet acceptable presentation standards of scholarly work in the above mentioned discipline.

McGranaghan, R. M. (Ph.D., Aerospace Engineering)

Determining global ionospheric conductivity in the satellite and data assimilation age and assessing its influence on the Magnetosphere-Ionosphere-Thermosphere system

Thesis directed by Prof. Delores J. Knipp

This work focuses on determining how effectively the upper atmosphere, as a medium, transmits the influence of an electric field into differential charge motion (current). This effect is called conductivity. Conductivity modulates height-specific energy deposition in the ionosphere and thermosphere, and is therefore critical to the study of the Earth space environment. Conductivity is one of the most difficult parameters in the geospace system to study because it is not directly observed. Past efforts to model conductivity have relied on simplifying assumptions: 1) all particles incident on the ionosphere have a Maxwellian particle energy distribution, and 2) that conductivity can be collapsed to the height-integrated conductance in a thin shell at ∼120 km. Data, tools, and computational capabilities are now available for exploring the height-specific and/or height-dependent effects *free of assumptions on the functional form of precipitating particles. The key to the improvements presented in this dissertation is a complex systems approach through which cutting-edge mathematical tools and computational techniques are utilized to improve modeling and understanding of conductivity.* My work addresses outstanding problems in conductivity modeling that have existed for nearly three decades, permitting the first global height-specific views of how solar and magnetospheric energy influence the dynamics of the ionosphere and thermosphere. Further, I have developed methods that eliminate the Maxwellian assumption for large-scale conductivity calculations; a key step toward capturing conductivity features on finer scales and during heightened geomagnetic activity. My work also promotes much more effective and efficient use of under-used geospace observations in data assimilation and forecasting. The outcome is significantly improved conductance and conductivity modeling capabilities that underpin a system science approach to understanding geospace interactions at smaller scales and higher resolution.

This work has four facets, each addressing a limitation in the current state of conductivity modeling: 1) characterization of high-latitude particle precipitation and its combination with the effects of solar ionization; 2) creation of the conductivity model; 3) identification of the characteristic features of the ionospheric conductivity and capturing these features in a covariance model; and 4) creation of a means to estimate the dynamic global distribution of conductivity via optimal interpolation. The engineering application of this work is in the realm of satellite drag, which is the aspect of low Earth satellite motion most affected by upper atmospheric energy deposition.

The key contributions of this dissertation are: 1) a new model of height-dependent ionospheric conductivity, with a computationally efficient version now freely available to the community (*McGranaghan et al.*, 2014, 2015a); 2) the ability to study conductivity from directly observed in-situ electron energy spectra, free of any assumption on the functional form (*McGranaghan et al.*, 2015a,b); 3) a new picture of the height-dependent ionospheric conductivities utilizing advanced computational tools and organized as empirical orthogonal functions (EOFs) (*McGranaghan et al.*, 2015b); 4) a sophisticated statistical estimation method to understand conductivity influence on the complex electrodynamics of the magnetosphere-ionosphere-thermosphere (MIT) system (*McGranaghan et al.*, 2016, submitted and revised); 5) more accurate conductivity distributions to better specify the MIT system on small scales, bringing ground- and space-based observations into closer agreement (*McGranaghan et al.*, 2016, submitted and revised); and 6) a three-dimensional EOF analysis of the height-dependent conductivities. These contributions represent several 'firsts' in the geospace sciences: 1) the first combination of computationally efficient parameterizations with advanced particle transport algorithms to study conductivity; 2) the first large-scale analysis of directly calculated ionospheric conductivity free of assumption of the incident electron energy spectra; 3) the first characterization of the primary modes of ionospheric conductivity variability as EOFs; 4) the first comparison of height-integrated and height-dependent ionospheric conductivities in the context of a three-dimensional conductivity analysis; and 5) the first optimally interpolated data assimilative analysis of the conductivity.

Dedication

to my parents,

Kathleen and Mark McGranaghan

to my brothers and sister,

Andrew, Joe, and Maureen McGranaghan

and to my partner through it all,

Rachel Bush

Acknowledgements

I acknowledge the tireless and energetic efforts of my advisor, Dr. Delores Knipp, over the past four years. Her enthusiasm and joy of discovery have been infectious throughout my graduate career. My passion for the space sciences and the success of this work are largely the result of her commitment and mentorship.

I also acknowledge my committee members: Drs. Tomoko Matsuo, Jeffrey Thayer, Jeffrey Parker, and Doug Nychka. Their sustained efforts made this work as strong as possible and guided me to become a better scientist, engineer, and researcher.

I would like to thank my family from the bottom of my heart for their daily support, love, and laughs; for sharing in the good times, and being there for me in the bad. They each constantly make me a better version of myself. Rachel Bush deserves a special thanks for putting up with me, helping keep everything in perspective, and being my constant rock during the past six years. I could not have completed this dissertation without their inspiration.

I thank each of my friends, a list that is far too long to include here, but full of truly wonderful and supportive people.

I would also like to thank Liam Kilcommons, Rob Redmon, and Ellen Cousins for the collaborations we have enjoyed over the past few years. They consistently addressed my questions about DMSP and SuperDARN data, ionospheric electrodynamics, and a number of other topics I needed to understand.

I acknowledge each of my close colleagues at the High Altitude Observatory for their mentorship and friendship. I would specifically like to thank Stan Solomon, Bill Lotko, Mary Hudson,

Mike Wiltberger, Art Richmond, Scott McIntosh, Gang Lu, Wenbin Wang, Alan Burns, Liyang Qian, Hanli Liu, Qian Wu, Astrid Maute, and Joan Burkepile.

Thank you to the people who provided crucial technological support and guidance, Steve Hart and Kim Nesnadny. They helped me during crises of dying hard drives and computer coffee spills over the years (of which there were more than a few).

I would like to thank all of my friends at the University of Colorado, specifically McArthur Jones Jr., Daniel Bryant, Vu Nguyen, Matt Talpe, Vicki Hsu, Bobby Stillwell, Greg Lucas, Federico Gasperini, Reham Elhawary, Mike Croteau, Dimitri Krattiger, Ashwin Yerasi, Yining Shi, Alice Bradley, Ryan Handzo, Ben Bradley, Jason Leonard, Jon Herman, Jules Feldhacker, John Stark, and Jake Cooke. They have each enriched the past five years of my life and helped make this dissertation possible.

To George Born, a true mentor to me and incredible man to all. He changed the course of my entire life by bringing me to Colorado. I feel extremely fortunate to have been able to learn from him and benefit from his guidance.

Thank you to the Department of Aerospace Engineering Sciences at the University of Colorado Boulder. Participating in this program will remain one of the the most impactful and rewarding experiences of my life.

Thank you to the National Science Foundation Graduate Research Fellowship, which funded this dissertation work.

Thank you to the Los Alamos National Laboratory Space Weather Summer School, which provided me with the Vela Fellowship to pursue this research over the summer 2014 and the high performance computing access that helped make this dissertation possible.

Finally, I must thank all of the mentors and colleagues I have had the good fortune of working with over my graduate career.

Contents

Chapter

Tables

Table

Figures

Figure

Chapter 1

Preface: Why 3-D conductivity?

Some of the most deep-rooted engineering and operational concerns associated with satellite drag and collision avoidance are related to the scientific challenge of describing the three-dimensional distribution of upper atmospheric conductivity. As I describe shortly conductivity links energy sources to energy dissipation in the upper atmosphere.

For decades the scientific community has struggled to obtain global maps of ionospheric conductivities at high-latitudes with the spatial and temporal scales to match the details of auroral substorm phenomena (*Brekke and Moen*, 1993) and/or processes in the dayside cusp (*Deng et al.*, 2013). Historical treatment of ionospheric conductivity lacks continuous simultaneous observations that provide sufficient spatial and temporal coverage. However, new observations are forthcoming, and, perhaps most importantly, new techniques exist to obtain the most utility from all observations. These developments are making a 3-D picture of the ionosphere, and the electrodynamics, possible. The work in this dissertation addresses the shortcomings in current and past conductivity analyses and details a drastic improvement in the modeling of conductivity.

The ionospheric current systems, and the electrodynamics underlying their distribution, link the magnetosphere and ionosphere to neutral atmospheric circulation and couple the system from the solar wind through the bottom of the upper atmosphere (∼80 km). A number of electrodynamic processes are driven by solar wind-magnetosphere-ionosphere interactions (*Richmond and Thayer*, 2000; *Lotko*, 2007; *Amm et al.*, 2008; *Cowley*, 2000). The coupling between these regimes is largely controlled by a complex system of field-aligned, Hall, and Pedersen currents. To truly understand

these current systems, 3-D spatial and temporally evolving distributions are needed to solve the dynamics of the system, for which the salient equations are fundamentally coupled as demonstrated by (*Vasyliunas*, 1970). Accurate representation of the ionospheric distribution of currents, fields, and conductivity is crucial.

Currents and electric fields depend on conductivity as shown in Ohm's law:

$$\mathbf{J} \quad = \tilde{\sigma} \cdot \mathbf{E}' = \sigma_P \mathbf{E}'_{\perp} + \sigma_H \hat{\mathbf{B}} \times \mathbf{E}' + \sigma_{\parallel} \mathbf{E}_{\parallel}, \tag{1.1}$$

where σ_H and σ_P are the Hall and Pedersen conductivities named for E. H. Hall (*Hall*, 1879) and P. O. Pedersen (*Pedersen*, 1927), respectively. $\mathbf{E}'$ is the effective electric field, $\mathbf{B}$ is the magnetic field, and $\mathbf{J}$ is the current density. Whereas σ_P and σ_H are conductivities oriented perpendicular to the background magnetic field, $\sigma_{\parallel}$ is the conductivity along the magnetic field line. Similarly, $\mathbf{E}_{\parallel}$ is the magnetic field-aligned component of the electric field. The total conductivity is a tensor parameter given by:

$$\tilde{\sigma} = \begin{bmatrix} \sigma_P & -\sigma_H & 0 \\ \sigma_H & \sigma_P & 0 \\ 0 & 0 & \sigma_{\parallel} \end{bmatrix}. \tag{1.2}$$

Conductivity in the upper atmosphere provides an electrodynamic feedback that is important for an understanding of solar wind-magnetosphere coupling and magnetospheric configuration (*Lu et al.*, 2001; *Raeder et al.*, 2001; *Ridley et al.*, 2004; *Ebihara et al.*, 2004; *Lotko et al.*, 2014). From the magnetospheric perspective, ionospheric conductivity not only regulates the trans-magnetosphere-ionosphere field-aligned currents (*Streltsov and Lotko*, 2004; *Liemohn et al.*, 2005; *Lotko*, 2007; *Lu et al.*, 2007), but also plays a significant role in the modification of magnetopause geometry, magnetosheath flow, and, as a result, the extent to which magnetic flux from the solar wind is delivered to the magnetosphere (*Merkine et al.*, 2003; *Siscoe et al.*, 2004; *Ridley et al.*, 2004; *Lotko et al.*, 2014). Conductivity controls the configuration of the field-aligned currents mapping from the magnetosphere down into the ionosphere, as well as the system of closure currents within the ionosphere itself. These current systems are mechanisms of direct forcing of the Earth's upper

atmosphere through the input of electromagnetic energy in the form of Poynting flux and by the dissipation of this flux as Joule heating.

The partitioning of the Poynting flux between upward and downward field-aligned currents is organized by the ionospheric conductivity (*Evans et al.*, 1977). Likewise, the Joule heating is distributed according to the pattern of Pedersen conductivity in the ionosphere (*Wilson et al.*, 2006; *Sutton et al.*, 2009; *Crowley et al.*, 2010; *Li et al.*, 2011; *Deng et al.*, 2013). The ionosphere acts as a dissipator for the $\mathbf{J} \times \mathbf{B}$ force, which is largely controlled by the distribution of electric fields in the ionosphere (*Deng et al.*, 2013). These phenomena require knowledge of the region's current systems and electric fields.

Historically, magnetic perturbations measured from the ground have been used to infer current patterns in the ionosphere (*Kamide et al.* (1981), aka the Kamide-Richmond-Matsushita (KRM) method). The inversion of magnetometer data for this purpose relies on the thin-sheet approximation of the ionosphere, whereby all currents are assumed to close in a thin spherical shell at a given altitude, typically 110 km. The resulting system of currents is often referred to as the equivalent currents. However, several important issues exist with this method: 1) little or no information can be obtained about the height distribution of the currents; 2) the relative importance of the various current systems is unobservable (i.e. under a uniform conductance distribution only the equivalent, height-integrated, Hall currents are visible from the ground, and the Pedersen and field-aligned currents produce no signature in the ground-based magnetometer data (*Fukushima*, 1969, 1976)); and 3) equivalent currents, by themselves, can only provide a qualitative description of the ionospheric electrodynamics and rely on knowledge of the conductances or electric fields to specify the true ionospheric and field-aligned currents (*Amm and Viljanen*, 1999). Similar issues arise from attempts to characterize the ionospheric electrodynamics using geomagnetic indices. While geomagnetic indices can provide a proxy for the scale of the ionospheric current system, they cannot provide a global view of the structure. Further, *Kamide and Richmond* (1982) showed that the ionospheric electric field obtained from geomagnetic indices is highly dependent on the conductivity and thus is less reliable than the electric fields given by techniques that use more direct

observations from satellites and radar. They also emphasize the importance of capturing gradients in the ionospheric conductivity (see also *Cousins et al.* (2015a)) and cite the determination of a suitable distribution of conductances as the primary difficulty in the application of the theory for nonuniform conductivity.

In a broader sense, conductivity is the key element that links almost every aspect of the general circulation models (GCMs). The Thermosphere Ionosphere Electrodynamics General Circulation Model (TIEGCM) (*Richmond et al.*, 1992) and the Global Ionosphere Thermosphere Model (GITM) (*Ridley et al.*, 2006), have been extremely useful in interpreting observations and verifying hypotheses determined from other means. These GCMs yield a large degree of qualitative agreement with observations, but also contain differences that may largely be due to uncertainties in the high-latitude energy inputs (*Codrescu et al.*, 1995). Particularly, it is known that the Joule heating, one of the main energy sources of the upper atmosphere, is a function of the electric field in the ionosphere. Fluctuations in the electric field occur on a variety of temporal and spatial scales and are extremely difficult to characterize (*Matsuo and Richmond*, 2008; *Cosgrove et al.*, 2011; *Cousins and Shepherd*, 2012), especially during substorm activity. Problematic in the GCMs is a reliance on statistical averages to quantify the electric field. Statistical averages lead to an overly simplistic characterization of the ionospheric electrodynamic environment and what can amount to significant errors in the model output in general. Uncertainties and disagreement in the electric fields specified by the GCMs are exacerbated by poor knowledge of ionospheric conductivities.

The Assimilative Mapping of Ionospheric Electrodynamics (AMIE) procedure (*Richmond and Kamide*, 1988) is often used to provide distributions of electrodynamic quantities for the GCMs. AMIE brings together diverse sets of remote and in-situ ionospheric observations in a Bayesian analysis scheme with the assumption of multivariate normal prior and observational errors to estimate electrodynamic quantity distributions (*Richmond et al.*, 1988; *Knipp*, 1989; *Richmond*, 1992). Both as a self-consistent model of the ionospheric electrodynamics and as input to the GCMs, AMIE has significantly contributed to knowledge of magnetosphere-ionosphere-thermosphere (MIT) linkages, and has been applied to MIT problems in wide measure.

Recently, *Matsuo et al.* (2015) adapted the AMIE procedure to incorporate large quantities of space-based magnetometer data (see example in *Knipp et al.* (2014)). The updated AMIE model is designated AMIE NextGen, and one of the primary objectives is to extend AMIE to ingest both ground- and space-based magnetometer data. Thus, there is a pressing need to improve the height-dependent conductivity, so that these new data sets can be merged with ground- and space-based electric field observations. The results presented in this dissertation contribute to the AMIE NextGen effort to expand the utility of the AMIE procedure by improving the conductivity estimation, and supplying a significantly improved conductivity covariance model for the AMIE NextGen procedure (*McGranaghan et al.*, 2015b). The modeling improvement is especially pronounced during storm times. These accomplishments are significant given the importance of determining where energy from external drivers is deposited in the atmosphere. Lack of such information contributes to the large uncertainty in neutral density specification, especially during storm times. AMIE, and similar procedures, calculate a solution for the electrostatic potential, Φ, from which the complete macroscale electrodynamic state of the ionosphere can be specified under certain simplifying assumptions using Maxwell's equations:

$$\mathbf{E} = -\nabla\Phi \tag{1.3}$$

$$\mathbf{J}_{\perp} = \bar{\bar{\Sigma}} \cdot \mathbf{E} \tag{1.4}$$

$$\mathbf{J}_{\parallel} = \nabla \cdot \mathbf{J}_{\perp} \tag{1.5}$$

$$\nabla \times \delta\mathbf{B} = \mu_0 \mathbf{J}, \tag{1.6}$$

where:

$\mathbf{E}$ = electric field

$\bar{\bar{\Sigma}}$ = conductance distribution (assumed given *a priori*)

$\mathbf{J}_{\perp}$ = horizontal currents

$\mathbf{J}_{\parallel}$ = field-aligned currents

$\mathbf{B}$ = magnetic field

μ_0 = permeability of free space.

The field-aligned currents are derived from the divergence of the horizontal currents, $\mathbf{J}_{\parallel} = \nabla \cdot \left(\bar{\bar{\Sigma}} \cdot \mathbf{E}\right)$. Therefore, the conductance *and* its gradient are important (*Knipp*, 1989; *Sofko et al.*, 1995; *Connors*, 1998; *Cousins et al.*, 2015a). AMIE provides distributions of height-integrated conductivity (conductance) as a first step in the procedure, though the estimates are built on a formulation based on a Maxwellian auroral spectrum (*Robinson et al.*, 1987). Because auroral particle precipitation occurs in distinctive regions such as the cusp, low-latitude boundary layer (LLBL), central plasma sheet (CPS), and boundary plasma sheet (BPS) and the characteristics of precipitation across regions vary greatly (*Newell et al.*, 1991; *Newell and Meng*, 1992; *Newell et al.*, 1996a,b; *Hardy et al.*, 2008; *Newell et al.*, 2009; *McIntosh and Anderson*, 2015), simply assuming a Maxwellian distribution to describe all high-latitude precipitation can introduce large errors in conductivity specification. Replacing this base assumption is an important breakthrough for the space science community and will be a lasting contribution of this dissertation to the field.

Idealized studies have shown the importance of the height distribution of conductivity (*Huang and Burke*, 2004; *Burke et al.*, 2009). Past work on 3-D conductivity has been limited by: 1) the available observations, namely 1-D ionosondes, 2-D magnetometer systems, and 2-D treatment of satellite particle precipitation spectra; and 2) a lack of observations causing too heavy a reliance on geomagnetic indices. Two-dimensional approximations of the conductivities are unable to deal with the localized heating and ionospheric modification that influence this coupling of the upper atmospheric plasma and neutral environments. **A 3-D model of the ionospheric conductivity**

based on observations and estimation theory can directly address this uncertainty in the GCMs and the outstanding issues in the AMIE procedure.

In Chapter 2, I: 1) review the physics inherent in conductivity modeling, (Sections 2.1-2.2); 2) provide a historical perspective in this relatively young field of research (Section 2.2.7.3); and 3) outline the outstanding issues preventing robust conductivity estimates (Section 2.3). Chapter 3 explores the use of global indices and proxies for ionospheric specification and prediction and identifies the limitations associated with this approach. Subsequently, I present a new approach to conductivity modeling that advances the understanding of ionospheric conductivity itself and improves ionospheric electrodynamics specification and benefits the future of upper atmospheric and magnetospheric research (Chapters 4 - 7). In Chapter 8, I apply this new approach in three dimensions and compare the 2-D and 3-D conductivities. I provide improvements through this doctoral research that have eluded the field for 30 years. The broader impacts of this work are detailed throughout.

Chapter 2

Introduction

In this chapter I introduce the salient topics surrounding ionospheric conductivity, creating the basis for the remainder of the dissertation.

2.1 Geospace system

Geospace (the region encompassing the thermosphere, ionosphere, magnetosphere, and solar wind flowing past the Earth - see Figure 2.1) is a closely-coupled, interactive dynamical system. This section contains a brief introduction to the primary system components (i.e. the magnetosphere, ionosphere, and thermosphere).

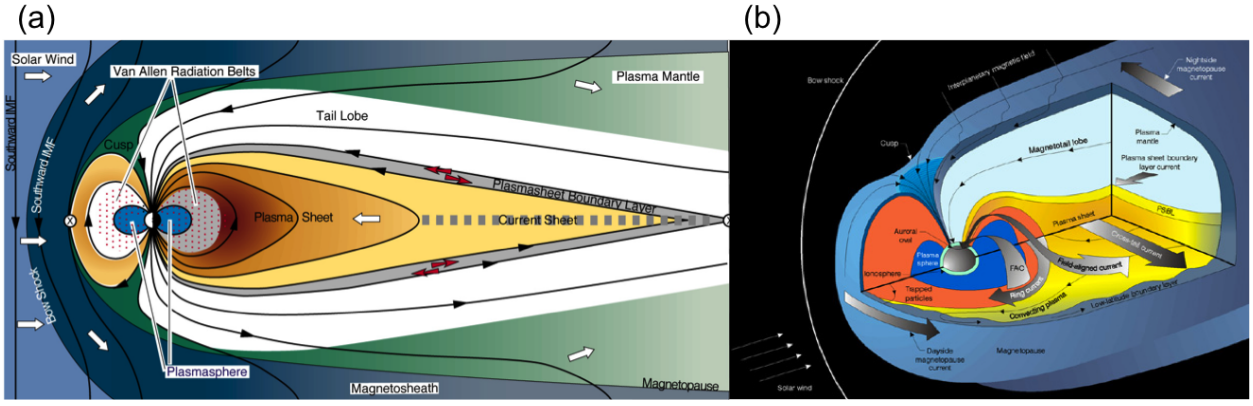

Figure 2.1: Schematic illustration of the geospace environment: (a) the solar wind-magnetosphere connection in a view of the noon-midnight meridian plane with principal magnetospheric particle regions labeled (image adapted from *The Sun-Earth Connection*, Patricia H. Reiff, Rice University); and (b) a detailed look at the magnetosphere-ionosphere connection with principal boundaries, regions and current systems shown (image adapted from Southwest Research Institute Magnetospheric Multiscale Mission webpage).

2.1.1 Magnetosphere

The magnetosphere is the region surrounding the Earth created by the balance of the Earth's magnetic field pressure and the solar wind plasma and magnetic pressures. This equilibrium is a function of the terrestrial magnetic field strength, solar wind conditions, and spatial location with respect to the Earth-Sun orientation and determines the magnetopause, or the boundary between the solar wind and the magnetosphere. For typical solar wind speeds (∼300-900 km s^{-1} (*Cowley*, 1995)) and given a terrestrial surface magnetic field strength of ∼30,000 nT at the equator the magnetopause lies ∼ 10 Earth radii (R_E) at the upstream (sunward) location. On the downstream side, the magnetotail extends many tens to hundreds of R_E. The supersonic solar wind is slowed to subsonic speeds by a standing shock upstream from the magnetopause. Across the bow shock, the flow is slowed, compressed, and heated, forming a plasma region known as the the magnetosheath.

The interaction between the magnetosphere and solar wind drives the solar-terrestrial connection and is governed by the interplanetary magnetic field (IMF) that threads the solar plasma. Two characteristics of the IMF primarily determine the extent of this interaction: 1) how closely the field is tied to, or 'frozen-into', the solar wind plasma (*Kivelson and Russell*, 1995); and 2) the orientation with respect to the Earth's terrestrial magnetic field. When the magnetic field and plasma are strongly tied together (i.e. when the frozen-in flux condition holds) the plasma satisfies $\mathbf{E} + \mathbf{v} \times \mathbf{B} = 0$, where $\mathbf{E}$ is the electric field, $\mathbf{v}$ is the velocity, and $\mathbf{B}$ is the magnetic field, and the time rate of change of magnetic flux along the path of a fluid element is zero. Under these conditions the solar wind and magnetospheric plasmas cannot interact. However, as the frozen-in condition is relaxed the IMF diffuses relative to the plasma in the magnetopause, and the IMF and terrestrial magnetic fields interact in a process known as magnetic reconnection (*Dungey*, 1961; *Eastwood et al.*, 2013; *Cassak*, 2016). The extent and location of reconnection is strongly dependent on the IMF orientation. Figure 2.2 shows the Dungey model of magnetic reconnection and details that reconnection preferentially occurs under southward IMF conditions (top). Figure 2.2a shows the reconnection geometry believed to be most effective for energy transfer between the solar

wind the geospace.

Reconnection produces a linkage between IMF field lines and terrestrial field lines, resulting in "open" magnetic field lines with one end connected to the Earth and the other in the solar wind (*Russell*, 2000). When the IMF has a southward component he newly formed field lines experience large tension forces that accelerate plasma towards the flanks of the magnetosphere on the dayside and then slows the plasma as the field lines are stretched antisunward. The net result is a transfer of a fraction of the solar wind energy to the magnetosphere. The magnetic energy stored in the magnetotail is then released via reconnection as the tail field lines are forced together, causing acceleration of plasma into the magnetosphere itself as well as downtail. The plasma and reconnected field move from the magnetotail towards the Earth and eventually reach the dayside where the process is repeated. This cycle represents a circulation of magnetospheric plasma known as the Dungey cycle of magnetospheric convection (*Dungey*, 1961). The Dungey cycle imposes a large-scale convection of plasma on the ionosphere as plasma moves along with the footpoints of the convected magnetic field lines. Figure 2.3 shows a schematic of the Dungey cycle for southward IMF and the ionospheric projection of the plasma and magnetic field motion (inset).

Reconnection does occur under northward IMF conditions (Figure 2.2b-c), though the reconnection occurs towards the poles of the terrestrial magnetic field (*Gosling et al.*, 1991) rather than the subsolar point as with southward IMF conditions. The effect on the magnetosphere is markedly different, sometimes producing focused convection that stirs open field lines in the polar cap (*Crooker*, 1992; *Raeder et al.*, 1995).

2.1.1.1 Magnetospheric plasma populations

The magnetosphere is composed of several principal plasma populations, shown schematically in Figure 2.4 and summarized in Table 2.1.

The magnetosheath is located just outside of the magnetopause and consists of warm plasma (100 eV – 1 keV). In the dayside cusp locations (one in each hemisphere) the magnetosheath plasma has direct entry to the Earth's ionosphere. As the magnetosheath plasma moves Earthward

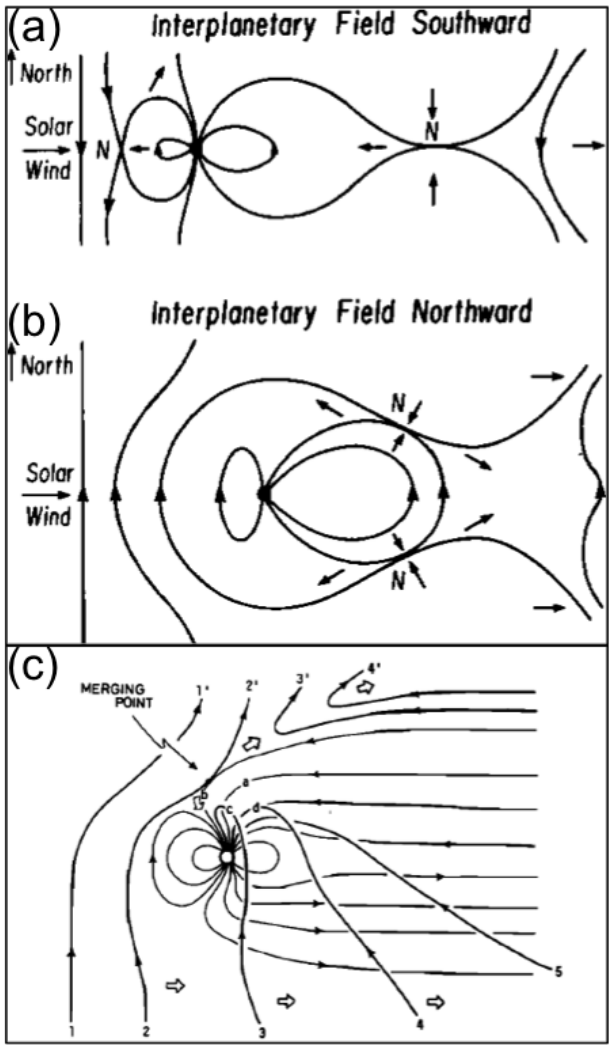

Figure 2.2: (a) *Dungey* (1961) model of magnetic reconnection for southward IMF (top) and (b) northward IMF (middle). (c) *Maezawa* (1976) model of magnetic reconnection for northward IMF (bottom).

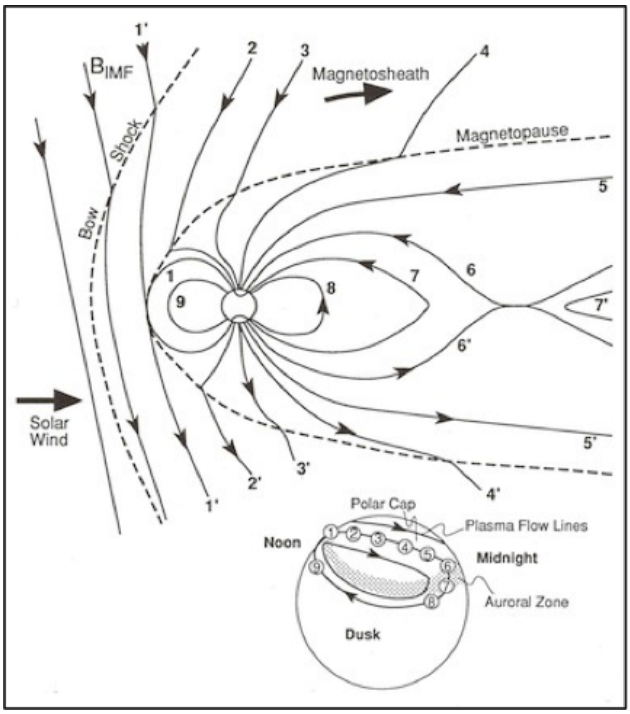

Figure 2.3: Schematic of the Dungey cycle of magnetospheric convection. The inset figure shows the ionospheric projection of the plasma and magnetic field motion. Figure from *Kivelson and Russell* (1995).

Table 2.1: Magnetospheric plasma populations and approximate characteristics[1].

Population	Energy	Density	Location
Magnetosheath	100 eV - 1 keV	$\sim$4 n_{sw}	>10 R_E upstream and on flanks
Plasma mantle	$\sim$100 eV	0.01-1 cm^{-3}	–
Inner-magnetotail	10 eV - 100 eV	variable	100-200 R_E downstream
Plasma sheet	few keV	$\sim$1 cm^{-3}	ionosphere – magnetotail
Plasmasphere	1 eV	$\sim$50-2000 cm^{-3}	$\sim$1-6 R_E
Ring current	10-100 keV	$\sim$1 cm^{-3}	just outside equatorial plasma sheet
Inner radiation belt	0.1-10 MeV	highly variable	1-2 R_E
Outer radiation belt	0.1-10 MeV	highly variable	4-7 R_E

[1] Table values compiled from *Kivelson and Russell* (1995) and (*Borovsky and Cayton*, 2011, and references therein).

it encounters continuously increasing magnetic field strength, and is repelled and deflected toward the outer portion of the magnetotail, forming the plasma mantle. The plasma in the mantle is convected toward the mid-magnetotail as it flows downstream, eventually reaching the inner part of the tail at distances $>$ 100 R_E. This location is characterized by low energies (10-100 eV). The inner-magnetotail at distances closer to Earth ($<$ 100 R_E) is populated by ionospheric outflow (polar wind in Figure 2.4). The Earthward regime of relatively dense ($\sim$1 cm^{-3}) and hot (few keV) plasma is known as the plasma sheet. The hot population of the plasma sheet gives way to corotating plasma at the Earthward boundary. The region of corotation is known as the plasmasphere. The plasmasphere is a torus-shaped region occupying the section of the magnetosphere roughly between 1-6 R_E. This region is closely tied to the ionosphere, corotates with the Earth, and is filled largely by outflowing ionospheric ions. Due to the influence of both the hot plasmas of the magnetosphere and the cold plasmas of the topside ionosphere at either boundary, the plasmasphere is highly variable. Just beyond the plasma sheet in the equatorial plane is the highly variable ring current population, sourced by energized magnetospheric plasma, and is characterized by hot, tenuous plasma.

Finally, the radiation belts consist of two concentric rings, one populated by highly energetic electrons (outer belt) and and the other by protons (inner belt) that partially overlap with the plasmasphere.

Each magnetospheric location has a projection into the ionosphere, mapping along magnetic

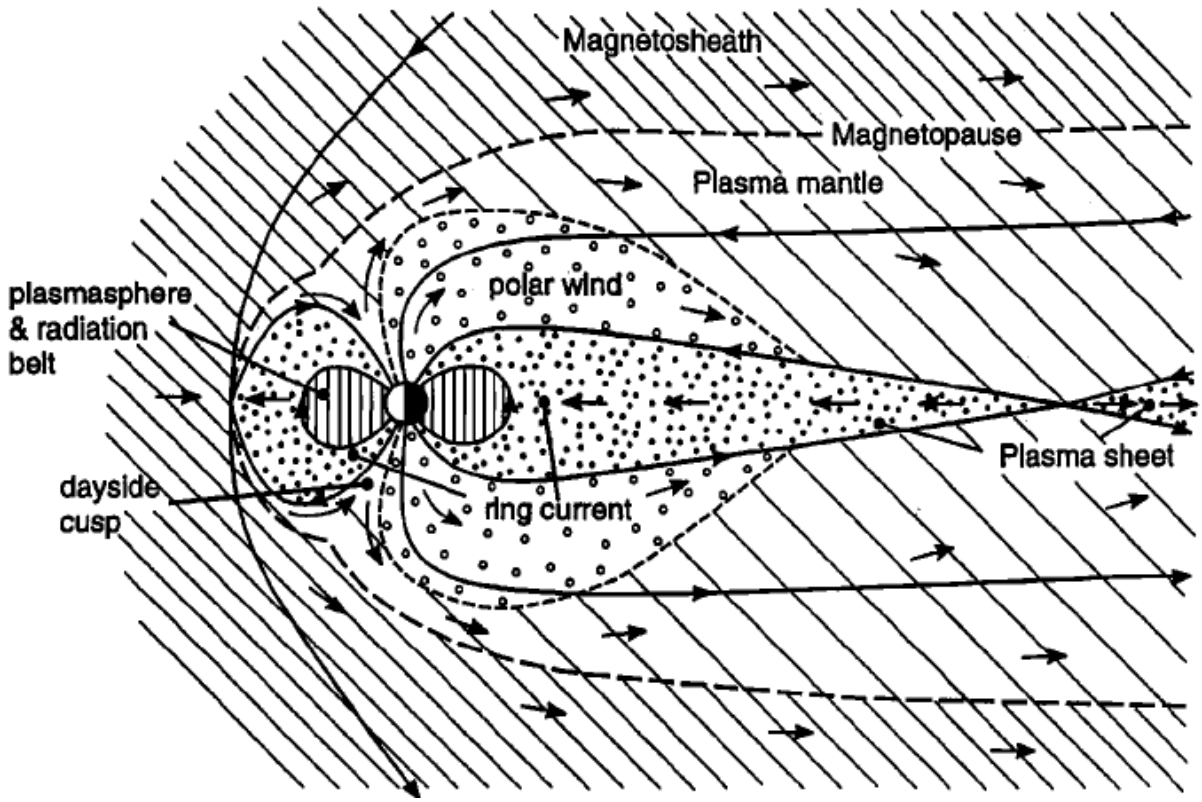

Figure 2.4: Schematic of the principal plasma populations of the magnetosphere. Figure from *Cowley* (1995).

field lines to their Earthward footpoints located in the high-latitude ionosphere.

2.1.2 Ionosphere

The ionosphere is the region of Earth's upper atmosphere composed of partially ionized plasma that extends from roughly 60 to 1000 km (from the top of the lower atmosphere to the bottom of the magnetosphere). The ionospheric plasma is created primarily by photoionization of neutral molecules via solar extreme ultraviolet (EUV) and soft x-ray radiation (*Schunk and Nagy*, 2009). However, in certain locations, such as the high-latitudes and auroral region, particles precipitating from the magnetosphere can be the dominant ionization mechanism. Though the low, mid, and high latitudes exhibit different behavior due to unique dominant physical processes, the electron density variation with altitude that characterizes the ionospheric structure has the same basic structure at all latitudes. The basic structure consists of three layers called the D, E, and F Regions (Figure 2.5).

The D Region ionosphere primarily exists on the dayside, and is essentially destroyed by nightside ion recombination. In the D and E Regions chemical processes are dominant and molecular ions are most abundant. Specifically, NO^+, O_2^+, and N_2^+ are the major E Region ions and the plasma density is $\sim 10^5\ cm^{-3}$, while the neutral density is $\sim 10^{11}\ cm^{-3}$. Therefore, the E Region plasma is weakly ionized. The F Region is divided into F1 (~150-250 km) and F2 (>250 km) layers and marks the altitude regime where transport processes become important. The plasma density maximizes in the F2 Region, but remains roughly two orders of magnitude smaller than the neutral density ($\sim 10^6\ cm^{-3}$ at maximum in the F2 Region versus $\sim 10^8\ cm^{-3}$ for the neutral density in the same location) such that the plasma in this region is partially ionized. In the topside ionosphere, above the F2 Region, the plasma becomes fully ionized and plasma transport processes completely control the dynamics.

The ionosphere is discussed in further detail in the context of conductivity below in Section 2.2.

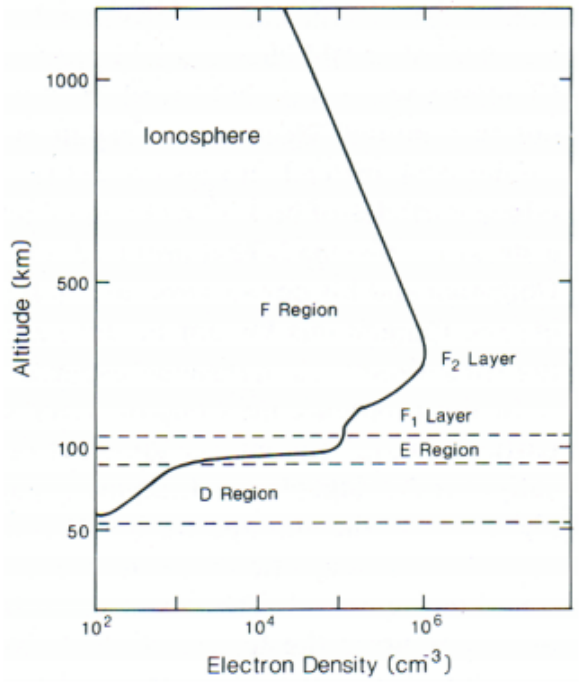

Figure 2.5: Typical daytime ionospheric electron (plasma) density altitudinal profile. Figure from *Kivelson and Russell* (1995).

2.1.3 Thermosphere

The ionosphere is collocated in space with the neutral component of Earth's upper atmosphere, the thermosphere. Figure 2.6 shows the constituent ion and neutral vertical density profiles throughout the upper atmosphere.

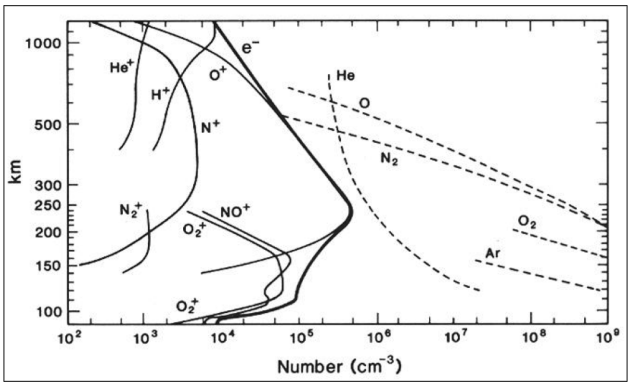

Figure 2.6: Upper atmospheric constituent density altitudinal profiles. Figure from *Schunk and Nagy* (2009).

The thermospheric density distribution is determined primarily by photodissociation of the dominant N_2 and O_2 molecules and through diffusion-enabled gravitational separation of different neutral constituents. As a result, the heavier molecules dominate at lower altitudes while lighter atomic species dominate at higher altitudes (*Schunk and Nagy*, 2009). The neutral densities decrease exponentially with altitude. At altitudes below ∼110 km the thermosphere is turbulent and thermospheric constituents are well-mixed. Between 110-500 km, diffusion is more important, and the constituents are diffusively separated. In this regime charged-neutral interactions are most important, closely coupling the ionosphere and thermosphere. Above 500 km, neutral densities, and their collisions with other neutral or ionized constituents, are low such that ionosphere-thermosphere (IT) interactions are minor.

2.1.4 System coupling

The magnetosphere and ionosphere are strongly coupled, interacting electromagnetically and through the exchange of mass. The electromagnetic interactions are strongest and are primarily

determined by the system of currents flowing along magnetic field lines, or field-aligned currents (FACs), between the two regimes (see Figure 2.7 reproduced from *Le et al.* (2010)). As shown, these currents map into and out of the high-latitude ionosphere where field lines are essentially radial.

FACs are carried by the motion of electrons and ions along magnetic field lines. The degree to which these particles are tied to, or frozen into (as introduced above), the magnetic field is determined by the ratio of the particles' collision frequency with neutral particles to the angular gyrofrequency around the field line (*Richmond and Thayer*, 2000). At altitudes greater than ∼200 km, the gyrofrequencies are much larger and the particles move along the field lines. Below 200 km, in the collisional ionosphere, these particles undergo differential motion due to differences in collision frequencies with the neutral particles. The differential motion and current continuity cause the FACs to close horizontally in the ionosphere. These horizontal closure currents, oriented either perpendicular (Hall) or parallel (Pedersen) to the ionospheric electric field are critical to the dynamics and configuration of both the ionosphere and magnetosphere (*Iijima and Potemra*, 1976a, 1978; *Iijima*, 2000). The ionospheric effects subsequently drive changes in the thermospheric state. The parameter that governs the closure paths of FACs through the ionosphere is the ionospheric conductivity, and it therefore exerts large influence over the entire MIT system. The conductivity is the central focus of this dissertation.

2.2 Conductivity

Electrodynamic processes largely dictate ionospheric dynamics and energetics. To characterize these electrodynamic processes, it is important to understand the system of electric fields and currents present in this region as well as their temporal and spatial variations. Electric fields, **E**, and currents, **J** can be related if knowledge of the conductivity is available. It is instructive to first briefly mention the physical basis of conductivity. Electrical conductivity describes the ability of a medium to carry electrical current. It is the reciprocal of resistivity and measured in units of *mhos/m*, or equivalently *Siemens/m*.

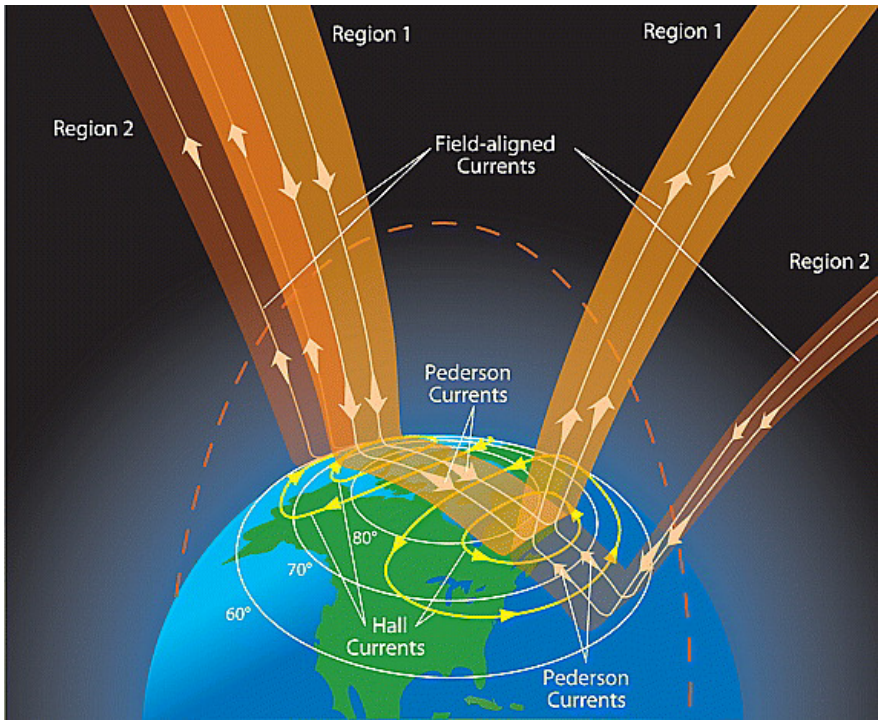

Figure 2.7: Schematic representation of the large-scale field-aligned currents (FACs) coupling the magnetosphere to the high-latitude ionosphere. The horizontal closure paths in the ionosphere perpendicular and parallel to the electric field are known as the Hall and Pedersen currents, respectively. Figure reproduced from *Le et al.* (2010).

To relate electric fields to currents, one must begin with the momentum equation for the charged ionospheric particles in a reference frame that is rotating with the neutral gas (the development in this section follows those given by *Kamide* (1988); *Schunk and Nagy* (2009)):

$$\begin{aligned}\rho_s \frac{D_s \mathbf{u}_s}{Dt} + \nabla p_s + \nabla \cdot \tau_s - n_s e_s(\mathbf{E} + \mathbf{u}_s \times \mathbf{B}) \\ + \rho_s \left[-\mathbf{G} + 2\Omega_r \times \mathbf{u}_s + \Omega_r \times (\Omega_r \times \mathbf{r})\right] \\ = \sum_t n_s m_s \nu_{st}(\mathbf{u}_t - \mathbf{u}_s) + \sum_t \nu_{st} \frac{z_{st}\mu_{st}}{kT_{st}} \left(\mathbf{q}_s - \frac{\rho_s}{\rho_t}\mathbf{q}_t\right),\end{aligned} \tag{2.1}$$

where:

$\mathbf{r}$ = radius vector from the center of the Earth

Ω_r = angular rotation rate of the Earth

$\mathbf{q}_s$ = heat flow of species

τ_s = stress on the species

ρ_s = mass density of species

n_s = number density of species

$\mathbf{u}_s$ = average drift velocity of species

p_s = gas pressure of species

μ_{st} = reduced mass

T_{st} = reduced temperature

ν_{st} = momentum transfer collision frequency

z_{st} = Chapman-Cowling integrals

e_s = electron charge

$\mathbf{G}$ = acceleration due to gravity

$\mathbf{E}$ = electric field

$\mathbf{B}$ = geomagnetic field

T_{st} = reduced temperature

$$\frac{D_s\mathbf{u}_s}{Dt} = \frac{\partial \mathbf{u}_s}{\partial t} + (\nabla \times \mathbf{u}_s) \times \mathbf{u}_s + \nabla\left(0.5\mathbf{u}_s^2\right)$$

= convective derivative

k = Boltzmann's constant,

and the subscript s refers to the specie being considered.

In this work, the ionospheric electrodynamics are the primary focus, thus I neglect the effects of pressure gradients, gravity, and stress forces presently. When electric fields influence dynamic

motion in a strongly magnetized volume (such as the Earth's ionosphere), the currents are normally broken down into components along and across **B**. Because electric current density is given by $\mathbf{J} = ne\mathbf{u}$, we must solve for velocities to get currents. The electric current density and Ohm's law (Eq. 1.1) can be combined to allow us to solve for conductivities.

If we first consider the cross-**B** flows, we can simplify Eq. 2.1 with the reasonable assumption that the electric field dominates the perpendicular flow:

$$-\frac{e_j}{m_j}\left(\mathbf{E}_\perp + \mathbf{u}_j \times \mathbf{B}\right) = \sum_t \nu_{jt}(\mathbf{u}_t - \mathbf{u}_j), \tag{2.2}$$

It is understood that the electric field can cause motion of both electrons and ions across the magnetic field, so in Eq. 2.2 subscript j refers to electrons or one of the ion species and the summation over t includes all other species.

Let us first look at the ion motion. Eq. 2.2 for the ion constituents can be simplified with three assumptions: 1) momentum exchange due to collisions with electrons is negligible due to the much smaller mass of electrons, 2) transfer of momentum due to ion-ion collisions is small compared to ion-neutral collisions because ion drifts are very similar and the neutral density is much greater than ion densities, and 3) a single neutral drift velocity is consistent for all neutral constituents. With these assumptions Eq. 2.2 for ions becomes:

$$-\frac{e_i}{m_i}\left(\mathbf{E}_\perp + \mathbf{u}_i \times \mathbf{B}\right) = \sum_n \nu_{in}(\mathbf{u}_i - \mathbf{u}_n). \tag{2.3}$$

This equation must be solved for the perpendicular average ion drift velocity, $\mathbf{u}_{i\perp}$ (recall that the present development is focused on the component of motion perpendicular to **B**). Let us first rotate to a reference frame rotating with the neutral wind ($\mathbf{u}_i \rightarrow \mathbf{u}'_i + \mathbf{u}_n$) and simplify the notation for the ion collision summation, $\sum_n \nu_{in} \rightarrow \nu_i$. This gives:

$$-\frac{e_i}{m_i}\left(\mathbf{E}'_\perp + \mathbf{u}'_i \times \mathbf{B}\right) = \nu_i(\mathbf{u}'_i) \tag{2.4}$$

$$-\frac{e_i}{m_i\nu_i}\left(\mathbf{E}'_\perp + \mathbf{u}'_i \times \mathbf{B}\right) = (\mathbf{u}'_i) \tag{2.5}$$

$$-\frac{e_i}{m_i\nu_i}\mathbf{E}'_\perp + \frac{\omega_{c_i}}{\nu_i}\mathbf{u}'_i \times \mathbf{b} = \mathbf{u}'_i, \tag{2.6}$$

where:

$$\mathbf{E}'_\perp = \mathbf{E}_\perp + \mathbf{u}_n \times \mathbf{B} = \text{effective electric field}$$
$$\omega_{c_i} = \frac{e_i B}{m_i} = \text{cyclotron frequency (or gyrofrequency))}$$
$$\mathbf{b} = \frac{\mathbf{B}}{B}.$$

The individual velocity components can be solved for using a Cartesian reference frame with $\mathbf{E}'_\perp$ along the x-axis and $\mathbf{b}$ along the z-axis. Often in current calculation procedures, the magnetic field lines are assumed to be radial at high-latitudes. This allows a simplification in the electrodynamic calculations in this region that I will introduce later. From an isolation of the velocity components and a reformulation in terms of vectors, we see:

$$\mathbf{u}'_{i\perp} = \frac{e_i}{m_i}\left(\frac{\nu_i}{\nu_i^2 + \omega_{c_i}^2}\mathbf{E}'_\perp - \frac{\omega_{c_i}}{\nu_i^2 + \omega_{c_i}^2}\mathbf{b} \times \mathbf{E}'_\perp\right), \tag{2.7}$$

where, transforming back to the original reference frame ($\mathbf{u}'_i \rightarrow \mathbf{u}_i - \mathbf{u}_n$) yields:

$$\mathbf{J}_{i\perp} = n_i e_i \mathbf{u}_{n\perp} + \sigma_i\left(\frac{\nu_i}{\nu_i^2 + \omega_{c_i}^2}\mathbf{E}'_\perp - \frac{\omega_{c_i}}{\nu_i^2 + \omega_{c_i}^2}\mathbf{b} \times \mathbf{E}'_\perp\right). \tag{2.8}$$

Here, $n_i e_i \mathbf{u}_{n\perp}$ is the perpendicular ion current and $\sigma_i = \frac{n_i e_i^2}{m_i \nu_i}$ is the ion conductivity. The equations for the electrons are very similar assuming that the neutral density is typically much greater than the ion density, which allows the electron-ion collisional momentum exchange to be neglected. The only change is in the sign of the electric charge:

$$\mathbf{J}_{e\perp} = -n_e e_e \mathbf{u}_{n\perp} + \sigma_e\left(\frac{\nu_e}{\nu_e^2 + \omega_{c_e}^2}\mathbf{E}'_\perp - \frac{\omega_{c_e}}{\nu_e^2 + \omega_{c_e}^2}\mathbf{b} \times \mathbf{E}'_\perp\right), \tag{2.9}$$

where similar relationships to the ion momentum equation exist:

$$\mathbf{J}_{e\perp} = n_e e_e \mathbf{u}_{n\perp}$$
$$\nu_e = \sum_n \nu_{en}$$
$$\sigma_e = \frac{n_e e_e^2}{m_e \nu_e}$$
$$\omega_{c_i} = \frac{|e|B}{m_e}.$$

The total perpendicular current density is defined as the sum of the electron and all ion perpendicular current densities, which yields:

$$\mathbf{J}_\perp = \left(\sum_i n_i e_i - n_e e\right) \mathbf{u}_{n\perp} + \sigma_P \left(\mathbf{E}_\perp + \mathbf{u}_\perp \times \mathbf{B}\right) + \sigma_H \mathbf{b} \times \left(\mathbf{E}_\perp + \mathbf{u}_\perp \times \mathbf{B}\right). \tag{2.10}$$

The component conductivities, Pedersen, σ_P, parallel to $\mathbf{E}_\perp$ and Hall, σ_H, perpendicular to $\mathbf{E}_\perp$, are given by:

$$\sigma_P = \sum_i \sigma_i \frac{\nu_i^2}{\nu_i^2 + \omega_{c_i}^2} + \sigma_e \frac{\nu_e^2}{\nu_e^2 + \omega_{c_e}^2}, \tag{2.11}$$

and

$$\sigma_H = -\sum_i \sigma_i \frac{\nu_i \omega_{c_i}}{\nu_i^2 + \omega_{c_i}^2} + \sigma_e \frac{\nu_e \omega_{c_e}}{\nu_e^2 + \omega_{c_e}^2}. \tag{2.12}$$

If we now look at the component of the current along $\mathbf{B}$, or the field-aligned component, we must again start with Eq. 2.1. Immediately, some simplifications can be made. Due to the small electron mass, the momentum transfer to them is negligible and both terms on the left hand side modulated by the electron mass can be neglected. Second, the heat flow terms are small between electrons, ions, and neutrals in a partially ionized plasma and can also be neglected. Finally, the stress on the species, τ_s, is proportional to $\mathbf{u}_i - \mathbf{u}_u$ and can be neglected for most ionospheric applications. This yields:

$$\nabla_\parallel p_s + n_s e_s \mathbf{E}_\parallel = \sum_t n_s m_s \nu_{st} (\mathbf{u}_t - \mathbf{u}_s)_\parallel, \tag{2.13}$$

where $\mathbf{E}_\parallel$ is an applied electric field whose magnitude is much greater than the polarization electric field, which is ignored, given the mobility of charge carriers. Because of the much greater mobility of electrons along $\mathbf{B}$, the electron drift velocity is much greater than that of the neutrals or ions. If we choose to neglect these smaller drift velocities and write Eq. 2.13 in terms of the electron momentum, it becomes:

$$kT_e \nabla_\parallel n_e + k n_e \nabla_\parallel T_e + n_e e \mathbf{E}_\parallel = -\left(\sum_i \nu_{ei} + \sum_n \nu_{en}\right) n_e m_e \mathbf{u}_{e\parallel}, \tag{2.14}$$

where the substitution $p_e = n_e k T_e$ has been made. The field-aligned current density can be defined as $\mathbf{J}_\parallel = -e n_e \mathbf{u}_{e\parallel}$, and Eq. 2.14 becomes:

$$\mathbf{J}_\parallel = \sigma_e \left(\mathbf{E}_\parallel + \frac{k T_e}{e n_e} \nabla_\parallel n_e \right) + \bar{\varepsilon}_e \nabla_\parallel T_e, \tag{2.15}$$

where:

$$\sigma_e = \frac{n_e e^2}{m_e \left(\sum_i \nu_{ei} + \sum_n \nu_{en} \right)} = \text{parallel electrical conductivity}$$

$$\bar{\varepsilon}_e = \frac{n_e e k}{m_e \left(\sum_i \nu_{ei} + \sum_n \nu_{en} \right)} = \text{current flow conductivity due to thermal gradients.}$$

In the limiting case where the applied electric field dominates the pressure terms, Eq. 2.15 reduces to Ohm's law $\mathbf{J}_\parallel = \sigma_e \mathbf{E}_\parallel$.

Both field-aligned and perpendicular current expressions contribute to the high-latitude electrodynamic state of the ionosphere, but I first focus on the perpendicular component whose altitude-dependence is a key piece in describing where energy is deposited in the atmosphere.

The calculation of the perpendicular conductivities is an indirect one. Thus, there are additional calculations and considerations to be made with the knowledge of energy input and determining conductivity distributions throughout the ionosphere. Namely, the considerations can be broadly categorized into four contributing factors:

- geomagnetic field,
- collisions,
- ion production, and
- electron and proton/ion transport.

These factors have been incorporated into the methodology I present in Chapter 4.

Thermospheric winds also affect the dynamics of the IT system (*Hagan and Forbes*, 2002; *Forbes et al.*, 2003; *Wu et al.*, 2008a,b), however this work focuses on the ionizing sources and

electrodynamic processes and thus only solar radiation and particle precipitation are given detailed treatment.

2.2.1 Contributing factor: Geomagnetic field

The intrinsic magnetic field controls the motion of charged particles in the ionosphere. Charged particles are constrained to move along these magnetic field lines unless acted upon by a force able to separate the two. Collisions and drift forces are the two primary disruptors of charged particle motion along the Earth's magnetic field lines. Therefore, to a large degree, the magnetic field directs the dynamics of charged particles throughout the entire atmosphere and organizes the effects that external driving processes have on the ionosphere. At ionospheric altitudes ($\sim$ 100-1000 km) it is appropriate to model this field using the International Geomagnetic Reference Field (IGRF) (*International Association of Geomagnetism and Aeronomy, Working Group V-MOD. Participating members et al.*, 2010), which is a well-established and commonly-used numerical model of the internal field and is updated roughly every five years. The IGRF model represents the internal magnetic field $\mathbf{B}(r, \theta, \phi, t)$ in terms of a scalar potential $V(r, \theta, \phi, t)$, for which the relationship is $\mathbf{B} = -\nabla V$. V is represented as a finite potential:

$$V(r, \theta, \phi, t) = a \sum_{n=1}^{N} \sum_{m=0}^{n} \left(\frac{a}{r}\right)^{n+1} [g_n^m(t) \cos m\phi + h_n^m(t) \sin m\phi] \times P_n^m(\cos\theta), \tag{2.16}$$

where:

r = radial distance from center of the Earth

g_n^m and h_n^m = Gauss coefficients

a = magnetic reference spherical radius, 6371.2 km

θ = geocentric co-latitude

ϕ = east longitude

$P_n^m(\cos\theta)$ = Schmidt quasi-normalized Legendre functions.

The expansion coefficients are obtained by fits of the magnetic potential to a set of ground-based and satellite magnetometer measurements on a global scale. The resulting field represents the constant magnetic field and its secular variation.

2.2.2 Contributing factor: Collisions

Collisions disrupt magnetic field-aligned motion of charged particles. Here, a more complete discussion is provided.

Basic principles in the ionosphere organized by collisions

Collisional processes in the ionosphere are directly dependent on the densities of the charged and neutral particle populations, for which higher densities correspond to higher collision frequencies. The electron density profile exhibits a layered structure at all latitudes, with distinct layers called *D*, *E*, and *F* Regions. The ionosphere is described by these three regions because the dominant physical process in a particular altitude region is largely determined by the electron density and the collision frequency. Conductivities perpendicular to the background magnetic field, Hall and Pedersen, peak in the E-region (∼90-160 km) and I therefore focus on this layer.

Figure 2.8 [Jeff Thayer *personal communication*, 2016], shows a general picture of the high-latitude E Region ion and electron mobilities and current direction perpendicular to the background magnetic field as a function of altitude. The altitude dependence of the current density is inherently tied to the collisions that electrons and ions undergo with the neutral species. Figure 2.8 ignores the electron-neutral collisions.

In Figure 2.8 the pink vector labeled $\vec{V}_e$ represents the velocity of the electrons, and the blue vector labeled $\vec{V}_i$ is the ion velocity. The resultant current is shown in green and labeled $\vec{j}_\perp$ (signifying perpendicular to the background magnetic field which is directed into the page). The velocities, $\vec{V}_e$ and $\vec{V}_i$, and the current, $\vec{j}_\perp$, are the same as those represented by $\mathbf{u}_e$, $\mathbf{u}_i$, and $\mathbf{J}_\perp$ in the previous section, respectively. The direction of $\vec{j}_\perp$ with respect to the perpendicular electric

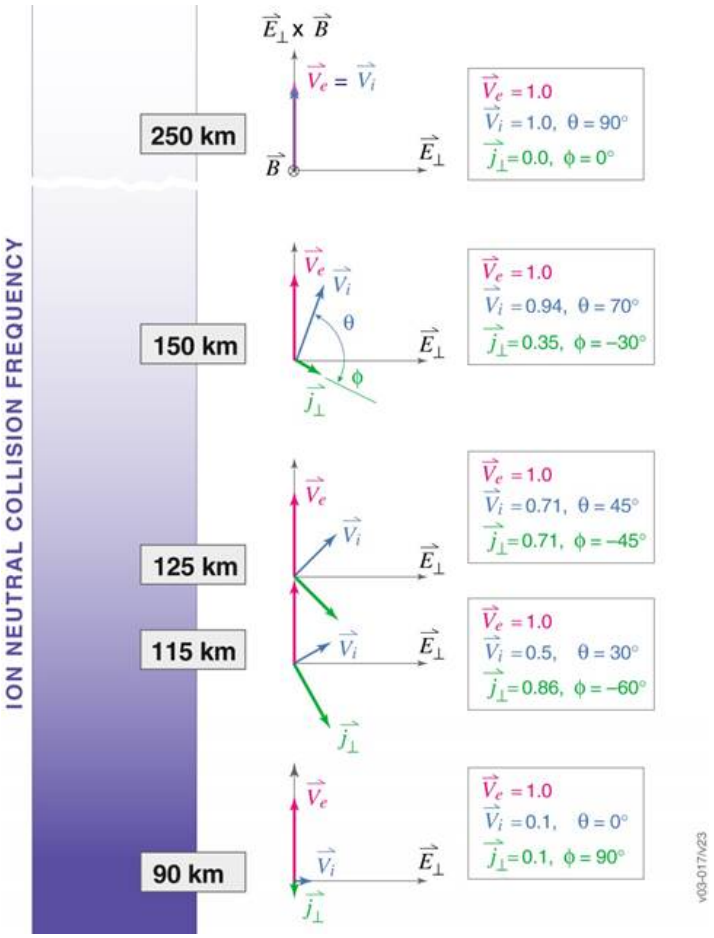

Figure 2.8: Altitude dependency of the perpendicular ionospheric current $\vec{j}_\perp$. The magnetic field is directed into the page and the perpendicular electric field is to the right. $\vec{V}_e$ and $\vec{V}_i$ are the velocities of the electrons and ions, respectively. Image citation: Jeff Thayer [*personal communication*, 2016].

Table 2.2: Typical ionospheric parameters by region (*Kivelson and Russell*, 1995).

Region	Altitude km	Electron density cm^{-3}	Dominant constituent(s) –	Ion-neutral collision frequency s^{-1}	Electron-neutral collision frequency s^{-1}	Predominant energetics
D	60-90	10^2-10^4	NO^+, O_2^+	$> 3 \times 10^3$	$> 10^5$	collisional
E	90-160	10^5	NO^+, O_2^+	1.5×10^3	5×10^4	geomagnetic field
F	160-300	10^5-10^6	O^+	1	10^3	$\mathbf{E} \times \mathbf{B}$

field is given by:

$$\phi = \tan^{-1}\left(\frac{-\nu_{in}}{\omega_{c_i}}\right), \tag{2.17}$$

where ν_{in} represents the ion-neutral collision frequency and ω_{c_i} is the ion gyrofrequency. The $\mathbf{E}\times\mathbf{B}$ direction is towards the top of the figure. At altitudes greater than 200 km, generally considered outside of the E-region, the ion and electron motions are minimally affected by collisions with neutral particles. However, as the altitude decreases the more massive ions begin to be deflected from $\mathbf{E}\times\mathbf{B}$ drift motion and a current develops. These currents can be broken down into components perpendicular and parallel to the electric field, the Hall and Pedersen currents, respectively. The direction and strength of the electric field-driven currents change dramatically as a function of altitude primarily due to the ion-neutral collision frequency. Near 120 km, the $\frac{\nu_{in}}{\omega_{c_i}}$ ratio reaches a value of one and the Hall and Pedersen currents are nominally equal. Below 120 km, the ions are effectively tied to the motion of the neutrals because ν_{in} exceeds ω_{c_i} significantly, and in this regime the current is small and almost exclusively in the Hall direction.

Table 2.2 gives a general overview of the ionospheric collisions and electron densities. This table provides a heuristic for the behavior in each ionospheric region and is a useful reference for the remainder of this dissertation.

Collisions are inherently tied to the energetics and dynamics of the ionosphere. Two forms of collision are important in the IT system: 1) elastic collisions where the mass, momentum, and energy of the colliding particles are conserved and no particles are created or destroyed, and 2) inelastic collisions in which the internal states of the particles are altered and particles may be created or destroyed. As a heuristic principle, elastic collisions dominate for low energies and inelastic

collisions become increasingly dominant as the relative kinetic energy increases (*Banks et al.*, 1974).

Elastic collisions

Elastic collisions are not causes of ionization, chemical reactions, or electronic excitation and thus are not important to these terms in ionospheric continuity. However, elastic collisions have a greater effect on momentum perturbation (transport processes) than do ionization processes and are important in terms of ionospheric momentum. The Boltzmann collision integral governs the rate of change of a velocity distribution due to binary elastic collisions $\left(\frac{\delta f_s}{\delta t}\right)$ and is given by:

$$\frac{\delta f_s}{\delta t} = \int\int d^3 v_t d\Omega g_{st} \sigma_{st}(g_{st}, \theta)(f'_s f'_t - f_s f_t), \tag{2.18}$$

where:

$d^3 v_t$ = velocity-space volume element for the target species, t

$g_{st} = |\mathbf{v}_s - \mathbf{v}_t|$ relative speed of colliding particles s and t

$d\Omega$ = element of solid angle in colliding particles' center of mass reference frame

θ = center of mass scattering angle

$\sigma_{st}(g_{st}, \theta)$ = differential scattering cross-section, defined as the number of molecules scattered per solid angle $d\Omega$, per unit time, divided by the incident intensity

$f'_s f'_t = f_s(\mathbf{r}, \mathbf{v}'_s, t) f_t(\mathbf{r}, \mathbf{v}'_t, t)$ where the primes indicate the distribution functions are evaluated with the particle velocities after the collision.

In order to evaluate the Boltzmann collision integral, we require differential scattering cross-sections. The differential cross-section for a given collision is a function of the interparticle force laws, relative velocity, and the impact parameter, which is the perpendicular distance from one particle to the second particle in the scattering plane. The general equation for the scattering angle will not be derived here, but is given:

$$\chi(b, g) = \pi - 2 \int_{r_m}^{\infty} \frac{b}{r^2} \left[1 - \frac{b^2}{r^2} - \frac{2V(r)}{\mu g^2}\right]^{-0.5} dr, \tag{2.19}$$

where:

$$r_m, \theta_m = \text{coordinates of closest approach}$$

$$\chi = \pi - 2\theta_m = \text{scattering angle}$$

$$b = \text{impact parameter}$$

$$g = \text{relative velocity}$$

$$V(r) = \text{inter particle potential energy function.}$$

In laboratory measurements a beam of particles are fired at target particles and the differential scattering section is measured. The differential angle can be used to calculate the total scattering and momentum transfer cross-sections. When dealing with a particle velocity distribution, transfer collision integrals, which represent the change in a transport property like energy or momentum, are important. Transfer integrals play a role in the current work because they allow a determination of the physical effects due to elastic collisions.

Inelastic collisions

Whereas elastic collisions contribute to transport processes, inelastic collisions change the makeup of the ionosphere. Inelastic collisions cause a change in the internal states of the colliding particles and are increasingly important as the relative kinetic energy between the particles grows. These collisions are responsible for the chemical kinetics, photoionization, and impact ionization processes that occur in the ionosphere and therefore play a fundamental role in the structure, composition, and dynamics. In the remainder of this subsection, the most important chemical kinetic processes are discussed, then the related topic of ion production is examined in the following subsection.

In the ionosphere, the two most important chemical processes are: 1) charge exchange and 2) recombination. Charge exchange processes take the general form:

$$A + B^+ \rightarrow A^+ + B.$$

Charge exchanges are important in the momentum and energy equations as well as in ion chemistry. The accurate characterization of these reactions determines how well a model can

describe the ion and neutral populations as well as the dynamics governing the region.

Recombination reactions can take two forms, symbolically:

$$\text{1) radiative recombination: } A^+ + e \rightarrow A^* + \text{photon}(\lambda)$$

$$\text{2) dissociative recombination: } AB^+ + e \rightarrow A + B,$$

where A^* signifies that A must be in an excited state. Typically, dissociative recombination reactions can result in different products that can be represented by different branches from the same reactants. These branches distinctly affect the system and must be appropriately defined. Currently, laboratory and space-based measurements coupled with theoretical physics provide the best accepted values, often tabulated according to the state of the ion and temperature of the electrons. Recombination is an ion loss process. In order to provide a full characterization of the upper atmosphere, the ion production processes must also be understood. This is the objective of Section 2.2.3.

2.2.3 Contributing factor: Ion production

Ions are produced in the upper atmosphere primarily as a result of two drivers: 1) solar ultraviolet/extreme ultraviolet (UV/EUV) radiation and 2) magnetospheric particle precipitation.

Solar radiation

Photoionization is the inverse process to radiative recombination. The solar coronal, coronal-chromospheric transition, and chromospheric regions emit radiation shortward of roughly 120 nm. The radiation corresponding to this upper limit and extending down to the x-ray portion of the spectrum is absorbed by the primary neutral constituents of the upper atmosphere: O, O_2, and N_2. Three processes affecting the upper atmosphere ionization occur as a result of solar radiation (primarily in the EUV wavelength range): 1) photoionization due to photons, 2) photoionization due to photoelectrons (or secondary electrons created from the initial photoionization process), and 3) dissociative ionization. On the chemical kinetics side of things, dissociation is also a byproduct

of solar radiation absorption in the upper atmosphere, but this is a process dealing entirely with neutrals and is therefore not discussed further here.

The photoionization process produces free electron-ion pairs. When the photon energy exceeds the ionization energy of the neutral gas specie, the excess is deposited either as electron kinetic energy or as excitation energy for the associated ion. The majority of excess energy is absorbed by the electron because it is much less massive than the ion. Ion production from photoionization can be divided into a primary ionization term due to the incident photon and secondary ionization terms due to the resulting energetic photoelectron:

$$X + \text{ photon}(\lambda) \rightarrow X^+ + e^- \qquad \text{primary photoionization} \tag{2.20}$$

$$e^- + X \rightarrow X^+ + e^- \qquad \text{secondary ionization.} \tag{2.21}$$

The secondary ionization term in which an energetic photoelectron collides with a neutral to produce an ion-electron pair is called impact ionization. Therefore, to determine ion production due to solar sources we must know the photoelectron production rate, which is a function of altitude, energy, and solar zenith angle:

$$P_e(E, \chi, z) = \sum_l \sum_s n_s(z) \int_0^{\lambda_{si}} I_\infty(\lambda) e^{\tau(\lambda,\chi,z)} \sigma_s^i(\lambda) p_s(\lambda, E_l) d\lambda, \tag{2.22}$$

where:

$$\sigma_s^i(\lambda) = \text{ wavelength-dependent total ionization cross-section}$$

$$p_s(\lambda, E_l) = \text{ branching ratio for a given final ion state with energy level } E_l$$

$$\lambda_{si} = \text{ threshold wavelength for neutral species } s,$$

and the summations are conducted over all species, s, and ion states, l. This integral is often approximated by the Chapman production function (*Chapman*, 1931a,b) by assuming: 1) monochromatic incident radiation, 2) an atmosphere made up of a single absorbing specie whose height-dependence is purely exponential given by a constant scale height, and 3) a planar and horizontally-stratified atmosphere.

Characterization of the energy distribution of photoelectrons is of utmost importance. The energy describes how far into the atmosphere an electron can penetrate. From laboratory results roughly 34 eV is lost from an electron due to each ionization. The electron will no longer penetrate nor ionize when all kinetic energy has been lost.

Magnetospheric particle precipitation

Photoionization produces photoelectrons that can cause secondary ion production by means of impact ionization. Particles precipitating from the magnetosphere are analogous to photoelectrons and are another source of ion production due to impact ionization. Therefore, their effects are qualified and quantified in the same manner as photoelectrons. The energy distributions (i.e. intensities) of these precipitating particles must be accurately described in order to characterize the amount of ionization they produce and the altitudes where they deposit energy. In addition to determination of where in the ionosphere these particles stop, their energy distributions also identify the magnetospheric source regions of the particles (*Vasyliunas*, 1970, 1972; *Hardy et al.*, 1987; *Newell et al.*, 1991; *Newell and Meng*, 1992).

The next logical consideration is to determine how the electrons, whether photoelectrons or magnetospheric precipitating electrons, are transported through the atmosphere. This is discussed next in Section 2.2.4.

2.2.4 Contributing factor: Electron transport

The interaction between auroral electrons and the upper atmosphere is characterized by a wide variety of flow conditions modulated by collisions and energy redistribution. Quantitative descriptions of these processes are complicated, requiring knowledge of atmospheric composition, density, and pressure and ionization and excitation cross-sections. Transport equations have been developed in an attempt to capture the relevant physics and accurately determine where specific collisional processes occur, and where the energy from the incoming electrons is deposited in the

atmosphere. Such transport equations can be derived from the Boltzmann equation:

$$\frac{\partial f_s}{\partial t} + \mathbf{v}_s \cdot \nabla f_s + \mathbf{a}_s \cdot \nabla_{\mathbf{v}} f_s = \frac{\delta f_s}{\delta t}, \tag{2.23}$$

where

$f_s(\mathbf{r}, \mathbf{v}_s, t)$ = velocity distribution function of species s

(i.e. probability density function in phase space $(\mathbf{r}, \mathbf{v})$,

∇ = gradient operator in configuration space,

∇_v = gradient operator in velocity space,

$\mathbf{v}_s = \frac{d\mathbf{r}}{dt}$ = velocity of the particles,

$\mathbf{a}_s = \frac{d\mathbf{v}}{dt}$ = acceleration of the particles,

$\frac{\delta f_s}{\delta t}$ = represents the effects of collisions instantaneously changing particle velocity.

Figure 2.9 shows a schematic representation of the configuration and velocity spaces represented by the velocity distribution function, $f_s(\mathbf{r}, \mathbf{v}_s, t)$.

The electron intensity at a given location is required to calculate ionization, energy deposition, and optical emissions. The transport calculations can be initialized with synthetic electron spectra, spectra observed by instruments aboard rockets or satellites, or with internal electron sources from photoionization (*Lummerzheim et al.*, 1989). Solutions to the electron transport equation have been devised in several forms: Monte-Carlo simulations (*Berger et al.*, 1970), two-stream models (discussed further below), and multi-stream models (*Strickland et al.*, 1976; *Lummerzheim et al.*, 1989). A review of electron transport codes up until 1980 was provided by *Stamnes* (1980). Hybrid approaches have also been devised, such as a combination of Monte-Carlo (MC) methods with two-stream codes (*Solomon*, 2001).

The model I develop for this work relies on the two-stream formulation of electron transport. A brief review of this method is provided for context. *Banks* (1966a); *Banks and Nagy* (1970); *Nagy and Banks* (1970) treated this problem through a study of the processes affecting the energy

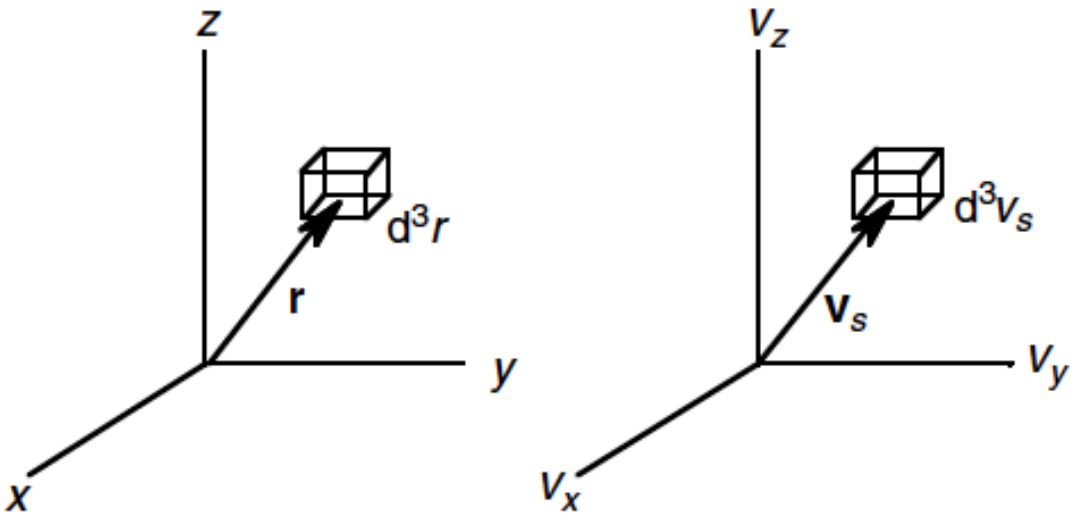

Figure 2.9: Volume element, d^3r, about position vector, $\mathbf{r}$, in configuration space (left) and volume element, d^3v_s, about velocity vector, $\mathbf{v}_s$, in velocity space (right). The velocity distribution function, $f_s(\mathbf{r}, \mathbf{v}_s, t)$, corresponds to the number of particles of species s located in d^3r in configuration space, with velocities in d^3v_s in velocity space, and at time t. Image reproduced from *Schunk and Nagy* (2009).

and space distribution of the electrons. Their models solved a two-stream continuity model of the atmosphere in which electron fluxes traveled either up or down magnetic field lines and explicitly included energy loss and scattering processes by means of energy-varying cross-sections.

Banks et al. (1974) extended the earlier work through a division of auroral electron particles by energy. They used the prior model to describe auroral electrons with energies < 500 eV for which discrete energy loss processes dominate and added a new model for electrons with energies $>$ 500 eV which consisted of continuous energy losses and the Fokker-Planck diffusion equation. The resulting model yielded complete energy spectra of auroral electrons over all altitudes. This electron transport algorithm is implemented in the GLobal AirglOW (GLOW) model (*Solomon et al.*, 1988), which is used extensively in this work. Appendix B provides a complete formal description and mathematical derivation of the two-stream electron transport approximation used in GLOW.

Ultimately, the transport models must yield ionization rates and ion and neutral constituent density profiles in order to provide an understanding of the atmosphere. *Roble and Ridley* (1987), for the purpose of the thermosphere general circulation models (TGCMs), developed an analytic procedure for fast numerical evaluation of ionization rates and constituent profiles caused by electron precipitation. The work therein is still used in large part in current TGCMs, with slight modifications.

2.2.5 Contributing factor: Proton/Ion transport

Ions obey the same fundamental laws as their smaller negatively charged counterparts, but obviously require a completely separate development of momentum transfer collision cross-sections, collision frequencies, and energy transfer rates. *Banks* (1966b) addressed these and resonance terms for ions following the methods leading to the development of equivalent terms for the electrons in *Banks* (1966a).

Fundamentally, the minute mass of the electron compared to the proton or any ion specie creates differential behavior in the upper atmosphere. Whereas an electron's gyrofrequency to neutral collision frequency ratio (in the terminology of Equation 2.17: $\frac{\omega_{ce}}{\nu_{en}}$) is well above unity

until roughly 80 km altitude, protons and ions obtain a value of unity well above 100 km. The more massive particles are much less mobile in the upper atmosphere and move with the neutral atmosphere at altitudes below $\sim$ 120 km. As a result, electrons are the primary charge carriers in the ionosphere and the current is directed opposite of the direction of electron bulk motion. The electrical currents, determined by the two populations of particles together, govern the particle energy deposition profiles of the upper atmosphere.

Hardy et al. (1989) and *Galand et al.* (2001) have both concluded that proton precipitation represents a minority of total auroral precipitation, but that 15%, a significant percentage, is a good estimate. Ion production models have been used to supply the GCMs with proton precipitation information (*Galand et al.*, 1999, 2001). More recently, *Fang et al.* (2007a,b,c, 2013) used data derived from NOAA POES satellite particle precipitation information to supply this input. Though proton precipitation can be a significant source of conductivity modification in certain situations and specific locations, this dissertation focuses on the effects due to electron precipitation, which are much more widespread.

2.2.6 Pulling together the theory and contributing factors to calculate conductivity

Next, I describe the process of determining conductivity from the available information, including the models that can be utilized and the observations that can drive them. The first step in arriving at conductivity profiles requires an accurate characterization of the ionizing sources. The two primary sources, solar radiation and magnetospheric particle precipitation, have already been detailed. Subsequently, treatment of the particle transport must be addressed. This, too, was discussed above. The particle transport treatment results in a description of the redistribution of the atmosphere according to the energy of the source terms, background atmosphere, and resulting chemistry.

The atmospheric chemistry for the purposes of conductivity calculations can be described by collision frequencies. The frequencies used for the work in this dissertation are obtained from

Schunk and Nagy (2009):

$$\begin{aligned}
\frac{1}{N_{O_2}}\nu_{O_2^+-O_2} &= 2.59\times10^{-11}\sqrt{\frac{T_i+T_e}{2}}\left[1-0.073\log_{10}\frac{T_i+T_e}{2}\right]^2 \\
\frac{1}{N_{O_2}}\nu_{O^+-O_2} &= 6.64\times10^{-10} \\
\frac{1}{N_{O_2}}\nu_{NO^+-O_2} &= 4.27\times10^{-10} \\
\frac{1}{N_O}\nu_{O^+-O} &= 3.67\times10^{-11}\sqrt{\frac{T_i+T_e}{2}}\left[1-0.064\log_{10}\frac{T_i+T_e}{2}\right]^2 f_{cor} \\
\frac{1}{N_O}\nu_{NO^+-O} &= 2.44\times10^{-10} \\
\frac{1}{N_O}\nu_{O_2^+-O} &= 2.31\times10^{-10} \\
\frac{1}{N_{N_2}}\nu_{O_2^+-N_2} &= 4.13\times10^{-10} \\
\frac{1}{N_{N_2}}\nu_{NO^+-N_2} &= 4.34\times10^{-10} \\
\frac{1}{N_{N_2}}\nu_{O^+-N_2} &= 6.82\times10^{-10},
\end{aligned} \tag{2.24}$$

where the temperature dependent terms denote resonant reactions, and the constants denote non-resonant reactions. The term f_{cor} has a default value of 1.5 and is representative of the Burnside correction (*Burnside et al.*, 1987) for the O^+-O reaction. This term was empirically determined to improve agreement between general circulation models and observed winds and electron densities (*Nicolls et al.*, 2006). The collision frequencies can then be found in units of [1/s]:

$$\begin{aligned}
\nu_{O_2^+} &= \nu_{O_2^+-O_2}+\nu_{O_2^+-O}+\nu_{O_2^+-N_2} \\
\nu_{O^+} &= \nu_{O^+-O_2}+\nu_{O^+-O}+\nu_{O^+-N_2} \\
\nu_{NO^+} &= \nu_{NO^+-O_2}+\nu_{NO^+-O}+\nu_{NO^+-N_2} \\
\nu_{en} &= 2.33\times10^{-11}N_{N_2}T_e\left(1-1.21\times10^{-4}T_e\right)+ \\
&\quad 1.82\times10^{-10}N_{O_2}\sqrt{T_e}\left(1+3.6\times10^{-2}\sqrt{T_e}\right)+ \\
&\quad 8.9\times10^{-11}N_O\sqrt{T_e}\left(1+5.7\times10^{-2}\sqrt{T_e}\right).
\end{aligned} \tag{2.25}$$

Equations 2.24 and 2.25 can be used to determine the conductivity profiles given the ion and

electron density profiles:

$$\sigma_P = \frac{q_e}{B}\left[N_{O^+}\frac{r_{O^+}}{1+r_{O^+}^2} + N_{O_2^+}\frac{r_{O_2^+}}{1+r_{O_2^+}^2} + N_{NO^+}\frac{r_{NO^+}}{1+r_{NO^+}^2} + N_e\frac{r_e}{1+r_e^2}\right] \tag{2.26}$$

$$\sigma_H = \frac{q_e}{B}\left[-N_{O^+}\frac{1}{1+r_{O^+}^2} - N_{O_2^+}\frac{1}{1+r_{O_2^+}^2} - N_{NO^+}\frac{1}{1+r_{NO^+}^2} + N_e\frac{1}{1+r_e^2}\right], \tag{2.27}$$

where:

$$r_x = \frac{\text{collision frequency}}{\text{gyro frequency}} = \frac{\nu_x}{\omega_x} \tag{2.28}$$

$$\omega_x = \frac{q_e B}{m_x}. \tag{2.29}$$

Figure 2.10 shows typical noontime mid-latitude Hall (σ_H), Pedersen (σ_P), and parallel ($\sigma_\parallel$) conductivities. The Hall conductivity peaks in the E-region while the Pedersen conductivity peaks somewhat higher in altitude. The parallel conductivity continues to increase with altitude. Though it may seem that currents along **B** would be much larger than currents across **B**, this is not the case in the lower ionosphere. The parallel currents cannot continue to increase in the poorly conducting lower ionosphere, but must instead find a closure path that moves across field lines (*Richmond and Thayer*, 2000). As a result, the parallel and perpendicular current densities are linked. Further, the Hall-to-Pedersen conductivity ratio is clearly height-dependent. There is considerably more variability in the auroral zone conductivity profiles due to the irregularity of auroral ionization by particle precipitation (*Richmond and Thayer*, 2000).

2.2.7 Salient historical research on conductivity

I have shown that conductivity is dependent on a number of factors, including the external drivers (solar radiation and particle precipitation), ionization rates and profiles, the neutral atmosphere, collisions and chemistry, and the intrinsic magnetic field. The atmospheric research community over the past several decades has attempted to characterize each of these factors with

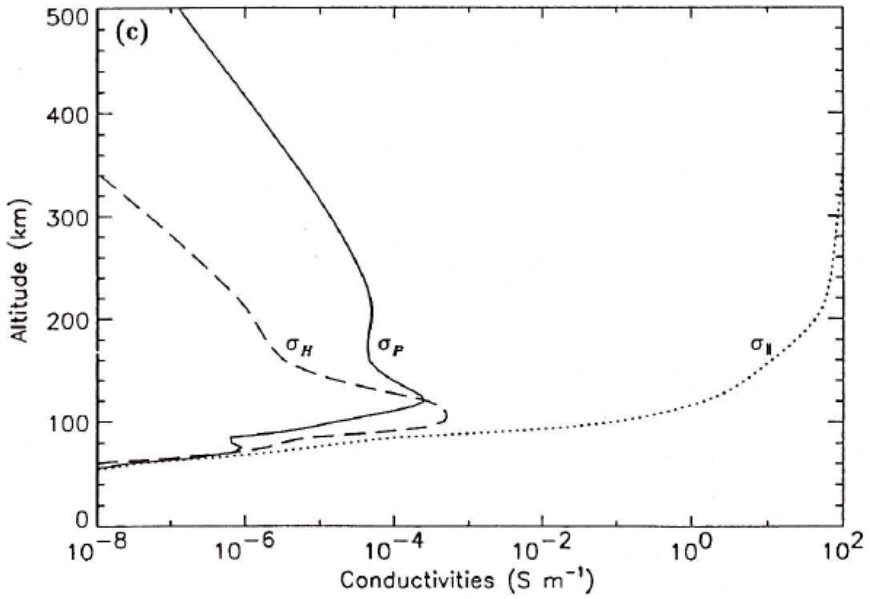

Figure 2.10: Typical noontime mid-latitude ionospheric conductivity profiles (σ_H (Hall), σ_P (Pedersen), and $\sigma_\parallel$ (Parallel) conductivities). Image reproduced from *Richmond and Thayer* (2000) (their Figure 4c).

varied approaches. I discuss these next and finish with an overview of legacy conductivity research. This section highlights the outstanding issues in conductivity modeling and leads into an outline of this dissertation.

I first focus on the past research with regard to the external drivers: 1) solar radiation and 2) particle precipitation.

2.2.7.1 Solar radiation

The solar extreme ultraviolet (EUV) flux is a fundamental upper atmosphere energy input (*Kutiev et al.*, 2013). Direct and detailed observations of the solar X-ray to EUV spectrum have historically been sparse and/or spectrally broadband. Therefore, reference spectra and solar activity scaling factors compiled from various data sets coupled with computer models have been the primary means of representing the full solar spectrum and energy deposition into the upper atmosphere. Solar reference spectra attempt to capture the absolute fluxes for all salient wavelengths, between those resolved by direct instrument observations and containing wavelengths beyond observation bounds.

Two of the most commonly used solar reference spectra are: 1) F74113 (*Heroux and Hinteregger*, 1978) and 2) SERF1 (*Hinteregger et al.*, 1981).

The F74113 spectrum was compiled from measurements taken by an April 23, 1974 rocket flight and observations made by the AE-C satellite (*Heroux and Hinteregger*, 1978). This spectrum is representative of solar minimum conditions and has been widely used. *Hinteregger et al.* (1981) devised a new model referred to as the Solar Electromagnetic Radiation Flux 1 (SERF1) model. SERF1 was the first empirically-based high-resolution solar flux model and uses two proxies as drivers: 1) a two-variable $F_{10.7}$ representation (daily and 81-day averaged) and 2) an EUV class model which scales the EUV flux from solar minimum conditions for each wavelength.

Subsequently, *Tobiska and Barth* (1990) combined solar Lyman α flux with $F_{10.7}$ as indices for the full-disk solar EUV variation. They found that Lyman α was an effective indicator of chromospheric EUV emission and $F_{10.7}$ was representative of the transition region and coronal

EUV emissions. These results were formalized into the SERF2 model, and extended in the EUV91 model (*Tobiska*, 1991). A good review of the observations and work supporting solar EUV flux modeling up until 1993 is given by *Tobiska* (1993).

In 1994, the EUV solar flux model for Aeronomic Calculations (EUVAC) was created to address shortcomings of the SERF models in the solar soft x-ray irradiances (*Richards et al.*, 1994). Namely, the irradiances in the solar soft x-ray region were increased by a factor of 2 to 3. Several authors have since created several EUV proxy models, including SERF2 and EUV91, already discussed above, EUV97 (*Tobiska and Eparvier*, 1998), and SOLAR2000 (*Tobiska et al.*, 2000). The EUVAC model serves as the basis for the solar energy input portion of the model that is developed and used extensively in this dissertation. Chapter 4 shows that EUVAC allows the use of a lower-resolution 37-wavelength bin without loss of accuracy (*Richards et al.*, 1994; *Qian et al.*, 2009; *McGranaghan et al.*, 2015a). Fewer bins yielded increased computational efficiency for solar flux calculations without sacrificing accuracy.

2.2.7.2 Magnetospheric particle precipitation

Magnetospheric particle precipitation is the second primary form of upper atmospheric energy deposition. Global patterns of this precipitation can be used to describe the ionospheric projection of magnetospheric particle populations and thereby represent an important piece of magnetosphere-ionosphere coupling. The particles themselves cause a modification of the neutral and ionized atmosphere through collisions and the resulting chemistry.

Particles can follow a variety of pathways from the solar wind and the magnetosphere into the upper atmosphere. Figure 2.11 shows a schematic diagram of magnetospheric regions and their upper atmospheric projections. The overwhelming majority of particles entering the upper atmosphere are found in latitudes $> \sim 55°$ due to structuring of Earth's magnetic field (see the field line traces into the high-latitude regimes in Figure 2.4). Typically, electrostatic analyzers aboard high-latitude orbiting satellites provide number and energy flux information that can be used to

determine the source region and ionization properties of the particles.

There have been two primary methods to compile global maps of the ionospheric projections of magnetospheric particle populations: 1) create a global or local time picture using a set of closely-studied individual passes (*Frank and Ackerson*, 1971; *Hoffman and Burch*, 1973), or 2) build a global picture by dividing the region of interest into zones of magnetic local time, geomagnetic latitude, and activity level using large data sets to obtain the average value of each quantity of interest within each bin (*Feldstein*, 1966; *McDiarmid et al.*, 1976; *Wallis and Budzinski*, 1981; *Spiro et al.*, 1982; *Hardy et al.*, 1985, 2008). The second technique is known as the zone-divided approach. Fundamentally, these methods depend on knowledge and analysis of the energetic particle spectra, or flux as a function of energy. These are typically manipulated into integrated fluxes, in which the integration is performed over particle instrument energy channels, and average energies, defined as the integral energy flux divided by the integral number flux:

$$E_{avg} = \frac{JE_{tot}(\Omega)}{J_{tot}(\Omega)}, \tag{2.30}$$

where, in discrete notation:

$$\begin{aligned} JE_{tot}(\Omega) &= \text{integral energy flux} \\ &= \sum_i E_i j(E_i) \Delta E(i, i+1) \\ J_{tot}(\Omega) &= \text{integral number flux} \\ &= \sum_i j(E_i) \Delta E(i, i+1) \end{aligned}$$

Both integrated and average quantities provide significant insight into magnetospheric source regions, altitude of energy deposition, and general extent of ionosphere-magnetosphere coupling (*Hardy et al.*, 1985). *Fuller-Rowell and Evans* (1987) further organized precipitation data into hemispheric power, an auroral activity index originally developed by *Foster et al.* (1986) and which is a widely used representation of the level of MI coupling.

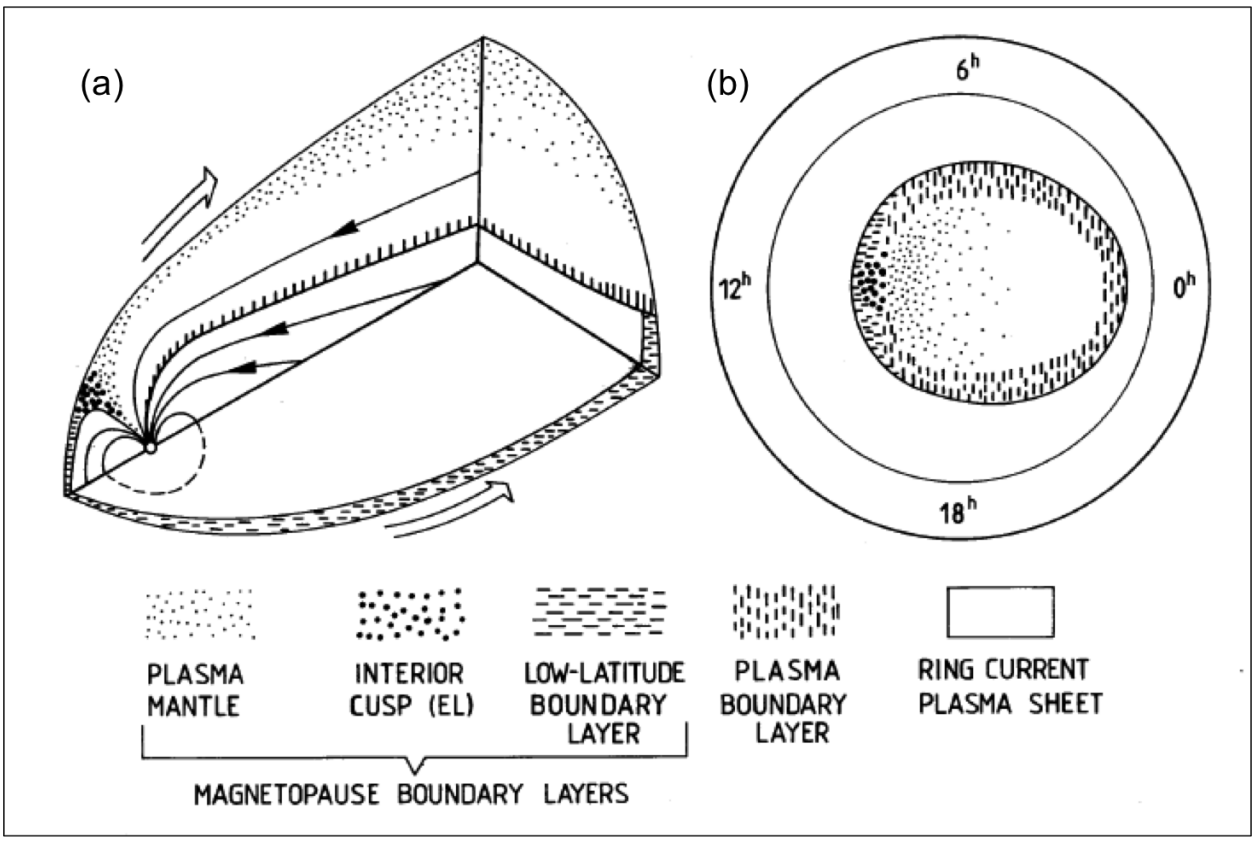

Figure 2.11: Schematic diagram of the ionospheric mapping location of magnetospheric regions. (a) Magnetospheric regions and (b) their ionospheric projections. Image reproduced from *Vasyliunas* (1979).

The results of the *Fuller-Rowell and Evans* (1987) work, which are parameterized in the 10-bin hemispheric power index (HPI), have served as input to high-latitude ionospheric calculations, including within the first step of the AMIE procedure in calculating conductance (*Knipp et al.*, 1989; *Knipp et al.*, 1994). *Fuller-Rowell and Evans* (1987) used the characteristic energy of observed electron energy spectra to fit the spectra to an assumed functional form and then used these fit-spectra to inform the model creation. Therefore, two simplifying assumptions are incorporated into the *Fuller-Rowell and Evans* (1987) model: 1) the conductances are limited to discrete distributions according to HPI; and 2) the energy spectra take an assumed form determined by the characteristic energy. This dissertation characterizes the particle precipitation in more specific terms than the HPI and assumed spectral forms, and I specifically compare with the *Fuller-Rowell and Evans* (1987) model in Chapter 7.

Newell et al. (1991) created a database of auroral precipitation boundaries and structure based on DMSP F7 and F9 satellite observations. *Newell and Meng* (1992) used plasma characteristics obtained from a zone-divided approach to more accurately characterize the magnetospheric particle precipitation. In both studies, precipitation regions were specifically divided according to their magnetospheric source, including polar, cusp, low latitude boundary layer, boundary plasma sheet, central plasma sheet, and photoelectron-based (i.e. sunlight). They then created probability maps for observing certain precipitation as a function of the defined zones. *Newell et al.* (2002) leveraged much of this work to create the Oval Variation, Assessment, Tracking, Intensity, and Online Nowcasting (OVATION) model to locate the auroral oval and quantify its intensity. OVATION is a tool useful for both data archival and space weather nowcasting purposes. Building on this body of work, *Newell et al.* (2007) then derived an empirical coupling function to proxy solar wind-magnetospheric coupling by means of precipitation data, several ground-measurement indices, and other measures of magnetospheric activity many of which rely on ground- and ionospheric-based observations. They showed that most magnetospheric phenomena exhibited high correlation with this coupling function, indicating that the signatures of solar wind-magnetospheric coupling are evident in the upper atmosphere. Subsequently, *Newell et al.* (2009) created finer bins in MLT and MLAT

and separately categorized precipitation in one of four categories: 1) ion diffuse, 2) electron diffuse, 3) quasi-static electric field-accelerated (monoenergetic), and 4) Alfvénic fluctuation-accelerated (broadband). Finally, this study replaced the Kp dependence by categorizing precipitation instead according to the empirical coupling parameter derived in *Newell et al.* (2007).

Newell et al. (2010) conducted a detailed study of the seasonal variations of auroral precipitation using 22 years of DMSP particle precipitation data. Separate treatment was given to each of the four types of aurora, day and night, and solar minimum and maximum conditions and the results were organized into the OVATION Prime model, an extension of the OVATION model. This model has undergone recent improvements, namely in an extension to higher disturbance levels (*Newell et al.*, 2014). Despite the vast improvement in characterization of auroral precipitation over the past few decades, in all studies the diffuse aurora was still assumed to be characterized solely by Maxwellian energy distributions.

One means of more specific characterization of auroral particle precipitation is shown in Figure 2.12. Figure 2.12 displays two characteristic DMSP particle spectra obtained from the SSJ instrument on the F18 satellite: (a) an energy spectrum that can be well-approximated by the Maxwellian distribution and (b) an energy spectrum that clearly exhibits a high-energy tail and thus a departure from the Maxellian distribution. These spectra were specifically chosen to illustrate that precipitation in adjoining high-latitude regions can vary greatly. Statistical treatments inherently assume that average precipitation characteristics, Maxwellian and unimodal distributions, for example, sufficiently describe high-latitude precipitation overall. However, these assumptions have been shown to be suspect (*Hardy et al.*, 2008). The work presented here eliminates such assumptions and instead uses the particle distributions directly measured by the DMSP spacecraft.

McIntosh and Anderson (2015) studied the Maxwellian assumption limitation and created maps of auroral precipitation characterized first as either diffuse or accelerated and then further characterized the diffuse precipitation by one of three energy distributions: 1) Maxwellian, 2) Lorentzian, or 3) Ellison-Ramaty. They used an extensive DMSP particle precipitation data set to demonstrate a clear latitudinal and Kp dependence of particle spectra. Throughout the auroral oval,

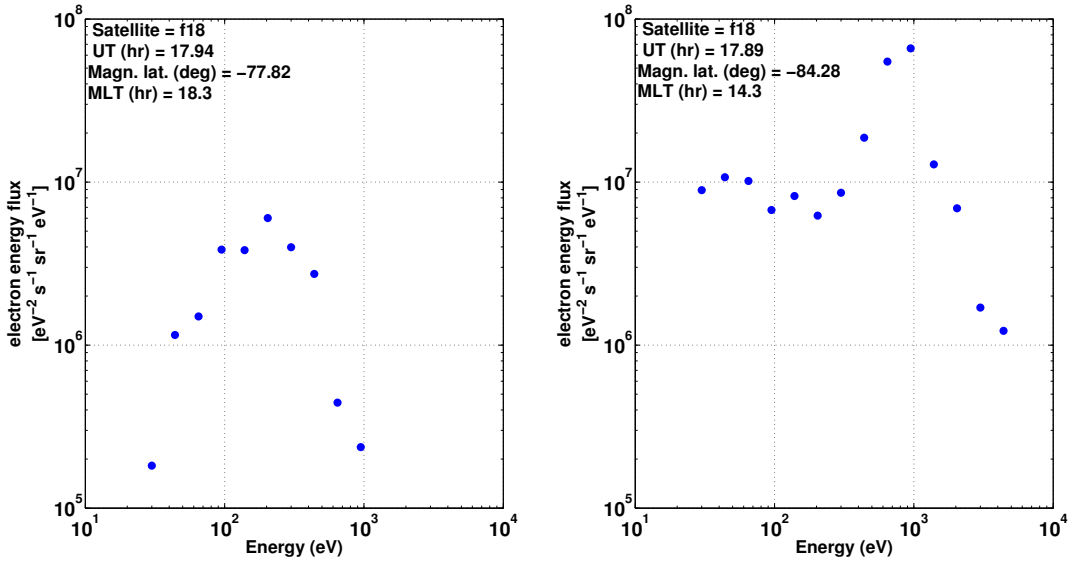

Figure 2.12: Typical DMSP satellite particle energy spectra obtained from the F18 satellite. (a) Spectra that can be well described by a Maxwellian distribution and (b) spectra that displays departure from the Maxwellian distribution with a high-energy tail. Both figures are plotted on log-log scale and show the number flux of electrons on the vertical axis and energy on the abscissa.

diffuse precipitation was predominantly characterized by Maxwellian and Lorentzian distributions, with the percentage best-fit by the Maxwellian distribution notably falling off with increasing Kp. Beginning at Kp = 3, Lorentzian and Ellison-Ramaty distributions begin to better characterize the precipitation. The accelerated precipitation, which includes monoenergetic and broadband, in different regions of MLT and MLAT were characterized by each of the three tested distributions. Maps created by *McIntosh and Anderson* (2015) are available to the community.

The zone-divided approach provides valuable information about magnetospheric particle precipitation and has greatly contributed to a broad understanding of the associated ionospheric features. However, the inherent averaging in this technique results in a general smoothing of spatial and temporal variations. Consequently, the field of research surrounding ionospheric electrodynamics, and specifically conductivity, has been subject to the same spatial and temporal averaging (*Amm et al.*, 2008). Both the particle precipitation and conductivity are subject to quickly changing features, often during substorms and geomagnetically-active period, on the order of 10s of kilometers spatially and 10s of minutes temporally (*Heppner et al.*, 1993). In this dissertation we improve temporal and spatial resolution through refined conductivity modeling.

2.2.7.3 Conductivity

In this historical perspective on conductivity research and modeling, focus is placed on studies of both ionization production and conductivity itself. In the early 1970s, the Chatanika, Alaska incoherent scatter radar (ISR) data was used to analyze high-latitude ionospheric electric fields and new methods were developed to also study the conductivity in this region. *Brekke et al.* (1974) determined that the relationship between the applied electric field and the ground-measured magnetometer perturbations is modulated by the E-region neutral winds and the altitude-dependent Pedersen and Hall conductivities. They suggested that correlations between surface magnetic perturbations and ionospheric currents could only be reliably made if simultaneous and extended observations of the ionospheric electric field, E-region conductivities, and E-region neutral winds exist. They studied these variables on a diurnal basis using ISR data. The Chatanika data only

provided height-integrated E-region neutral winds, so it was necessary to calculate height-integrated current densities under the assumption that the current flowing in the ionosphere can be approximated as an infinite, uniform sheet, otherwise known as the ionospheric equivalent current. *Kamide and Brekke* (1975) examined height-integrated ionospheric currents deduced simultaneously from Chatanika radar data and an Alaska meridian chain of magnetometers and found that the current densities in the ionosphere are significantly underestimated using the infinite sheet approximation. They also showed that the discrepancy can be mitigated somewhat if the sheet current approximation is modified to allow a finite latitudinal width.

Evans et al. (1977) examined the electrodynamics of an auroral arc using the Polar 3 rocket flight measurements. The energy loss algorithm of *Rees* (1963) and an assumed background neutral atmosphere were used to determine ion production rates. The procedure neglected electrons whose energy was below 500 eV to avoid applying an energy loss model for low energy electrons. An assumption of chemical equilibrium and the use of empirical recombination coefficients allowed the inference of the electron density profiles which were then applied to calculate Pedersen and Hall conductivities. The conductivities were then used to allow an in-depth electrodynamic analysis of the auroral arc. Further, the relationship between the electrodynamics and the resultant Joule heating was examined. The significance of this work lies in the fact that height-dependent and fine-scale conductivities enabled a detailed description of the ionospheric energetics within an auroral arc.

Wallis et al. (1976) recognized the problems that simplistic conductivity models can cause. They showed using ISIS 2 satellite observations and coincident magnetometer perturbations that conductivity gradients can be as important as electric field gradients as the source of horizontal current divergence. *Wallis and Budzinski* (1981) used essentially the same process as the Evans study to calculate conductivities, but primarily made three improvements: 1) calculations were conducted over a greater latitude range using ISIS 2 data, 2) ionization due to background and solar sources were included, and 3) extrapolations above 200 km were performed because they recognized that ionization in this region was significant when conductivities were integrated to find

E-region conductances. Due to the longer duration study, they were also able to bin the results depending on whether Kp was greater than or less than three. The work of Wallis emphasized the importance of the spatial and temporal variability of ionospheric conductivity in influencing the closure path of field-aligned currents.

Vickrey et al. (1981) attempted to resolve conductivity on finer spatial and temporal grids using three 24-hour sets of continuous observations by the Chatanika ISR during periods of different magnetic conditions and different seasons. The steady state altitude profiles of energy deposition derived by *Rees* (1963) were applied to compute conductivities. They found that during an auroral substorm the onset of precipitation causes regions of enhanced conductivity to intensify and move equatorward and during recovery recede poleward and lose intensity. They showed that these variations can occur on a time scale as rapid as a few minutes.

Several studies then used various combinations of data from satellites, ground magnetometers, radars, and rocket flights to study energy deposition as a result of particle precipitation and conductivity (*de la Beaujardiere et al.*, 1981; *Robinson et al.*, 1981; *Vondrak and Rich*, 1982). *Spiro et al.* (1982) focused on smoothed particle precipitation data from the AE-C and -D satellites to characterize a coarsely-binned global distribution of auroral particle energy flux and average energy for different levels of geomagnetic activity as determined by the Kp and AE indices. Pedersen and Hall conductances were inferred from simple empirical fits to the energy deposition results of *Vickrey et al.* (1981) assuming Maxwellian electron distributions. Though this study was incapable of capturing fine-scale or height-dependent structure in the conductivity, it successfully showed the auroral electrojet index is an important indicator of auroral particle energy input and behavior of the Pedersen and Hall conductances.

In the early 1980s, methods began to emerge to determine the electrodynamic state of the ionosphere. *Kamide et al.* (1981) presented a numerical scheme through which ground magnetic measurements were used to estimate the 2-D ionospheric currents, field-aligned currents, and the associated electric field. This method, which is known as the Kamide-Richmond-Matsushita (KRM) method, differed from previous work in that it was not limited by uniform or very simple conduc-

tivity distributions. Two caveats accompany that statement: 1) in the model, the conductivity distribution is assumed given or observed and 2) in their initial study, the authors assumed a very simple distribution for lack of better input. KRM assumes an electrostatic electric field, the validity of Ohm's law (linear relation between all variables), and considers no neutral wind effects. The results showed consistency with past work when estimating relatively long-lived ionospheric disturbances, but showed increased difficulty in reproducing electrodynamics of more transient events, namely substorms. They attributed the difficulty primarily to an inability to estimate conductivity distributions from ground magnetic perturbations alone during such events.

Later in the same decade, *Richmond and Kamide* (1988) devised the Assimilative Mapping of Ionospheric Electrodynamics (AMIE) procedure (see also *Richmond* (1992)). AMIE carries out an objective multivariate functional analysis of high-latitude ionospheric electrodynamic variables, specifically electric potential, ionospheric currents, and magnetic field perturbations. AMIE is built on the same set of assumptions already discussed for KRM. AMIE differs by using data assimilation based on optimal interpolation theory that is capable of inferring electrodynamic variables from many types of observation.

KRM, and subsequently AMIE, have greatly contributed to our current understanding of the ionosphere and its linkage to the magnetosphere. AMIE continues to be an invaluable tool in the study of the ionospheric system. However, these methods emphasize that, despite the advances in the knowledge of ionospheric conductivity, a reliable model encapsulating global- and local-scale variations to drive these electrodynamic calculations remains problematic. Additionally, both methods assume a conductance distribution is provided *a priori*. It should be noted that the first step in the AMIE procedure is to estimate corrections to the background conductance distribution (*Knipp*, 1989).

During this period, an increase in the number of observations of magnetospheric particle precipitation by polar orbiting satellites allowed refinement of conductivity distributions at high-latitudes (*Robinson et al.*, 1987; *Hardy et al.*, 1987; *Fuller-Rowell and Evans*, 1987). *Robinson et al.* (1987) created a set of well-known and frequently-used formulas for Pedersen and Hall conductances

which assume Maxwellian energy distributions for incoming electrons, hereafter referred to as the Robinson formulas:

$$\Sigma_P = \frac{40\bar{E}}{16 + \bar{E}^2}\Phi_E^{1/2} \tag{2.31}$$

$$\frac{\Sigma_H}{\Sigma_P} = 0.45(\bar{E})^{0.85}, \tag{2.32}$$

where:

$$\bar{E} = \text{ average energy}$$

$$\Phi_E = \text{ energy flux.}$$

These formulas were developed as empirical fits to the *Vickrey et al.* (1981) results. The Robinson formulas have been used in wide measure to calculate conductance from precipitation data, but it is important to note that large errors in the conductances are associated with a departure from the Maxwellian distribution (*Wallis et al.*, 1979; *Lin and Hoffman*, 1982; *Murphree et al.*, 1983; *Hardy et al.*, 2008; *Newell et al.*, 2009; *McIntosh and Anderson*, 2015). Thus, these formulas only remain valid over a specific, and limiting, set of electron energies, and require correction factors at average energies below 500 eV and above 2 keV. Nevertheless, the Robinson formulas have been effectively used over the past several decades to aid in ionospheric study, especially in AMIE storm studies.

During this period, conductivity estimates resulting from solar radiation absorption and particle precipitation began to come together. *Moen and Brekke* (1993) derived an empirical relationship between the Hall and Pedersen conductances and solar zenith angle and flux. *Watermann et al.* (1993) compared the conductivities inferred from satellite and radar data to those found using the photoionization models, and distinguished between the two causes of conductivity enhancement. *Lummerzheim et al.* (1997) used the Ultraviolet Imager (UVI) instrument on the POLAR satellite to calculate high time-resolution global estimates of auroral conductance, rather than just the along-track estimates begun by *Knipp* (1989) and continued in these more recent studies. *Ahn et al.* (1998) developed an empirical conductance model based on ionospheric conductance deduced

from Chatanika radar data and magnetic disturbances from the nearby College Alaska magnetic station.

Finer resolution statistical particle precipitation maps and enhanced knowledge of high-latitude conductance as a whole led to studies focused on substorm activity, regional variation, and properties of conductance that had been neglected to this point. *Lester et al.* (1996) used EISCAT radar observations in the AMIE procedure to study substorm activity. *Galand and Richmond* (2001a) derived conductances for ion precipitation, and found that ions can be a significant source of conductance enhancement at times. *Ridley et al.* (2004) performed a quantification of the nonlinear relationship between ionospheric conductivity and the global magnetosphere (e.g. beyond Ohm's law). *Vanhamäki and Amm* (2007) modified the KRM approach in order to serve regional analyses of the ionospheric electrodynamics. Several studies have analyzed conductivities in the context of case studies or specific phenomena, such as the bulge-type auroral substorm (*Gjerloev and Hoffman*, 2000; *Gjerloev et al.*, 2007) or auroral arcs (*Dahlgren et al.*, 2014).

The advent of the field of conductivity research has largely been limited to 1- or 2-D. However, with observational constraints becoming less of an obstacle (e.g. sustained DMSP satellite program, Swarm satellite mission, EISCAT and Advance Modular Incoherent Scatter (AMISR) radar projects, etc.) and advances in assimilative techniques (e.g. (*Matsuo et al.*, 2002, 2005; *Matsuo and Forbes*, 2010; *Matsuo et al.*, 2012; *Cousins et al.*, 2013a,b)), the future of conductivity research can be developed in a 3-D framework (*Amm et al.*, 2008).

2.3 Addressing outstanding issues in conductivity modeling: Aims and objectives of this dissertation

From this historical perspective, we can identify several outstanding issues that have hindered the development of robust conductivity models:

- lack of direct observations of conductivity,
- assumption of an equivalent ionospheric current (2-D approximation),

- assumption of Maxwellian distribution for the energy spectrum of precipitating particles,
- reliance on proxies and/or indices of geomagnetic activity and particle precipitation,
- use of sparse observations to obtain a global picture, and
- lack of resolution of fine-scale spatial and temporal structure.

These issues raise important questions for the field of conductivity modeling that drive the research conducted in this dissertation. Table 2.3 outlines these questions and the chapters where they are addressed.

Table 2.3: Science questions and where they are addressed in this dissertation.

Question	Chapter(s)
How limited are analyses of the magnetosphere-ionosphere-thermosphere (MIT) system that rely on proxies and/or indices of geomagnetic activity and particle precipitation?	3
How can indirect observations be used most effectively to study ionospheric conductivity and how can we overcome the sparsity of such observations?	4, 5, 8, 7
Can we overcome assumptions on the energy spectrum of precipitating particles to analyze ionospheric conductivities?	4, 7
What are the limitations of a two-dimensional representation of the ionosphere?	8
What are the three-dimensional characteristics of the ionospheric conductivities?	8
Can we specify conductivities on finer spatial and temporal scales than current statistical models and, if so, what influence do these finer scales have on the specification of ionospheric electrodynamics?	7

Next, I detail my approach to address these questions and provide an outline for this dissertation.

2.4 Scientific contribution

In this dissertation, I build a self-consistent conductivity model on first principal assumptions that is capable of reproducing realistic height-resolved conductivity profiles over the entire high-latitude ionosphere (>45° magnetic latitude). In a broader context, I show how this approach:

1) improves specification of the ionospheric electrodynamics; 2) better incorporates diverse observations in assimilative ionospheric electrodynamics analyses; and 3) supports the trend in space sciences toward smaller scale and higher resolution specification.

The key contributions of this dissertation are:

(1) A new model of height-dependent ionospheric conductivity and a computationally efficient version now freely available to the community (*McGranaghan et al.*, 2014, 2015a);

(2) The ability to study conductivity from directly observed in-situ electron energy spectra, free of any assumption on the functional form (*McGranaghan et al.*, 2015a,b);

(3) A new picture of the height-dependent ionospheric conductivities utilizing advanced computational tools (*McGranaghan et al.*, 2015b);

(4) A sophisticated statistical estimation method to understand conductivity influence on the complex electrodynamics of the MIT system (*McGranaghan et al.*, 2016, submitted and revised);

(5) More accurate conductivity distributions to better specify the MIT system on small scales, bringing ground- and space-based observations of this regime into closer agreement (*McGranaghan et al.*, 2016, submitted and revised); and

(6) A three-dimensional EOF analysis of the height-dependent conductivities.

These contributions represent several 'firsts' in the geospace sciences:

(1) The first combination of computationally efficient parameterizations with advanced particle transport algorithms to study conductivity;

(2) The first large-scale analysis of directly calculated ionospheric conductivity free of assumption of the incident electron energy spectra;

(3) The first characterization of the primary modes of ionospheric conductivity variability as EOFs;

(4) The first comparison of height-integrated and height-dependent ionospheric conductivities in the context of a three-dimensional conductivity analysis; and

(5) The first optimally interpolated data assimilative analysis of the conductivity.

In summary these scientific contributions, and the modeling capabilities that enabled them, overcome 30 years of assumption-limited physics and modeling to bring a new view of conductivity, currents and fields that control drivers and responses in the geospace system. The outcomes of this work, therefore, will be a key component for the understanding and modeling of the geospace system from a holistic point of view (e.g. geospace system science) (*Vassiliadis*, 2006).

2.5 Organization of this dissertation

In Chapter 3 I introduce the complex coupled geospace system and the proxied approach to understanding the energy coupling by summarizing the in-depth analysis of solar wind-magnetosphere-upper atmosphere response to high speed streams produced by the sun (*McGranaghan et al.*, 2014). That discussion highlights the benefit of using diverse observations, and illustrates that a reliance on proxies and indices can limit our ability to understand and forecast geospace phenomena. These limitations motivate the need to characterize ionospheric conductivity. Chapter 4 provides the details of the improved ionospheric conductivity modeling accomplished through this Ph.D. research. Chapters 5, 6, and 8 apply the modeling improvements to create new fundamental understanding of the Hall and Pedersen conductivities, first in two dimensions and then extended to incorporate the height dependency in three-dimensional analyses.

A limitation encountered in this research is that observations useful for conductivity calculations are typically limited either to a given satellite track or to a fixed location on the ground and are thus sparse. Spreading this information effectively to create a global model gives rise to stability and accuracy issues that require a robust estimation process to adequately address. Chapter 7 details the optimal interpolation technique used to overcome this challenge to improve global high-latitude specification of conductance.

Finally, Chapter 9 summarizes the critical findings of this research and makes recommendations for future study. A legacy of this work is the importance of the application of cutting edge mathematical tools and computational techniques to advance understanding of complex geospace phenomena.

Chapter 3

Importance of geospace system science to energy coupling in the Magnetosphere-Ionosphere-Thermosphere (MIT) system: Impact of equinoctial high-speed streams on thermospheric responses

3.1 Introduction

The relative lack of understanding and inability to appropriately model ionospheric conductivity is a key barrier to conduct system science geospace research. In the absence of conductivity understanding, which provides direct system coupling information, analyses rely on indirect measures of geospace and their connections, such as geomagnetic activity indices and proxies. This short chapter comments on the indirect approach to geospace system science and serves two purposes: 1) to introduce the solar terrestrial connection and the geospace system; and 2) to demonstrate that past attempts to understand the MIT system have been limited by lack of ability to directly specify system connections. We make reference to the extensive statistical study of the impacts of solar wind high speed streams (HSS) from *McGranaghan et al.* (2014) to emphasize the importance of accurately modeling parameters such as the ionospheric conductivity to more directly understand, and ultimately predict, the geospace environment.

The following section summarizes *McGranaghan et al.* (2014) as an illustrative example of geospace analysis conducted with a reliance on proxies and indices to determine system connections. Section 3.2.1 provides concluding remarks and connects the findings of *McGranaghan et al.* (2014) to the importance of conductivity modeling. The final section sets the stage for the rest of the dissertation.

3.2 *McGranaghan et al.* (2014): An illustrative example of geospace analysis using proxied system connections

In *McGranaghan et al.* (2014) we examined thermospheric neutral density response to 172 solar wind HSSs and the associated stream interfaces during the equinox seasons of 2002-2008. HSSs produce prolonged enhancements in satellite drag. We found responses to two drivers: 1) the equinoctial Russell-McPherron (R-M) effect, which allows the azimuthal component of the interplanetary magnetic field (IMF) to project onto Earth's vertical dipole component; and 2) coronal streamer structures, which are extensions of the Sun's meso-scale magnetic field into space. For this statistical study events for which the IMF projection was antiparallel to the dipole field were classified as "Effective-E", otherwise they were "Ineffective-I". Effective orientations enhanced energy deposition and subsequently thermospheric density variations. The IMF polarities preceding and following stream interfaces at Earth produced events that were: Effective-Effective-EE; Ineffective-Ineffective-II; Ineffective-Effective-IE; and Effective-Ineffective-EI. These categories were additionally organized according to their coronal source structure: helmet streamers (HS-EI and HS-IE) and pseudo-streamers (PS-EE and PS-II). Approximately 65% of these combinations were HS-EI or HS-IE.

We investigated the geospace responses to these different structures with ACE satellite solar wind plasma and IMF data and geomagnetic indice data from the NASA OMNI service, CHAllenging Minisatellite Payload (CHAMP) satellite neutral density data, and three LEO proxies for the energy dissipation: 1) hemispheric power from the National Oceanic and Atmospheric Administration (NOAA) Polar Operational Environmental Satellites (POES) satellites; 2) Joule heating proxy (JHP) calculated using the empirical relationship derived by *Knipp et al.* (2004); and 3) NO emissions measured by an instrument onboard the Thermosphere Ionosphere Mesosphere Energetics and Dynamics (TIMED) satellite.

With these data *McGranaghan et al.* (2014) used a superposed epoch analysis to study the effects of 112 HS CIR-HSSs and 60 PS CIR-HSSs on the solar wind and Earth's geospace environ-

ment, specifically focusing on neutral density. We showed that some CIR-HSS combinations are predisposed to more efficiently energize the thermosphere especially during equinox. This predisposition can be traced from structures at the Sun, into the solar wind, and through intermediate energy paths into thermospheric density. New in that study was an assessment of the seasonal Russell-McPherron effect on CIR-HSS-driven neutral density enhancement that revealed thermospheric density response can be categorized into four combinations of effective/ineffective regimes. In ineffective-to-effective (HS-IE) flow-transitions across equinoctial CIR-HSSs, the neutral density enhancement was 60% above background. Only a 35% enhancement occurred for ineffective to ineffective (PS-II) transitions. For CIR-HSS events with "Effective" IMF orientation in the high-speed flow regime (HS-IE and PS-EE), the ground based indices and LEO and proxy measures of geoeffectiveness were significantly enhanced relative to events for which there was an "Ineffective" IMF orientation in the high-speed flow regime. Interestingly, in the pre-CIR slow-flow regimes only the pseudo-streamer events with "Effective" IMF orientation (PS-EE) produced enhanced ground and space responses. Unlike the HS-EI events, which are synonymous with the "calm-before-the-storm" (*Borovsky and Denton*, 2013), PS-EE events were the sources of a moderate level of ongoing driver/response activity that pre-conditioned the neutral atmosphere for shortened intervals of density upheaval after CIR passage due to enhanced NO emissions. We believe that this unexpected behavior can be traced back to small-scale coronal 'web-like' structures of PS events versus larger-scale current sheet structures of HS events. These seemingly small distinctions translated to significant differences in the thermosphere.

As shown in previous, but more limited studies, the thermosphere responds to enhanced solar wind driving in the post-CIR flow regime of high-speed streams (*Lei et al.*, 2011; *Chen et al.*, 2012). In a superposed-epoch sense, the associated neutral density enhancement is ∼40% above background. This enhancement slowly tapers over the course of three or more days.

Intertwined with the R-M effect we identified an important preconditioning effect on and in the thermosphere that was associated with solar wind structuring. We found HS events to generally have similar, smooth solar wind speed profiles, while the PS events are less uniform. Pre-CIR flow

originating in helmet streamers allows the entire geospace system to settle to a 'calm before the storm' low energy state. This state supports rapid thermosphere scale-height expansion when CIRs and their subsequent high-speed flow arrive at Earth. Pre-CIR flow originating in the less uniform regimes surrounding PS-EE events allows episodic energy deposition to the thermosphere. This episodic energy input has a dual influence: 1) the thermosphere does not reach a 'calm before the storm' energy minimum, rather, the thermosphere experiences a low-level of ongoing energy input; 2) the punctuated energy deposition, as suggested by the hemispheric particle power and Joule heating proxy, produce thermosphere nitric oxide (NO) whose cooling properties tend to offset the heating produced by geomagnetic activity. The result is a, somewhat counter-intuitive, weak and short-lived ∼34% density enhancement for effective-to-effective (EE) flow transitions. The ineffective-to-ineffective (II) flow transitions, which are less influenced by NO, experience a delayed, but longer-lived, density enhancement of ∼50%. Overall, we identify that HS and PS events produce systematically different impacts on the thermosphere and explain the large relative density enhancement in three out of the four CIR-HSS geoeffectiveness categories.

We found that the thermosphere exhibits hysteresis that contributes to a more complex response to solar wind flow regimes surrounding coronal pseudo-streamers, than to flow regimes surrounding coronal helmet streamers. The response is modulated during equinox by the R-M effect.

The findings above suggest that improvement in forecasting neutral density response to high-speed streams can be realized days in advance of the CIR-HSS arrival. Forecasters can apply knowledge of seasonal driving, recurrence patterns along with observations of the approaching coronal hole structures from the Sun's eastern hemisphere to provide multi-hour to multi-day forecasts of thermospheric neutral density enhancement. Additional prognostic information can be garnered from space- and ground-based observations of the finer-scale coronal structure in terms of pseudo and helmet streamers. A three-day history of upwind solar wind data and LEO NO emissions can provide a measure of the likely preconditioning in the geospace system. In turn this preconditioning controls the likely range of thermospheric neutral density response to CIR-HSS

systems. Ultimately, we created a new probabilistic forecasting framework based on solar wind input and proxied energy coupling in geospace. We concluded that forecasts in this paradigm suffer from a dependence on statistically observed responses rather than detailed understanding of the physical connections between the solar wind and ionosphere-thermosphere system.

3.2.1 Importance of conductivity modeling to upper atmospheric specification: Understanding to the point of prediction

This study motivates the remainder of this dissertation in two important ways, by demonstrating that: 1) while indirect measures and proxies of the geospace system provide useful information, they are not capable of serving detailed specification and prediction objectives; and 2) fundamental understanding of the intermediate energy pathways between the solar wind and upper atmosphere is critical to current and future needs for geospace system modeling and prediction. The crucial parameter in the modeling of energy exchange in geospace, and perhaps the most difficult to study and, correspondingly, most uncertain, is the ionospheric conductivity. In the following chapters we, therefore, address this key barrier to geospace system science.

Chapter 4

Conductivity Modeling

4.1 Introduction

The ionosphere-thermosphere is highly dynamic, driven in part by incident solar photons and precipitating particles that vary as a function of latitude, longitude, and altitude. Ionization rates as functions of driving conditions and spatial location are essential for determining the dynamic structure of the ionosphere and, through ion-neutral interactions, the thermosphere as well. Several global models exist to calculate the ionization and resulting redistribution of the incident particle energy in the ionosphere-thermosphere (IT) system, including physics-based, coupled thermosphere-ionosphere models like TIE-GCM (*Richmond et al.*, 1992), CTIPe (*Millward et al.*, 2001), and GITM (*Ridley et al.*, 2006); data assimilative models such as GAIM (*Schunk et al.*, 2004); and empirical models such as IRI (*Bilitza*, 2001). The work we present in this chapter is twofold: 1) detail the GLobal AirglOW (GLOW) model of upper atmospheric ionization rates, chemistry, and conductivity; and 2) apply the flexibility and speed of a parameterized atmospheric ionization model in place of a full particle transport code. We have made the latter product freely available to the community.

The computational burden of sophisticated particle transport codes, applied globally, make this approach to atmospheric specification intractable in large models and in applications where many evaluations of the model must be performed, such as the analysis of on-orbit satellite data. Thus far none of the IT models offer the flexibility of computational efficiency coupled with high accuracy while also delivering a full characterization of the IT ionization state. The global circu-

lation models (GCMs) demonstrate increasing accuracy, but are extremely difficult to deconvolve if one only needs a portion of the full capability, and are thus computationally restrictive for such applications. On the other hand, the existing empirical models are largely considered reasonable *a priori* estimates of the IT system, but additional information must be included for studies desiring high accuracy. There is a notable lack of middle ground between these two extremes.

Several models have been developed to fill this gap, namely particle transport models capable of locally specifying the IT system given solar and auroral particle inputs and latitude/longitude location (*Richards and Torr*, 1986; *Solomon et al.*, 1988; *Lummerzheim et al.*, 1989; *Lummerzheim and Lilensten*, 1994; *Strickland et al.*, 1999). These models offer greater flexibility than the GCMs, but are still largely first-principles models, and thus rely on computationally-intensive particle transport algorithms. Additionally, they do not allow for subsequent transport effects and instead must be run at all locations of a desired IT analysis grid to specify the complete system over that grid, which increases the computational cost. In the first portion of this chapter we address the GLobal AirglOW (GLOW) (*Solomon et al.*, 1988) model, which is primarily used in this dissertation. We detail how this model is used to perform widespread analyses of the ionospheric conductivities. The essential elements are the use of: 1) Defense Meteorological Satellite Program (DMSP) in-situ particle data to specify the auroral particle input; and 2) high performance parallel computing to permit extensive model evaluations. In this work on the order of 10^8 GLOW model evaluations with DMSP input are performed.

In many applications access to high performance computing resources and ability to perform parallelized simulations are not possible. Thus, in the second part of this chapter we focus on the difficult problem of parameterizing the particle transport algorithms. Recent modeling efforts have produced parameterizations that can reproduce well the capabilities of sophisticated two-stream/multi-stream electron transport models (*Fang et al.*, 2008, 2010; *Solomon and Qian*, 2005) and Monte Carlo proton transport models (*Fang et al.*, 2013) with a dramatically reduced computational cost. Here we bring together the desirable features of each approach, namely flexibility and computational tractability. To my knowledge, this work represents the first time that

the flexibility of these models has been combined with the computational advantage of particle transport parameterizations. The goal of this latter portion is to describe the implementation and performance of a fast, parameterized version of the GLOW model, hereafter called GLOWfast, and to make the community aware of this new code.

This second part provides a fast, parameterized model to study global upper atmospheric ionization rates, ion and electron densities, height-resolved conductivity, and incoming energy redistribution due to incident solar and streaming electron energy upon the upper atmosphere. We implement together, for the first time, elements from a robust upper atmospheric model and computationally efficient parameterizations of the primary ionospheric ionization sources in a compact code capable of specifying the perturbations in the IT system. This new parameterization, which is widely available, will serve as an important tool for the IT modeling community in support of upcoming missions, such as the Ionospheric CONnection Explorer (ICON) (*Immel*, 2012) and Global-scale Observations of the Limb and Disk (GOLD) (*Eastes*, 2009).

This chapter proceeds first with a complete description of the GLOW model, including its use to analyze DMSP in-situ particle data, and then with a detailed presentation of the GLOWfast model. The GLOWfast portion is broken down into methodology (Section 4.4), performance comparison of the parameterized code for 3026 different input parameter sets in both the atmospheric results and computational improvement (Section 4.5), and, finally, a discussion and remarks summarizing and concluding the chapter (Section 4.6).

4.2 The GLobal AirglOW model of upper atmospheric ionization rates, chemistry, and conductivity.

The GLobal AirglOW (GLOW) model is used to determine the effects due to incident solar radiation and auroral electrons on the ionosphere (*Solomon et al.*, 1988; *Solomon and Abreu*, 1989; *Bailey et al.*, 2002). GLOW adopts a radiative transfer method for calculating these effects and implements the two-stream electron transport code of *Nagy and Banks* (1970) between 80-200 km, primarily the E-Region ionosphere. GLOW computes two primary ionization profiles: 1) direct

photoionization, due to incident solar flux and 2) electron impact ionization, resulting from both incident auroral electrons and photoelectrons (secondary electrons created in the photoionization interactions). Direct photoionization is computed in two steps, beginning with unattenuated solar flux as a function of wavelength: 1) the Beer-Lambert law is applied layer-by-layer through a model thermosphere, for which any neutral atmosphere can be used (here we use the NRLMSISE-00 model (*Picone et al.*, 2002)) to determine the solar actinic flux in each spectral interval and 2) branching ratios and total absorption cross-sections are multiplied by the actinic flux to give species- and process-specific rates for ionization, dissociative ionization, and dissociation due to solar photons. We use the solar EUV flux model for Aeronomic Calculations (EUVAC) of *Richards et al.* (1994) as the input solar spectrum. Figure 4.1 shows a schematic flowchart representation of the GLOW model, including inputs (blue), model components (black), and outputs (green). The conductivity module was created and implemented as part of this dissertation.

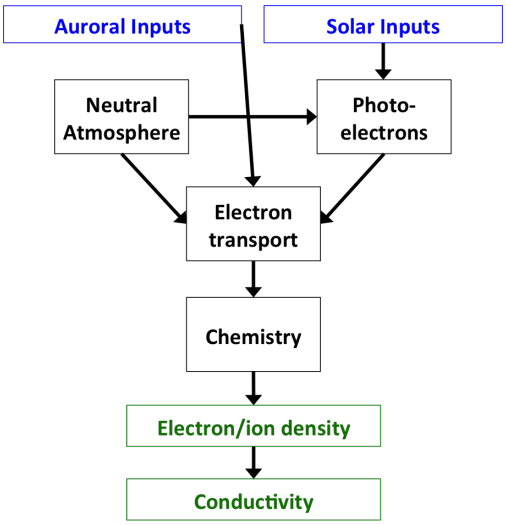

Figure 4.1: Schematic showing the components of the GLOW model. Inputs are shown in blue, model components in black, and outputs in green. The conductivity module was created and implemented as part of this dissertation (see Section 4.2.3).

Electron impact ionization in GLOW relies on computationally-intensive radiative transport methods. These calculations include input photoelectron production energy spectra as a function of altitude throughout the ionosphere, which are calculated during the photoionization process intro-

duced above in combination with the residual energy from these ionizations, and auroral electron energy spectra at the topside boundary of the ionosphere, which must be specified and are typically assumed to adhere to some chosen energy distribution. GLOW can handle any incident electron spectra, but is designed typically for both Maxwellian and high-energy tail, or Kappa, incoming auroral electron energy spectra, the choice of which can be driven by geophysical considerations (*McIntosh and Anderson*, 2015). A complete derivation of the particle transport algorithm used in the GLOW model is provided in Appendix B and Section 4.2.1 discusses the various methods used in this dissertation to specify the input energy spectra.

4.2.1 Input electron energy spectra

The GLOW model accepts any input auroral electron spectra, provided the spectra is defined on the model grid. Assumed functional forms are commonly used as convenient input to the model. Maxwellian, Kappa (Maxwellian with a high energy tail), and monoenergetic spectra are among the most frequently used spectra to describe auroral processes.

4.2.2 Use of the GLOW code with DMSP in-situ particle data

However, Chapter 2 discussed the limitations associated with such assumed functional forms. We overcome such assumptions through the use of the Defense Meteorological Satellite Program (DMSP) in-situ particle data to provide input spectra.

GLOW is used with immense volumes of in-situ particle data from the DMSP satellites to compute altitude profiles of the ionization rates, densities, and conductivities. Such extensive evaluations of the GLOW code, and its full particle transport algorithm, are made possible over an entire high-latitude analysis grid by code parallelization and high performance computing.

4.2.3 Extending the GLOW model for height-resolved conductivity

We extend the capabilities of the GLOW model by incorporating a subroutine that performs a first-principles calculation of the Pedersen and Hall ionospheric conductivities. The conductivities

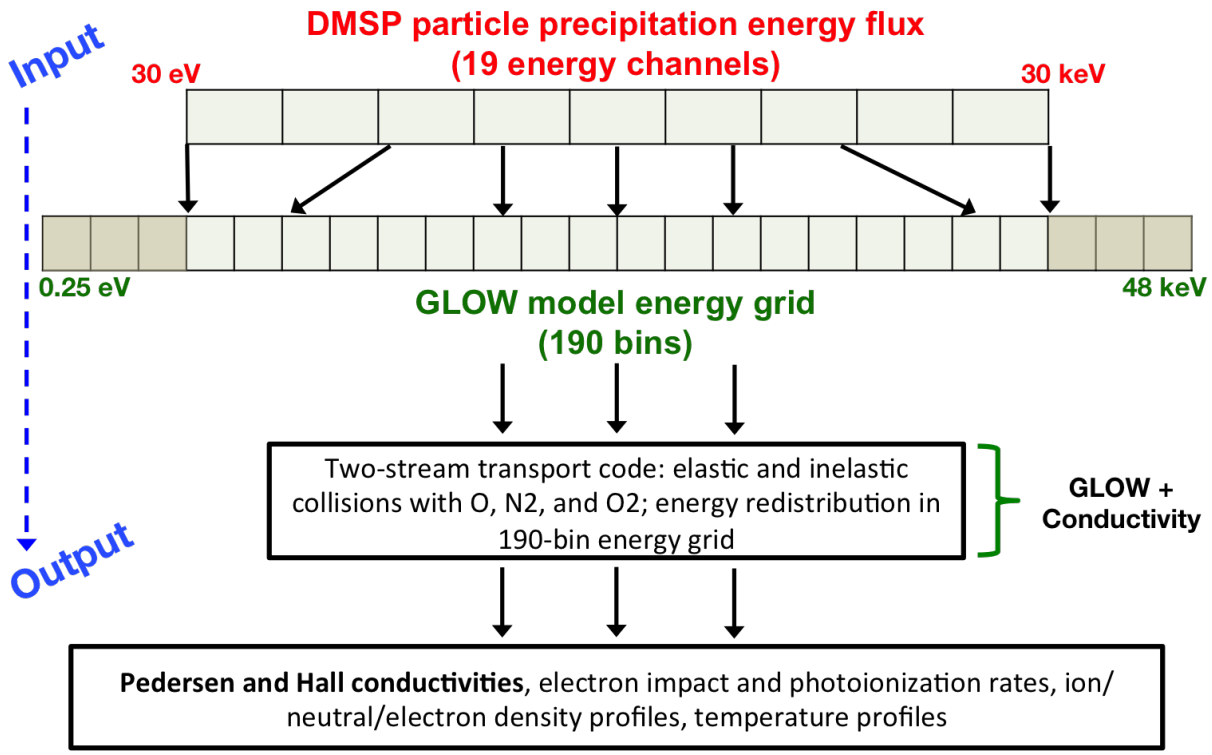

Figure 4.2: Schematic showing the use of DMSP in-situ energetic electron precipitation observations with the GLOW model. The DMSP SSJ particle detector provides electron energies in 19 logarithmically spaced energy bins between 30 eV and 30 keV. The DMSP input spectra are interpolated to the 190 bin GLOW model energy grid. The electron energies are not extrapolated beyond the 30 eV - 30 keV bounds of the DMSP SSJ instrument, but these bins are used in the model because they are important during the energy redistribution calculations performed by GLOW. Given the input spectra, the GLOW model performs two-stream electron transport calculations to produce height-dependent conductivities, density and temperature profiles, and ionization rates. The 'GLOW+conductivity' designation indicates that this dissertation provides the extension of the original GLOW model to include conductivity calculations. This extension is described in Section 4.2.3.

are computed using the equations (*Richmond et al.*, 1992):

$$\sigma_P = \frac{q_e}{B}\left[N_{O^+}\frac{r_{O^+}}{1+r_{O^+}^2} + N_{O_2^+}\frac{r_{O_2^+}}{1+r_{O_2^+}^2} + N_{NO^+}\frac{r_{NO^+}}{1+r_{NO^+}^2} + N_e\frac{r_e}{1+r_e^2}\right] \tag{4.1}$$

$$\sigma_H = \frac{q_e}{B}\left[-N_{O^+}\frac{1}{1+r_{O^+}^2} - N_{O_2^+}\frac{1}{1+r_{O_2^+}^2} - N_{NO^+}\frac{1}{1+r_{NO^+}^2} + N_e\frac{1}{1+r_e^2}\right], \tag{4.2}$$

where:

$$r_s = \frac{\text{collision frequency}}{\text{gyrofrequency}} = \frac{\nu_s}{\omega_s} \tag{4.3}$$

$$\omega_s = \frac{q_e B}{m_s}. \tag{4.4}$$

Here q_e is the magnitude of the charge of an electron, B is magnetic field strength, m_x is mass, and N_x is number density. Collision frequencies are governed by equations laid out in Section 2.2.6 (Equations 2.24 and 2.25). All other parameters (densities, temperatures, magnetic field strengths) are calculated within the GLOW code. Note that the 1-D electron density calculation in GLOW neglects transport effects through wind and chemical reactions, which can adversely affect the accuracy in certain situations. Transport effects become more important outside of the E-Region ionosphere, and therefore GLOW only calculates density profiles between 80-200 km and assumes empirical forms for F-Region altitudes. In light of the limits of the local approximation, we limit our analysis to the E-Region and caution users about the accuracy of model results outside of this altitude range.

4.3 A fast, parameterized version of GLOW: GLOWfast

In this section, we introduce a parameterized, updated, and extended version of the GLOW model, called GLOWfast, that significantly reduces computation time and provides comparable accuracy in upper atmospheric ionization, densities, and conductivity. We extend GLOW capabilities by: 1) implementing the nitric oxide empirical model; 2) providing a new model component to

calculate height-dependent conductivity profiles from first principles for the 80-200 km region (discussed above in Section 4.2.3); and 3) reducing computation time. The computational improvement is achieved by replacing the full, two-stream electron transport algorithm with two parameterizations: 1) photoionization (QRJ from *Solomon and Qian* (2005)) and 2) electron impact ionization (F0810 from *Fang et al.* (2008, 2010)). We find that GLOWfast accurately reproduces ionization rates, ion and electron densities, and Pedersen and Hall conductivities independent of the background atmospheric state and input solar and auroral activity. These results suggest that GLOWfast may be even more appropriate for low characteristic energy auroral conditions. We demonstrate in a suite of 3028 case studies that GLOWfast can be used to rapidly calculate the ionization of the upper atmosphere with few limitations on background and input conditions, and support these results through comparisons with electron density profiles from COSMIC.

4.4 GLOWfast methodology

We use the GLOW model to calculate the 1-D altitude profiles of ionization and dissociation rates, ion and electron densities, and the extension that computes height-resolved Pedersen and Hall conductivities. To distinguish between the full, detailed above, and fast, introduced below, versions of the GLOW model, we label all results from the full GLOW model 'GLOWfull' for the remainder of this chapter (note that results generated outside of this chapter use the GLOWfull model, which is, therefore, simply called 'GLOW' in all other chapters of this dissertation). However, as introduced above, such radiative transfer methods are often computationally prohibitive. For example, consider a global imaging mission, such as GOLD, making measurements at a temporal cadence of 30 minutes. In order to simulate the observed emissions at each point of a 2.5° latitude $\times$ 5.0° longitude grid over the course of one day using GLOWfull, it could take 4 to 16 core-hours, depending on the processor, compiler, and number of altitude levels.

Therefore, to overcome the computational burden of the GLOWfull model, we implement for the first time together two previously developed parameterizations of upper atmospheric ionization: 1) electron impact ionization (*Fang et al.*, 2008, 2010) (hereafter F0810) and 2) photoionization

(*Solomon*, 2001) and appropriately label the results of this confluence 'GLOWfast'. The result of this effort is a versatile and fast model that yields appropriate, upper atmospheric specification and is freely available to the broader community.

Figure 4.3 schematically shows the contribution we make in this work. We highlight the two primary improvements to the GLOWfull model: 1) addition of an empirical model of nitric oxide (discussed below in Section 4.4.0.1) and 2) addition of a subroutine that calculates height-resolved conductivity (discussed above in Section 4.2.3). We also depict the splintering of the GLOW model into GLOWfull, involving full radiative transfer methods, and GLOWfast, implementing the F0810 and QRJ parameterizations together as discussed in Sections 4.4.1 and 4.4.2, respectively. Finally, we show a rough estimate of the computational advantage that the new GLOWfast model provides. This computational improvement was calculated by taking the mean of the computation times for each of the 3028 test cases analyzed in this study. A standard deviation of the normalized computation time of 4 was also computed. The exact computational improvement is obviously platform- and implementation-specific.

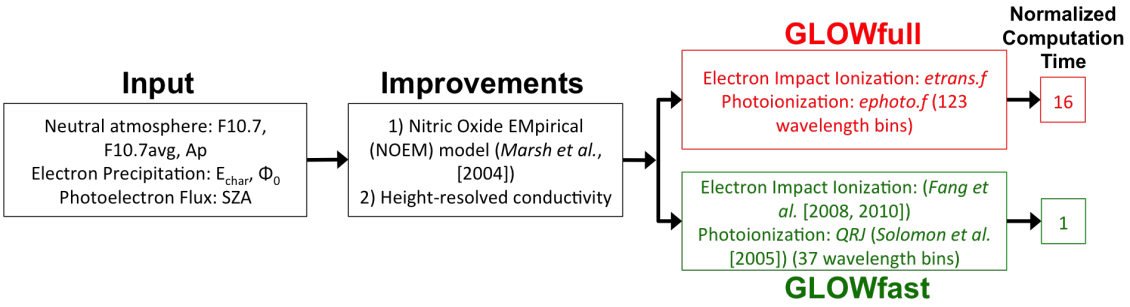

Figure 4.3: Schematic showing the components of GLOWfull, modifications and replacements made for GLOWfast, and approximate normalized computational benefit. Note that the original GLOW model is called GLOWfull to distinguish from GLOWfast in this chapter, but, because it is used to generate the results in the remainder of this dissertation, is simply called GLOW in subsequent chapters.

4.4.0.1 Improving the *a priori* nitric oxide density profiles: Nitric Oxide Empirical Model (NOEM)

GLOW originally included a crude estimate of the nitric oxide (NO) density based on a non-auroral profile obtained during low-to-moderate solar activity. This profile is taken as a constant in the example cases delivered with the GLOW model. To this point, users have been required to use this *a priori* profile, or manually modify the routines to supply their own. However, because NO density is a key parameter for accurately modeling the E-region ionosphere (*Bailey et al.*, 2002; *Solomon*, 2006), GLOW has been updated to include a better approach to NO density specification.

Based on data from the Student Nitric Oxide Explorer (SNOE) satellite obtained between March 1998 and September 2000 (*Solomon et al.*, 1996), *Marsh et al.* (2004) performed an Empirical Orthogonal Function (EOF) analysis, the results of which were used to construct a compact, three-dimensional model of NO density, given a planetary magnetic index, day of year, and 10.7 cm solar radio flux ($F_{10.7}$, in solar flux units where 1 sfu = 1×10^{-22} $\mathrm{Wm^{-2}Hz^{-1}}$). This model is called the nitric oxide empirical model (NOEM). We incorporate NOEM into the GLOW model to improve NO density specification.

4.4.1 Electron impact ionization

We adopt the *Fang et al.* (2008, 2010) parameterizations, hereafter called F0810, to calculate the ionization due to incident energetic electrons on the upper atmosphere. This parameterization was created based on a robust fit to sophisticated electron transport results under a large variety of atmospheric conditions, and represents a significant improvement over previous parameterization efforts. The multi-stream transport code of *Lummerzheim et al.* (1989); *Lummerzheim and Lilensten* (1994) quantifies the effects at lower incident electron energies ($E_{mono} < 50$ keV) where angular scattering is important, and the two-stream code used within GLOW quantifies the effects at energies between 50 keV and 1 MeV. The F0810 parameterization has been validated for energies between 100 eV - 1 MeV, and therefore covers virtually the entire range of upper

atmosphere-affecting energetic electrons with magnetospheric origin.

Electron impact ionization rates in the GLOWfast model are calculated in three steps: 1) the spectra of incident energetic electron precipitation is divided into contiguous monoenergetic beams, 2) the resultant contribution of each beam to the overall ionization is calculated using the F0810 parameterization, which assumes an isotropic angular distribution for each beam, and 3) the total ionization is calculated by a summation of these results. The product is a total ionization rate at the given location. For the purpose of detailed atmospheric analysis, including conductivity calculations, this must be divided into species-dependent ionization rates, for which we use the relationships given by *Rees* (1989). The branching ratio calculations are reproduced from *Rees* (1989) here:

$$\eta\left(N_2^+\right) = \frac{0.92n\left(N_2\right)}{\Delta} q_T, \tag{4.5}$$

$$\eta\left(O_2^+\right) = \frac{n\left(O_2\right)}{\Delta} q_T, \tag{4.6}$$

$$\eta\left(O^+\right) = \frac{0.56n\left(O\right)}{\Delta} q_T, \tag{4.7}$$

where $n\left(S\right)$ is the number density of species S, q_T is the total ionization rate due to precipitating electrons, and Δ is given by:

$$\Delta = 0.92n\left(N_2\right) + n\left(O_2\right) + 0.56n\left(O\right). \tag{4.8}$$

Another method to perform this partitioning was prescribed by *Jones and Rees* (1973) and is used in the thermosphere general circulation model (TGCM, (*Roble and Ridley*, 1987)). In both methods, these relationships are functions of the number densities of the desired species, either N_2, O_2, or O, numerical factors that account for the differences in ionization cross-section

magnitudes, and the total ionization rate. However, the *Jones and Rees* (1973) method includes additional factors meant to accommodate dissociative ionization in addition to direct ionization, the mathematical sources of which are unclear. We employ the *Rees* (1989) method and instead allow the GLOW chemistry model, *gchem.f*, to handle partitioning due to dissociative ionization subsequent to electron impact ionization calculations.

All results displayed in Section 4.5 are generated using Maxwellian distributions and are thus fully specified by the characteristic energy (E_{char}, half of the mean energy) and energy flux (Φ_0). In the remainder of the dissertation, however, we incorporate the directly-measured particle spectra into GLOW for the purposes of representing the high-latitude ionization source more accurately (see *McGranaghan et al.* (2014) and Section 4.2.2 and Figure 4.2 of this dissertation). This capability will be made available as part of the GLOWfast package.

4.4.2 Photoionization

We increase the efficiency of photoionization calculations within GLOW in two primary ways. First, we reduce the resolution of the wavelength grids used to describe the solar spectrum from 123 in GLOWfull to 37 in GLOWfast. Second, we replace the two-stream treatment of the photoelectrons by a parameterization. These two steps were designed and carried out by *Solomon and Qian* (2005) for the purpose of increasing computational efficiency in the Thermosphere-Ionosphere-Electrodynamics Global Circulation Model (TIE-GCM) (*Richmond et al.*, 1992). The resulting model is identified in TIE-GCM as QRJ which represents a convolution of heating rate (Q) with RJ (O_2 dissociation rate) from historical convention.

The low-resolution solar spectrum wavelength grid was designed to use coarse resolution where cross-sections for major atmospheric constituents exhibit slow variation with solar spectrum and high resolution when the cross-section structure is more dynamic (see Fig. 1a in *Solomon and Qian* (2005)). In regions of significant band structure, the low-resolution spectrum uses multiple overlapping bins to allow the model to produce a more realistic altitude distribution than could be obtained with single bins. The EUVAC solar proxy model of *Richards et al.* (1994) was adapted to

Table 4.1: Instances of comparison for Figures 4.4-4.9 between GLOW and GLOWfast.

		Comparison Designation *Comparison #*		
Input Parameters	Units	Auroral Ionization -Dominated 1 (Figure 4.4)	Solar Ionization -Dominated 2 (Figure 4.5)	Variational Study 3-3026 (Figures 4.6-4.9)
F10.7	sfu	50	70	[50 100 150]
Ap	nT	5	1	[5 20 40]
E_{char}	keV	variable	0	[0.5, 0.750, 1.0, 1.25, 1.50 1.75, 2.0, 3.0, 5.0, 7.50 10.0, 50.0, 75.0, 100.0]
Φ_0	erg $cm^{-2}s^{-1}$	1	1	1
Lat	deg	70	0	[60,70,80]
Long	deg	0	178	[0, 45, 90, 135, 180, 225, 270, 315]
SZA	deg	133.4	3.4	variable (determined indirectly by other inputs)

this low-resolution structure in the same work of *Solomon and Qian* (2005) and is used to specify the solar input in this work.

The atmospheric cross-sections for each major constituent are adapted to the low-resolution spectrum by averaging the high-resolution cross-section values across each interval and weighting the results by solar energy flux at each wavelength, yielding a low-resolution spectrum of total cross-sections. Branching ratios are then used to describe specific processes, namely ionization, dissociative ionization, and dissociation in the same manner described in Section 4.2.

The efficacy of the reduced wavelength bin approach has already been demonstrated in *Solomon and Qian* (2005) and will not be demonstrated again here. Rather, we will show comparisons between GLOWfull results and those obtained when all parameterizations have been included, GLOWfast in complete form.

4.5 Results and Discussion

4.5.1 Electron impact ionization: GLOWfull vs. GLOWfast

Comparison of the electron impact ionization calculations performed using the full two-stream electron transport code and the F0810 parameterization are made to assure the efficacy of the fast, parameterized version. The results of the two-stream code, *etrans.f*, in GLOWfull are used as a baseline. Our goal is to compare the performance of the GLOWfast and GLOWfull models for electron impact ionization. Thus, we initialize the background ionosphere and thermosphere at winter solstice conditions to ensure that auroral precipitation is the dominant externally-perturbing feature to the mid- and high-latitude ionosphere. Additionally, we choose 70° latitude, 0° longitude, and 0 hr local solar time to force a large solar zenith angle to further suppress the effects of solar photoionization. The results are shown in Figure 4.4.

The GLOWfast model reproduces the results of the GLOWfull code remarkably well, and provides a ∼15-fold computational improvement (the computational advantage is roughly a factor of 17 at lower characteristic energies, but drops to a factor of 10 for the 100 keV case). Average differences in maximum electron impact ionization rate are roughly 14.5% and the average difference in altitudes of maximum ionization are 3.5 km, though typically closer to 1-2 km. In some cases the differences are larger. The difference in maximum electron impact ionization rate for 1000 eV is ∼30% and the peak altitude difference for 100 eV is ∼15 km. Note that we compute the percent differences in this chapter as (GLOWfast - GLOWfull)/GLOWfull. At lower characteristic energies the parameterization tends to underestimate the altitude of a given level of electron impact ionization. However, this is only pronounced at characteristic energies near the bottom of the application range of F0810, that is, when the incident energy is below 1 keV. To explain why lower characteristic energies produce greater differences between GLOWfull and GLOWfast, we point to differences in the angular scattering calculations within multi-stream (which the F0810 parameterization was fit to at characteristic energies below 50 keV) and two-stream (strictly used in GLOWfull) transport methods as the likely cause. *Stamnes* (1981) reported that two-stream

electron transport calculations can underestimate downward electron flux intensities at low altitudes (<200 km) for lower incident electron energies when compared with multi-stream calculations. This explains why GLOWfast yields greater peak electron impact ionization rates in Figure 4.4, and also why those differences diminish for higher incident energies. Based on these observations, we suggest that GLOWfast may be more appropriate than GLOWfull for lower incident electron energies. We discuss this further in Section 4.5.3.

For this chapter, all electron impact ionization results will be the combination of incident auroral electrons as well as secondary electrons caused by photon flux. F0810 handles the incident auroral electrons while QRJ handles photoelectron ionization.

4.5.2 Photoionization: (*Richards et al.*, 1994) (primary incident photons) + (*Banks et al.*, 1974) (photoelectrons) vs. QRJ parameterization implemented in GLOW

These results will show QRJ as implemented in GLOWfast vs. the GLOWfull model in the situation of no auroral precipitation.

In Figure 4.5, we analyze the ionization rate profiles when the only source of ionization is the direct solar radiation. We isolate the photoionization by zeroing out the incident auroral particle energy flux and examining a case with a nearly overhead sun (SZA $\sim 0°$) during summer solstice. Moderate solar activity ($F_{10.7} = 70$) and low geomagnetic activity (Ap = 1) prescribe the background neutral and ionized atmospheres.

The QRJ parameterization yields excellent agreement with the GLOWfull model results. Figure 4.5(a) shows the comparison of the photoionization rates. These rates require no transport calculations and thus the only difference between GLOWfull and GLOWfast computations is the wavelength resolution. Figure 4.5(a) illustrates that there is little difference in the two model results due to the change in spectral bins from 123 to 37. The only discrepancy occurs below the bottom boundary of the model (80 km) and relates to the fact that the EUVAC reference spectrum at full 123-bin resolution extends to zero in the lowest wavelength bin (5 - 10 nm; note the lower

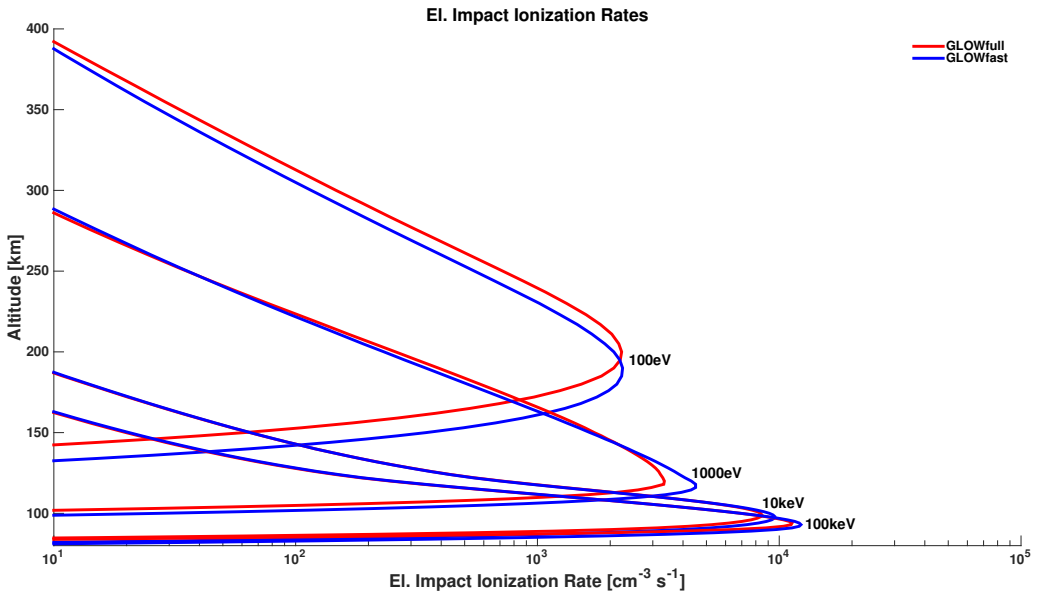

Figure 4.4: Comparison of electron impact ionization rates obtained from the GLOWfull (red curves) and GLOWfast (blue curves) methods. Comparisons for four representative precipitating electron energies (E_{char} = 0.1, 1, 10, and 100 keV) in a background atmosphere created using $F_{10.7}$ = 50 and Ap = 5 are shown. All simulations were conducted for a winter day (Dec. 21) and solar zenith angle of 133.4° (latitude = 70°, longitude = 0°, local solar time = 0 hr). The precipitating electron energy flux is $\Phi_0 = 1$ erg $\cdot$ cm^{-2} $\cdot$ s^{-1}.

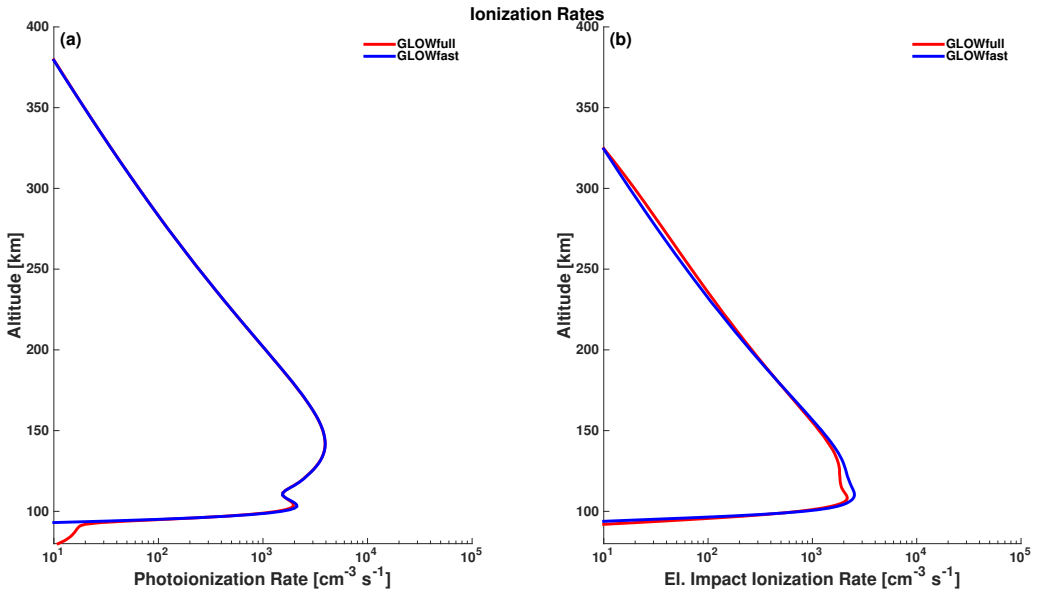

Figure 4.5: Comparison of: (a) photoionization rates and (b) electron impact ionization rates obtained from the GLOWfull (red curves) and GLOWfast (blue curves) methods. Comparisons in a background atmosphere created using $F_{10.7} = 70$ and Ap $= 1$ are shown. Both simulations were conducted for a summer day (Jun. 21) and solar zenith angle of $\sim 0^\circ$ (latitude $= 0^\circ$, longitude $= 178^\circ$, local solar time $= 0$ hr). The precipitating electron energy flux was zeroed out ($\Phi_0 = 0$ erg $\cdot$ cm^{-2} $\cdot$ s^{-1}) in order to suppress ionization due to auroral particles.

bound was later extended to 1.8 nm) thus producing no change in the photoionization profile. In contrast, the EUVAC reference spectrum at reduced 37-bin resolution was extended to 0.05 nm at the lowest bin and rebinned to 1 nm resolution by *Solomon and Qian* (2005), resulting in a finite reference flux in the lowest bin. Therefore, GLOWfast computes non-zero photoionization rates in this wavelength range. Figure 1(c) and Table A1 in *Solomon and Qian* (2005) further elucidate this minor difference.

Solar ionization produces secondary electrons, which are handled with full, two-stream transport in GLOWfull and, by contrast, with the QRJ parameterization in GLOWfast. Figure 4.5(b) contains the resultant photoelectron impact ionization comparison of the two approaches. Only minor differences exist, including a $\sim 17\%$ difference in the peak ionization rate and a 2 km difference in the altitude of peak ionization rate.

4.5.3 GLOWfull vs. GLOWfast comparison for 3024 different input conditions

The GLOWfull model has been validated with sophisticated Monte Carlo simulations (*Solomon*, 2001) and thus validation of GLOWfast can be conducted by direct comparison with the full model. The final column of Table 4.1 details the extensive trade space of input conditions that were used for these comparisons (cases 3-3026). This trade space was chosen to vary the background neutral atmosphere (F10.7, Ap, latitude, and longitude), input photoionization source (F10.7, solar zenith angle (SZA)), and input auroral electron precipitation (E_{char}). We chose June 21, 1999 as the input date to provide solar zenith angles below 90° at high-latitudes so that non-negligible photoionization and auroral ionization occurred simultaneously. Table 4.1 provides the necessary information to reproduce the results in this chapter.

Figures 4.6-4.9 show the statistical results. Figure 4.6 demonstrates that GLOWfast is able to reliably reproduce GLOWfull results over a wide range of characteristic electron energies. Differences in the peak ionization rate are generally less than 30%, while the altitude of peak ionization rate is regularly reproduced within a couple kilometers. At low characteristic energies, where angular scattering is increasingly important and peak ionization rates are broader, the differences are

larger, though remain well-modeled by GLOWfast. The electron impact ionization rate results are consistent with Figure 3 in *Fang et al.* (2010). It is important to note that the difference between the full and fast models, both in the peak ionization rate and in the altitude of the peak (i.e. both Figures 4.6a and 4.6b) particularly at the low energy end, is in large part due to the difference in the angular scattering calculation. The F0810 parameterization calculated ionization due to lower energy electrons (<50 keV) using a multi-stream model, in which angular scattering is more accurately accounted for than in the two-stream approach used in GLOWfull. Figure 2 from *Fang et al.* (2010) compares the F0810 parameterization, the results of the first principles models on which it was based, and the previous range calculation-based Spencer-Lummerzheim parameterization (*Lummerzheim*, 1992; *Spencer*, 1959) on which the parameterization technique was obtained. The graphic shows that the agreement between F0810 and the first principles models persists from 100 eV - 1 MeV. While the Spencer-Lummerzheim parameterization agrees above ∼3 keV, it does not yield reliable results below this energy where multi-stream effects become important. Thus, in those results F0810 more capably reproduced multi-stream effects than two-stream models. However, due to the uncertainty of the collisional cross-section data that are used in these models, we cannot reach a definite conclusion about which method is more accurate without direct comparison with a multi-stream model. The differences in the two approaches diminish with increasing incident electron energy because the scattering cross-sections become strongly peaked in the forward direction and angular scattering becomes correspondingly less important. For characteristic electron energies >50 keV the F0810 parameterization is based on the GLOWfull model rather than a multi-stream model and thus multi-stream effects no longer contribute to the difference shown in Figures 4.6a and 4.6b. The differences here are small, ∼5% in peak ionization rate and ∼1 km in altitude of the peak ionization rate, and represent minor differences between F0810 and the two-stream electron transport calculation of GLOWfull. Our results are in general agreement with the total ionization rate comparison shown in Figure 4 of *Solomon* (1993).

Figure 4.7 shows the differences in primary ion constituent column densities as a function of characteristic energy for cases 3-3026. The column densities were calculated by integrating

over all E-Region altitudes (80-200 km) and computing the percent differences between GLOWfull and GLOWfast results. Figures 4.7(a)-(d) show the ion constituent differences rarely exceed 10% and usually match within 5% for characteristic energies of 1 keV or higher. The relatively simple ionization rate partitioning that we use (see Section 4.4.1) likely contributes to the offsets for each ion constituent in Figures 4.7(a)-(d). E-Region ion lifetimes are relatively short and GLOW accordingly assumes photochemical equilibrium. The electron column density, then, is a good measure of the overall agreement between the two models in terms of composition. In Figure 4.7(e) there is excellent agreement between GLOWfull and GLOWfast electron column densities, where mean differences are consistently under 5%. Referring to Equations 4.1 and 4.2 it is apparent that good agreement among ion and electron densities should correspond to good agreement in the Pedersen and Hall conductivities. Figure 4.8 verifies this.

Finally, Figure 4.9 provides a comparison of photoionization rates for each case as a function of solar zenith angle. The only difference in this computation between GLOWfull and GLOWfast is the spectral resolution. Therefore, Figure 4.9 shows that the implementation of the 37-bin spectral resolution of *Solomon and Qian* (2005) results in differences no greater than 1-2% and 1-2 km in peak photoionization rates and altitudes, respectively.

4.5.4 Validation with COSMIC electron density profiles

The Constellation Observing System for Meteorology, Ionosphere, and Climate (COSMIC) is a mission, launched in 2006, that uses Global Positioning Services Radio Occultation (GPSRO) techniques to obtain electron density profiles (EDPs) along the atmospheric tangent point (*Lei et al.*, 2007; *Schreiner et al.*, 2007; *Yue et al.*, 2014). COSMIC EDPs have been validated using ground-based measurements and models (*Lei et al.*, 2007) and provide unprecedented coverage of ionospheric electron content (*Yue et al.*, 2011, 2012). As a result, this data set provides an opportunity for validation of the GLOWfast model. Figure 4.10 shows four comparison cases between specific COSMIC EDPs and Fuller-Rowell and Evans-driven GLOWfull and GLOWfast EDPs in the summer E-Region ionosphere during summer conditions (June 1, 2013). For summer

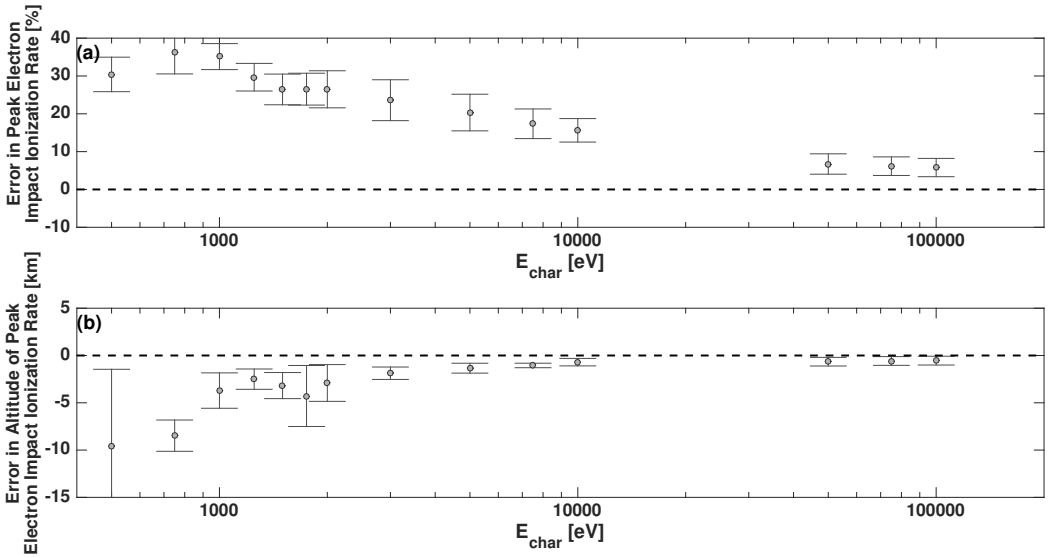

Figure 4.6: Differences in electron impact ionization rate altitude profiles as a function of characteristic electron energy incident on the topside ionosphere. These results correspond to the trade space detailed in final column of Table 4.1. Percent differences are calculated by comparing the profiles from the GLOWfull and GLOWfast models for: (a) peak ionization rate and (b) altitude of peak ionization rate. For each characteristic energy the mean differences (filled circles) and standard deviations (error bars) are computed for 216 background input conditions, yielding a total of 3024 test cases.

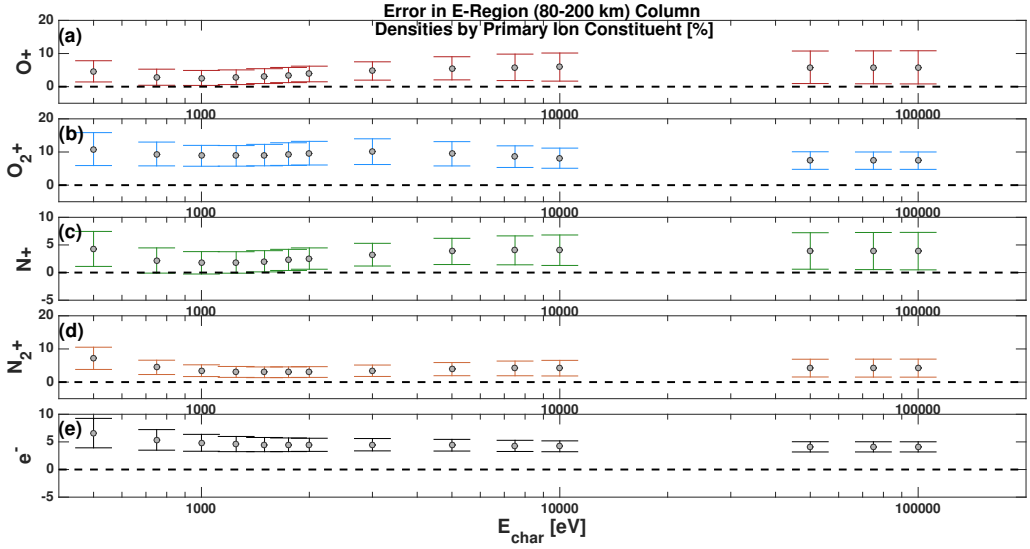

Figure 4.7: Differences in primary ion constituent column densities as a function of characteristic electron energy incident on the topside ionosphere. These results correspond to the trade space detailed in final column of Table 4.1. Percent differences are calculated by comparing the column densities from the GLOWfull and GLOWfast models for: (a) $O+$, (b) O_2+, (c) $N+$, (d) N_2+, and (e) e^-. For each characteristic energy the mean differences (filled circles) and standard deviations (error bars) are computed for 216 background input conditions, yielding a total of 3024 test cases. Column densities are computed by integrating the ion densities over E-Region altitudes (80-200 km).

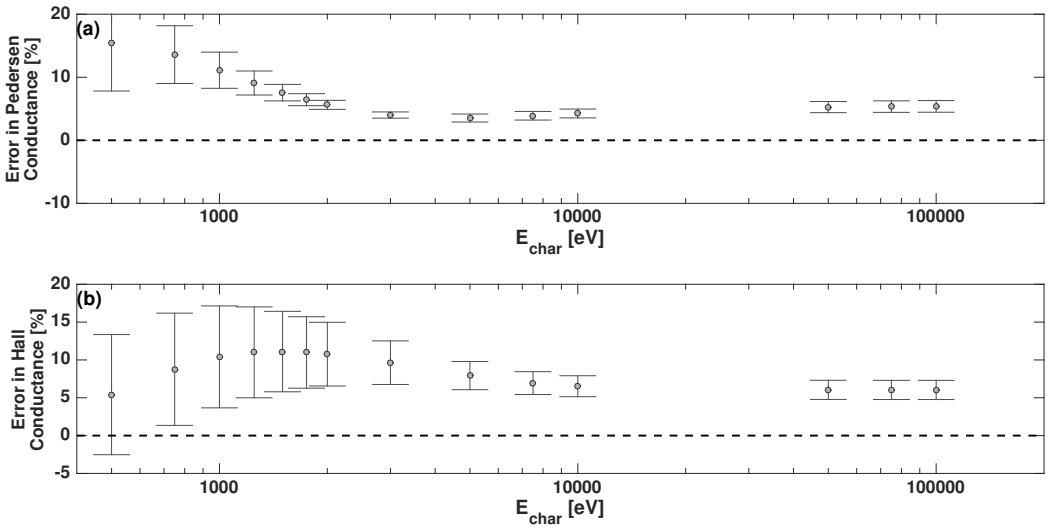

Figure 4.8: Differences in height-integrated conductivity (conductance) as a function of characteristic electron energy incident on the topside ionosphere. These results correspond to the trade space detailed in final column of Table 4.1. Percent differences are calculated by comparing the profiles from the GLOWfull and GLOWfast models for: (a) Pedersen conductance and (b) Hall conductance. For each characteristic energy the mean differences (filled circles) and standard deviations (error bars) are computed for 216 background input conditions, yielding a total of 3024 test cases.

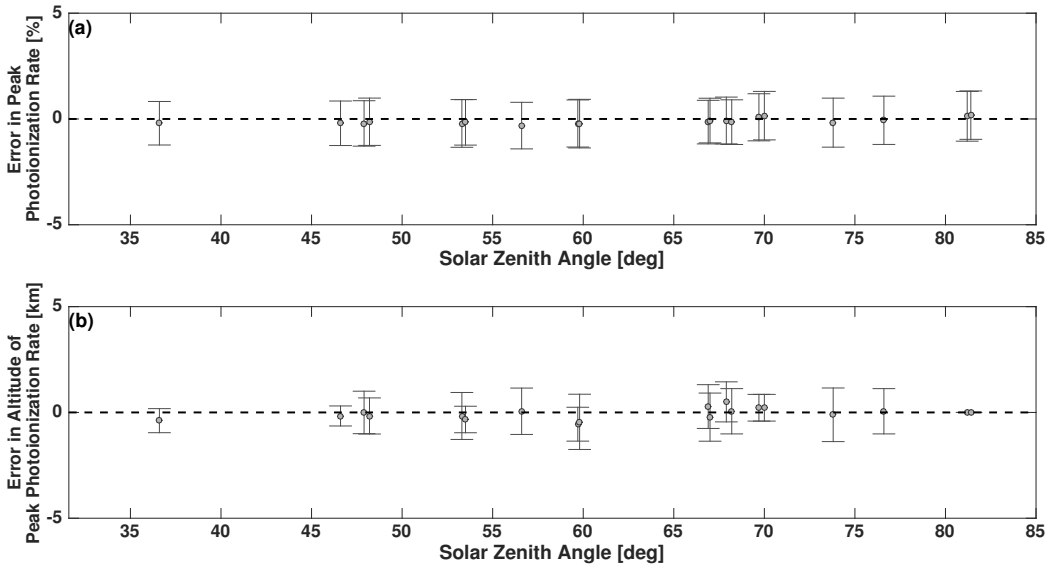

Figure 4.9: Differences in photoionization rate altitude profiles as a function of solar zenith angle. These results correspond to the trade space detailed in final column of Table 4.1. Percent differences are calculated by comparing the profiles from the GLOWfull and GLOWfast models for: (a) peak photoionization rate and (b) altitude of peak photoionization rate. 23 different solar zenith angles are included in the 3024 test cases in Table 4.1, ranging from $36 - 96^{\circ}$. For each solar zenith angle between $36 - 82^{\circ}$ the mean differences (filled circles) and standard deviations (error bars) are computed.

conditions COSMIC has been shown to be most accurate based on comparisons with ground-based data (*Sheng et al.*, 2014). We chose the comparisons in Figures 4.10(a)-(d) to be a set representative of varying spatial and geophysical conditions, ensuring that photoionization and electron impact ionization were both non-negligible. The spatial and geophysical information for each comparison is shown on each panel. The F10.7 and Ap daily-averaged values for June 1, 2013 were 101.8 sfu and 58 nT, respectively. Based on the location of each EDP from COSMIC we obtained the flux, Φ_0, and characteristic energy, E_{char}, data from the statistical maps prepared by *Fuller-Rowell and Evans* (1987) using TIROS-NOAA satellites precipitation data. These data were binned in 1° magnetic latitude by 2° magnetic local time, and thus the precipitation information used for these comparisons represents bin-averaged values based on the COSMIC RO location. We set the COSMIC RO location to be the tangent location at which the EDP maximum was observed, and then drove GLOWfull and GLOWfast with these conditions.

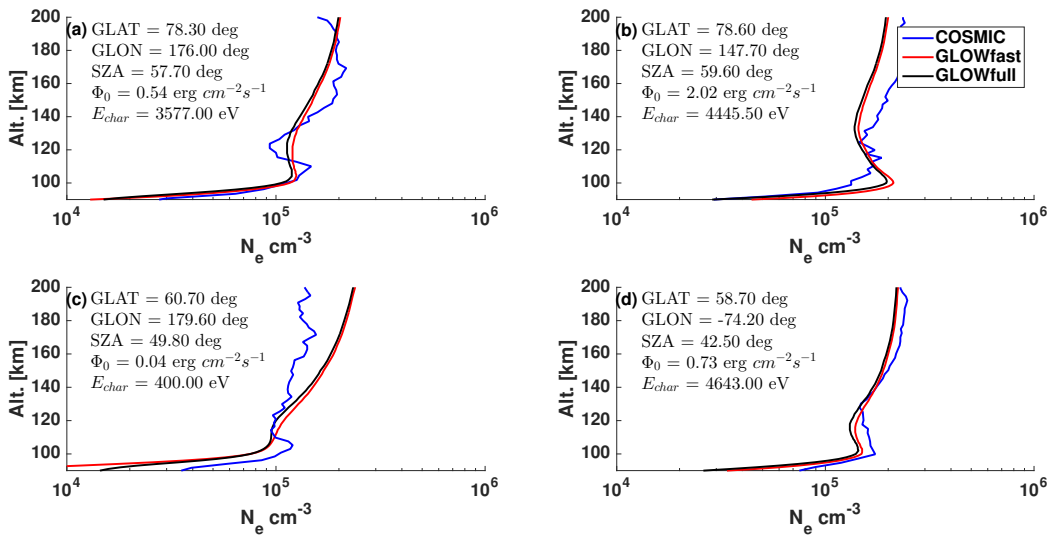

Figure 4.10: Comparison of COSMIC, GLOWfull, and GLOWfast E-Region electron density profiles for a variety of spatial and geophysical conditions (cases (a)-(d)). All comparisons take place during summer conditions (June 1, 2013), when COSMIC profiles are typically more accurate (see text). The daily-averaged F10.7 and Ap values for June 1, 2013 were 101.8 sfu and 58 nT, respectively.

Figure 4.10 shows good agreement between COSMIC event EDPs, GLOWfull, and GLOW-

fast EDPs in the E-Region ionosphere. GLOWfull and GLOWfast match closely throughout, as expected from the results shown in Figure 4.7(e). The COSMIC event EDPs follow these profiles with only minor differences. There are several sources of error in COSMIC EDPs. The most significant is the assumption of spherical symmetry in the Abel inversion procedure used to obtain the profiles (*Lei et al.*, 2007). A 'smearing' factor due to satellite motion during the RO retrieval process can also complicate the profiles. Additionally, GLOWfull and GLOWfast EDPs were generated using a statistically averaged auroral model which does not capture the details of the incoming particle spectrum or energy flux at a particular place or time. Each of these effects likely contribute to the minor differences in COSMIC and GLOW EDPs, however, in certain cases, these errors can become much more significant and contribute to large disagreement between the resulting profiles.

The agreement between COSMIC, GLOWfull, and GLOWfast generally falls off towards the bottomside E-Region boundary. At these altitudes residual phase noise passing through the dual-frequency ionospheric calibration for COSMIC profiles adds additional error (*Schreiner et al.*, 2007), and makes the COSMIC information less reliable. Discrepancies among GLOWfull and GLOWfast results likely come from differences in the high- and low-resolution spectra and atmospheric cross-sections at the highest and lowest wavelengths (radiation that penetrates furthest into the atmosphere) for GLOWfull and GLOWfast, respectively (see Figure 1 in *Solomon and Qian* (2005)). In light of these promising results, we target a larger COSMIC comparison as future work. We discuss this effort further in Chapter 9.

4.6 Conclusions

In this chapter we introduced the GLobal AirglOW (GLOW) upper atmospheric model (*Solomon et al.*, 1988) that is extensively used in this dissertation research. The development was divided into two parts: 1) a description of the GLOW model that performs complete radiative electron transport calculations; and 2) the development of a fast, parameterized version of the GLOW model, called GLOWfast. The former discussion provided details of the GLOW model electron transport, auroral electron energy input from DMSP in-situ electron energy observations, a new

extension to robustly calculate height-dependent ionospheric conductivities, and high performance computing techniques used to enable extensive model evaluations. The latter discussion detailed the development of the GLOWfast model for which two previously derived parameterizations were used to replace the computationally-intensive electron transport algorithm in GLOW, namely *Fang et al.* (2008, 2010) for electron impact ionization (F0810) and *Solomon and Qian* (2005) for photoionization (QRJ). The GLOWfast model also incorporated the Nitric Oxide Empirical Model (NOEM) (*Solomon et al.*, 1996) to calculate *a priori* nitric oxide profiles.

An extensive validation of the GLOWfast model was performed, and the results are briefly summarized here. GLOWfast produced an order of magnitude computational improvement without sacrificing accuracy and provided an additional benefit over the full model at lower energies. This low energy benefit is a result of the fact that the F0810 parameterizations for energies below 50 keV were fit using a multi-stream model (*Lummerzheim et al.*, 1989; *Lummerzheim and Lilensten*, 1994). The F0810 parameterization models multi-stream effects at energies less than 50 keV while GLOWfull does not. These effects are increasingly important as characteristic energy diminishes. We suggest that GLOWfast may be more appropriate at low energies than GLOWfull. However, in lieu of uncertainties in particle cross-sections, a direct comparison with a multi-stream model is necessary to investigate further. Such a comparison is an important subject of future work.

The F0810 and QRJ parameterizations represent a balance between efficiency and accuracy and are therefore imperfect. Because it was built from the GLOW model, GLOWfast inherits some of the same limitations (these are detailed at the model source code location on the NCAR High Performance Storage System and are available on request from Stan Solomon *stans@ucar.edu*). In particular, the model results are limited to the 80-200 km range. Further, though the F0810 parameterization has been validated for energies between 100 eV and 1 MeV, caution should be used when attempting to analyze these high energy ionization impact situations with GLOWfast. Additionally, for QRJ, *Solomon and Qian* (2005) acknowledge that a small discrepancy in the O_2 ionization rates at high solar zenith angles could be improved by the addition of a few more spectral bins.

In 3026 test cases we demonstrate excellent agreement between the full and fast versions of the model by comparing electron impact ionization rates (Figure 4.6), ion and electron column densities (Figure 4.7), Pedersen and Hall conductances (Figure 4.8), and photoionization rates (Figure 4.9). Errors in all quantities were consistently below 10% and more often below 5%. We further validated GLOWfast results against GLOWfull and COSMIC electron density profiles in Figures 4.10(a)-(d), and demonstrated good agreement in the E-Region ionosphere.

Overall F0810 and QRJ represent highly accurate parameterizations for upper atmospheric ionization and are the best currently available. We anticipate GLOWfast becoming a useful tool for the atmospheric modeling community, especially in light of upcoming Earth-observing missions like ICON and GOLD.

In the remainder of this dissertation, the GLOWfull model is used to generate results, and is, therefore, simply called GLOW outside of this chapter.

Chapter 5

New fundamental picture of ionospheric conductance: Empirical Orthogonal Functions (EOFs) analysis

5.1 Introduction

Understanding the extent and nature of variance in the space environment is extremely important to our ability to predict this complex system. Therefore, a major space physics and space weather challenge is the development of succinct relationships between geospace variability and the solar and geomagnetic drivers. In this and the next chapter (Chapter 6) we provide the first ever characterization of the primary modes of ionospheric Hall and Pedersen conductance variability as empirical orthogonal functions (EOFs). In Chapter 8 we extend the technique to provide the first ever characterization of height-dependent conductivity variability as EOFs. In these investigations, we characterize dominant modes of auroral variability and their relationship to drivers by comprehensively data mining $> 10^8$ (hundreds of millions) one-second satellite particle spectra data. This is the first large-scale analysis of directly calculated ionospheric Hall and Pedersen conductances completely free of assumption of the incident electron energy spectra. Further, this is the first time that a comprehensive principal component analysis has been applied to satellite particle precipitation data, yielding a number of new physical insights into the auroral processes summarized in this and the following two chapters. Given the extent to which EOFs have advanced our knowledge of the atmospheric and space sciences (*Hannachi et al.*, 2007, and references therein), the EOFs presented here are an important advancement for our understanding of auroral processes and magnetosphere-ionosphere coupling.

This chapter introduces the conductance EOF technique and analysis and presents the results during the decline and minimum of the solar cycle. Chapter 6 then extends these analyses to examine EOFs (and hence the variability in the ionospheric conductances): 1) as a function of IMF clock angle; and 2) as a function of geomagnetic activity (specifically the Kp index). Chapter 8 details the fully three-dimensional EOFs. Each of these results allow improved modeling of the background error covariance needed for ionospheric assimilative procedures and improved understanding of MI coupling processes, which is the subject of Chapter 7. We provide an outlook on future studies of the conductance and conductivity variabilities in terms of EOFs in Chapter 9.

The patterns in this chapter are derived from six satellite-years of Defense Meteorological Satellite Program (DMSP) particle data acquired during the rise of solar cycles 22 and 24. The 60 million DMSP spectra were each processed through the GLOW model. These calculations, based on directly-measured energetic particle spectra from the DMSP satellites, allow us to bypass the Maxwellian assumption. This important improvement to conductivity modeling (*Christon et al.*, 1991; *Aksnes et al.*, 2002; *Hardy et al.*, 2008; *McIntosh and Anderson*, 2015) permits a robust calculation of the ionospheric Pedersen and Hall conductances and represents the first large-scale analysis of ionospheric conductances completely free of assumption of the incident electron energy spectra. We show that the mean patterns and first four EOFs capture ∼50.1 and 52.9% of the total Pedersen and Hall conductance variabilities, respectively. The mean patterns and first EOFs are consistent with typical diffuse auroral oval structures and quiet-time strengthening/weakening of the mean pattern. The second and third EOFs show major disturbance features of magnetosphere-ionosphere (MI) interactions: geomagnetically-induced auroral zone expansion in EOF2 and the auroral substorm current wedge in EOF3. The fourth EOFs suggests diminished conductance associated with ionospheric substorm recovery mode. We identify the most important modes of ionospheric conductance variability.

The objective of this chapter is to characterize primary modes of conductance variability as described by EOFs and to interpret them geophysically. EOFs of the Hall and Pedersen conductances, herein represented using the polar-cap spherical harmonics basis, are obtained by a

sequential nonlinear regression analysis of observations along DMSP satellite trajectories and ordered by their variance. These EOFs and their amplitudes can be used to describe the spatial and temporal coherence of the Pedersen and Hall conductances in a manner similar to that reported by *Matsuo et al.* (2002, 2005) and *Cousins et al.* (2013a,b) for electric field variability and *Cousins et al.* (2015b,a) for field aligned current variability. My results allow for improved modeling of the background error covariance needed for ionospheric assimilative procedures (*Richmond and Kamide*, 1988; *Matsuo et al.*, 2005). Here we present the dominant modes of variability of the ionospheric conductance derived from 60 million DMSP particle observations in 1987 and 2010.

This chapter is laid out as follows: Section 5.2 details the data and methodology we use to create the EOFs. In Section 5.3 we provide the results, which are then discussed and expanded upon in Section 5.4. Finally, we conclude with the primary findings and significance of the work in Section 5.5 and lead in to Chapters 6 - 8, which extend these analyses.

5.2 Methodology and Data

5.2.1 Introduction to Methodology

EOF analysis is a member of the family of Principal Component Analysis (PCA) or the Natural Orthogonal Component (NOC) algorithms, originally described by *Pearson* (1901). The objective is to reduce the dimensionality of a dataset consisting of multiple inter-correlated variables, while preserving the maximum variation (*Joliffe*, 2002; *Wilks*, 2011; *A et al.*, 2012). The result of PCA is a set of base functions, or EOFs, where each succeeding function is orthogonal to all previously estimated functions and describes as much variance present in the data as possible. Appendix C provides further details about EOFs, including useful references.

Here we describe the version of Empirical Orthogonal Function (EOF) analysis that applies to sparse and irregularly spaced data. The EOF method in this work is different from the classical PCA technique, which carries out an eigenvalue decomposition on the variance-covariance matrix for a particular set of observations. Rather, in light of the sparsity and irregularity of the data (see

Section 5.2.2), we take the approach laid out in *James et al.* (2000) and *Matsuo et al.* (2002) in which a 'reduced rank, mixed effects model' is used. This method attempts to directly estimate the EOFs rather than estimating them from the full covariance matrix and subsequent eigenvalue decomposition. In order to perform a direct estimation, the observations are represented by an additive model, consisting of the overall mean ($\bar{\mathbf{\Sigma}}$ in this study) and a truncated set of EOFs (i.e. $\sum_v \mathcal{EOF}^{(v)}$). Each term in the model is estimated sequentially after the contribution from each previously estimated term is removed. We provide the mathematical formalism for this next.

We define the conductance variability as a residual field which encompasses all perturbations from the mean conductance:

$$\mathbf{\Sigma}' = \mathbf{\Sigma} - \bar{\mathbf{\Sigma}}. \tag{5.1}$$

We decompose the conductance variability at a given time t into dominant modes represented by EOFs (i.e. principal components):

$$\begin{aligned} \mathbf{\Sigma}'(\mathbf{r}, t) = \alpha^{(1)}(t) \cdot \mathcal{EOF}^{(1)}(\mathbf{r}) + \ldots \\ \alpha^{(v)}(t) \cdot \mathcal{EOF}^{(v)}(\mathbf{r}) + \mathbf{e}'(\mathbf{r}, t), \end{aligned} \tag{5.2}$$

where $\mathbf{r}$ denotes spatial position (magnetic latitude (MLAT) and magnetic local time (MLT)), $\alpha^{(v)}(t)$ are time-dependent coefficients of the vth EOF, and $\mathbf{e}'(\mathbf{r}, t)$ is the residual after removing the mean and sum of weighted EOFs from $\mathbf{\Sigma}$. Essentially, EOFs represent 2-D time-invariant spatial modes of conductance variability and $\alpha^{(v)}(t)$ represent temporal modes that scale the spatial modes in time.

5.2.2 Data Set

We perform EOF analysis on conductances obtained from the GLOW model driven with DMSP spacecraft electron precipitation measurements as described in Section 4.2.2. We provide additional details relevant to the current focus here. The DMSP spacecraft fly in polar orbits at

~850 km altitude with orbital periods between 90-105 minutes (*Rich et al.*, 1985). We use the in-situ electron precipitation observations from the Special Sensor J versions 4 (SSJ/4) and 5 (SSJ/5) instruments (*Hardy et al.*, 1984; *Kadinsky-Cade et al.*, 2004). Data processing of the count rates from both versions of the instrument provides complete electron and ion energy spectra recorded every second for energies between 30 eV and 30 keV in 19 logarithmically spaced bins. We only use spectra poleward of |45°| MLAT to ensure that the SSJ instruments are pointed near the local zenith, which is inside the bounce loss cone at DMSP orbital altitudes above |45°| MLAT, thus sampling the Earthward streaming particles. In this high-latitude region, the spatial resolution of the precipitation observations is $\sim 0.1^{\circ}$ in latitude. Further details of the electron precipitation data and its preparation can be found in *Hardy et al.* (2008). In terms of the calibration of these instruments, the DMSP spacecraft each undergo an in-flight calibration (IFC) procedure (*Emery et al.*, 2006). As a means of inter-satellite calibration the average IFC factor across all SSJ/4 and SSJ/5 instruments is used as a reference with which to normalize the individual IFC factors (*R. Redmon and E. Holeman*, personal communication, 2015).

For this study, we process six satellite years of DMSP in-situ energetic electron precipitation observations to create a data set of more than 60 million raw spectra, at one-second cadence in the specified high-latitude region, from which to estimate mean patterns and EOFs. The six years are provided by DMSP satellites F6-F8 during 1987 and F16-F18 during 2010. The choice of temporal coverage was driven by two factors: 1) DMSP orbital planes that spanned most magnetic local time sectors, and 2) sufficiently broad levels of geomagnetic activity to capture the different modes of variability. Figures 5.1a-d show the spatial coverage in both hemispheres by these two sets of satellites in altitude adjusted corrected geomagnetic coordinates (AACGM) (*Baker and Wing*, 1989).

We analyzed solar activity data ($F_{10.7}$ and sunspot number, Figures 5.1e-f, respectively) and geomagnetic indices (Kp and AE, Figures 5.1g-h, respectively) from NASA OMNIWeb for 1987 and 2010. Figures 5.1e-h show that while the $F_{10.7}$ index is quite similar for 1987 and 2010, the sunspot number and level of geomagnetic activity are considerably higher for 1987. Dashed blue and red

lines, respectively, show yearly quartiles in 1987 and 2010 in Figures 5.1e-h. The data spread is greater in 1987 than 2010 for all parameters, indicating more large storms and deeper quiet periods in 1987. To reduce ionospheric pre-conditioning complications from generally heightened solar background, we chose data from near solar minimum (SILSO data/image, Royal Observatory of Belgium, Brussels, http://www.sidc.be/silso) which correspond to periods of low-to-moderate solar activity. A likely difference between these data and solar maximum data is the peak values in the mean conductance patterns, given the level of solar irradiance.

In order to represent the primary modes of variability in a single set of EOFs, we do not bin the observations by geomagnetic activity. This choice was governed by our primary objective, which is to create a set of EOFs that can be used in data assimilative procedures as a compact representation of the background model error covariance for ionospheric conductances. Moreover, this allows us to discuss the overall primary modes of variability rather than those associated with specific levels of activity. This approach lends itself to more general application. We investigate EOFs produce by binning the input data in Chapter 6.

We focus exclusively on the electron precipitation in this work. Proton precipitation and associated conductivity can be significant under specific conditions and in certain locations, such as the equatorward boundary of the auroral zone near midnight local time (*Galand and Richmond*, 2001a). Extending our analysis to include protons is left as future work.

5.2.3 Using the GLobal airglOW (GLOW) model in the EOF analysis

The GLOW model is discussed at length in Chapter 4, but brief details germane to the current chapter are provided here for convenient reference. The GLOW model is used to determine the effects due to precipitating auroral and photoelectron fluxes on the ionosphere (*Solomon et al.*, 1988; *Solomon and Abreu*, 1989; *Bailey et al.*, 2002). GLOW adopts a radiative transfer method of calculating these effects and implements the two-stream electron transport code of *Nagy and Banks* (1970). Background neutral and ionized atmospheres are calculated using the Mass Spectrometer and Incoherent Scatter Radar (MSIS) model (*Picone et al.*, 2002) and International Reference

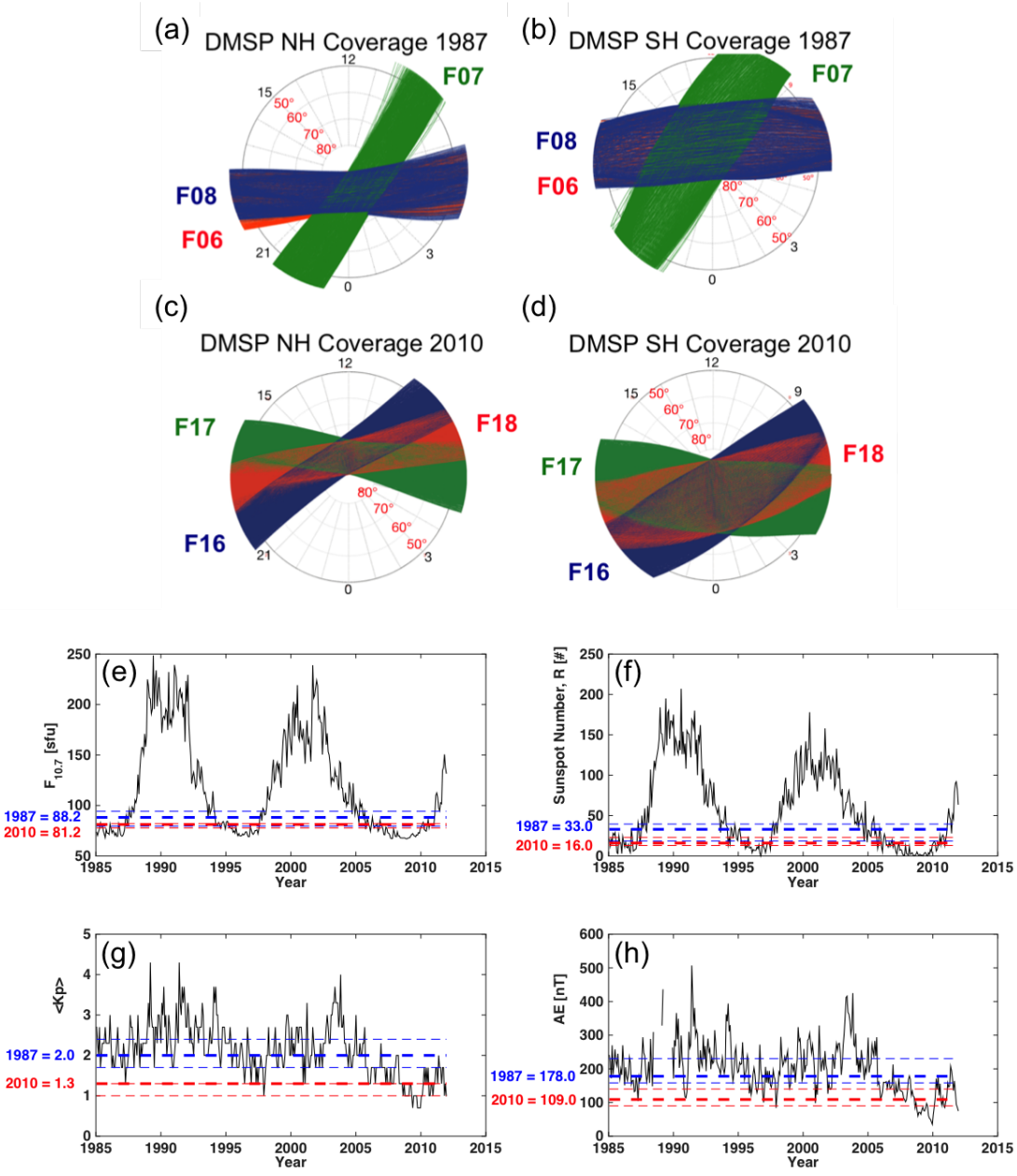

Figure 5.1: (a-d) Spatial coverage from the DMSP F6-F8 (1987) and F16-F18 (2010) satellites for EOF construction, in magnetic coordinates. Northern and southern hemisphere coverage provided in: (a)-(b) 1987 and (c)-(d) 2010. (e-h) Temporal coverage from the DMSP satellites showing solar and geomagnetic activity comparisons in 1987 and 2010. 27-day averages from 1985-2012 for: (a) $F_{10.7}$ index [sfu], (b) sunspot number [#], (c) Kp index, and (d) AE index [nT]. The median, upper, and lower quartile values are shown by the dashed lines for 1987 (blue) and 2010 (red). The values to the left of figures (e-h) represent the medians.

Ionosphere (IRI) model (*Bilitza*, 1990), respectively. IRI electron density profiles are supplied to ensure stability of the electron transport calculation, but are subsequently replaced by the calculated electron densities below 200 km altitude. Therefore, IRI profiles are not used in the final conductance calculations. We use the GLOW model to calculate ionization and dissociation rate profiles, ion and electron densities, and height-resolved Pedersen and Hall conductivities (*Solomon et al.*, 1988). GLOW computes ion and electron densities under the assumption of photochemical equilibrium. The photochemical equilibrium assumption is generally good below 200 km. Further discussion of this point is provided by *Richards et al.* (2010). Calculations of the Pedersen and Hall conductivities are performed using Equations 4.1 and 4.2. For this study we integrate the conductivity profiles over 80-200 km altitude to yield ionospheric conductances. Because they are not directly observed but are fed to the estimation procedure as observations, they are hereafter referred to as pseudo-observations. Only conductance EOFs integrated between 80-200 km are presented in this Chapter, but our methods are easily applied to conductance and conductivity determination at specific altitudes and altitude ranges. These applications are studied in Chapter 8.

GLOW contains a background source of ionization separate from the solar and auroral precipitation sources: the background 'nighttime' ionization. The background ionization was designed to conform to the Thermosphere-Ionosphere General Circulation Model (TIGCM) (*Roble et al.*, 1988) and takes into account fluxes from the stellar background and multiple scattering of solar atomic hydrogen emissions in the geocorona (*Strobel et al.*, 1980). The background ionization is small compared with that created by precipitating particles and the effect on these results is not significant except to ensure a non-zero level of ionization, and thus non-zero conductances, at all times.

Further details about the GLOW model can be found in *Solomon et al.* (1988), *McGranaghan et al.* (2015a), and Chapter 4 of this dissertation.

5.2.4 Empirical Orthogonal Functions (EOFs) and Related Data Processing

We fit the pseudo-observations to the same spherical-cap harmonics basis functions used in the assimilative mapping of ionospheric electrodynamics (AMIE) procedure (*Richmond and Kamide*, 1988). These basis functions are generalized Legendre functions at high latitudes with appropriate low-latitude extensions that satisfy a zero Laplacian requirement. We select the 50 basis functions that represent the first 50 principal modes in the background error covariance also developed in that work. The resolution of the basis functions is roughly 2.5°.

The nonlinear regression analysis to determine each EOF is performed by minimizing the following cost function (*Matsuo et al.*, 2002):

$$L^{(v)} = \sum_{t}^{T} \sum_{r}^{R} \left[\mathbf{Y}_{rt}^{(v)} - \alpha_t^{(v)} \sum_{k}^{K} \beta_k^{(v)} \mathbf{X}_{krt} \right]^2 + \lambda \sum_{k}^{K} |\beta_k|. \tag{5.3}$$

where:

v = EOF number

$\mathbf{Y}_{rt}^{(v)}$ = vector containing R residual pseudo-observations at a location r in an EOF analysis block t

$\alpha_t^{(v)}$ = weighting factor for EOF analysis block t

$\beta_k^{(v)}$ = regression coefficient

$\mathbf{X}_{krt}$ = kth basis function evaluated at location r in an EOF analysis block t

K = number of basis functions chosen

$\lambda \sum_{k}^{K} |\beta_k|$ = L^1 norm penalty term and λ is the nonnegative regularization parameter.

The process is nonlinear because the spatial coefficients, $\beta_k^{(v)}$, and temporal coefficients, $\alpha_t^{(v)}$, are estimated iteratively. An EOF 'analysis block' is defined as a 1-hour period over which all available DMSP observations are accumulated, and represents the resolution of the temporal modes (e.g. α).

The highly variable nature of ionospheric conductivities introduces significant stability issues in the EOF estimation process. We used the Least Absolute Shrinkage and Selection Operator

(LASSO) (*Tibshirani*, 1996) regularization to handle this instability. Generally, LASSO introduces an L^1 norm penalty term ($\lambda \sum_k^K |\beta_k|$ in Equation 5.3) to the least squares estimation and therefore minimizes the sum of the squared errors plus the absolute value of the regression coefficients. The tuning parameter, λ, determines the amount of regularization, where the limiting case of $\lambda = 0$ yields the non-regularized optimization solution. LASSO regularization is most applicable in situations where there are a moderate number of meso-scale effects, and thus LASSO is deemed appropriate for the objectives of this study.

The typical scaling convention used in principal component analysis, $\sum_k \left(\beta_k^{(v)}\right)^2 = 1$, is applied to circumvent the non uniqueness of the analysis (the equations are still valid if a constant is multiplied throughout) along with a constraint to force orthogonality:

$$\sum_k^K \beta_k^{(v)} \beta_k^{(v-n)} = 0 \qquad\qquad n = 1, ..., v-1. \tag{5.4}$$

A suitable mean, which is invariant with time, must be calculated and removed from the data before the EOF calculations can be performed. We calculate the mean, or $\sum_k \left(\beta_k^{(0)} \mathbf{X}_{krt}\right)$, through a linear minimization regression of $L^{(0)}$ in Equation 5.3 with $\alpha_t^{(0)} = 1$ and the constraint on $\beta_k^{(0)}$ shown in Equation 5.4 lifted.

The EOFs are then computed from these residual data in a sequential manner. For instance, the first EOF depends on pseudo-observations with the mean component removed, $\mathbf{Y}_{rt}^{(1)} = \mathbf{Y}_{rt}^{(0)} - \sum_k \left(\beta_k^{(0)} \mathbf{X}_{krt}\right)$, and is estimated using regression on Equation 5.3. The cost function is smooth in this work and thus defining a set number of iterations is sufficient to obtain convergence. Once an EOF is found, three steps are taken: 1) its contribution to the pseudo-observations is removed; 2) a Gram-Schmidt orthogonalization (*Demmel*, 1997) transforms the new residual set to a space orthogonal to all previous EOFs (Equation 5.4); and 3) Equation 5.3 is minimized to identify the next EOF. Orthogonality is enforced during the iterative fitting procedure. We determine the maximum order (v) of the EOF series as those components that describe 50% of the variability in the data, which yields v=4 in this work. This is also the point at which the percentage variation

described by subsequent individual EOFs falls below 5%, and is thus deemed an appropriate number of EOFs to analyze in this manuscript.

To demonstrate the effect of regularization, we provide a comparison of mean Hall conductance patterns without (Figure 5.2a) and with (Figure 5.2b) regularization. In Figure 5.2 (and subsequent figures below) the region interior to the solid black curves on each polar plot delineate areas well-supported by observations. Structure outside of these lines are artifacts of the estimation procedure. Clearly the non-regularized pattern can yield non-physical negative conductances (note the different color axes limits) where the estimation is not constrained. These can then inappropriately influence estimation even within the observational bounds. The LASSO regularization successfully stabilizes the estimation while still capturing the important geophysical features present in the non-regularized result (primarily the auroral oval structure). The LASSO slightly mutes some features, which results from regularization in general.

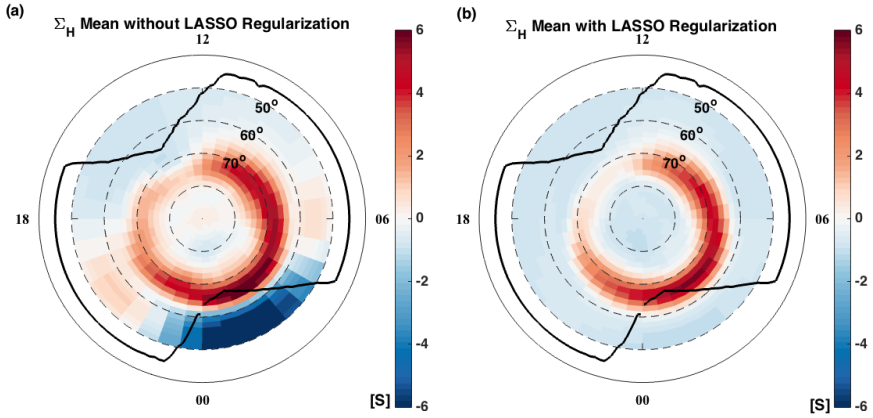

Figure 5.2: Mean Hall conductance patterns. (a) Without regularization and (b) with LASSO regularization.

The DMSP conductance pseudo-observations require additional processing prior to being used in this estimation. They were averaged over 60 s (roughly 4° MLAT) to produce $\sim$ 22 averaged pseudo-observations from each of the $\sim$ 28 daily polar passes. After accounting for missing data in the DMSP databases, we processed roughly 40,000 high-latitude passes, resulting in over a million

pseudo-observations ($\sim$ 60 million 1-second spectra each providing one pseudo-observation, which are averaged over 60 seconds) with fairly even seasonal distribution. Data processed in this manner yield variability on meso and global scales.

We provide Figure 5.3 to detail the observational characteristics. Figure 5.3a shows the distribution of data counts in the northern and southern hemispheres during the 24 month period of interest, including the 60 s averaged pseudo-observations resolved on an equal-area grid for easy visual interpretation. In estimating the EOFs we use the pseudo-observations at their actual geomagnetic coordinates. We assumed hemispheric conjugacy in order to provide sufficient data coverage in MLAT and MLT. Despite the conjugacy assumption, Figure 5.3 shows that the magnetic local time coverage of the F6-F8 and F16-F18 satellites is not complete, lacking pseudo-observations in the low latitudes in pre- to post-midnight and post-noon local time sectors. These data gaps can create estimation instability in the EOF regression procedure, and are further motivation for the use of regularization. Figures 5.3b-c show bin-averaged Hall and Pedersen conductances, respectively, in units of Siemens.

In this analysis we use the term 'analysis block,' defined by t in Equation 5.3, to refer to the 1-hour time step for the EOF process. Note these analysis blocks, hereafter simply blocks, are different than a DMSP orbit over the high-latitude region. EOF blocks have a set start and end time and contain all pseudo-observations available during that period (see Figure 5.4e and explanation below). This choice provides a short enough window to capture the meso- and global-scale time variations in the data and a long enough window for sufficient data coverage to constrain the fits. One α from Equation 5.3 is estimated for each block, while the EOFs are time-invariant. Each 1-hour block contained roughly 79 sixty-second averaged pseudo-observations, and we processed $\sim 14,000$ hourly blocks over the course of 1987 and 2010.

Since our primary interest is the conductance variability due to precipitating particles, which is the more unsteady and uncertain component of ionospheric conductance (*Reiff*, 1984; *Knipp*, 1989; *Brekke and Moen*, 1993; *Germany et al.*, 1994), we excluded the solar ionization component from the GLOW calculations. Although solar ionization is excluded, the general level of solar

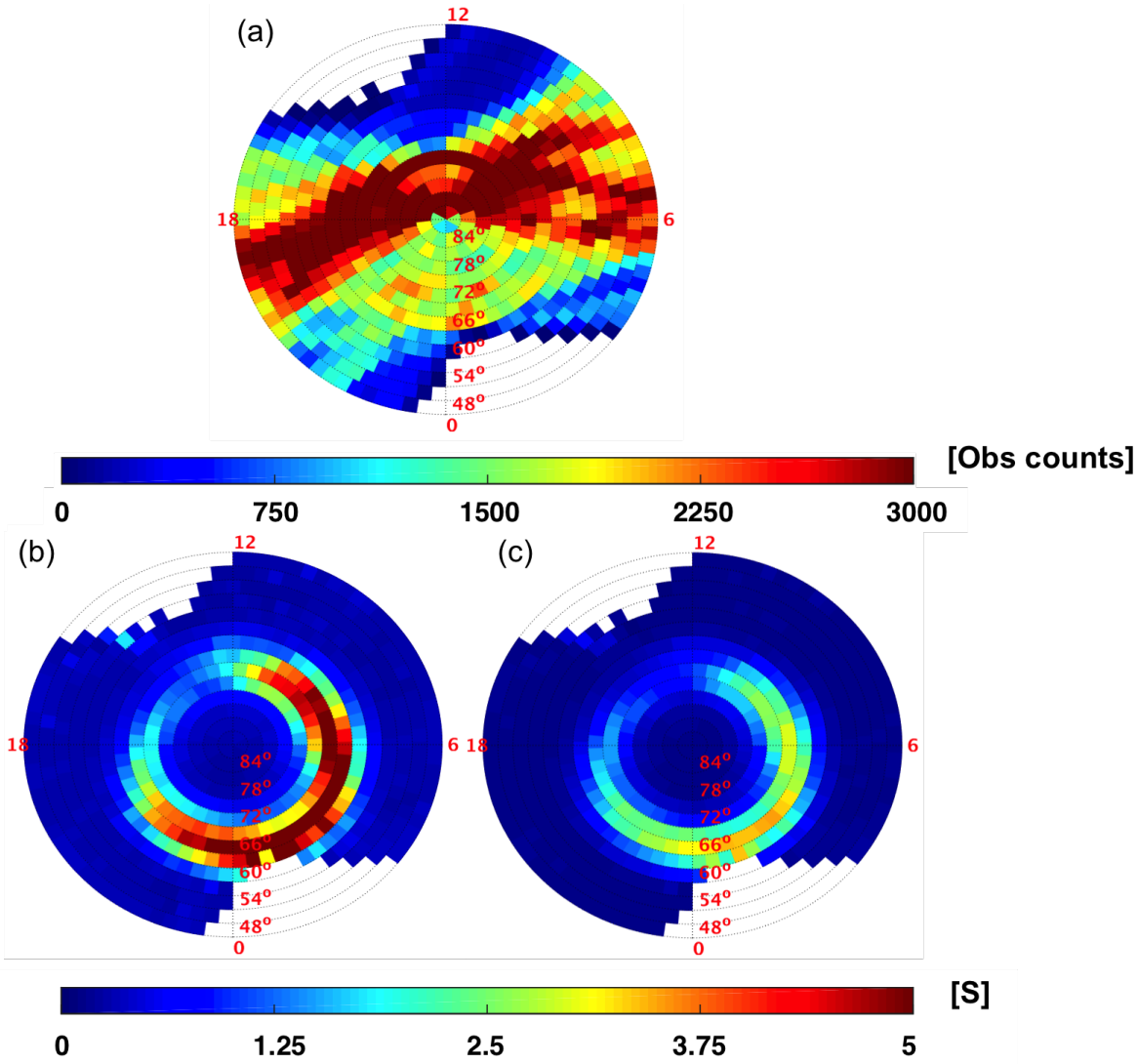

Figure 5.3: (a) Conductance observation density, (b) Hall conductance means, and (c) Pedersen conductance means in equal-area grids for the complete set of 60-second averaged, northern and southern hemisphere pseudo-observations. Conductances means are shown in units of Siemens [S]. The pseudo-observations in these bin-averages are the complete data set after averaging the raw spectra, precipitated through the GLOW model.

activity impacts the GLOW model through the $F_{10.7}$ and Ap dependence of the background neutral and ionized atmospheres. In Section 5.4 we discuss a different approach to treat solar and auroral conductance components simultaneously.

Figure 5.4 provides a step-by-step overview of the data and methods used in this work. In Figure 5.4a we show a single northern hemisphere pass of the DMSP F16 satellite in AACGM coordinates on January 15, 2010, a day used in the creation of the EOFs. Superimposed on the dusk-to-dawn satellite track are the total electron energy fluxes calculated at a 1-second cadence from the SSJ/5 instrument observations. On this very quiet day (average Kp = 1) there are only small enhancements in the auroral zones, which are confined to high MLATs. Figure 5.4b shows a sample electron energy flux spectrum observed at 80° MLAT and 14 MLT during the pass in Figure 5.4a. Spectra like this are calculated from SSJ observations at a 1-second cadence and are used as input to the GLOW model, resulting in conductivity profiles for that time and location. Figure 5.4c shows the GLOW Hall and Pedersen conductivities for this spectrum. The Hall conductivity peaks near 110 km, while the Pedersen profile has a smaller peak closer to 120 km. Each profile shows significant vertical structure.

Figure 5.4d gives the Hall (in blue) and Pedersen (in red) conductances along the satellite track shown in Figure 5.4a. The markers represent the conductances calculated at the same 1-second cadence of the SSJ/5 instrument (each marker is an altitude-integrated conductance calculated from an energetic electron spectrum (Figure 5.4b) and its corresponding conductivity profile (Figure 5.4c), and these conductances are the pseudo-observations introduced above. The dashed lines represent the 60-second smoothed averages used to drive the EOF estimation process. The conductances, even during a quiet period, are highly dynamic and introduce significant stability issues in the EOF estimation without smoothing.

Finally, Figure 5.4e shows how this information is used to estimate EOFs. We accumulate pseudo-observations over a 1-hour estimation time step (an EOF block), corresponding to the time resolution of the EOF temporal coefficients, from all available satellites and from both hemispheres. Figure 5.4e shows the available pseudo-observations during the first hour on January 15, 2010,

which captures the first half of the F16 orbit from Figure 5.4a. Data from a single block are used to estimate a single α coefficient while all data are used to estimate β coefficients.

5.3 Results

Figure 5.5 shows the mean and first four EOFs for the Hall (a-e) and Pedersen (f-j) conductances. We limit our discussion to areas with observational support. The maximum and minimum values for the mean of each conductance are in units of Siemens [S]. Each EOF pattern is shown on a scale of -0.5 to 0.5. The EOF signs are arbitrary since their contribution can be either added to or subtracted from the mean pattern. Hereafter, we will denote Hall and Pedersen EOFs as HEOF and PEOF, respectively.

The mean Hall and Pedersen conductance patterns (Figures 5.5a and f) capture $\sim 60\%$ of the variability and the general quiet-time auroral features shown in the conductance maps in Plates 3a and 4a of *Fuller-Rowell and Evans* (1987), Figure 2 of *Newell et al.* (1996c), and Plates 10 and 12 of *Ridley et al.* (2004). The patterns are generally consistent with precipitation of eastward-convecting plasma sheet electrons in the post-midnight MLTs, which in turn, produce a broad crescent-shaped region of diffuse auroral electron precipitation as shown in *Hardy et al.* (1987) and Figure 5 of *Newell et al.* (2009). This diffuse electron precipitation is the dominant contributor to the global precipitation budget (*Winningham et al.*, 1975; *Newell et al.*, 2009).

The patterns in HEOF1 and PEOF1, constituting $\sim$33.7 and 29.3% of the variation, respectively, have a similar pattern to the large-scale mean conductance and likely represent a strengthening and weakening of the large-scale, quasi-permanent conductances from variability of electron precipitation in magnetic local time (*Newell et al.*, 2009; *McIntosh and Anderson*, 2015).

HEOF2 ($\sim$ 10.2% of the overall variability) and PEOF2 ($\sim$ 11.8%) show an enhancement region equatorward of the location of EOF1 patterns which is most likely representative of an expansion of the auroral zone brought on by electron precipitation tied to geomagnetic activity. The enhanced component centered at midnight local time, expands beyond dusk in the westward direction and beyond dawn eastward, and remains relatively constant in latitudinal width and location,

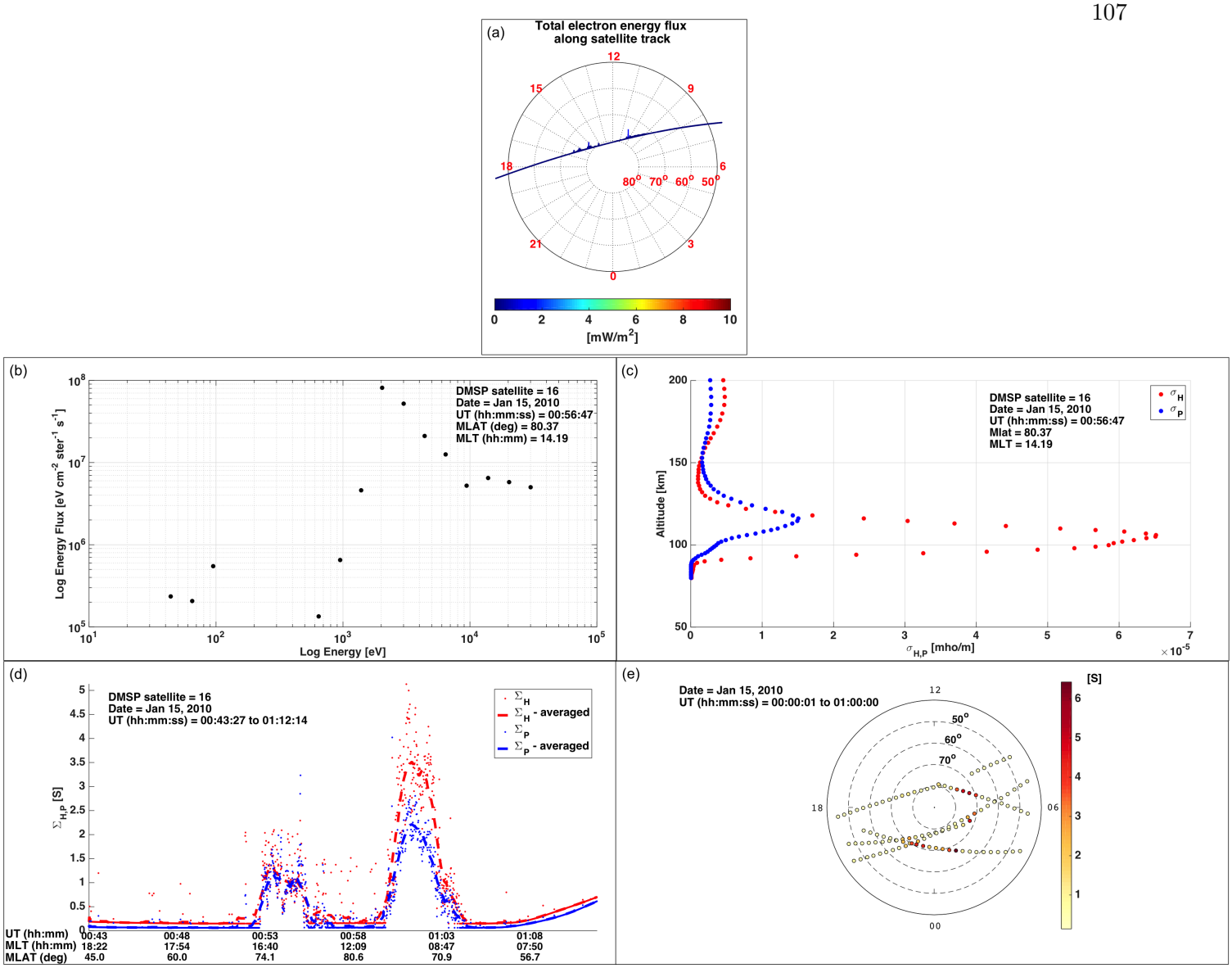

Figure 5.4: Overview of the observations and processing prior to EOF estimation. (a) DMSP F16 satellite northern hemisphere orbit on January 15, 2010 shown looking down on the north pole with the sun off to the top of the figure. Superimposed on the altitude adjusted corrected geomagnetic MLAT and MLT coordinates are the total electron energy fluxes [mW m^{-2}] which are calculated at a 1-second cadence from DMSP observations. (b) Sample electron energy flux spectrum [eV cm^{-2} $ster^{-1}$ s^{-1} ΔeV^{-1}] observed during the F16 pass shown in (a). These spectra are also obtained at a 1-second cadence. (c) Hall (red) and Pedersen (blue) conductivities [S/m] calculated from the spectrum shown in (b) using the GLOW model as detailed in the text. (d) Hall (red) and Pedersen (blue) conductances [S] (integrated between 80-200 km) along the F16 pass shown in (a). The dots represent the values calculated at the 1-second cadence of DMSP measurements and the dashed lines represent the 60-second averages used for EOF estimation. (e) The accumulation of observations that contains the F16 pass shown in (a) for EOF temporal mode estimation using a 1-hour analysis time step (one EOF block is shown). Observations are accumulated from all the DMSP satellites available on this date and in this 1-hour time window and include observations from both hemispheres.

occupying latitudes between $60 - 70°$. These features are characteristic of general equatorward expansion of the auroral oval with geomagnetic activity (*Hardy et al.*, 1985, 1987; *Fuller-Rowell and Evans*, 1987; *Lummerzheim et al.*, 1991). There are subtle differences in the dawnside and duskside patterns. The dawnside enhanced region extends slightly further toward noon local time, but remains centered at roughly 65° MLAT. On the other hand, the duskside features subside just past 1800 MLT and show a slight trend toward higher MLATs with decreasing MLT, reaching $\sim 70°$ MLAT at dusk. Finally, there is a region of opposite sign at polar latitudes extending throughout the entire dawnside.

HEOF3 and PEOF3 signify $\sim 5\%$ of the variability and both exhibit two strong features with opposite sense surrounding the midnight meridian. The pre-midnight component is broader in latitude, extending from $\sim 65°$ to greater than 75° MLAT and covering roughly three hours in local time. The post-midnight signature is more confined in latitude and is opposite in sign. These signatures are consistent with modulation of electron precipitation associated with the divergence of the cross-magnetotail current into the ionosphere during auroral substorms, or the substorm current wedge (SCW) (*McPherron et al.*, 1973; *Pytte et al.*, 1976; *Elphinstone et al.*, 1996; *Gjerloev and Hoffman*, 2002; *Kepko et al.*, 2014).

EOF4s exhibit a dominant signature in the midnight-to-post-midnight local time sector, span roughly three hours MLT at 70° MLAT, and capture $\sim 4\%$ of the variability. The features in Figures 5.5e and j are smaller in scale, and likely represent a substorm recovery mode.

To ensure the efficacy of our EOF patterns we carried out a bootstrap estimation procedure in which 40 different sets of EOFs were estimated from 40 different randomly selected subsets, comprising 2500 blocks, or roughly 200,000 pseudo-observations. Although not shown here, we find that the first two EOFs were largely invariant between each run, while the next two EOFs exhibited similar features, though not always in the same order, and some subsets contained different features in the higher orders. These results indicate that our estimation procedure is robust to the number of pseudo-observations used.

Figure 5.5k shows the percentage of the overall variation in the conductance pseudo-observations,

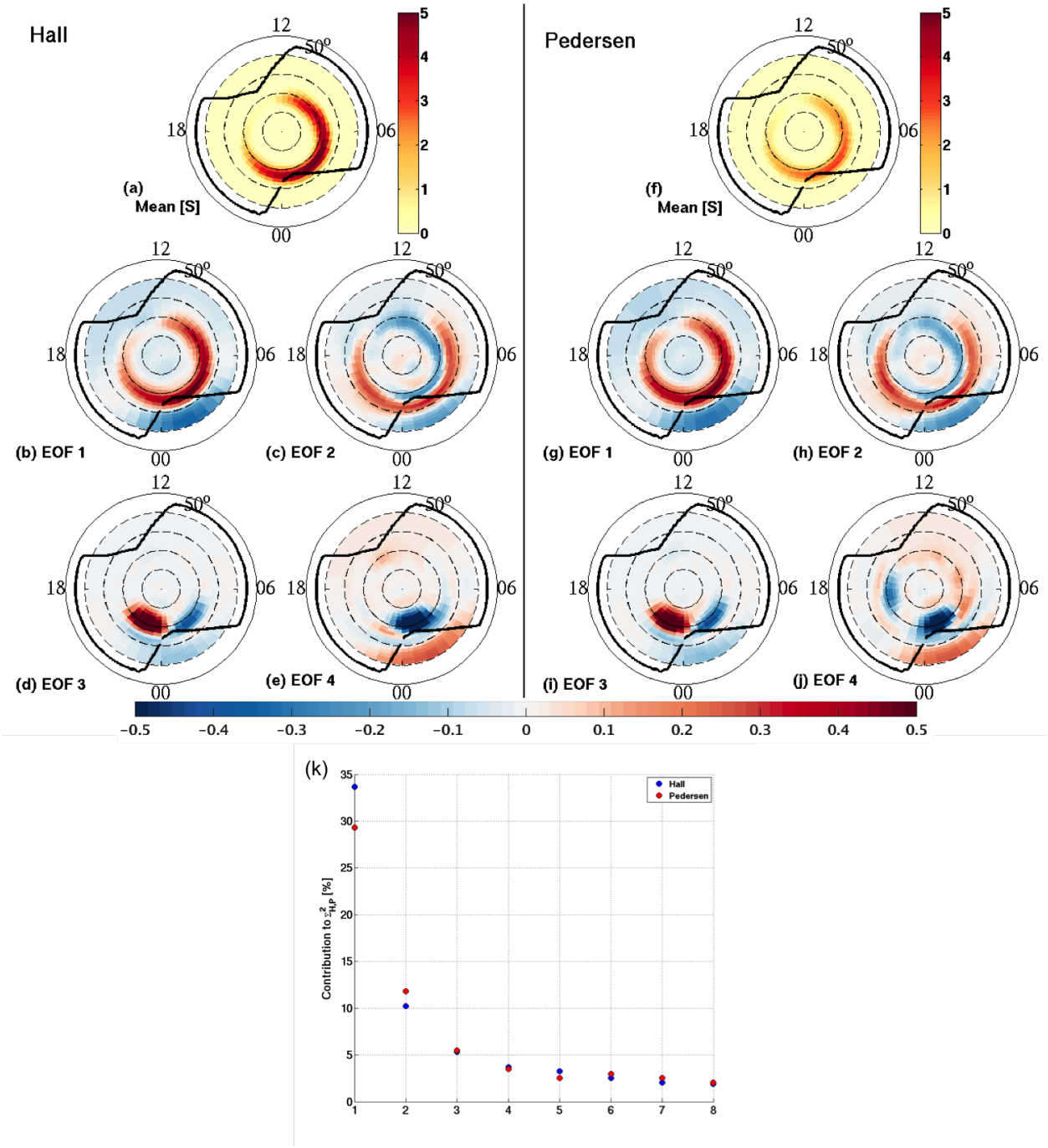

Figure 5.5: EOF results for the Hall and Pedersen conductances. Mean and first four EOFs for Hall (a-e) and Pedersen (f-j) conductances, in magnetic coordinates. The low-latitude limit on all polar plots is 50° and dashed lines are plotted at 10° increments up to 80°. The solid black curves indicate the boundaries of observational support. (k) Percent of the total variation in the total pseudo-observations captured by the first eight EOFs for the Hall (blue) and Pedersen (red) conductances. The first four EOFs capture 52.9% and 50.1% of the total variation for the Hall and Pedersen conductances, respectively. EOFs 5-8 describe an additional 10% for each conductance.

Σ^2, that is captured by EOFs 1-8 for Hall (blue markers) and Pedersen (red markers) conductances. We show the percentage variation captured by EOFs 5-8, for which the spatial patterns are not provided, to illustrate that these higher-order EOFs capture an increasingly small percentage of the overall variation in the data. The amount of variability is represented by the percent reduction in the cost function (Equation 5.3) when the contribution from each EOF is subtracted from the residual observations (i.e., the sum of the squared distance from the mean). The first four EOFs capture 52.9% and 50.1% for the Hall and Pedersen conductance variability, respectively. EOFs 5-8 describe an additional 10% for each conductance.

To explore the possible drivers of the dominant modes of variability represented by the EOFs in Figures 5.5b-e and g-j, we correlated the temporal modes, or the time series of coefficients of each EOF (α_t) which represent the strength of each EOF at a given time period, with the corresponding time series of various solar wind parameters and solar and geomagnetic indices. We computed correlations for solar wind parameters {speed, pressure, density, and magnetic field components in geocentric solar magnetic (GSM) coordinates}; geomagnetic indices {auroral electrojet indices (AE, AU, and AL), SuperMAG indices (auroral electrojets: SME, SMU, SML; and ring current: SMR) (*Newell and Gjerloev*, 2011a, 2012), planetary index (Kp), polar cap index (PC), and disturbance storm time index (Dst)}; and specialized coupling functions {the interplanetary electric field (E_Y = -V_{SW} × $B_{Z,GSM}$), the Borovsky coupling function (CF) (*Borovsky*, 2013), and the Newell CF (*Newell et al.*, 2007)}.

Some aspects of the correlations are noteworthy: 1) Since indices represent imperfect proxies for ionospheric phenomena, which themselves often respond in a nonlinear manner to many different drivers, we are encouraged by the fact that several of the correlation coefficients between the indices and higher-order EOFs are greater than 0.5; 2) The more localized the EOF features, the less likely they are to be correlated with the parameters. This is why correlations generally decrease for higher-order EOFs (*Matsuo et al.*, 2002; *Cousins et al.*, 2013a). Thus, low correlations do not necessarily mean a relationship does not exist. Alternatively, high correlations demonstrate a relationship exists, but do not necessarily provide information about causation; 3) EOFs are not

necessarily organized according to physical cause. They capture the direction of most variability in the data subject to the constraint that it is orthogonal to each previous, more prominent, direction of variability, and irrespective of the correlation with physical drivers (*Cosgrove et al.*, 2014).

Table 5.1 displays the top three correlations and the percentage variation described for each EOF shown in Figure 5.5 as well as our geophysical interpretation. The HEOF1 and PEOF1 temporal coefficients exhibit correlation magnitudes around 0.55 with the high-latitude magnetic indices. Though not tabulated, both Hall and Pedersen conductances correlate well with the Borovsky and Newell CFs (~ 0.45).

The HEOF2 and PEOF2 temporal modes are even more strongly correlated with the auroral electrojet indices than EOF1. Further, both conductances also exhibit stronger positive correlations with the Newell and Borovsky CFs (> 0.5) and strong negative correlations (~ -0.6) with the ring current indices (Dst and SMR), which decrease with increasing geomagnetic activity.

The EOF3 temporal modes are most strongly correlated the auroral electrojet indices, though the correlations are reduced from EOFs 1 and 2 (correlations between 0.1-0.2). The Newell CF, PC, and Dst/SMR indices exhibit similar magnitude correlations.

The spatial distribution and correlations associated with the third EOFs suggest a connection to substorm activity, which we examined further by recomputing correlations for each EOF3 after thresholding the values of the SuperMAG equivalent of the AL index, the SML index, to be less than -150 nT. In so doing, the correlations between EOF3 and the SuperMAG auroral electrojet indices increased by a small amount ($\sim 7\%$).

We also examined the magnitude of α_t coefficients for HEOF3 and PEOF3 during periods of substorms. Larger $|\alpha_t|$'s indicate the pattern is stronger at a given time. To identify substorm times we used the SuperMAG substorm event database which gives the time of substorm expansion phase onsets as observed by the SML index (*Newell and Gjerloev*, 2011a,b). During substorm periods the median alpha coefficients for the HEOF3 was notably enhanced over the median calculated over all coefficients (for HEOF3: 4.5 in 1987 and 5.5 in 2010 versus 2.0 for all α's). In contrast, the PEOF3 median values showed little response (2.1 in 1987 and 2.8 in 2010 versus 2.4 for all alphas),

Table 5.1: Properties of Hall and Pedersen EOFs[1,2]

Properties of the first four Hall EOFs				
EOF	1	2	3	4
Mode	Strengthening/Weakening	Auroral zone broadening	Substorm current wedge	Recovery/small-scale features
Contribution to Σ_H^2	33.67	10.20	5.33	3.72
Top Correlation	AE/PC: 0.60	AE: 0.72	SME/SMU: 0.17	SME: 0.21
2nd Correlation	AL: -0.57	AL: -0.69	AL/SML: -0.15	SML: -0.20
3rd Correlation	SME/Kp: 0.57	AU: 0.66	AE: 0.14	SMR: -0.19
Properties of the first four Pedersen EOFs				
EOF	1	2	3	4
Mode	Strengthening/Weakening	Auroral zone broadening	Substorm current wedge	Recovery/small-scale features
Contribution to Σ_P^2	29.30	11.80	5.51	3.49
Top Correlation	PC: 0.56	AE: 0.78	SMU: 0.16	Kp: 0.22
2nd Correlation	Kp: 0.54	AL: -0.74	SME: 0.14	AU/dst: 0.21/-0.21
3rd Correlation	AE: 0.54	AU: 0.73	SML/Newell: -0.11/0.11	PSW: 0.20

[1] Correlation coefficients are given for the three parameters that correlate most strongly with the EOFs.
[2] Correlations are based on a Pearson linear product-moment calculation.

consistent with smaller Pedersen conductance response to substorms (*Gjerloev and Hoffman*, 2002).

The temporal modes of HEOF4 and PEOF4 correlate with the SuperMAG auroral electrojet, Kp, and Dst indices. The patterns as shown are negative in the dominant feature near midnight LT (blue features), meaning that conductance diminishes as geomagnetic activity subsides.

5.4 Discussion

In this section we explore the geophysical interpretation of each EOF in more depth and outline the important paths for future work.

EOF1:

HEOF1 and PEOF1 are likely predominantly representative of central plasma sheet (CPS) precipitation which is a relatively stable feature in terms of ionospheric precipitation, varying primarily in terms of latitude and intensity with geomagnetic activity (*Winningham et al.*, 1975; *Newell et al.*, 2009; *Thorne et al.*, 2010). Electrons from the CPS have been directly associated with diffuse precipitation into the ionosphere (*Sandford*, 1968). *Hardy et al.* (1987) connected the diffuse precipitation to increases in ionospheric conductivity, and *Thorne et al.* (2010) showed that resonant scattering of electrons by chorus band waves are a dominant source of diffuse precipitation. The locations of resonantly scattered electrons shown by *Thorne et al.* (2010) (their Figure 2) and the

conductance maps created by *Hardy et al.* (1987) (their Plate 1 for Hall and Plate 2 for Pedersen conductances) are both consistent with our EOF1 patterns. An especially striking relationship exists between our results and Figure 2a of *Thorne et al.* (2010), which shows the diffuse auroral emissions captured by PIXIE X-ray emission measurements and demonstrates the enhancement as a function of the Kp index. We found a similar relationship between EOF1 and Kp as shown by the positive correlation in Table 5.1.

EOF2:

In contrast to the CPS source of diffuse electron precipitation, the boundary plasma sheet (BPS) is marked by accelerated electron precipitation and is much more variable, displaying more dependence on geomagnetic activity and leading to more structured, and in certain situations, localized ionospheric signatures (*Winningham et al.*, 1975; *Newell et al.*, 1996a). EOFs 2 are suggestive of conductances driven by structured precipitation originating in the BPS.

HEOF2 and PEOF2 likely capture the conductance signatures of electron precipitation associated with magnetospheric convection. The temporal modes for these spatial patterns correlate well with the auroral electrojet indices ($\sim$ 0.7-0.8), Kp and PC (0.6), the Newell and Borovsky CFs ($\sim$ 0.5-0.6), and several other geoeffective parameters ($\geq$0.5). The most prominent feature (Figures 5.5c and h) is an equatorward expansion of the auroral zone represented by the positive conductance region between $60^\circ - 70^\circ$ latitude and extending from pre-dusk to midnight and to post-dawn from midnight. *Kamide and Kokubun* (1996) showed that this convection-driven component of the auroral electrojets is dominated by high conductivity. Therefore, as activity increases and the auroral zone broadens latitudinally due to increased electron precipitation a corresponding increase in the conductance occurs. Stronger conductances permit stronger electrojets to flow, and we accordingly found large correlations between these patterns and the auroral electrojet indices. The auroral electrojet indices correlations are stronger for EOF2 than EOF1, which suggests that the EOF2 patterns are more strongly associated with geomagnetic activity and with accelerated electron precipitation, while those in EOF1 are created by diffuse precipitation, though further investigation is needed.

Our EOF2s indicate a relationship with field-aligned currents (FACs), especially given that the magnetospheric convection component of the auroral electrojets has been linked to enhancements of the DP-2 FAC system (*Clauer and Kamide*, 1985). FACs are carried by the inflow and outflow of ionospheric electrons, and conductivity changes are expected to be closely related. Figure 5.6(a) shows the large-scale Region-1/2 FACs during moderate (left) and strong (right) geomagnetic activity (reproduced from *Iijima and Potemra* (1978)). The component out of the ionosphere (shown by the white bars) represents electrons precipitating in and causes conductance enhancements. The white bars in Figure 5.6 and our second EOFs are generally consistent in terms of MLAT and MLT. We additionally see general agreement between our high-latitude negative conductance feature extending throughout dawnside LTs and the downward Region 1 FAC (shown by black bars and carried by electrons moving away from the ionosphere). The absence of a similar duskside feature for the low-latitude FACs could be a result of the regularization process suppressing these lower-latitude features. A correspondence between our results and large-scale Region-1/2 FACs (*Iijima and Potemra*, 1978) speaks to the importance of this study given that the goal is to aid in ionospheric data assimilation, in which FACs are a crucial component.

EOF3:

HEOF3 and PEOF3 suggest electron precipitation associated with the SCW (*McPherron et al.*, 1973; *Pytte et al.*, 1976; *Elphinstone et al.*, 1996; *Gjerloev and Hoffman*, 2002; *Kepko et al.*, 2014). The local time extent of the pre- and post-midnight features in Figures 5.5d and i is in general agreement with the 6-hour local time (90°) width of the SCW specified in a phenomenological sense by *Gjerloev et al.* (2007). *Kepko et al.* (2014) conducted an extensive study of the SCW, including historical information, and concluded that the large-scale organization of this feature originally identified by *McPherron et al.* (1973) remains valid. In this picture, the western edge of the wedge is collocated with a region of intense upward field aligned current (downward electron precipitation) that is the westward edge of the westward traveling surge (WTS). *Sergeev et al.* (1996) presented several case studies of optical auroral images associated with the SCW and concluded that the western bulge region is the area of brightest auroral luminosity, and it is generally accepted

that the auroral bulge is the region of bright, expanding auroras associated with substorm onset. The brighter regions in optical images are caused by electron precipitation which in turn cause conductance enhancements, and indeed *Kamide et al.* (1996) showed that the ionospheric electrojets in this pre-midnight SCW location are carried by enhanced conductances. These enhancements are realized in the pre-midnight signatures in both HEOF3 and PEOF3. Alternatively, *Kamide et al.* (1996) found that the post-midnight electrojets associated with the SCW were carried by a strong electric field, rather than enhanced conductances. *Davies and Lester* (1998) found a tendency in regions of moderate to strong electric field values, such as those produced in the post-midnight sector during substorms, for enhancements in the electric field to be accompanied by decreases in ionospheric conductances. We correspondingly find less pronounced and negative features in the post-midnight LT location.

The strongest auroral luminosities in the SCW signature have been shown to occur during substorm onset (*Gjerloev and Hoffman*, 2002), consistent with the pre-midnight signatures captured in the third EOFs. Though the latitudinal agreement is not perfect (note *Gjerloev and Hoffman* (2002) used optical images to conduct their statistical analysis of substorm onset and limited their event database through several criterion), the statistical location of onset found in that study (their Figure 6) is in remarkable agreement with the pre-midnight enhancement shown in our Figures 5.5d and i.

The SCW interpretation of EOF3 is supported by correlations with auroral electrojet indices and the Newell CF, through increased correlations when only periods of AL<-150 nT were included (a common criteria for substorm occurrence), and by enhanced temporal modes (e.g. larger αs) during periods of substorm onset as identified from SuperMAG data.

Although our EOFs, which represent averaged features, do not capture the many complexities and high variability associated with the SCW, they successfully describe the fundamental and averaged picture. Our results demonstrate that, although the MLT distribution of auroral onsets is wide, the MLT location of the SCW is quite stable and occurs primarily in the 2300 location, which is in close agreement with the findings of *Frey et al.* (2004) and *Clausen et al.* (2013). Figure

5.6b shows the characteristics of a generic substorm aurora and is reproduced here from *Kepko et al.* (2014) (following from the work of *Fujii et al.* (1994) and *Gjerloev and Hoffman* (2002)). The SCW is fed by electron precipitation into the ionosphere (upward FACs) within the auroral bulge pre-midnight while a region of mixed upward and downward FACs post-midnight contributes to more tenuous conductances. This agrees with our results.

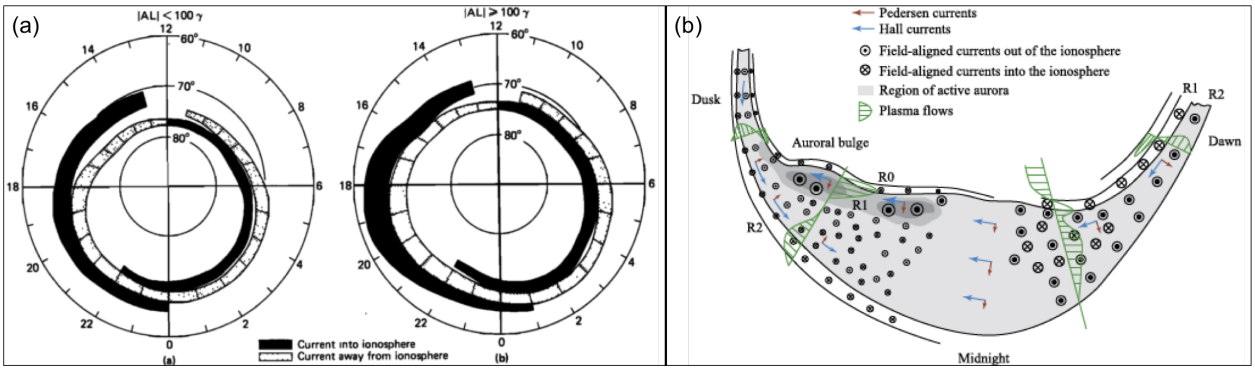

Figure 5.6: Reproduced figures showing: (a) large-scale Region-1/2 FACs during moderate (left) and high (right) geomagnetic activity (from *Iijima and Potemra* (1978)); and (b) generic isolated substorm aurora features (from *Kepko et al.* (2014)).

Further, we know that the temporal evolution of substorms is highly variable, and can be as short as a few minutes or as long as several hours (*Pellinen et al.*, 1994). Thus, EOFs may not describe features that commonly translate and rotate in spatio-temporal space, which is common to substorm events and their ionospheric projections (*Provan et al.*, 2004). Despite these complications, we believe these EOFs are capturing basic substorm phenomena.

EOF4:

Both HEOF4 and PEOF4 are suggestive of the substorm recovery during which the ionosphere is returning to a pre-disturbed state. Thus, the prominent feature at midnight to post-midnight LTs is probably associated with a different phase of the auroral substorm than the features shown in EOF3. The fact that a recovery mode is represented as primary in these results is significant given the relative lack of attention substorm recovery has received in comparison to substorm growth and expansion (*Opgenoorth et al.*, 1994). Consistent with recovery, conductance decreases should

exhibit a correlation with geomagnetic activity indicators. The correlations of EOF4 with the SME, Kp, and Dst indices indicate this is so. Although the correlations show appropriate trends, the geophysical interpretation of such higher-order EOFs is complicated by the orthogonality constraint. Additionally, these higher-order modes capture increasingly smaller amounts of the variability in the data (specifically between 3.7% and 3.5% for HEOF4 and PEOF4, respectively). There are small-scale features apparent throughout the high-latitude regime, which become ubiquitous as the EOF order increases. This is a well-known feature of EOF analysis. Despite the diminishing size of the spatial features, these and even higher-order EOFs are likely still geophysically significant and thus important for the purposes of error covariance creation.

Notably absent from EOFs 1-4 is a dayside cusp signature. There are two reasons for this: 1) highly variable geomagnetic location of the cusp (*Zhou et al.*, 2000); and 2) hemisphere-dependent response of the cusp location to the IMF B_Y component. The first explanation corresponds to a weaker cusp signal in any one geomagnetic location over the course of the analysis, and thus does not produce a strong response mode overall (hence it does not appear in EOFs 1-4). However, several features in higher-order EOFs are suggestive of cusp influence. The second explanation alludes to the fact that the northern and southern hemisphere cusps shift oppositely in MLT in response to IMF B_Y. These shifts essentially counter-act in our results due to the assumption of observation conjugacy.

Although this study examines height-integrated conductances, we point out that the analysis shown in Figures 5.4b and c yields three-dimensional conductivity information and therefore permits future extension to three-dimensional study, which we will explore in a follow-on paper.

Future Work:

There are five paths for future work to further constrain the estimation process: 1) determination of the sensitivity of the EOF analysis to a particular data set and regularization technique; 2) introduction of additional pseudo-observations (conductance information); 3) inclusion of ion precipitation; 4) addition of solar-induced conductance; and 5) consideration of observational errors. Items 1 and 2 can be addressed in the near-term. The work of *Nicolls et al.* (2014) details

additional promising regularization techniques. Additional conductance pseudo-observations may be obtained from the FAST particle precipitation database (*Carlson et al.*, 2001) and electron density profiles from the Constellation Observing System for Meteorology, Ionosphere, and Climate (COSMIC) (*Schreiner et al.*, 2007; *Lei et al.*, 2007). Conductance EOF results obtained solely from FAST pseudo-observations will be presented in a future paper.

Items 3 and 4 are mid-term efforts. Proton precipitation can be significant under certain conditions and at specific locations (*Galand and Richmond*, 2001a). Further, we have not investigated the conductance variability due to solar EUV. The solar-induced conductance gradient across the day-night terminator causes significant estimation issues with the procedure used here. A solution is complicated by the nonlinear nature of the conductance calculations in Equations 4.1 and 4.2 which precludes a simple linear addition of the solar and particle precipitation conductance components, however, using locally-supported wavelets (*Kozelov et al.*, 2008) as basis functions in the estimation process offers a potential solution.

Regarding item 5, ongoing efforts at the National Geophysical Data Center (NGDC) (*Redmon et al.*, 2015a) in cooperation with several universities will yield reliable estimates of observational uncertainties for the DMSP satellites. However, this is a long-term effort.

There are two applications in which these EOFs can be used to study specific events. In the first instance, one can reconstruct auroral conductance patterns during quiet and storm times through evaluation of Equations 5.1 and 5.2 and construct a model based on EOFs as has been demonstrated for thermospheric neutral density by *Lei et al.* (2012) and for Poynting flux by *Cosgrove et al.* (2014). In the second, these EOFs can be combined with event-specific observations and an optimal interpolation scheme to yield conductance maps for specific events, in the same way that *Matsuo et al.* (2005) and *Cousins et al.* (2013b) performed adaptive estimation of the EOF temporal modes of the ionospheric electrostatic potential. However, these applications are beyond the scope of this paper. We will specifically explore the second application in a follow-on publication.

5.5 Conclusions

EOFs have provided significant value to the atmospheric and space sciences (*Hannachi et al.*, 2007). We have applied this technique to quantify the extent and nature of ionospheric conductance variance for the first time. This work represents the first application of principal component analysis to satellite particle precipitation data and, to date, the only characterization of the dominant modes of auroral variability and their relationship to drivers free of an assumption about the incident electron energy spectra. We investigate the auroral variability by directly ingesting in-situ satellite measurements of high-latitude electron precipitation to the GLOW model to produce conductance pseudo-observations. We interpret the mean patterns to represent the general quiet-time auroral features seen in previous statistical studies of the conductances.

Pedersen and Hall EOFs 1-4 described $\sim$ 50% of the total variation in the conductance pseudo-observations. HEOF1 and PEOF1 represent intensifications of the quiet-time auroral zone and can be attributed to strengthening/weakening of the diffuse precipitation-induced conductances. The hallmark of the EOF1 patterns is an extended latitudinal and longitudinal variability of the main features of the average patterns (Figure 5.5a and Figure 5.5f). EOF2 and EOF3 likely represent two distinct components of the auroral electrojets as suggested by *Baumjohann* (1982) and later expanded upon by *Kamide et al.* (1996); *Kamide and Kokubun* (1996). In this interpretation EOF2 would be associated with general magnetospheric convection during southward IMF and EOF3 would be associated with the pre-midnight westward electrojet surge and substorm current wedge. EOF4 represents a substorm recovery mode, an important finding in light of the fact that substorm recovery has historically received less treatment than substorm growth and recovery phases (*Opgenoorth et al.*, 1994).

We have interpreted the EOFs geophysically, and find that the EOF estimation successfully captures the primary modes of variability of the Pedersen and Hall conductances reported in many previous studies within areas supported by observations, a finding that gives credence to the statistical method. We explored the possible drivers of the dominant modes of variability represented

by these EOFs through correlations of the attendant temporal modes with the corresponding time series of solar wind parameters, geomagnetic indices, and specialized activity proxies. Based on the spatial patterns and temporal mode correlations we suggest that the first four modes of conductance variations are associated with diffuse and structured precipitation, field-aligned currents, and substorm phenomena.

Thus, we have established a fundamental observational-based picture of the ionospheric conductance variability that allows us to overcome assumptions that have influenced, and in many ways limited, conductance estimation and understanding for the past three decades. To our knowledge no such picture of the primary modes of variability has been created before. Because clear signatures of magnetosphere-ionosphere (MI) coupling processes are present in the primary modes of variability, we suggest that an error covariance model built from these EOFs will allow better representation of MI coupling in global ionospheric and magnetospheric models. This emphasizes the importance of this work and that to follow.

Future work will introduce and assimilate new sources of conductance data to produce a single set of EOF patterns for the Pedersen and Hall conductances from multiple sources with associated realistic uncertainties. Ultimately, our results will be used to create a model error covariance for ionospheric conductance that is based on observations. This work forges a path for reconstructing conductance maps during both quiet and storm time. In a subsequent paper we show in a week-long event study that the EOF analysis is superior to other approaches for estimating full-coverage, high-latitude conductance maps. We will also apply the estimation process detailed in this study to discrete altitude levels to obtain knowledge of Pedersen and Hall conductivities thus supporting new conductivity modeling efforts needed for the next generation of assimilative ionospheric models.

Chapter 6

Expansion of conductance EOFs analysis: Supporting a more robust and complete fundamental picture

6.1 Introduction

We now expand the analysis of conductance variability introduced in Chapter 5 by investigating EOF patterns obtained from subsets of the same data used in the previous chapter (DMSP F6-F8 in 1987 and F16-F18 in 2010) binned according to: 1) interplanetary magnetic field (IMF) clock angle; and 2) Kp index. Our objective is to identify connections between an important driver of geomagnetic activity (the IMF transverse direction) and a robust indicator of geomagnetic activity (the Kp index) and the ionospheric conductances.

Binning the data prior to estimation of the EOFs serves two purposes: 1) provides mean patterns that can be used to create condition-specific background conductance models for the optimal interpolation of conductances (discussed further in Chapter 7); and 2) permits an understanding of the relationship between the conductances and information commonly used to specify geomagnetic activity. The latter will be useful in creating an empirically-determined conductance model for space weather applications in ionospheric forecasting. Such efforts will be able to rely on the relationships identified in this chapter.

Note that the methodology used to construct the results in this chapter is the same as that detailed in Chapter 5, and, therefore, the terminology identified previously will be used here unless otherwise explicitly stated.

6.2 Hall and Pedersen conductance EOFs as a function of geomagnetic activity and interplanetary magnetic field (IMF) clock angle

6.2.1 Kp index

The planetary K-index, or Kp index, is based on three-hour measurements of the K-indices, which are quasi-logarithmic local indices of geomagnetic activity. The Kp index is calculated as a weighted average of the most disturbed horizontal component of the magnetic field as determined from the worldwide K-indices (*Bartels et al.*, 1939), each providing a measurement at a different location. The algorithm used to determine Kp gives a result on a scale from 0-9, with each level further divided into + and − categories (i.e. a Kp index of 1 is subdivided into 1−, 1, and 1+ for weaker, middle, and stronger activity levels, respectively). The Kp index is an indicator of magnetospheric activity, correlating strongly with many magnetospheric processes, particularly magnetospheric convection (*Thomsen*, 2004). A Kp index of 0 represents extreme geomagnetic calm, while a Kp index of 9 represents extreme activity. Given the relationships between magnetospheric convection and the ionospheric conductances identified in the literature (*Wolf*, 1970; *Fedder and Lyon*, 1987; *Kamide et al.*, 1996; *Kamide and Kokubun*, 1996; *Davies and Lester*, 1998; *Ridley et al.*, 2004; *Lotko*, 2007; *Lotko et al.*, 2014; *McGranaghan et al.*, 2015b) and those discussed in relation to conductance EOFs in Chapter 5, we explore the mean and EOF patterns in the Hall and Pedersen conductances binned by Kp.

Figure 6.1 shows the observational characteristics in each Kp bin provided by the same six satellite years of DMSP in-situ energetic electron precipitation observations used in Chapter 5. The top row shows the distribution of data counts in the Northern and Southern hemispheres using the 60 s average pseudo-observations resolved on an equal-area grid for easy visual interpretation. Blue numbers to upper right in the top row of Figure 6.1 give the total number of observations in each Kp bin. The mean and EOFs presented in Figures 6.2 and 6.3 below are estimated using the pseudo-observations at their actual geomagnetic coordinates. The coverage is incomplete in LT, lacking observations in the low-latitude postnoon and premidnight to postmidnight regions. The

number of observations available decreases with increasing Kp. Beyond Kp=6^+ there are fewer than 800 observations in each bin and the spatial coverage is noticeably diminished. With this lack of data support the EOFs estimated for the Kp=7 and 8 bins are likely not significant and are not included below. We use the same LASSO regularization technique introduced in Chapter 5 to overcome these observational constraints.

The bottom two rows in Figure 6.1 show bin-averaged Hall and Pedersen conductances, respectively, in units of Siemens. The distribution of the Hall and Pedersen conductances show similar trends. In the low activity bins, the strong features are primarily in the postmidnight to postdawn LT sectors, corresponding to conductance enhancements caused by the predominance of diffuse precipitation due to pitch angle scattering of eastward drifting plasma sheet electrons (*Winningham et al.*, 1975; *Hardy et al.*, 1985; *Fuller-Rowell and Evans*, 1987; *Newell et al.*, 2009; *Korth et al.*, 2014). The intensity of the conductances increase and expand to lower geomagnetic latitudes with increasing Kp. Above ~Kp=2 the enhancements encompass a wide LT sector, extending from predusk to midnight and throughout the morning, and a broader range of magnetic latitudes, between ~60-72°. The latitudinal expansion continues with increasing Kp. Simultaneously the region in the postnoon LT sector where the conductances are not changed grows as well.

Figures 6.2 and 6.3 show the mean and first three EOFs for the Hall and Pedersen conductances, respectively. In the mean patterns, the color scale has been saturated to increase clarity. As we discuss below, the means show similar trends to those discussed above in relation to Figure 6.1. The important points are:

(1) at low levels of Kp conductance enhancements are co-located with diffuse precipitation of eastward drifting plasma sheet electrons;

(2) locations of enhancements expand in latitude and local time with increasing Kp;

(3) patterns suggest that enhancements increasingly reflect precipitation of accelerated electrons with increasing Kp; and

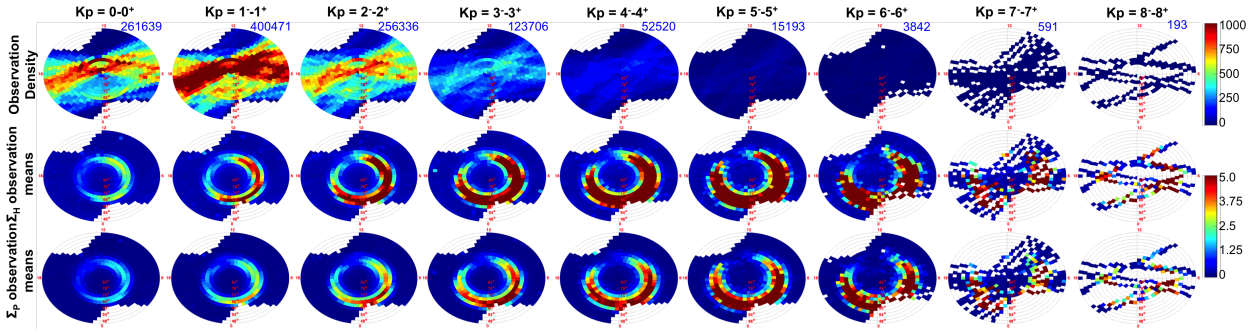

Figure 6.1: (top row) Conductance observation density from the DMSP F6-F8 (1987) and F16-F18 (2010) satellites for each of nine Kp bins. Kp increases from left to right. Blue numbers to upper right are the total number of observations for that Kp bin. (middle row) Hall conductance and (bottom row) Pedersen observation means in equal-area grids for the complete set of 60-second averaged, northern and southern hemisphere pseudo-observations. Conductances means are shown in units of Siemens [S]. The pseudo-observations in these bin-averages are the complete data set after averaging the raw spectra, precipitated through the GLOW model. Results are shown for each of the nine Kp bins. The color mapping for the top row and bottom two rows are shown at the right of the figure.

(4) Hall and Pedersen conductance trends are similar, with the Hall conductance exhibiting noticeably larger magnitudes. These appear in Figure 6.2 as extended latitudinal and local time enhancement regions due to the saturated color scale.

HEOF1 and PEOF1 represent strengthening/weakening of the mean patterns, as expected. However, these distributions now demonstrate the conductance variability for specific activity levels, adding granularity to the overall picture of variability. The distributions for Kp=6 are notable because of their local peaks in the post dusk and dawn LT regions. These are consistent with the patterns of monoenergetic precipitation during heightened activity identified by *Newell et al.* (2009) (see their Figure 3) and add credence to the interpretation that the conductance variability is increasingly controlled by accelerated, rather than diffuse, electron precipitation as activity rises. Monoenergetic precipitation is associated with greater characteristic electron energies. Using the $\frac{\Sigma_H}{\Sigma_P}$ ratio as a proxy for the characteristic energy of the precipitating electrons, *Vickrey et al.* (1981) found that the characteristic energies rise with the Kp index. *Schlegel* (1988) then extended this conclusion to explain a larger spread in conductance magnitudes with increasing Kp. *McIntosh and Anderson* (2015) more recently studied the best fit spectral types for DMSP energetic electron observations as a function of Kp and found: 1) all precipitation increased with Kp; 2) the percentage of Maxwellian best fit spectra (i.e. the spectral form most commonly associated with diffuse precipitation) decreased with increasing Kp; and 3) higher levels of Kp corresponded to precipitation better characterized by Kappa, monoenergetic, or broadband spectra (i.e. accelerated precipitation). Our EOFs are consistent with these studies, but also extend the understanding by capturing the entire high-latitude variability, separating it into independent modes of variability, and providing evidence of different variabilities driven by diffuse and accelerated electron precipitation.

HEOF2 and PEOF2 demonstrate clear Kp-dependence. Between Kp=2 and 5 the variability largely reflects enhanced magnetospheric convection, resulting in equatorward expansion of the regions of auroral conductance enhancement. This was discussed in detail in Chapter 5. However, at either extreme of activity the EOF2 patterns are remarkably different for a given conductance. At

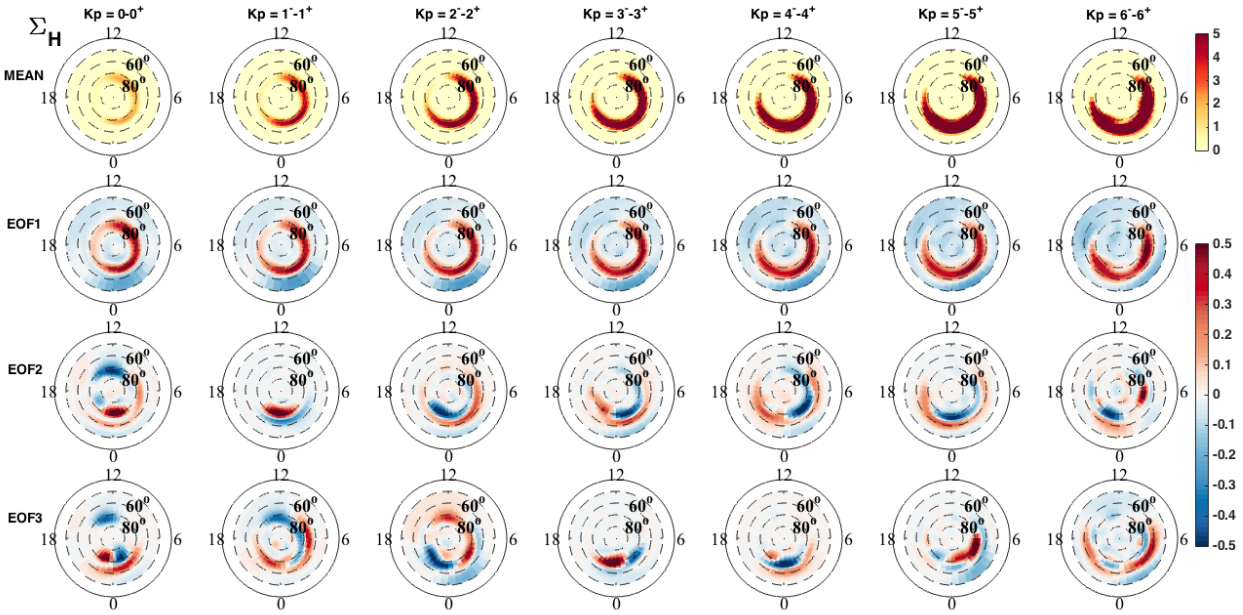

Figure 6.2: Hall conductance means and EOFs 1-3 created by first binning the DMSP data from 1987 and 2010 into seven distinct bins by the Kp index. The bins indicate activity is increasing from left to right in the figure.

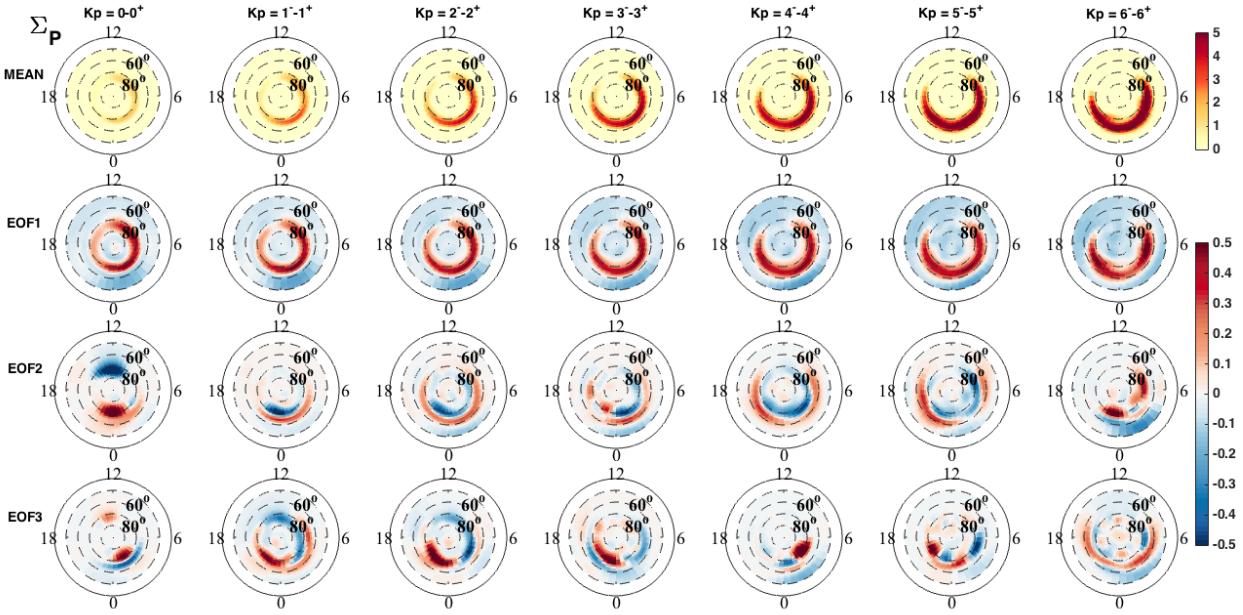

Figure 6.3: Pedersen conductance means and EOFs 1-3 created by first binning the DMSP data from 1987 and 2010 into seven distinct bins by the Kp index. The bins indicate activity is increasing from left to right in the figure.

the lowest levels of activity (Kp < 2) the variability is largely focused in the noon-midnight meridian. This may reflect the significantly reduced convection that occurs for such extreme quiet conditions at which times Region 1/Region 2 current systems are frequently not observed (*Gussenhoven*, 1988). During these periods of extreme quiet diffuse precipitation persists, but with small number flux and low characteristic energies (mostly below 1 keV) (*Meng*, 1981). This soft electron precipitation maps to the midnight LT sector on the nightside, the high-latitude polar cusp on the dayside, and a latitudinally-contracted auroral region throughout. The impact of these soft particles on ionospheric conductivities is an active area of research, focused on the F Region (>∼200 km). These characteristics are reflected in the midnight signatures of both the HEOF2 and PEOF2 patterns in the Kp=0 bin. HEOF3 and PEOF3 are characterized by smaller scale structure and likely localized energetic electron precipitation due to acceleration processes. Further investigation into the variability of these acceleration processes with Kp is important and will be the subject of future work.

We explore the possible drivers of the dominant modes of variability represented by the EOFs in Figures 6.2 and 6.3 using the same correlation analysis methodology detailed in Section 5.3. We correlated the strength of each EOF at a given time period, with the corresponding hourly time series of various solar wind parameters and solar and geomagnetic indices, including B_Z, B_Y, B_X, E_Y, the AE index, the Newell coupling function (*Newell et al.*, 2007) (NCF), and the Borovsky coupling function (*Borovsky*, 2013) (BCF). Figure 6.4 shows these correlations for EOF1 (top row, Figures 6.4a-g in order of increasing Kp) and EOF2 (bottom row, Figures 6.4h-n in order of increasing Kp). HEOF and PEOF correlations are shown by red and blue dots, respectively. Kp bins greater than 6^+ are not shown because of the very limited available data for the correlation analyses in these bins.

HEOF and PEOF amplitude correlations are similar. The consistent features are: 1) for both conductances when Kp > 1^+ the AE index is most strongly correlated with the EOF1 and EOF2 amplitudes; 2) with the exception of the Kp=1^--1^+ bin, correlations with B_Y, B_X are < |0.2|; and 3) with the exception of the Kp=1^--1^+ bin and a sign change in the HEOF2 amplitude correlations

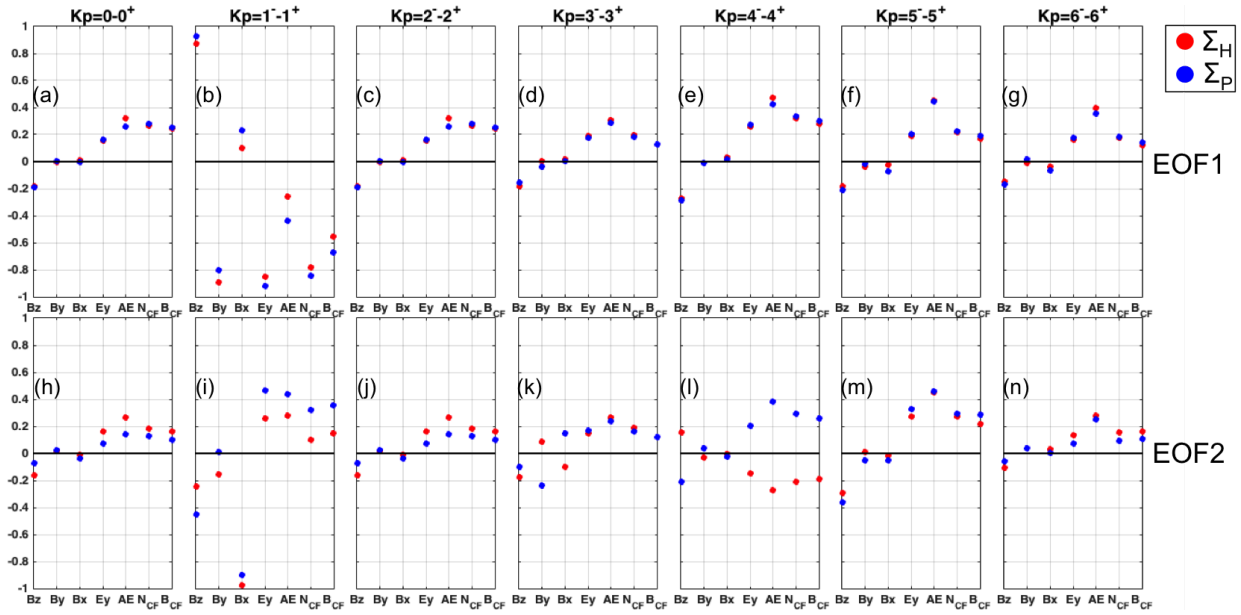

Figure 6.4: Correlations of Kp-binned EOF amplitudes with solar wind parameters (B_Z, B_Y, B_X, E_Y) and geomagnetic activity indicators (AE index, Newell coupling function (*Newell et al.*, 2007) (NCF), and Borovsky coupling function (*Borovsky*, 2013) (BCF)). HEOF and PEOF amplitude correlations are shown by red and blue dots, respectively. Correlations for EOF1 are given in the top row of plots (a-g), and those for EOF2 are given in the bottom row (h-n).

in the Kp=4^--4^+ bin (Figure 6.4l), the correlations are generally similar, but reduced, between EOF1 and EOF2 amplitudes (comparing the top and bottom rows for a given Kp bin).

The correlations of the Kp=1^--1^+ bin EOF amplitudes (Figures 6.4b and i) are interesting. In Figure 6.4b HEOF1 and PEOF1 amplitudes are both strongly correlated with northward ($+B_Z$) and dawnward ($-B_Y$) IMF. Because this bin is associated with quiet geomagnetic activity, these correlations may simply reflect the average IMF orientations for these Kp=1^--1^+ data, which is positive for B_Z and negative for B_Y in this bin, on average. We believe this also explains the large correlation between HEOF2 and PEOF2 amplitudes with $-B_X$, which is negative on average. However, the fact that the B_Z and B_Y components correlate with EOF1 amplitudes and B_X correlates with EOF2 amplitudes may be significant. This may indicate that B_Z and B_Y drive the conductivity variability more prominently than B_X. In other words, B_Z and B_Y may be first-order drivers of the variability while B_X is a second-order driver. This claim warrants further investigation.

Figure 6.4l (Kp=4^--4^+ bin) shows nearly equal and opposite correlations for the HEOF2 and PEOF2 amplitudes. We note that the signs of EOF amplitudes are arbitrary such that any pattern can be equally replaced by its negative. When the sign of an EOF spatial pattern is switched the sign of the amplitudes also switch, and, therefore, the correlations also change signs. Referring to HEOF2 and PEOF2 spatial patterns for the Kp=4^--4^+ in Figures 6.2 and 6.3, respectively, it is not clear that HEOF2 is simply the reverse of PEOF2 in terms of sign. Instead HEOF2 may be distinctly different than PEOF2 in this Kp bin. The dusk to midnight LT sector could be an indication that this is, in fact, true. The PEOF2 variability has two components at that LT sector, one at lower latitudes (between roughly 60-68°) and one in the opposite sense at higher latitudes ($\sim 68 - 78°$). Alternatively, HEOF2 appears to only contain the lower latitude component in the sector.

In general, these correlations support that ionospheric conductance variability exhibits clear, but not necessarily intuitive or linear, dependency on Kp. It is likely that a combination of solar wind parameters and geomagnetic indices would be better able to represent ionospheric conduc-

tance variability than any single parameter (*Weimer*, 2001; *Newell et al.*, 2007; *Borovsky*, 2013; *Cosgrove et al.*, 2014). We investigate the IMF clock angle dependence next, but a full exploration of conductivity dependence on solar wind parameters and geomagnetic indices is an avenue of future investigation. Such future investigation should note that binning data by a combination of geophysical parameters will reduce the amount of data that go into the EOF analysis, and the reliability of the resulting EOFs and amplitudes with the reduced data will have to be demonstrated.

6.2.2 IMF clock angle

The interplanetary magnetic field (IMF) clock angle, θ, is defined as:

$$\theta = \tan^{-1}\left(\frac{B_{\mathrm{Y,GSM}}}{B_{\mathrm{Z,GSM}}}\right), \tag{6.1}$$

where GSM refers to geocentric solar magnetic coordinates. This coordinate system is centered on the Earth and is defined with the z-axis pointing in the direction of the Earth's north dipole direction, x-axis directed from the Earth toward the center of the Sun, and y-axis completing the right hand coordinate frame. The clock angle defines the direction of the solar wind magnetic field vector in the yz-plane of the GSM coordinate system and is oriented such that the 0° direction is aligned with the z-axis. Thus, the clock angle (in degrees) is defined by the IMF $\mathrm{B_{Y,GSM}}$ and $\mathrm{B_{Z,GSM}}$ components:

$$\begin{aligned}
\theta = 0^\circ \quad &: \quad \mathrm{B_{Y,GSM}} = 0; \mathrm{B_{Z,GSM}} = (+) \\
\theta = 90^\circ \quad &: \quad \mathrm{B_{Y,GSM}} = (+); \mathrm{B_{Z,GSM}} = 0 \\
\theta = 180^\circ \quad &: \quad \mathrm{B_{Y,GSM}} = 0; \mathrm{B_{Z,GSM}} = (-) \\
\theta = 270^\circ \quad &: \quad \mathrm{B_{Y,GSM}} = (-); \mathrm{B_{Z,GSM}} = 0
\end{aligned}$$

The IMF is a critical driver of solar wind-magnetosphere-ionosphere coupling and the clock angle is often used as a proxy for the level of coupling that occurs (*Newell et al.*, 2007; *Borovsky*, 2013). It carries important implications for the spatial response of the magnetosphere-ionosphere

system to solar wind forcing as well as the variation of the parameters internal to the system (*Pettigrew et al.*, 2010; *Lockwood*, 2013; *McPherron et al.*, 2013; *Cosgrove et al.*, 2014; *Grocott and Milan*, 2014; *Zhang et al.*, 2014). Therefore, an understanding of the ionospheric conductances for different IMF clock angles is important. The mean and first two EOFs for the Hall and Pedersen conductances are estimated after binning the DMSP data from 1987 and 2010 by the IMF clock angle (see Figures 6.8-6.13). The clock angle bins are 45° wide, centered at 0, 45, 90, 135, 180, 225, 270, and 315°.

Figure 6.5 shows the observational characteristics in each IMF clock angle bin provided by the DMSP conductance pseudo-observations used in Chapter 5 and in the previous section. Blue numbers to upper right in Figure 6.5 give the total number of observations in each clock angle bin. The distribution of observations is relatively even across all bins, though with slightly fewer observations in those centered at 0° and 180° (∼72000 and ∼66600 observations, respectively, compared to ≥∼ 100000 in each of the other bins). This is typical of analyses involving the clock angle where higher occurrence frequencies are observed for bins that are not purely northward (0°) or southward (180°) (*Fear et al.*, 2012).

Figures 6.6 and 6.7 show bin-averaged Hall and Pedersen conductances, respectively, in units of Siemens for each clock angle bin. For each of the Hall conductance distributions in Figure 6.6 the auroral oval is enhanced between ∼60-70° MLATs and from dusk through midnight to noon LTs, and the peak enhancement, located at roughly 65° MLAT and in the post-midnight LT sector, increases as the IMF moves from northward (top row) to southward (bottom row). The Pedersen conductances exhibit essentially the same trend, but the peak values are smaller than the Hall conductances. There are indications of B_Y dependence, however these are likely muted here due to our assumption of hemispheric conjugacy, which was necessary to provide sufficient geomagnetic coverage for the EOF estimation.

Figures 6.8, 6.9, and 6.10 show the estimated Hall conductance mean, EOF1, and EOF2 distributions, respectively, each as a function of clock angle. Figures 6.11, 6.12, and 6.13 are the equivalent distributions for the Pedersen conductances. The mean patterns (Figures 6.8 and 6.11)

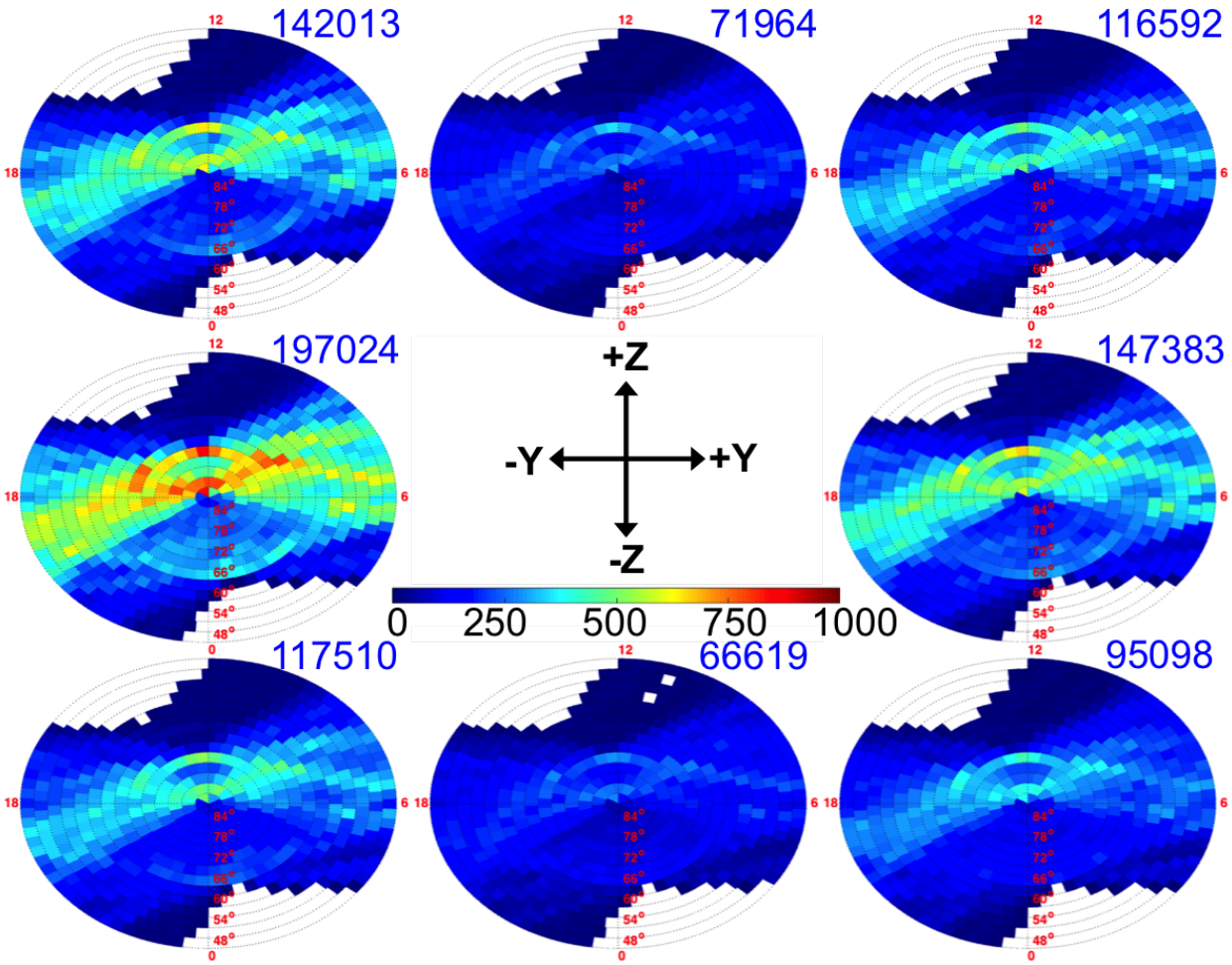

Figure 6.5: Conductance observation density from the DMSP F6-F8 (1987) and F16-F18 (2010) satellites for each of eight interplanetary magnetic field clock angle ($\tan^{-1}\left(\frac{B_{Y,GSM}}{B_{Z,GSM}}\right)$) bins in magnetic coordinates. The clock angle bins increase in 45° increments in the clockwise direction. Blue numbers at upper right are the total number of observations for that clock angle bin.

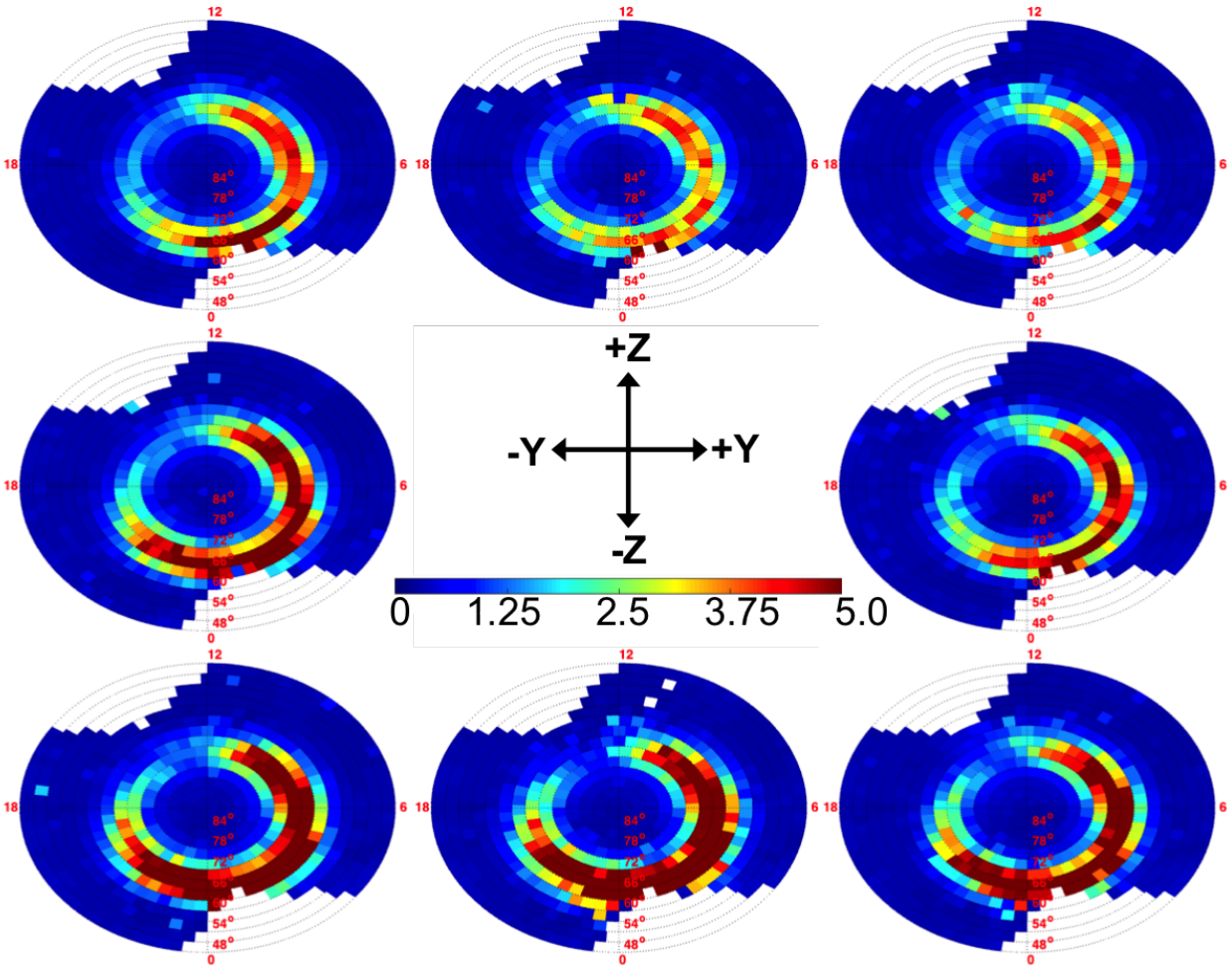

Figure 6.6: Hall conductance observation means from the DMSP F6-F8 (1987) and F16-F18 (2010) satellites in equal-area grids for the complete set of 60-second averaged, northern and southern hemisphere pseudo-observations. Conductances means are shown in units of Siemens [S]. The pseudo-observations in these bin-averages are the complete data set after averaging the raw spectra, which were used as input to the GLOW model. Results are shown for each of eight interplanetary magnetic field clock angle ($\tan^{-1}\left(\frac{B_{Y,GSM}}{B_{Z,GSM}}\right)$) bins in magnetic coordinates. The clock angle bins increase in 45° increments in the clockwise direction.

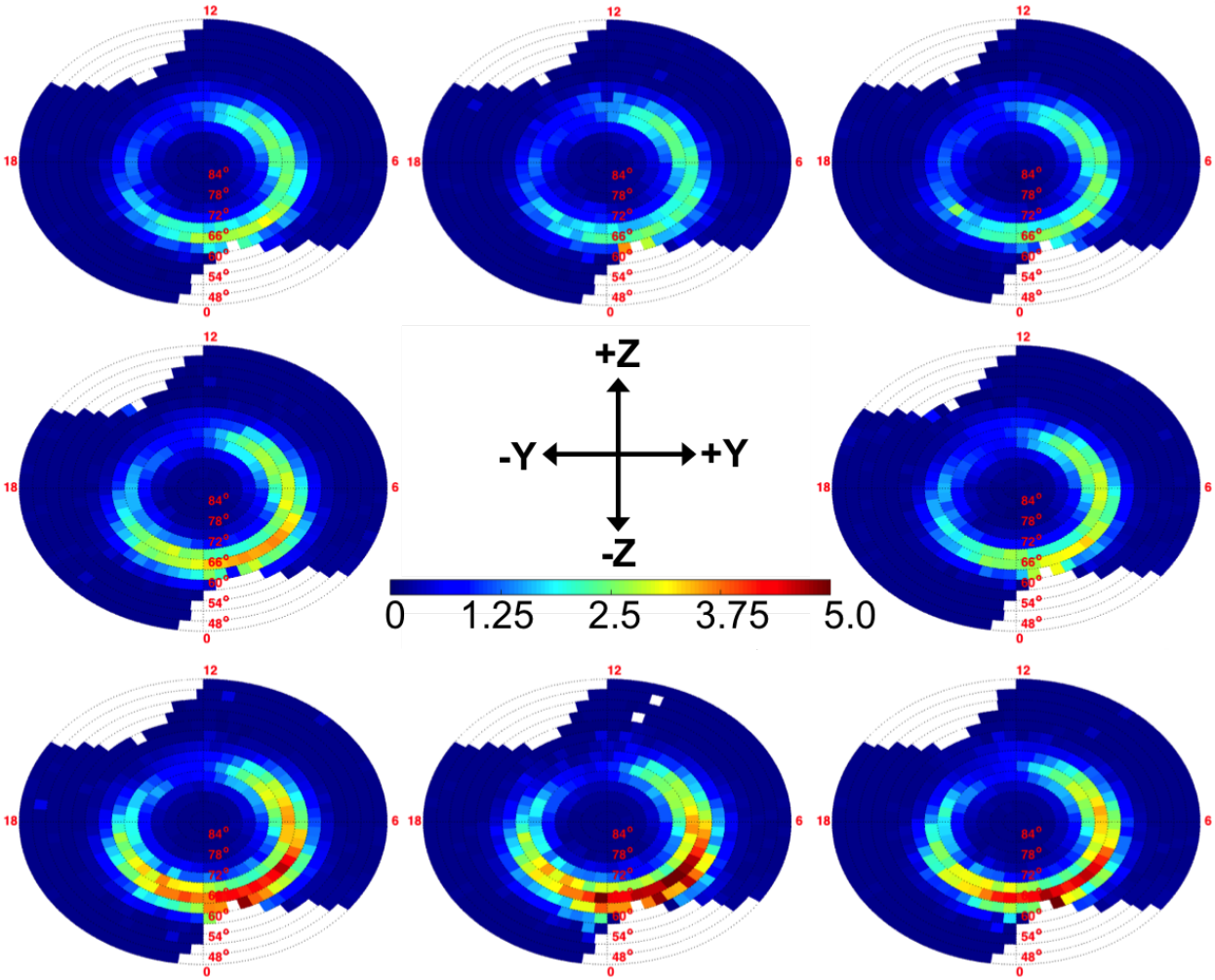

Figure 6.7: Pedersen conductance observation means from the DMSP F6-F8 (1987) and F16-F18 (2010) satellites in equal-area grids for the complete set of 60-second averaged, northern and southern hemisphere pseudo-observations. Conductances means are shown in units of Siemens [S]. The pseudo-observations in these bin-averages are the complete data set after averaging the raw spectra, which were used as input to the GLOW model. Results are shown for each of eight interplanetary magnetic field clock angle ($\tan^{-1}\left(\frac{B_{Y,GSM}}{B_{Z,GSM}}\right)$) bins in magnetic coordinates. The clock angle bins increase in 45° increments in the clockwise direction.

each primarily show an increase in peak conductance throughout the auroral region for southward-directed IMF, with the peak location in the ∼0100-0300 LT sector between 60-70° latitude. There are notable differences, however, between the Hall and Pedersen mean distributions. The important differences are: 1) in general, Σ_H is greater at a given geomagnetic location relative to Σ_P for all clock angles; and 2) there is greater dayside enhancement for Σ_H than Σ_P for clock angles without a southward component (middle and top rows in Figures 6.8 and 6.11). The dayside difference is remarkable for two reasons: 1) the absence of southward IMF, and accompanying strong driving of magnetospheric convection, allows 'signals' of additional geomagnetic activity to become apparent and indicates that ionospheric response to northward-dominant IMF is geomagnetically rich (*Knipp*, 1989); and 2) dayside differences between Hall and Pedersen conductances due to magnetospheric particle precipitation are relatively unexplored (*Coumans et al.*, 2004).

Figures 6.9 and 6.12 show the HEOF1 and PEOF1 patterns, respectively, which represent a strengthening/weakening of the mean patterns. It is interesting to note the first mode of variability is very similar for each clock angle direction. This is in contrast to the Kp-binned EOF1 patterns, which showed notable differences with increasing Kp. The difference suggests that conductance variability is more dynamic as a function of the Kp index than as a function of IMF clock angle. Our assumption of conjugacy likely explains why the IMF B_Y component does not create noticeable differences in the EOF1 patterns (compare across any row of Figure 6.9 or Figure 6.12), however, HEOF1 and PEOF1 are also similar between northward and southward-directed IMF (compare across any column of Figure 6.9 or Figure 6.12). The largest difference occurs between clock angle bins centered at 0° and 180°. In the $\theta = 0°$ bin the conductance variability is greater at higher latitudes and has a larger dayside component. Alternatively, in the $\theta = 180°$ bin the variability expands to lower latitudes and is focused on the nightside. This finding reflects the general picture of magnetic merging between the solar wind and magnetosphere shown in Figure 2.2a for southward IMF and Figure 2.2c for northward in the introduction to this dissertation.

EOF2 is more dependent on the clock angle than EOF1. In several of the bins for both HEOF2 and PEOF2 (Figures 6.10 and 6.13, respectively) the patterns are suggestive of the magnetospheric

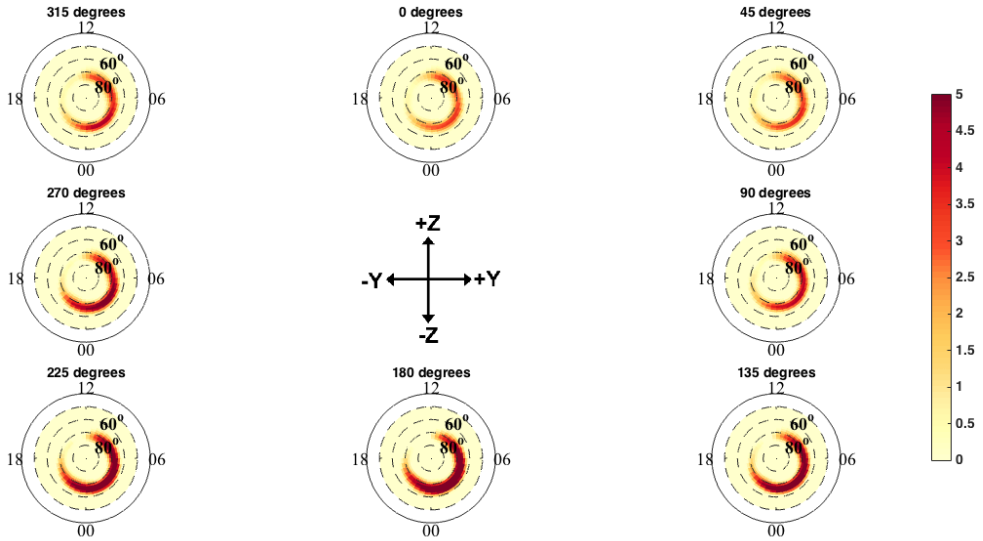

Figure 6.8: Mean Hall conductance patterns created by first binning the DMSP data from 1987 and 2010 into eight distinct bins by the interplanetary magnetic field clock angle ($\tan^{-1}\left(\frac{B_{Y,GSM}}{B_{Z,GSM}}\right)$), increasing in 45° increments in the clockwise direction. The conductance units are Siemens.

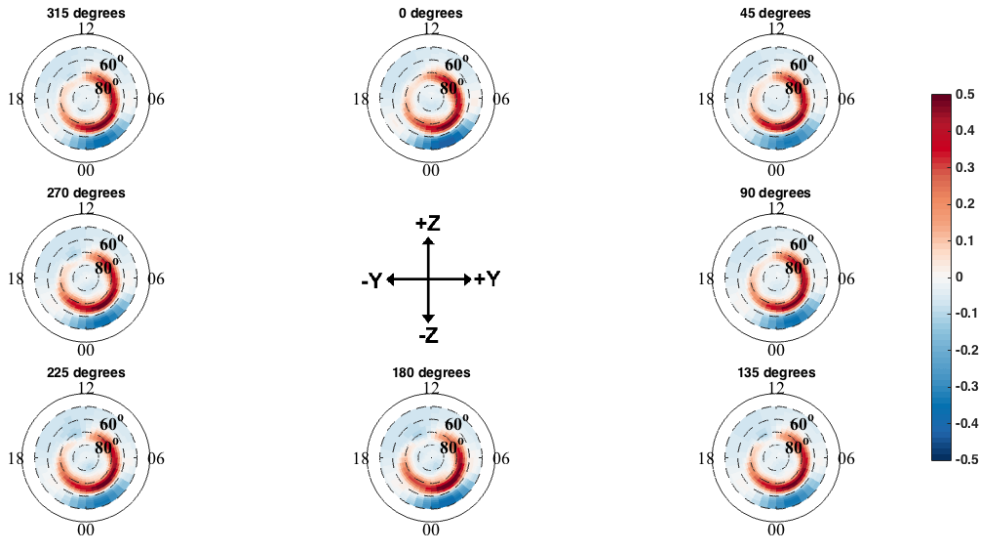

Figure 6.9: Same as Figure 6.8, but for Hall EOF1 patterns. The EOFs have been scaled to a -0.5 to 0.5 scale and use a diverging color scale as a result.

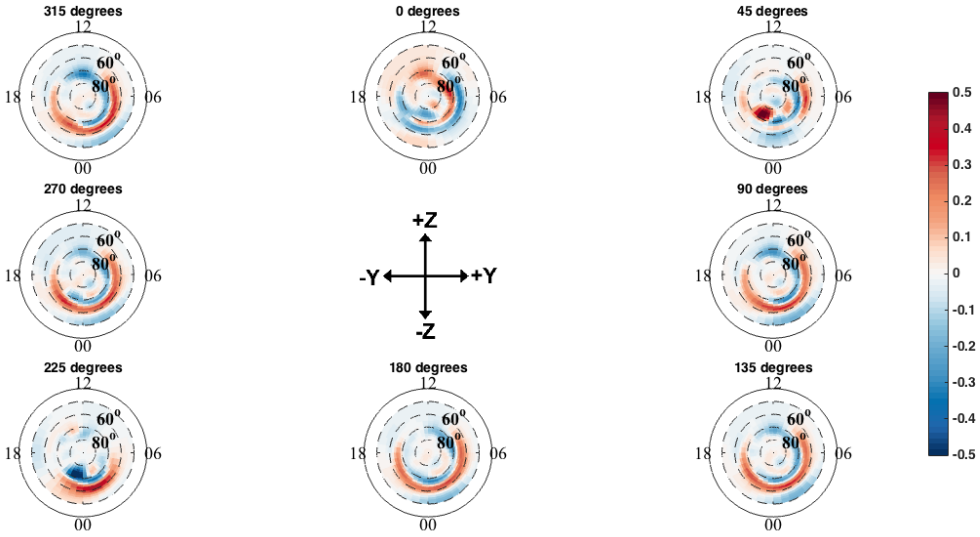

Figure 6.10: Same as Figure 6.8, but for Hall EOF2 patterns. The EOFs have been scaled to a -0.5 to 0.5 scale and use a diverging color scale as a result.

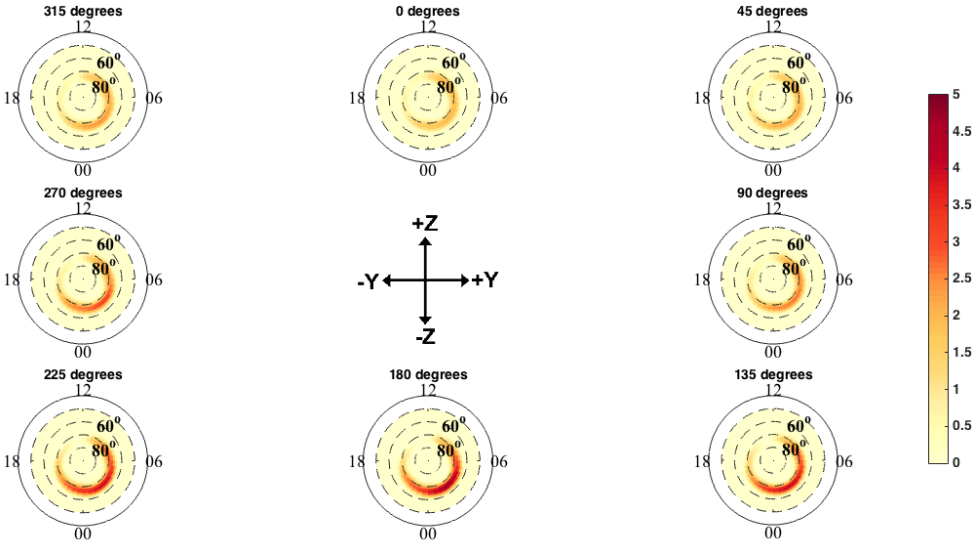

Figure 6.11: Mean Pedersen conductance patterns created by first binning the DMSP data from 1987 and 2010 into eight distinct bins by the interplanetary magnetic field clock angle ($\tan^{-1}\left(\frac{B_{Y,GSM}}{B_{Z,GSM}}\right)$), increasing in 45° increments in the clockwise direction. The conductance units are Siemens.

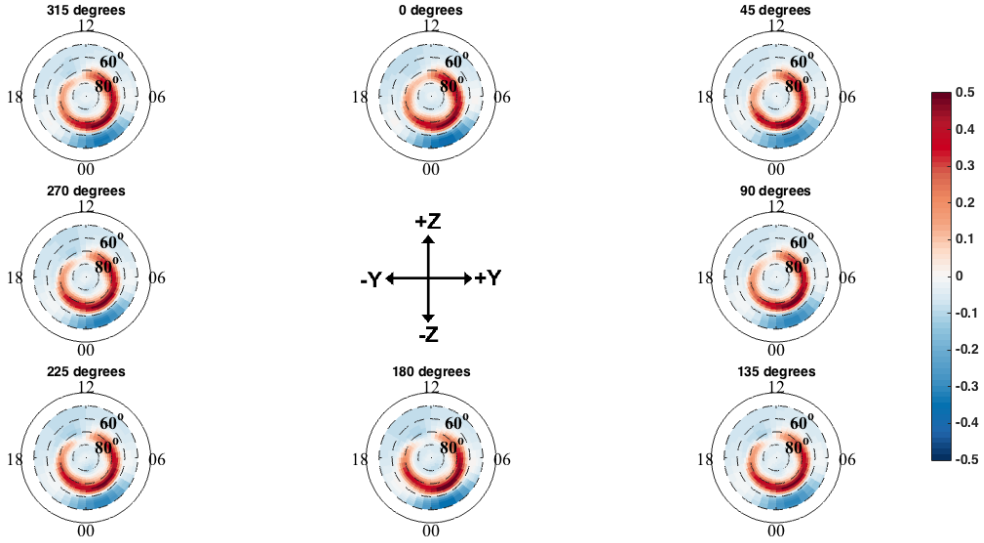

Figure 6.12: Same as Figure 6.11, but for Pedersen EOF1 patterns. The EOFs have been scaled to a -0.5 to 0.5 scale and use a diverging color scale as a result.

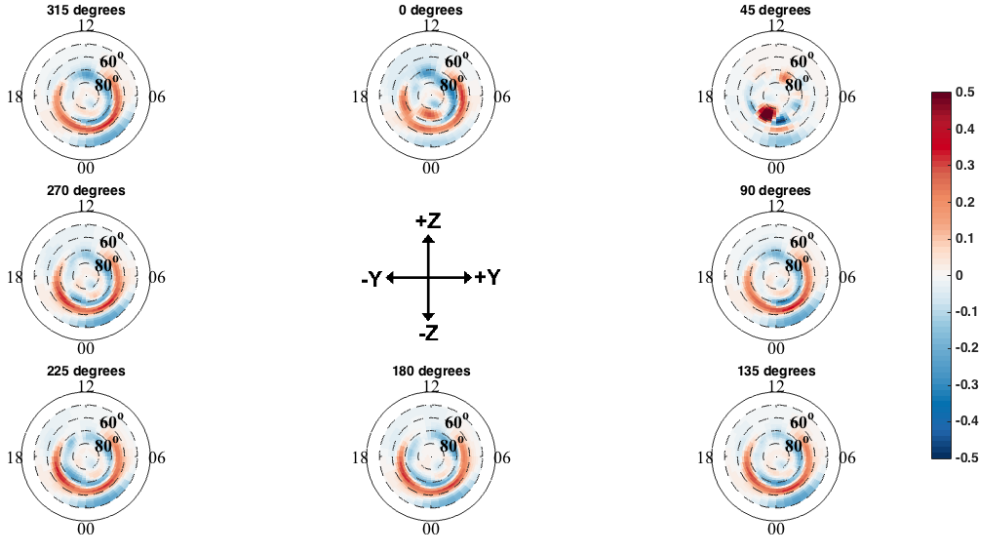

Figure 6.13: Same as Figure 6.11, but for Pedersen EOF2 patterns. The EOFs have been scaled to a -0.5 to 0.5 scale and use a diverging color scale as a result.

convection-driven mode of variability that was identified in Chapter 5 and is characterized by an equatorward expansion of the auroral oval. However, there are two notable exceptions: 1) HEOF2 in the $\theta = 0°$ bin; and 2) HEOF2 in the $\theta = 45°$ and $\theta = 225°$ bins and PEOF2 in the $\theta = 45°$ bin.

To investigate the unique pattern in HEOF2 for northward IMF ($\theta = 0°$ bin) we reiterate that the signs of the EOFs can be positive or negative, and any pattern can be equally replaced by its negative. In this chapter the signs of all patterns as shown have been systematically determined such that the unobserved, post-midnight, low latitude region (specifically the 45° MLAT 0200 LT grid location) is negative. This allows all patterns to be viewed on a consistent basis, which is conducive to identifying fundamental differences between the modes of variability. Therefore, it is significant that HEOF2 in the $\theta = 0°$ bin yields positive values in the high-latitude dayside region and negative values for the magnetospheric convection-driven component of the variability while the patterns in clock angle bins with either no or a reduced northward component of the IMF largely show the magnetospheric convection-driven variability as positive.

There is clearly a relationship between the component of variability that shows up as positive and the IMF B_Z component. We can use correlations of the EOF amplitudes with IMF B_Z to investigate the relationship. Figures 6.14 and 6.15 give the correlations of the EOF1 and EOF2 amplitudes as a function of clock angle bin, respectively. Referring to the $\theta = 0°$ bin in Figure 6.15 we find that the correlations of the HEOF2 and PEOF2 amplitudes are essentially equal and opposite (see the top middle panel of Figure 6.15). Because these correlations refer to the patterns as displayed in Figures 6.10 and 6.13, respectively, it is clear that the magnetospheric convection signature is correlated with southward B_Z, shown by the negative PEOF2-B_Z correlation, and the high-latitude dayside signature is correlated with northward B_Z, shown by positive HEOF2-B_Z correlation. We can conclude that the second primary mode of variability for the ionospheric conductances is strongly driven by the IMF B_Z component, with distinct spatially delineated patterns of variability for northward and southward IMF directions. This seems to illustrate that the absence of southward IMF conditions, and corresponding strong solar wind driving of the magnetosphere, allows different behavior to become apparent, and that this behavior is geomagnetically rich.

The second exceptional case occurs for HEOF2 and PEOF2 alike in the $\theta = 45°$ bin and for HEOF2 in the $\theta = 225°$ bin. The variabilities therein clearly depart from the latitudinally expanded auroral oval signature representative of magnetospheric convection. Instead, the structuring of the variability is significantly smaller scale and the most prominent feature occurs in the premidnight LT sector at MLATs greater than 70°. Figure 6.15 shows that these patterns are not well correlated with any of the selected solar wind parameters or geomagnetic indices, which makes a geophysical interpretation difficult. However, it is interesting that the premidnight signature in the HEOF2 pattern is of opposite sign in the $\theta = 45°$ and $\theta = 225°$ bins, suggesting a dependence on the IMF direction.

Finally, two general trends are illustrated in these results: 1) based on larger correlations between the HEOF1 amplitudes with solar wind parameters and geomagnetic indices (Figure 6.14), the quasi-permanent auroral zone Hall conductances are more responsive to solar wind and geomagnetic driving than their Pedersen counterparts; and 2) based on stronger correlations of PEOF2 amplitudes with solar wind parameters and geomagnetic indices (Figure 6.15)) the magnetospheric convection-driven Pedersen conductances are more responsive to solar wind and geomagnetic driving than their Hall counterparts. These trends warrant future study.

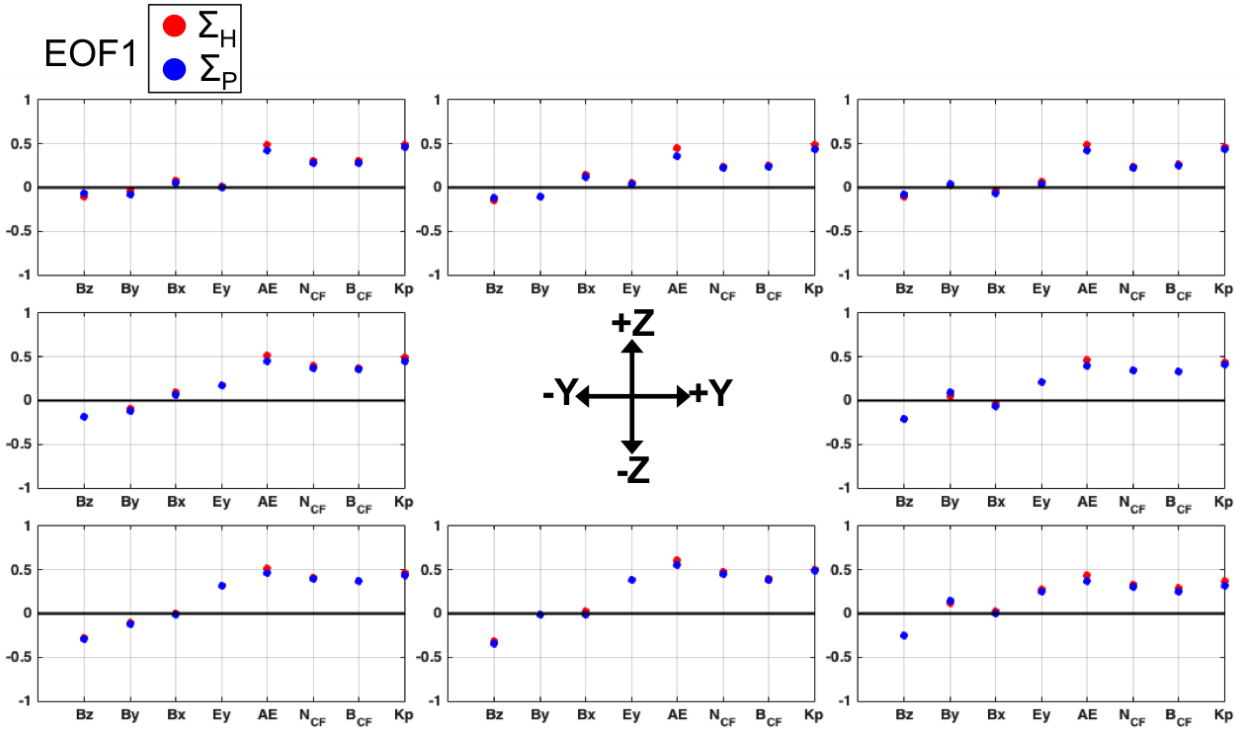

Figure 6.14: Correlations of IMF-binned EOF1 amplitudes with solar wind parameters (B_Z, B_Y, B_X, E_Y) and geomagnetic activity indicators (AE index, Newell coupling function (*Newell et al.*, 2007) (NCF), Borovsky coupling function (*Borovsky*, 2013) (BCF), and Kp index). HEOF1 and PEOF1 amplitude correlations are shown by red and blue dots, respectively.

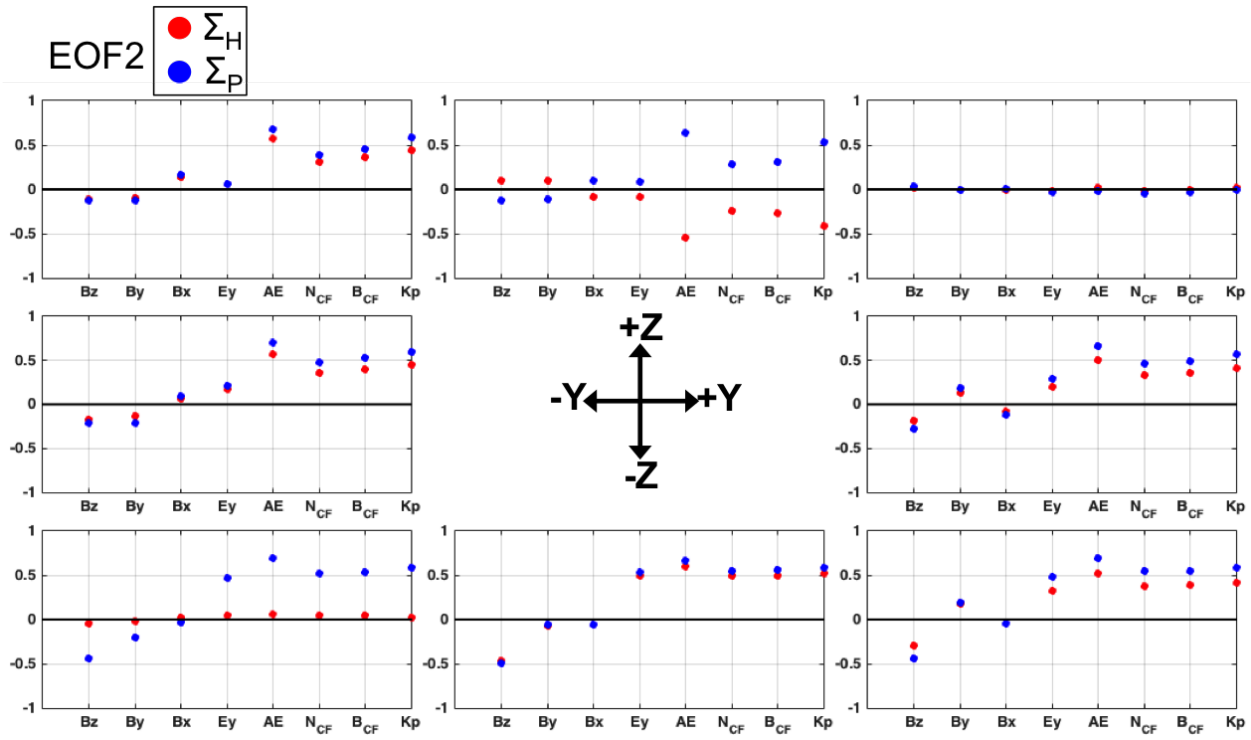

Figure 6.15: Same as Figure 6.14, but for EOF2 patterns.

6.3 Conclusion

This chapter represents a preliminary investigation into the dependence of ionospheric conductance variability, represented as Empirical Orthogonal Functions (EOFs), on the Kp index and IMF clock angle. We used the six satellite years of DMSP data previously used in Chapter 5 (DMSP F6-F8 in 1987 and F16-F18 in 2010), but binned according to the Kp index and, separately, the IMF clock angle. The primary takeaways are:

- the ionospheric conductance variability exhibits clear, but not necessarily intuitive or linear, dependency on Kp;
- though the mean patterns of the Hall and Pedersen conductances show IMF clock angle dependency, the first primary mode of variability (EOF1) does not;
- this is in contrast to the Kp-binned results, in which EOF1 varies appreciably with increasing Kp, suggesting ionospheric conductances are more dynamic as a function of Kp than IMF clock angle; and
- northward IMF conditions reveal geomagnetically rich behavior in the ionospheric conductances that are otherwise obfuscated by the strong driving during southward IMF conditions;

We have identified relationships between ionospheric conductance variabilities and the Kp index and IMF clock angle. Our results provide a foundation upon which empirical ionospheric conductance models can be created and parameterized by forecastable solar wind parameters and readily available geomagnetic indices. The nonlinear relationships between Kp and IMF clock angle and the ionospheric conductance variabilities suggest that a combination of parameters, rather than any single parameter, is likely better suited to build such a conductance model. *Cosgrove et al.* (2014) showed this to be true for Poynting flux, and created a parameterized model of the Poynting flux using the IMF clock angle, a solar wind coupling function, sin(dipole tilt angle), the solar wind

dynamic pressure, and the AL index. These are the same parameters used by *Weimer* (2001) to parameterize the high-latitude electric potential. A similar combination will likely better capture the ionospheric conductance variability better than any single parameter.

Though parameterizations, such as the *Weimer* (2001) and *Cosgrove et al.* (2014) models, are useful for MIT specification and space weather forecasting, we are motivated to specify ionospheric conductivities more accurately than previous statistical models, and, ultimately, to use such improved specification to understand conductivity to the point of prediction. Therefore, in the remainder of this dissertation we pursue ionospheric conductivity specification with advanced statistical estimation tools. In Chapter 7 we present an optimal interpolation technique that accomplishes these objectives.

Chapter 7

Optimal interpolation analysis of high-latitude ionospheric Hall and Pedersen conductivities: Application to assimilative ionospheric electrodynamics reconstruction

7.1 Introduction

Self-consistent analysis of multiple types of ionospheric electrodynamics observations requires correctly specified ionospheric conductivity distributions, especially at latitudes poleward of 45° where coupling between the magnetosphere and ionosphere is particularly strong (*Akasofu and Kan*, 1982; *Kirkwood et al.*, 1988; *Knipp*, 1989; *Connors*, 1998; *Gjerloev and Hoffman*, 2000; *Lu et al.*, 2001; *Raeder et al.*, 2001; *Crowley and Hackert*, 2001; *Aksnes et al.*, 2002; *Ridley et al.*, 2004; *Amm et al.*, 2008; *Wiltberger et al.*, 2009; *de Boer et al.*, 2010; *Lotko et al.*, 2014; *Korth et al.*, 2014; *Cousins et al.*, 2015a; *Marsal*, 2015). Since conductivity cannot be directly observed and even the indirect observations for the specification of ionospheric conductivity are sparse, modeling ionospheric conductivity distributions have mostly relied on limiting assumptions and smooth statistical maps for nearly 30 years. Conductivity, and its height-integrated quantity, conductance, depend on the level of solar photoionization and auroral particle impact ionization. The solar photoionization contribution to conductivity is relatively well characterized (*Robinson and Vondrak*, 1984, and references therein). However, relationships between the ionospheric conductance and auroral particle precipitation are more complex, and modeling the relationships adequately requires determination of an appropriate spectral form to specify the energetic electrons incident on the topside ionosphere, which is often assumed to be Maxwellian (*Robinson et al.*, 1987). Recent work

by *McGranaghan et al.* (2015a,b) and presented in the previous chapters of this dissertation has eliminated the need for a Maxwellian assumption in the conductance estimates, and shown that an improved picture of realistic conductance variability can be derived from empirical orthogonal function (EOF) analysis.

Conductance patterns are crucial to high-latitude electrodynamics analysis because conductance regulates the ionospheric closure of field-aligned currents (FACs) that couple the magnetosphere-ionosphere-thermosphere (MIT) system (*Kamide et al.*, 1996; *Amm et al.*, 2008; *Iijima*, 2000; *Coxon et al.*, 2014; *Lotko et al.*, 2014). *Lu et al.* (2001) found that without accurate conductance patterns the detailed features of FACs estimated using the Assimilative Mapping of Ionospheric Electrodynamics (AMIE) procedure (*Richmond et al.*, 1988; *Richmond*, 1992) can be unreliable. *Raeder et al.* (2001) performed a global simulation of the geospace environment modeling (GEM) substorm challenge event of November 24, 1996 and compared their results to extensive and varied observations and models and found that the simulation depended critically on the Hall and Pedersen conductances. In a few cases, the conductance conditions applied in those simulations failed to produce a substorm at all, and the authors therefore cited improved auroral conductances as an essential piece of future modeling improvements. Numerous other studies have also demonstrated the importance of improved ionospheric conductivity for understanding and modeling the MIT system (*Thayer et al.*, 1995; *Zhang et al.*, 2004; *Coumans et al.*, 2004; *Kihn and Ridley*, 2005; *Burke et al.*, 2006; *Lotko et al.*, 2014; *Cousins et al.*, 2015a).

The available statistical conductance maps capture conductance enhancements due to diffuse precipitation reasonably well (*Fuller-Rowell and Evans*, 1987; *Ahn et al.*, 1998), however to accurately specify the ionospheric electrodynamics it is essential to correctly represent discrete precipitation-induced enhancements and their locations (*Wilkinson et al.*, 1986; *Slinker et al.*, 1999; *Crowley and Hackert*, 2001; *Zhu et al.*, 2005; *Wiltberger et al.*, 2009; *Vorobjev et al.*, 2013; *Zhang et al.*, 2015), particularly during geomagnetically active periods (*Newell et al.*, 1996d, 2009, 2010; *Wing et al.*, 2013). In this regard, the current statistical models do not perform well. *Cousins et al.* (2015a), hereafter C2015, found that lack of conductance enhancements from discrete aurora,

or, equally important, misplacing these enhancements, created substantial inaccuracy in electrodynamics distributions in assimilative inverse procedures. Their conclusion is consistent with the findings of *Marsal et al.* (2012) who showed an underestimation of magnetic variations produced by ionospheric currents modeled by global circulation models. *Marsal et al.* (2012) attributed the underestimation to the ionospheric conductance model insensitivity to electron precipitation associated with strong upward FACs, which are known to be primarily carried by downward accelerated electrons and thus discrete precipitation (*Kamide and Rostoker*, 1977; *Waters et al.*, 2001; *Dahlgren et al.*, 2014). These results suggest that conductance models that are unable to reproduce or correctly locate enhancements due to discrete aurora preclude accurate electrodynamics analyses.

We address the issues above with a new optimal interpolation (OI) technique that can reconstruct the dynamically evolving global distribution of high-latitude ionospheric Hall and Pedersen conductance patterns from instantaneous conductance observations available along satellite tracks. The technique also uses a background conductance model and the uncertainty information associated with the background model and observations, and can yield an objective measure of the uncertainty associated with the estimated conductance patterns. One important component of this OI technique is use of a realistic background model error covariance that allows sparse observation information to be spread over a large analysis area. Past covariance models used for conductance analyses, such as those used in the AMIE procedure, were based on a heuristic model derived for electric field analyses (*Richmond and Baumjohann*, 1984; *Richmond and Kamide*, 1988; *Richmond et al.*, 1988). In reality, significant inhomogeneities (location variation) and anisotropies (direction variation) as well as temporal non-stationarity exist in the conductances. In this chapter, we incorporate a new background model error covariance of the ionospheric conductances that captures such variation using EOFs estimated directly from Defense Meteorological Satellite Program (DMSP) particle precipitation observations (*McGranaghan et al.*, 2015b), hereafter M2015. M2015 encapsulates the work presented in Chapter 5 of this dissertation and we hereafter use M2015 to refer to that work. This chapter represents the first time a global assimilative analysis of the Hall

and Pedersen conductances has been obtained from in-situ spectrally resolved particle precipitation observations.

We demonstrate the utility of the new OI technique by analyzing conductivity distributions during the passage of a magnetic cloud on November 30, 2011. We use the distributions to qualitatively and quantitatively determine the improvement in ionospheric electrodynamics specification on this date and throughout the surrounding week (November 26 - December 2, 2011). This week was chosen in order to address outstanding issues raised by C2015, who first examined this period. Further, we show that our optimally interpolated conductances agree closely in a qualitative sense with DMSP auroral imagery data. Quantitatively our OI conductance distributions reduce differences between AMIE predictions of the Super Dual Auroral Radar Network (SuperDARN) and the Active Magnetosphere and Planetary Electrodynamic Response Experiment (AMPERE) observations. Our results suggest the OI approach can improve assimilation of multiple types of ground- and space-based data for ionospheric electrodynamics specification. Ultimately, this chapter: 1) supports better use of the diverse observations available for high-latitude ionospheric electrodynamics specification, and 2) supports the *Cousins et al.* (2015a) assertion that more accurate models of the ionospheric conductance are needed to robustly assimilate ground- and space-based observations of ionospheric electrodynamics. We find that the OI conductance distributions better capture the dynamics and locations of discrete electron precipitation that modulate the coupling of the magnetosphere-ionosphere-thermosphere system.

In the following section we detail the methodology used to generate analyses of high-latitude conductance fields and introduce the various conductance models used for comparison in this chapter. Section 7.3 then provides the results, and the qualitative and quantitative evaluation of the optimally interpolated fields. Section 7.4 presents a discussion of the results. Finally, Section 7.5 provides concluding remarks and considerations for future work.

7.2 Methods

In this section we first describe the three primary components of the OI technique: 1) the observations (Section 7.2.1); 2) the OI equations (Section 7.2.2); and 3) the uncertainty information for the background model (Section 7.2.3) and the observations (Section 7.2.4). Finally, we detail the conductance models used for comparison in Section 7.2.5.

7.2.1 Observations

We use directly-measured electron energy spectra with the GLOW electron transport model to generate conductivity profiles due to auroral particle precipitation. Specifically, we process in-situ observations from the Special Sensor J version 5 (SSJ/5) instrument onboard the F16-F18 Defense Meteorological Satellite Program (DMSP) satellites (*Hardy et al.*, 1984; *Kadinsky-Cade et al.*, 2004) during the November 26 - December 2, 2011 period, and use these spectra as input to GLOW (*Solomon et al.*, 1988). Data processing of the count rates from the SSJ/5 instrument provides complete electron and ion energy spectra recorded every second for energies between 30 eV and 30 keV in 19 logarithmically spaced bins. We only use electron energy spectra poleward of |45°| MLAT to ensure that the SSJ/5 instruments are pointed near the local zenith, which is inside the bounce loss cone at DMSP orbital altitudes above |45°| MLAT, thus sampling the Earthward streaming particles. In this high-latitude region, the spatial resolution of the one-second cadence precipitation observations is $\sim 0.1°$ in latitude. The DMSP observations were averaged over 60 s (roughly 4° MLAT) prior to being used in the OI estimation procedure to yield results at mesoscale levels and to be consistent with M2015. Further details of the electron precipitation data and its preparation can be found in *Hardy et al.* (2008) and (*McGranaghan et al.*, 2015b).

The GLOW model yields altitude profiles of ionization and dissociation rates and ion and electron densities, which are used to compute profiles of the Hall and Pedersen conductivities. We integrate the conductivity profiles over the altitude range 80-200 km, the altitude range over which the GLOW model computes the electron density using radiative transfer methods, to produce

height integrated conductivities, or conductances. Because these conductances are not directly observed, but are fed to the estimation procedure as observations, they are hereafter referred to as pseudo-observations. Full details of the the pseudo-observation generation methodology, including the GLOW transport code with conductivity (GLOWcon), are provided in *McGranaghan et al.* (2015a) and Chapters 4 and 5 of this dissertation.

7.2.2 Optimal interpolation (OI) technique

To estimate complete high-latitude Pedersen and Hall conductance patterns we closely follow the AMIE technique of *Richmond and Kamide* (1988), the approach developed by *Matsuo et al.* (2005) and *Cousins et al.* (2013b) for electric potential, *Matsuo et al.* (2015) for field-aligned currents, and *Cousins et al.* (2015a) for estimating complete electrodynamics patterns from SuperDARN and AMPERE data. These works each employed an optimal interpolation (OI) technique in which observations, a background model, and their error properties are combined to produce optimal distributions in the least squares sense (*Kalnay*, 2003) and represented as expansions of basis functions which are introduced below. Our specific approach most closely follows that of *Matsuo et al.* (2015). Here we provide a brief overview of the method, and refer the reader to that work for a more complete discussion.

Suppose $\mathbf{y}$ is a vector of the total number of pseudo-observations, j, of the ionospheric conductances (either Hall or Pedersen) at observation locations, i.e. $\mathbf{y} = \left[(\Sigma_{H,P})_1 (\Sigma_{H,P})_2 \cdots (\Sigma_{H,P})_j\right]^{\mathrm{T}}$, then $\mathbf{y}$ is related to the state vector, $\mathbf{x}$, by:

$$\mathbf{y} = \mathbf{H}\mathbf{x} + \epsilon_r, \tag{7.1}$$

where $\mathbf{H}$ represents a forward operator mapping the state vector, $\mathbf{x}$, into observational space and ϵ_r is the sum of observational and truncation error. In this chapter the observations and state each represent the same variables, Pedersen or Hall conductances, and therefore $\mathbf{H}$ is essentially an interpolation between the state vector grid and observational locations.

Given the deviation of observations from the background state, i.e. the innovation vector:

$$\mathbf{d} = \mathbf{y} - \mathbf{H}\mathbf{x}_b, \tag{7.2}$$

the OI procedure adjusts the background state ($\mathbf{x}_b$) at each analysis time step. The goal of the procedure is to estimate this adjustment. In this chapter $\mathbf{x}_b$ is provided by the mean fields estimated in M2015 and we represent OI solutions as expansions of basis functions. We choose the polar cap spherical harmonic basis functions developed for the AMIE procedure (*Richmond and Kamide*, 1988) to express the conductance fields. The AMIE basis functions are a combination of generalized associated Legendre functions, and in this chapter are given with a colatitude limit of 40° and maximum longitudinal wave number of 12. The resultant resolution is 2.5° in latitude and 15° in longitude. Given appropriate information about the background model and observational errors, discussed below, the solution, or analysis ($\mathbf{x}_a$, $\mathbf{P}_a$), is:

$$\mathbf{x}_a = \mathbf{x}_b + \mathbf{P}_b\mathbf{H}^{\mathrm{T}} \left(\mathbf{H}\mathbf{P}_b\mathbf{H}^{\mathrm{T}} + \mathbf{R}\right)^{-1} \left(\mathbf{y} - \mathbf{H}\mathbf{x}_b\right), \tag{7.3}$$

$$\mathbf{P}_a = \left[I - \mathbf{P}_b\mathbf{H} \left(\mathbf{H}\mathbf{P}_b\mathbf{H}^{\mathrm{T}} + \mathbf{R}\right)^{-1} \mathbf{H}\right] \mathbf{P}_b, \tag{7.4}$$

where $\mathbf{P}_b$ is the background model error covariance expressed in geometric space, $\mathbf{x}_a$ is the analysis, $\mathbf{P}_a$ is the analysis error covariance, I is the identity matrix, and $\mathbf{R}$ is the observational error covariance. A more complete development of the OI equations (Equations 7.3 and 7.4) is provided in *Richmond and Kamide* (1988) and *Matsuo et al.* (2005).

At each analysis time step, $\mathbf{x}_a$ corresponds to a complete high-latitude conductance distribution and is represented as an n–dimensional vector. In this chapter, $n = 925$ and it corresponds to the AMIE grid on which the OI solution is resolved. The AMIE grid is evaluated at the resolution of 1.67° MLAT × 10° MLON and extends from the pole to 50° MLAT, thereby giving 25 MLATs and 37 MLONs, or 925 grid points. Resulting auroral conductances are thresholded at zero to prevent the conductances from taking negative values.

We perform this OI estimation using DMSP particle observations from the SSJ instrument, which we designate SSJ OI. A supplemental technique, introduced below, uses DMSP auroral

Table 7.1: OI estimation procedures used in this research.

OI estimation	Background covariance used	Observations used	Application in this research
SSJ OI	$\mathbf{P}_b$ or $\mathbf{P}_{b,aug}$	Pseudo-conductances from SSJ particle precipitation spectra	To generate complete high-latitude conductance distributions
SSUSI OI	$\mathbf{P}_b$	Pseudo-conductances from SSUSI characteristic energies and energy fluxes	To create $\mathbf{P}_{b,aug}$ for use in SSJ OI

imagery data from the Special Sensor Ultraviolet Spectrographic Imager (SSUSI) instrument to provide a better estimate of the background model error covariance. The supplemental OI estimation is referred to as SSUSI OI. Table 7.1 lists the differences between SSJ OI and SSUSI OI.

The background model error and observational error covariances, $\mathbf{P}_b$ and $\mathbf{R}$, determine how the observational and background model information (i.e. the innovation $\mathbf{d}$) is distributed over the analysis area. Covariance design is among the most important aspect of the OI estimation technique. When observations are sparse, characterizing the spatial coherence of errors of the background model in $\mathbf{P}_b$ and the observations in $\mathbf{R}$ is challenging. In Sections 7.2.3 and 7.2.4 we discuss the design of $\mathbf{P}_b$ and $\mathbf{R}$, respectively.

7.2.3 Background model error covariance modeling

Formally, $\mathbf{P}_b$ is given by $< (\mathbf{x}_b - \mathbf{x}) (\mathbf{x}_b - \mathbf{x})^{\mathrm{T}} >$. Here we design a new covariance model of the ionospheric conductances for use in the OI technique (Section 7.2.3.1), and then use SSUSI observations to improve this covariance model (Section 7.2.3.2).

7.2.3.1 DMSP SSJ EOF-based covariance

To account for anisotropy (directional dependency) and inhomogeneity (spatial dependency) in the correlations of the background model errors over the analysis domain we use the conductance EOFs and coefficients estimated by M2015 using DMSP particle observations, following *Matsuo et al.* (2005, 2015) and C2015.

In M2015, EOFs are used to represent the conductance variability, $\mathbf{\Sigma}' = \mathbf{\Sigma} - \bar{\mathbf{\Sigma}}$, where $\bar{\mathbf{\Sigma}}$ is the mean conductance. This variability is represented in terms of the EOFs:

$$\begin{aligned}\boldsymbol{\Sigma}'(\mathbf{r},t) = \alpha^{(1)}(t)\cdot\mathcal{EOF}^{(1)}(\mathbf{r}) + \ldots \\ \alpha^{(\nu)}(t)\cdot\mathcal{EOF}^{(\nu)}(\mathbf{r}) + \mathbf{e}'(\mathbf{r},t),\end{aligned} \tag{7.5}$$

where t is a time index, representing a discrete time, $\mathbf{r}$ denotes spatial position (magnetic latitude (MLAT) and magnetic local time (MLT)), $\alpha^{(\nu)}(t)$ are time-dependent coefficients of the νth EOF, and $\mathbf{e}'(\mathbf{r},t)$ is the residual after removing the mean and sum of weighted EOFs from $\boldsymbol{\Sigma}'$. Essentially, EOFs represent 2-D time-invariant spatial modes of conductance variability and $\alpha^{(\nu)}(t)$ represent temporal modes that scale the spatial modes in time. The EOFs define a ν-dimensional coordinate system in which the EOFs are the unit vectors and the $\alpha^{(\nu)}(t)$ values are the coordinates (*Wilks*, 2011). This new representation is a compact way to capture the variability in the ionospheric conductances and our goal is to parameterize the covariance model within the low-dimensional space defined by the EOFs.

We use the first eight EOFs and the covariance of EOF amplitudes of $\mathbf{P}_{b,\mathrm{EOF}}$ to model $\mathbf{P}_b$ as expressed by Equation 7.7. We further model the diagonal terms of this matrix by a power law according to the equation:

$$\mathbf{P}_{b,\ \mathrm{EOF}} \approx \mathrm{diag}(\mathbf{P}_{b,\ \mathrm{EOF}}\,(\zeta_{b1},\zeta_{b2})) = \zeta_{b1}\nu^{\zeta_{b2}} \qquad \nu = 1,2,...,8, \tag{7.6}$$

where ν is the EOF order and $\mathbf{P}_{b,\ \mathrm{EOF}}$ refers to the fact that $\mathbf{P}_b$ is represented in EOF space in Equation 7.6 in contrast to geometric space as in Equations 7.3 and 7.4. The conversion from EOF space to geometric space for application to Equations 7.3 and 7.4 is given by:

$$\mathbf{P}_b = \mathbf{E}\mathbf{P}_{b,\ \mathrm{EOF}}\mathbf{E}^{\mathrm{T}}, \tag{7.7}$$

where $\mathbf{E}$ is a 925 x 8 matrix.

Parameters in Equation 7.6 are specified by the square of the median absolute deviations (MADs) of the EOF amplitudes. We compute the MADs of the EOF amplitudes for each ν over all times that were used to estimate the EOFs in M2015. Given a one-hour time resolution as described in M2015 this corresponds to a total of nearly 14000 discrete times over the six satellite

years, which yields an estimate of the variability of the strength of each EOF mode and is thus suited to covariance model design. The square of the MADs is a more robust indicator of variability in this situation than, say, the variance, because the variance is disproportionately controlled by the influence of extreme values. The MADs are given by:

$$\text{median}\left(|\alpha^{(\nu)} - \bar{\alpha}^{(\nu)}|\right) \qquad \nu = 1, 2, ..., 8, \tag{7.8}$$

where $\bar{\alpha}^{(\nu)}$ is the median of $\alpha^{(\nu)}$. Figure 7.1 gives these values for Hall and Pedersen EOFs 1-8 (dashed lines) and the corresponding power law fit curves from Equation 7.6 (solid lines) and demonstrates that the parameterization is a good representation of the diagonal covariance matrix obtained from the EOF amplitudes. The values estimated for ζ_{b1} and ζ_{b2} in Figure 7.6 are assumed constant in time, yielding a time independent $\mathbf{P}_{b,\,\text{EOF}}$.

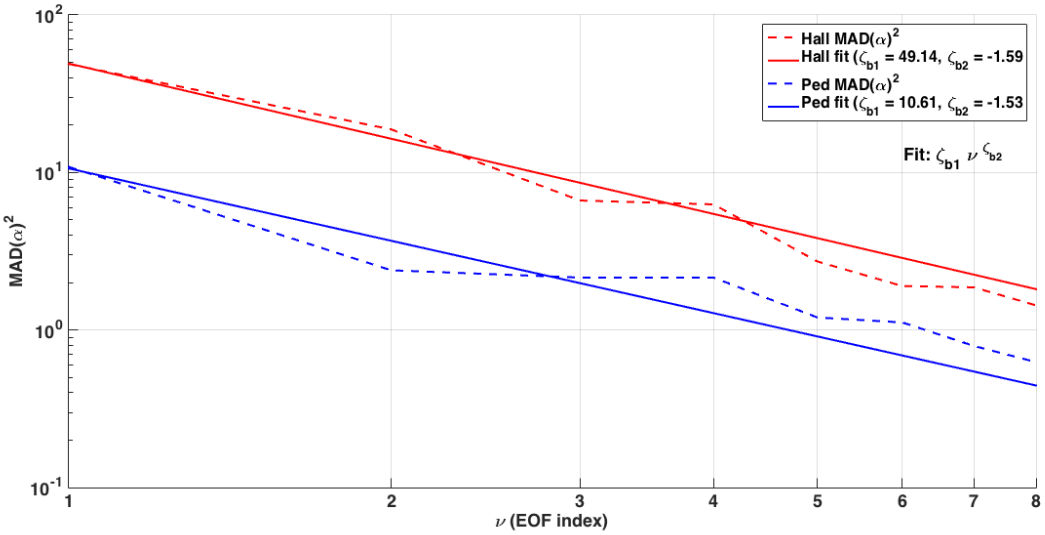

Figure 7.1: Square of the median absolute deviations of the $\alpha_t^{(\nu)}$ for the first eight EOFs (ν: 1-8) calculated in *McGranaghan et al.* (2015b) (dashed lines) and the corresponding power law fit curves (solid lines). Logarithmic scales are used on both axes.

7.2.3.2 DMSP SSUSI covariance augmentation

The use of EOFs in the manner described above, derived for Hall and Pedersen conductances in M2015, represents a data-driven approach to the covariance modeling problem, which is itself a new approach for estimation of ionospheric conductances. Given the importance of covariance in the OI procedure, we explore using additional observationally-based data to improve the covariance model. Therefore, we investigate the use of DMSP Special Sensor Ultraviolet Spectrographic Imager (SSUSI) data (*Paxton et al.*, 1992, 1993, 2002) to augment the EOF-based covariance. The data are supplied by the Johns Hopkins University Applied Physics Laboratory and are available at *http://ssusi.jhuapl.edu/*.

The SSUSI covariance augmentation procedure involves several steps enumerated here and then described in detail in the rest of this subsection.

(1) SSUSI characteristic electron energy and electron energy flux data products, estimated from SSUSI auroral emission observations, are used with the GLOW model to create height-integrated conductance pseudo-observations in the same way pseudo-observations were created from the SSJ particle data.

(2) To create a new background model error covariance matrix augmented by the SSUSI data, designated $\mathbf{P}_{b,aug}$, we form subsets of the total SSUSI pseudo-observations at each analysis time step with each subset consisting of 200 pseudo-observations.

(3) Each subset is optimally interpolated to create a complete high-latitude distribution of the Hall and Pedersen conductances. Subsets are used to provide many independent replications of the conductance fields from which a sample covariance at each time step can be calculated. In these OI estimations using SSUSI data (hereafter called SSUSI OI) $\mathbf{P}_b$ is prescribed by the EOF-based background model error covariance (see Section 7.2.3.1).

(4) Finally, a sample covariance is generated from these complete conductance distributions.

The result is $\mathbf{P}_{b,aug}$, a sample covariance matrix at each analysis time step conditioned on

both SSJ (through the EOF-based covariance model used as the background model error covariance in the SSUSI OI estimation) and SSUSI data.

Here we provide details of the general process outlined above. To calculate conductances from the SSUSI data we used the mean electron energy and electron energy flux products derived from the Lyman Birge Hopfield Long (LBHL) and Short (LBHS) bands using the method of *Germany et al.* (1990) and improvements summarized in *Sotirelis et al.* (2013, and references therein). The mean electron energy and electron energy flux products delivered with the SSUSI files are used to define the electron energy spectra input to the GLOWcon code under a Maxwellian assumption. The conductivity profiles are obtained in the same manner as those for the DMSP SSJ data, the only difference being the electron energy spectrum applied as the input to the GLOWcon code. We assume conjugacy for the SSUSI data. The SSUSI conductance pseudo-observations are bin-averaged using the AMIE grid described above, though the location of each observation is retained, such that all observations falling into a certain AMIE grid bin are assigned the bin-averaged conductance value assumed to occur at the location of the original SSUSI data point. The effect is to lower the resolution of the observations in terms of pseudo-conductance magnitudes, which makes the observations more consistent with the resolution of the OI. The motivation behind such spatial averaging follows similar justification for the use of lower resolution SSUSI observations in global data assimilative models (*Scherliess et al.*, 2004, 2006; *Schunk et al.*, 2004).

Observational uncertainties for the mean electron energies and electron energy fluxes are not yet delivered for the SSUSI data, so for this chapter uncertainties are estimated using a multistep process. At each analysis time step (one hour) all available data are searched for data points with at least four neighboring data points in the surrounding 2.5° latitude by 15° longitude region during the same one hour time period. This criterion is consistent with the spatial and temporal resolution of the analysis used in this chapter. Given the complicated and highly variable temporal relationships of ionospheric phenomena (*Cousins and Shepherd*, 2012; *Fuller-Rowell et al.*, 2001; *Grocott and Milan*, 2014), we do not have robust information on temporal discrepancies in the SSUSI data, especially on time scales shorter than an hour. As a result we assume all observations within a

given one hour time step provide equivalent information on the conductances, and, therefore, no uncertainty is incorporated to account for differences in observation times from the window's central time. Note that the ϵ_r term in Equation 7.1 includes both observational and truncation error, which supports the use of local variance as a measure of observational error. The standard deviation of each collection of neighboring pseudo-observation values is then assigned as the uncertainty value of the central data point. The local variance cannot be calculated for locations with fewer than four neighboring data points, so an uncertainty must be prescribed. In these cases a constant value equal to the median of all the standard deviation-based uncertainty values is used. This approach closely follows that used by *Cousins et al.* (2015b) to create an observation error covariance matrix for AMPERE magnetic perturbation observations.

To account for varying observation density on the grid used for the OI procedure, an additional factor equal to $1/(\textit{number of observations in bin})$ is applied such that locations with fewer observations are given larger uncertainties. Finally, to account for the assumption of conjugacy we apply an uncertainty inflation factor of two to the southern hemisphere when augmenting the northern hemisphere covariance model and vice versa.

At each analysis time step, one sample corresponds to a SSUSI OI estimate of a complete high-latitude conductance distribution, $\mathbf{x_a}$. The total number of samples at a given time step is m and the number of grid points is n, such that we have an $n \times m$–dimensional matrix, A, from which the sample covariance is calculated by:

$$\mathbf{P}_{b,aug}(i,l) = \frac{1}{m-1}\sum_{k=1}^{m}(A(i,k)-\mu_i)(A(l,k)-\mu_l)^{\mathrm{T}}, \tag{7.9}$$

where T represents the transpose and:

$$\mu_i = \frac{1}{m}\sum_{k=1}^{m}A(i,k) \tag{7.10}$$

is the mean at the i^{th} grid point. $\mathbf{P}_{b,aug}$ is the pairwise covariance calculated from each sample combination.

It is very important to note that SSUSI data treated in this manner are only used to improve the background model error covariance (i.e. to create $\mathbf{P}_{b,aug}$)and not as observations for the optimally interpolated conductance results presented below (SSJ OI). Thus, we do eliminate the Maxwellian assumption in the SSJ OI results.

7.2.4 Observational error covariance modeling

The observational error covariance used in the SSJ OI, $\mathbf{R}$, is given by $< \epsilon_r \epsilon_r^{\mathrm{T}} >$. We assume that observational errors are uncorrelated and independent, and thus that $\mathbf{R}$ is a diagonal matrix. Given that direct observational uncertainties of the conductance pseudo-observations by definition do not exist, the uncertainty in the average electron energy associated with each DMSP SSJ observation, averaged over 60 seconds, is presumed to reflect the measurement error, and we assume that these represent conductance uncertainties. The average electron energy uncertainty is a unit-less relative quantity and is computed from Poisson statistics based on the number of particle counts in each energy detector of the SSJ/5 instrument. In this manner the uncertainties are smallest under significant auroral signal and increase significantly outside the auroral zone (*Redmon et al.*, 2015b). The average energy uncertainty is roughly 40% greater than the total electron energy flux uncertainty, also delivered with the DMSP SSJ observations, and thus represents a conservative choice. An uncertainty value is available for each individual particle observation, and therefore each individual pseudo-observation (conductance), which makes construction of $\mathbf{R}$ straightforward:

$$\mathbf{R} = \mathrm{diag}\left[\left(\eta_{\mathrm{E_{avg}}}\right)_1 \left(\eta_{\mathrm{E_{avg}}}\right)_2 \cdots \left(\eta_{\mathrm{E_{avg}}}\right)_j\right], \tag{7.11}$$

where $\eta_{\mathrm{E_{avg}}}$ is the relative average electron energy uncertainty for an individual observation and j represents the number of observations available for a given analysis time step. This formulation gives identical $\mathbf{R}$ matrices for the Hall and Pedersen conductances. Note that this specification of $\mathbf{R}$ does not account for DMSP instrument calibration, temporal discrepancies, or representativeness error that arises from representing the conductance fields by finite-dimensional EOFs. In the future, an uncertainty quantification analysis for the pseudo-observations, taking into account uncertainties

in both the DMSP particle observations as well as the propagation of these uncertainties through the electron transport algorithm used to produce the pseudo-observations, could provide another means to estimate **R**. Such an analysis is beyond the scope of this chapter.

7.2.5 Conductance models used for comparison

We compare our results with a number of conductance models used to perform previous electrodynamic analyses. Table 7.2 provides a summary of the conductance models used.

7.2.5.1 Solar Conductance Model

The solar conductance model, which has been used in the AMIE procedure, is based on Chatanika incoherent scatter radar data and parameterized by solar zenith angle and the solar radio flux index, $F_{10.7}$. The equations are given by:

$$\Sigma_P(\chi, F_{10.7}) = \begin{cases} 0.5F_{10.7}^{2/3}\cos(\chi)^{2/3} & \text{for } \chi \leq 65, \\ \Sigma_P(65, F_{10.7}) - 0.22(\chi - 65) & \text{for } 65 < \chi \leq 100, \\ \Sigma_P(100, F_{10.7}) - 0.13(\chi - 100) & \text{for } \chi > 100, \end{cases} \tag{7.12}$$

$$\Sigma_H(\chi, F_{10.7}) = \begin{cases} 1.8F_{10.7}^{1/2}\cos(\chi) & \text{for } \chi \leq 65, \\ \Sigma_H(65, F_{10.7}) - 0.27(\chi - 65) & \text{for } \chi > 65, \end{cases} \tag{7.13}$$

where χ is the solar zenith angle in degrees and the conductances are in siemens. Following the AMIE procedure, the solar conductances are modified slightly to account for an inverse relationship with geomagnetic field strength (*Wallis and Budzinski*, 1981; *Richmond*, 1995).

7.2.5.2 FRE87 Auroral Conductances

The *Fuller-Rowell and Evans* (1987) statistical models of Hall and Pedersen conductances, hereafter FRE87, were created from particle data obtained from the National Oceanic and Atmospheric Administration TIROS polar-orbiting satellites, NOAA-6 and NOAA-7. The particle data

were used to infer electron total energy flux (integrated for energies between 300 eV and 20 keV) and characteristic electron energy, based on the peak in the measured electron differential energy flux. Though these models do not assume the incident electron energy spectra are Maxwellian, they do assume that the shape of each spectrum is completely specified by the characteristic energy. The conductances were then calculated using the equations, and subject to the same assumptions, of *Evans et al.* (1977). Hemispheric conjugacy was assumed in the model development. The models consist of discrete distributions, or maps, ordered by the hemispheric power auroral activity index (HPI) which ranges from 1-10 (*Evans*, 1987). The original model resolution was 1° MLAT × 8 minutes MLT. Each map consists of Hall and Pedersen conductances as well as the electron energy flux and characteristic electron energy.

7.2.5.3 R87 Auroral Conductances

Robinson et al. (1987), hereafter R87, developed empirical relationships between Maxwellian electron spectra and associated Hall and Pedersen conductances. These relationships depend on electron energy flux and characteristic electron energy and are known as the 'Robinson formulas':

$$\Sigma_P = \frac{40\bar{E}}{16 + \bar{E}^2}\Phi_E^{1/2}, \tag{7.14}$$

$$\frac{\Sigma_H}{\Sigma_P} = 0.45(\bar{E})^{0.85}, \tag{7.15}$$

where $\bar{E}$ is the average electron energy in keV and Φ_E is the electron energy flux in ergs/cm^2 s. In this chapter we generate complete R87 conductance maps using the FRE87-provided characteristic energies and energy fluxes. Therefore, the R87 model consists of discrete maps of Hall and Pedersen conductances for HPI values between 1-10 as well.

7.2.5.4 C2015 Auroral Conductances

C2015 evaluated a number of auroral conductance models, though we compare with only two here: 1) the original model; and 2) the 'optimal' model, which are respectively referred to as

C2015 I and C2015 II in this chapter. Both models used the Oval Variation, Assessment, Tracking, Intensity, and Online Nowcasting next generation (OVATION Prime) model of auroral diffuse precipitation (*Newell et al.*, 2009, 2010), which provides the average electron energy and electron energy flux, and the Robinson formulas (Equations 7.14 and 7.15) to compute the conductances. The difference between the two is in the background nightside conductance levels. C2015 I applied a realistic background in which the Pedersen and Hall conductances were specified to be greater than 0.4 S and 0.8 S (hereafter background I), respectively. C2015 II specified both to be greater than 4.0 S (hereafter background II). This artificial enhancement of the background level essentially accounts for effects of discrete aurora, but smooths over the conductance structures, obfuscating any errors associated with misspecified or missing precipitation. This approach effectively allowed SuperDARN and AMPERE data to be in closer agreement, which was the metric C2015 used to evaluate each conductance model, and is the reason for the label 'optimal model.'

7.2.5.5 M2016 Auroral Conductances

In this chapter we show that our OI conductance model, hereafter M2016, by the same metric used by C2015, can bring these data into closer agreement in the data assimilative inverse procedure without such artificial enhancements, and thus more accurately specify conductance enhancements due to precipitation. It is important to note that 'M2015' refers to the *McGranaghan et al.* (2015b) study while 'M2016' refers to the OI conductance model.

All M2016 models correspond to OI conductance distributions. In order to improve the robustness of the OI analyses, spatial localization is implemented by tapering the correlations of background model errors given by the covariance model described in Section 7.2.3 with a compactly supported fifth-order piecewise rational function (i.e. Equation 4.11 of *Gaspari and Cohn* (1999)). The tapering function depends on a length scale, $\frac{R_r \pi}{l}$, where R_r is taken to be the ionosphere reference height (110 km) from Earth center. The 'WL' and 'SL' designations refer to whether weak ($l = 6$, or 30° arc length) or strong ($l = 12$, or 15°) localization is applied to the background model covariance, respectively. Furthermore, the trailing *I*, *II*, or lack thereof refers to the background

Table 7.2: Auroral conductance models used in this research.

Auroral conductance Model	Details
Fuller-Rowell and Evans (1987) (FRE87)	Hemispheric power index-parameterized conductance maps, assuming electron energy spectrum could be reconstructed based only on the characteristic energy as measured by NOAA TIROS satellites
Robinson et al. (1987) (R87)	Empirical relationship between Maxwellian electron energy spectrum and Hall and Pedersen conductances; In this chapter complete high-latitude R87 maps are created using the characteristic energy and energy flux values from FRE87 model
C2015 I	Diffuse precipitation from OVATION prime auroral precipitation model *Newell et al.* (2009, 2010); no discrete precipitation; R87 relationships used to relate electron energy flux and average energy to conductance; Background I[1].
C2015 II	Same as C2015 I, but with background II[2].
M2016 WL	Weakly-localized optimally interpolated conductances using DMSP SSJ conductance pseudo-observations; EOF-based background covariance (see Section 7.2.3.1); No background applied
M2016 SL	Same as M2016 WL, but with strong localization
M2016 WL I	Same as M2016 WL, but with background I
M2016 SL I	Same as M2016 WL I, but with strong localization
M2016 WL II	Same as M2016 WL I, but with background II
M2016 SL II	Same as M2016 SL I, but with background II
M2016 WL I and SSUSI augment	EOF+SSUSI augmented background covariance (see Section 7.2.3.2)
M2016 SL I and SSUSI augment	same as M2016 WL I and SSUSI augment, but with strong localization

[1] Background I refers to nightside conductances $\Sigma_H > 0.8$ and $\Sigma_P > 0.4$.
[2] Background II refers to nightside conductances $\Sigma_{H,P} > 4.0$.

conductance level. *I* refers to background I, *II* to background II, and no background level is applied in the case that neither is included. Finally, the M2016 models with the *SSUSI augment* designation use the $\mathbf{P}_{b,aug}$ background model error covariance detailed in Section 7.2.3.2.

7.3 Results

To demonstrate the OI conductance model performance we estimate the Hall and Pedersen conductances throughout the period studied in *Cousins et al.* (2015a): November 26 through December 2, 2011 with special emphasis on the coronal mass ejection (CME) interval on November 30. This week was chosen in C2015 because it contains weak to moderate geomagnetic activity and relatively good SuperDARN data coverage. We perform qualitative and quantitative analyses to assess the performance of our OI technique by comparison first with statistical conductance models and subsequently with C2015 results.

Figure 7.2a-d shows the NASA OMNI solar wind observations (interplanetary magnetic field (IMF) in Figure 7.2a and speed in Figure 7.2b) and geomagnetic indices (auroral electrojet index in Figure 7.2c and Sym-H index in Figure 7.2d) for the period. Figures 7.2f-i show the same parameters for November 30, 2011. The hemispheric power index as devised by *Evans* (1987) and published by the National Oceanic and Atmospheric Administration Space Weather Prediction Center (NOAA SWPC, see *http://legacy-www.swpc.noaa.gov/ftpmenu/lists/hpi.html*) is given in

Figures 7.2e and j for the full period and November 30, respectively. On this date Figure 7.2f shows a strong southward turning of the IMF at ∼0900 UT, corresponding to the passage of a CME. The subsequent geospace disturbance is reflected in the enhanced AE index in Figure 7.2h and Sym-H index shown in Figure 7.2i. This activity persists for roughly 10 hours. Next we present OI conductance specification during this period and provide specific examples in the 1130-1230 UT window (during the main phase of the geomagnetic storm), shown by the blue box over Figures 7.2f-j.

7.3.1 OI analysis validation – Cross-validation study and comparison with FRE87 and R87 models

In this section we perform a cross-validation analysis of the OI results and compare with the statistical FRE87 and R87 models. In such an analysis the observations available for OI are divided into two sets: training and validation. The OI estimation is performed using the training set and the results are compared against the validation set. In other words, we artificially exclude a subset of observations and test the ability of the OI estimation using the remaining observations to predict the excluded set.

Figure 7.3 shows the predictive capability of the OI conductance technique compared with that of the FRE87 and R87 models along the DMSP F17 satellite path in the early hours of November 30. The OI results in Figure 7.3 refer to M2016 SL. In the OI results shown here, the F17 observations are the validation set (not used to perform the estimation), and, the F16 and F18 pseudo-observations are the training set (assimilated in the OI procedure). The F17 Hall and Pedersen conductance pseudo-observations along this dusk-to-dawn high-latitude pass are shown by the black traces in Figures 7.3b and c, respectively, and the corresponding locations are shown in the inset Figure 7.3a in geomagnetic coordinates. Figures 7.3b-c show the conductances estimated by the OI (blue), R87 (orange), and FRE87 (red) models at the locations of the F17 pseudo-observations. We note that the FRE87 and R87 conductance distributions were created from NOAA satellite particle precipitation data and Chatanika radar data, respectively, while the

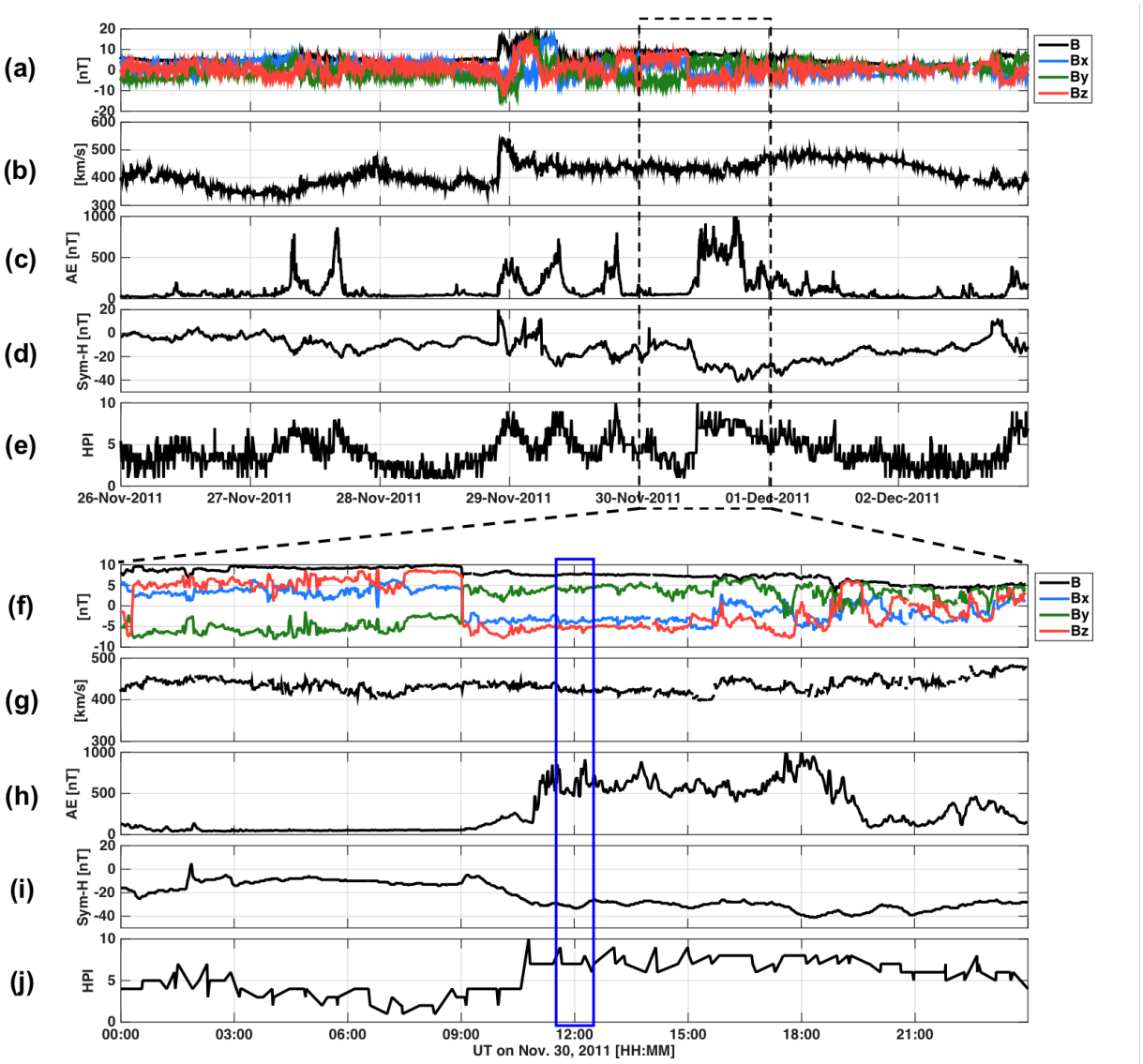

Figure 7.2: Solar wind data for the (a-e) November 26-December 2, 2011 period and (f-j) magnified for November 30, 2011. (a and f) IMF magnitude (black trace) and components; (b and g) solar wind speed; (c and h) AE index; (d and i) Sym-H index; and (e and j) hemispheric power index published by the NOAA Space Weather Prediction Center (*Evans*, 1987). The blue box highlights a specific period on November 30 which is discussed in Section 7.3.

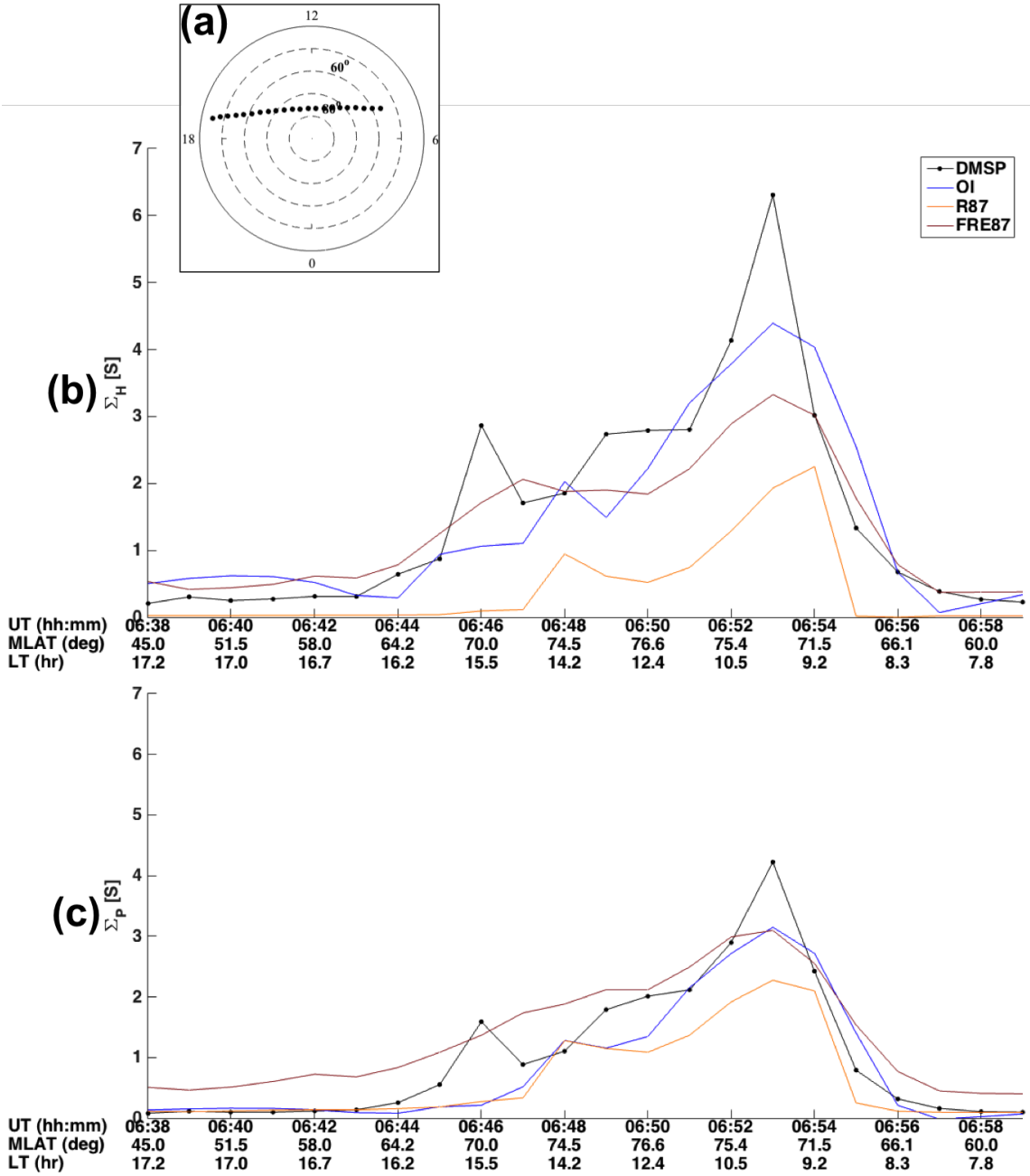

Figure 7.3: (a) Geomagnetic location of DMSP F17 observations during a dusk-to-dawn high-latitude northern hemisphere pass on November 30, 2011. The outermost dashed ring represents the 50° MLAT location and each ring moving inward is a 10° increment. Comparison of OI (blue), R87 (orange), and FRE87 (red) conductance model predictions for the F17 Hall (b) and Pedersen (c) conductance pseudo-observations during this pass. The OI results refer to the M2016 SL model (see Table 7.2) with F17 observations removed from the estimation and no background conductance level used.

M2016 conductance distributions are estimated from DMSP data, which are the data used for validation as well. Therefore, there may be a bias in favor of the M2016 conductances. However, the statistical nature of the FRE87 and R87 models as well as the assumptions those models use regarding the incident particle spectra are believed to be the most significant factors governing the differences between FRE87, R87, and M2016.

The R87 model generally underestimates the Hall and Pedersen conductances throughout the entire satellite pass and misses the peak at ∼0651 UT. The FRE87 prediction is better, providing closer agreement with the F17 pseudo-observations near the peak. However, it tends to overestimate the Hall conductances over the first portion of the pass and the Pedersen conductances over nearly the entire pass other than the peak. The OI results provide the best agreement throughout and better predict the peak Hall conductance at 0651 UT. None of the conductance models resolve the smaller peak near 0646 UT. In general the R87 and FRE87 models smooth the conductance results, as is expected due to the statistical nature of those models. The observation-prediction root mean square (RMS) difference for the OI, FRE87, and R87 model Hall conductances over this F17 pass are 0.76, 0.82, and 1.61 S, respectively. The respective values for the Pedersen conductances are 0.47, 0.52, and 0.65 S.

To assess the accuracy of each of these models, we performed a large-scale cross-validation analysis over the course of the entire week. RMS observation-prediction differences were calculated by randomly removing 30% of the DMSP SSJ pseudo-observations available at each one hour time step throughout the week and comparing these conductance pseudo-observations with the value predicted by four of the conductance models described in Section 7.2.5. Thirty percent was deemed an appropriate level for the validation set because it allowed enough observations for the training set to perform the OI while providing a large sample for the cross-validation analysis. Table 7.3 shows the results for the three conductance models in Figures 7.3b and c, as well as the M2016 weak localization (WL) model. The table contains the statistics (mean, median, standard deviation, and overall RMS) for the differences between the validation set and model-predicted conductances in Siemens. The OI models more closely predict the validation data. We provide a discussion of these

Table 7.3: Conductance model cross-validation study statistics for period from November 26 through December 2, 2011[1]

Observation-prediction difference statistic displayed		Conductance Model			
		R87	FRE87	M2016 SL[2]	M2016 WL[2]
[Mean, Median, St. dev.] $(\Sigma_{\mathbf{val}} - \Sigma_{\mathbf{pred}})$ **[S]**[3]	Σ_H	[0.31, 0.21, 1.48]	[-0.70, -0.31, 1.55]	[0.06, -0.05, 1.44]	[0.07, -0.04, 1.28]
	Σ_P	[-0.28, -0.03, 0.93]	[-1.07, -0.71, 1.15]	[0.10, 0.03, 0.71]	[0.14, 0.04, 0.75]
RMS $(\Sigma_{\mathbf{val}} - \Sigma_{\mathbf{pred}})$ **[S]**[3]	Σ_H	1.64	1.76	1.44	1.28
	Σ_P	0.96	1.58	0.72	0.76

[1] Observation-prediction statistics are calculated using the given conductance model to predict DMSP conductance pseudo-observations.
[2] No background conductance level was assumed for the OI models in these comparisons.
[3] All statistics are computed from the difference between the validation set conductances and the model conductance predictions.

differences in Section 7.4. We tested using different percentages for the validation set (up to 40%) and found that the results were largely insensitive to the specific percentage chosen, indicating that Table 7.3 is a robust representative of the general improvement in RMS provided by the current method.

To further illustrate the differences between the conductance models we provide Figure 7.4, which shows the complete high-latitude Hall and Pedersen conductance distributions at 1235 UT on November 30, 2011 ($Kp_{\text{3-hr avg}} = 3+$, $AE_{\text{1-hr avg}} = 627$ nT) for four conductance models: R87 (Figures 7.4a and e), FRE87 (Figures 7.4b and f), M2016 SL (Figures 7.4c and g), and M2016 WL (Figures 7.4d and h). In these distributions no background conductance is applied (i.e. neither background I nor background II is applied). All figures use the same colorbar, shown at the far right of the figure. The HPI for this time was 7, which defines the FRE87 maps and the characteristic energies and energy fluxes used in Equations 7.14-7.15 to calculate the R87 maps.

The statistical nature of the FRE87 and R87 models is clear in Figures 7.4a-b and Figures 7.4e-f, respectively, where the auroral enhancements extend over a broad range of MLAT from dusk to midnight through dawn to roughly 1100 MLT. Under such heightened geomagnetic activity, elevated conductances in the pre-midnight region are expected and are represented by broad latitudinal enhancements in both FRE87 and R87 conductances at that local time sector. However, there is a notable lack of structure. In contrast, the OI results in Figures 7.4c-d and Figures 7.4g-h capture more localized structure, for example, latitudinally-confined bands, expected during substorms in this MLT sector. The M2016 fields show duskside conductance enhancements,

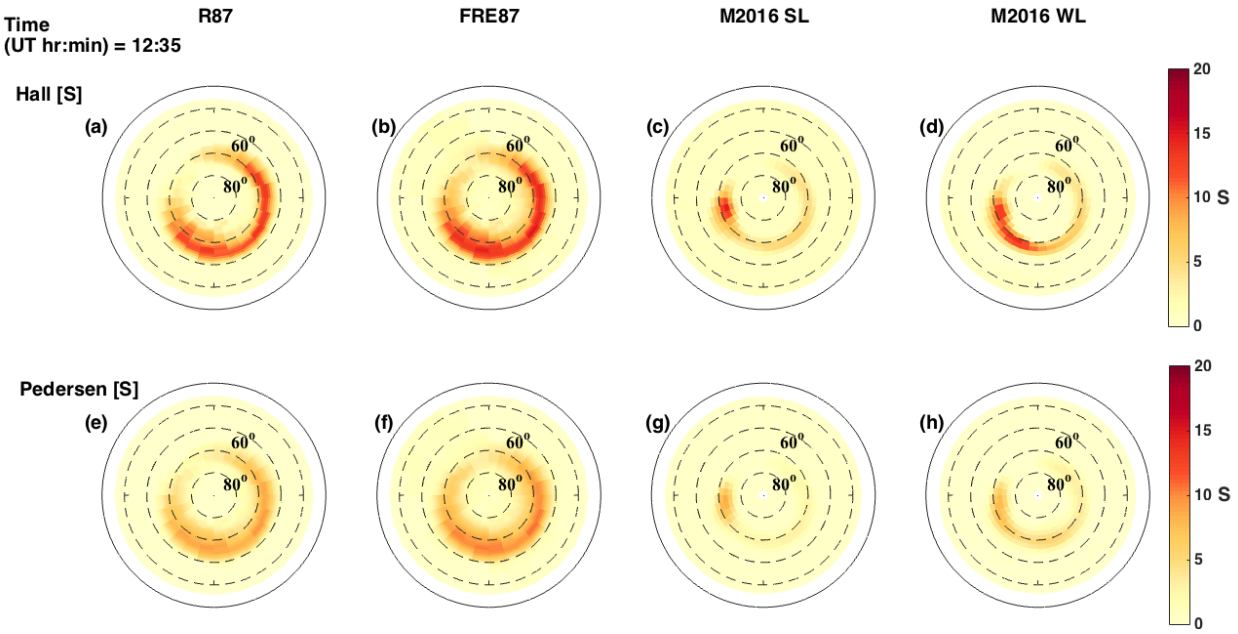

Figure 7.4: Complete high-latitude Hall and Pedersen conductance maps for the northern hemisphere on November 30, 2011 at 1235 UT. The outermost dashed ring on all polar plots represents the 50° MLAT location and each ring moving inward is a 10° increment. From left to right: R87, FRE87, M2016 SL, and M2016 WL Hall conductance (a-d) and Pedersen conductance (e-f) distributions. The R87 and FRE87 maps are resolved on a 1° MLAT × 1 hr MLT grid and the M2016 maps are resolved on the AMIE grid on which the estimation is performed (2° MLAT × 0.67 hr MLT). The HPI for this time was 7, which defines the FRE87 maps used and the characteristic energies and energy fluxes used in Equations 7.14-7.15 to calculate the R87 maps. The M2016 results are shown without an assumed background distribution.

where discrete precipitation is common during active geomagnetic conditions (*Newell et al.*, 2009). Further examination of the M2016 results reveals differences owing to the choice of localization strength. The SL confines the MLT extension of the strongest conductance enhancements to the dusk MLT sector, whereas the WL shows this strong enhancement extending into the pre-midnight and midnight MLT sectors.

7.3.2 Qualitative evaluation: DMSP SSUSI and FAC distributions

Auroral images obtained from the SSUSI instruments aboard the F16-F18 DMSP satellites provide a nearly global snapshot of auroral emissions. Given the relationships between auroral emissions and ionospheric conductances (*Solomon et al.*, 1988; *Lummerzheim et al.*, 1991; *Germany et al.*, 1994, 1997; *Sotirelis et al.*, 2013) these distributions can be used for qualitative comparisons with the conductance models assessed in this chapter (*Lummerzheim et al.*, 1991; *Aksnes et al.*, 2002; *Coumans et al.*, 2004; *Zhang and Paxton*, 2008).

Figure 7.5 shows qualitative comparisons of the M2016 WL I and C2015 I models with northern hemisphere SSUSI F16-F18 135.6 nm auroral images for an interval near 1200 UT, during the main phase of the storm. The Oxygen I 135.6 nm emission line is the strongest indicator of characteristic electron energy, and is thus a reliable optical measure of electron precipitation (*Germany et al.*, 1990). This quality makes auroral images at the 135.6 nm wavelength a useful comparison tool for the conductance distributions in this chapter. Figures 7.5a and d show, respectively, the Hall and Pedersen conductances for the M2016 WL I model for 1205-1215 UT, Figures 7.5b and e show the conductances for the C2015 I model, and Figures 7.5e and f show the differences (M2016 I - C2015 I). Figure 7.5g shows the F16, F17, and F18 135.6 nm auroral emissions for the 1135-1225 UT interval bracketing the 1205-1215 UT time window of the OI conductance distributions. The agreement between the M2016 WL I distributions and the auroral emission data is striking. There is strong ionization on the duskside and pre-midnight regions, likely driven by discrete energetic electron precipitation; the corresponding conductance enhancements are well characterized by the OI results. The color scale is limited to 10 S in order to compare more clearly with the C2015 I

model, which only includes diffuse precipitation. The maximum M2016 WL I Hall conductance in this interval is 32.9 S and occurs at (68°, 20.67) (MLAT, MLT) and the maximum Pedersen conductance is 10.7 S at the same location. In contrast, the maximum C2015 Hall and Pedersen conductances are 16.75 S and 9.85 S, respectively, and both occur at (64°, 1.33). In Figures 7.5c and f the areas where the M2016 model yields larger conductances than the C2015 I model are shown in red. These figures clearly show that the M2016 WL I model captures the conductance enhancements in the dusk, pre-midnight, and morning MLT regions where the SSUSI auroral images show ionization occurred. In contrast, the C2015 I model conductances lack enhancements in these locations. Throughout the entire high-latitude northern hemisphere, the OI results demonstrate much better agreement with the SSUSI data. The M2016 SL I model results are similar, but for brevity are not discussed.

The locations and intensities of FACs, particularly the upward component, are closely related to ionospheric conductances (*Lu et al.*, 1997; *Gjerloev and Hoffman*, 2002; *Iijima*, 2000; *Coxon et al.*, 2014; *Korth et al.*, 2014; *Marsal*, 2015). Figure 7.6 shows the northern hemisphere FACs (positive downward) estimated from the assimilative mapping procedure developed in C2015 (introduced below) when the conductance distributions shown in Figures 7.5a-f are used in the electrodynamics solution. Figure 7.6 shows that the M2016 WL I conductances contribute to a stronger Region 1/Region 2 (R1/R2) current system (*Iijima and Potemra*, 1976a, 1978) than the C2015 I conductances, which is consistent with this period of heightened geomagnetic activity. We provide further discussion of these comparisons in Section 7.4.

7.3.3 Quantitative evaluation: Impact of conductances on the inversion of SuperDARN and AMPERE observations

C2015 solves the optimization problem for ionospheric electrodynamics in two distinct ways: 1) in terms of electrostatic potential, following *Richmond et al.* (1988) and *Matsuo et al.* (2005); or 2) in terms of the magnetic potential (*Matsuo et al.*, 2015). The electrodynamics are represented as expansions of basis functions. Figure 7.7, reproduced from C2015, diagrams these two solution paths

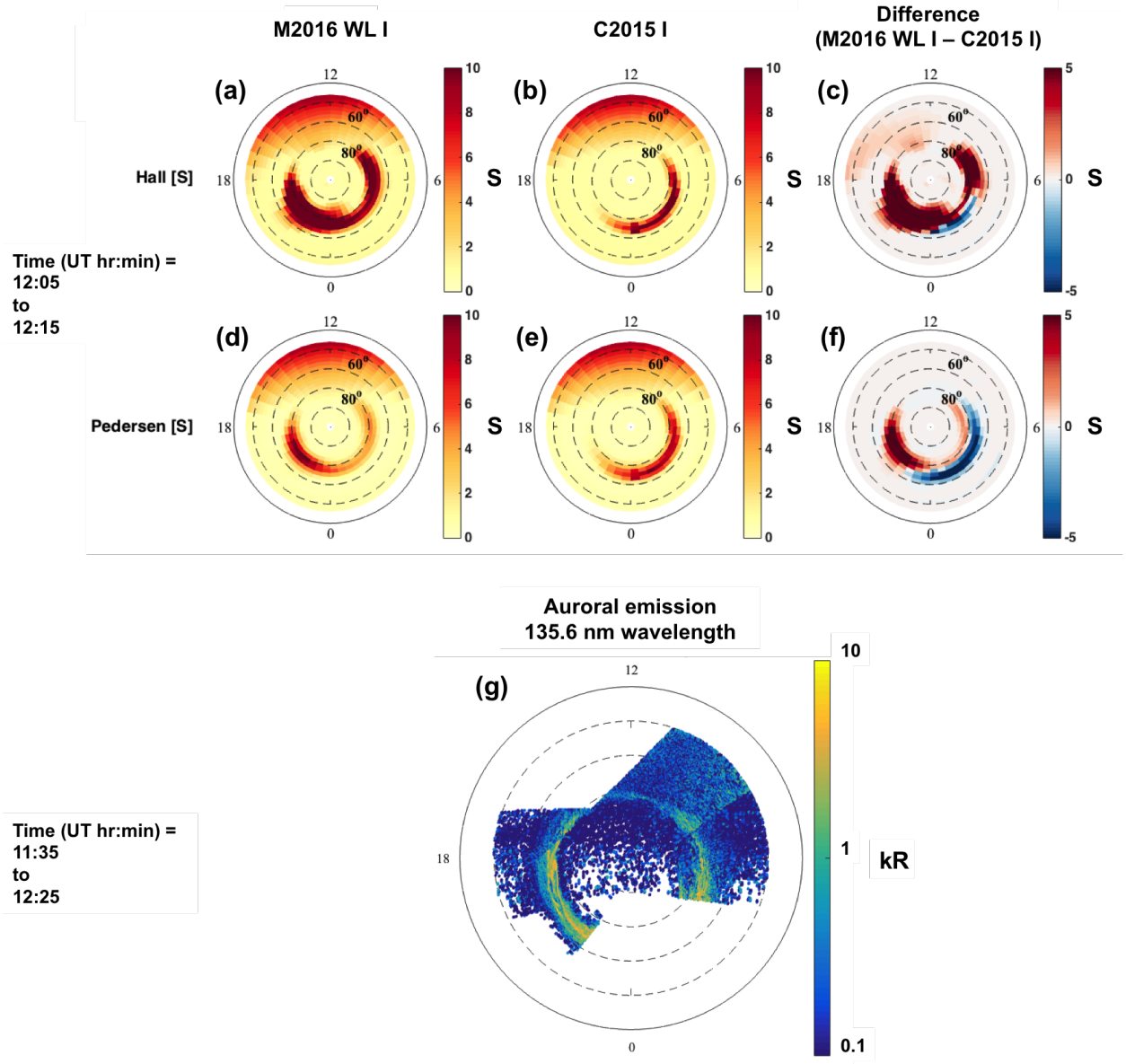

Figure 7.5: Complete high-latitude Hall and Pedersen conductance maps for the northern hemisphere on November 30, 2011 for 1205-1215 UT from the (a,d) M2016 WL I model, (b,e) C2015 I model, (e,f) difference (M2016 I - C2015 I). (g) DMSP F16-F18 SSUSI 135.6 nm auroral emission data from the encapsulating time period 1135-1225 UT.

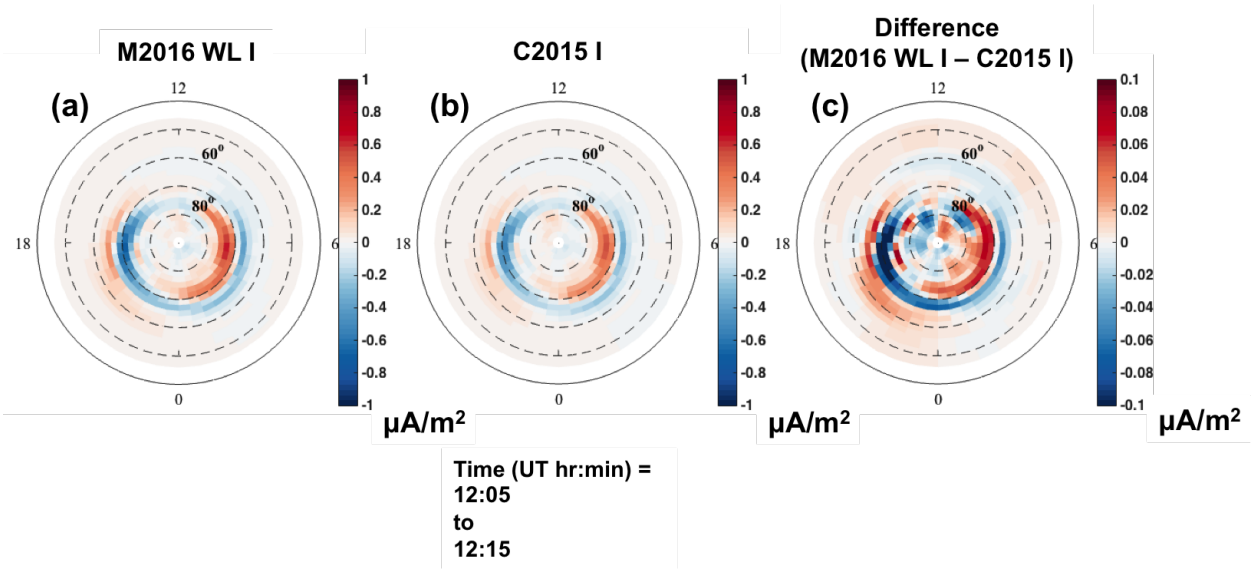

Figure 7.6: Field-aligned current (FAC) distributions (positive downward) estimated using the assimilative mapping procedure developed in C2015 and with the conductance models shown in Figure 7.5. FAC distributions using the: (a) M2016 WL I model (shown in Figures 7.5a and d); (b) C2015 I model (shown in Figures 7.5b and e. (c) Difference in the FAC distributions (FAC_{M2016} - FAC_{C2015})

(Figure 7.7a shows the electrostatic potential solution and Figure 7.7b shows the magnetic potential solution), including the primary variables involved, and indicates where knowledge of conductance is required. At any point in the diagram where an arrow contains the Σ symbol, knowledge of the conductance is required to relate those two parameters. The equations to calculate these solutions are provided in Appendix E. Assuming the conductance distributions are known, Equations E.1-E.7 represent linear relationships among the ionospheric electrodynamic parameters.

These two paths provide independent means to evaluate the conductance models of this chapter. C2015 developed a procedure to evaluate conductance models via a quantitative metric based on the comparison of AMPERE and SuperDARN data. We use their evaluation procedure. In the first case, the OI equations are solved in terms of electrostatic potential using SuperDARN data, and the estimated electrostatic potential distributions are combined with knowledge of the conductances to predict magnetic perturbation values at AMPERE locations. These predictions are compared with actual AMPERE observations and the median absolute deviation (MAD, $median$ (|predicted values − observations|)) statistics are computed. This path is labeled $V \rightarrow \delta B$. The second case reverses the process: AMPERE data are used to solve the OI equations in terms of magnetic potential and the estimation is combined with the conductance distributions to predict SuperDARN observations. This path is labeled $\delta B \rightarrow V$. Discrepancies between the observations and predictions result, to a large extent, from inaccuracies in the conductance models.

Table 7.4 provides a summary of the test results for November 30 alone (top row) as well as the entire week from November 26 through December 2 (bottom row). All conductance model results contain the same solar-produced conductance given by Equations 7.12-7.13. The background nightside values for each model are provided in the table for convenient reference.

Comparing cases with realistic background conductances (C2015 I, M2016 SL I, M2016 WL I, and M2016 WL I + SSUSI augment) we find that the M2016 models reduce the SuperDARN observation-prediction discrepancy by over 25% over the week, and by more than 40% on November 30, a period of relatively high geomagnetic activity. Further, the SSUSI covariance augmentation provides additional reduction in the discrepancy, demonstrating that an improved background

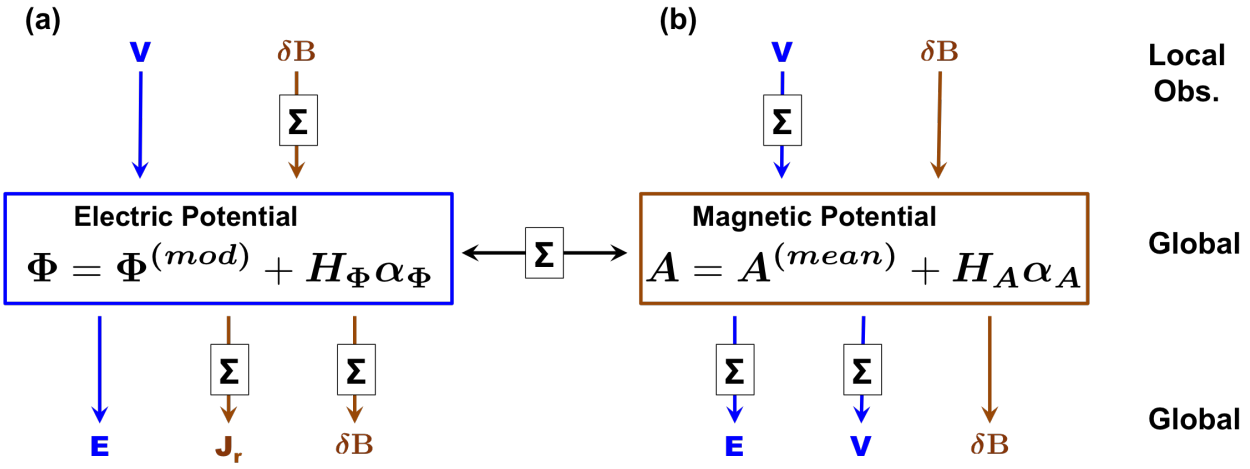

Figure 7.7: Schematic of ionospheric electrodynamic relationships and variables (reproduced from C2015), laid out to detail the OI procedure designed by C2015. Variables at the top represent local observations, from which a global (a) electric or (b) magnetic potential can be estimated as an expansion of basis functions, H. With global potentials, electrodynamic variables of interest, bottom of the schematic, can be calculated. Locations where a Σ lies over an arrow indicates that knowledge of the conductance is required to relate the variables on either side of the arrow.

Table 7.4: Conductance model evaluation[1]

	Median absolute deviations [m/s or nT]						
	Conductance Model (nightside values)	C2015 I $\Sigma_H > 0.8$; $\Sigma_P > 0.4$	C2015 II $\Sigma_{H,P} > 4.0$	M2016 SL I $\Sigma_H > 0.8$; $\Sigma_P > 0.4$	M2016 WL I $\Sigma_H > 0.8$; $\Sigma_P > 0.4$	M2016 WL II $\Sigma_{H,P} > 4.0$	M2016 WL I + SSUSI augment $\Sigma_H > 0.8$; $\Sigma_P > 0.4$
Nov. 30	δB → V	684.20	149.77	392.51	382.69	145.69	359.14
	V→ δB	36.88	39.03	37.03	37.03	38.98	37.84
Nov. 26-Dec. 2	δB → V	534.31	146.65	368.55	362.42	145.92	358.22
	V→ δB	33.91	34.67	34.05	33.95	35.54	33.98

[1] Median absolute deviation values are given for using SuperDARN to predict AMPERE (V→ δB) in nT and vice versa in m/s, with estimated uncertainty values of ∼ 0.2 nT and ∼ 1 m/s, respectively (*Cousins et al.*, 2015a).

model error covariance can enhance the OI estimation. On the other hand, the observation-prediction comparison results for the AMPERE data were relatively insensitive to the conductance model applied, as discussed further in Section 7.4.

Cases with the increased background conductances (C2015 II and M2016 WL II) reveal slightly lower MADs using the OI results, but the discrepancies are comparable. This suggests that such background levels essentially bring SuperDARN and AMPERE data into agreement by altering the overall conductance magnitude, rather than realistically describing the conductance spatial distribution.

Temporal and spatial evaluation metrics are also important. Figures 7.8 and 7.9 detail the observation-prediction comparisons for the northern hemisphere when MADs are binned by time and spatial location, respectively. Figures 7.8a-c show the Borovsky coupling function (BCF) (*Borovsky*, 2013) (black trace, left y-axis) and AE index (green trace, right y-axis), $V \rightarrow \delta B$ MADs, and $\delta B \rightarrow V$ MADs as a function of time, respectively, from November 26 through December 2, 2011. Figures 7.8e-f show the same traces magnified for November 30. The BCF is provided as a proxy for the amount of coupling that occurs between the solar wind and the magnetosphere at a given time (i.e. the amount of energy entering the system), and the AE index is provided as a similarly reliable proxy for the level of auroral activity. The red traces represent the observed-predicted differences when the C2015 I model was applied, while the blue traces show the differences using the M2016 WL I model. Both models contain realistic background conductance levels. The observation-prediction MADs using SuperDARN to predict AMPERE, shown in Figures 7.8b and e, are not heavily dependent on the conductance model. However, Figures 7.8c and f clearly show the reduced MADs obtained by using the M2016 WL I conductances for predicting the SuperDARN velocity from AMPERE δB throughout the interval. Additionally, when geomagnetic indices have large values, the benefit is even greater. Thus, the M2016 conductances bring SuperDARN and AMPERE observations into closer agreement, especially during geomagnetically active conditions.

Figure 7.9 similarly details the observation-prediction MADs, binned according to spatial location in the northern hemisphere, resulting from the OI analyses using AMPERE to predict

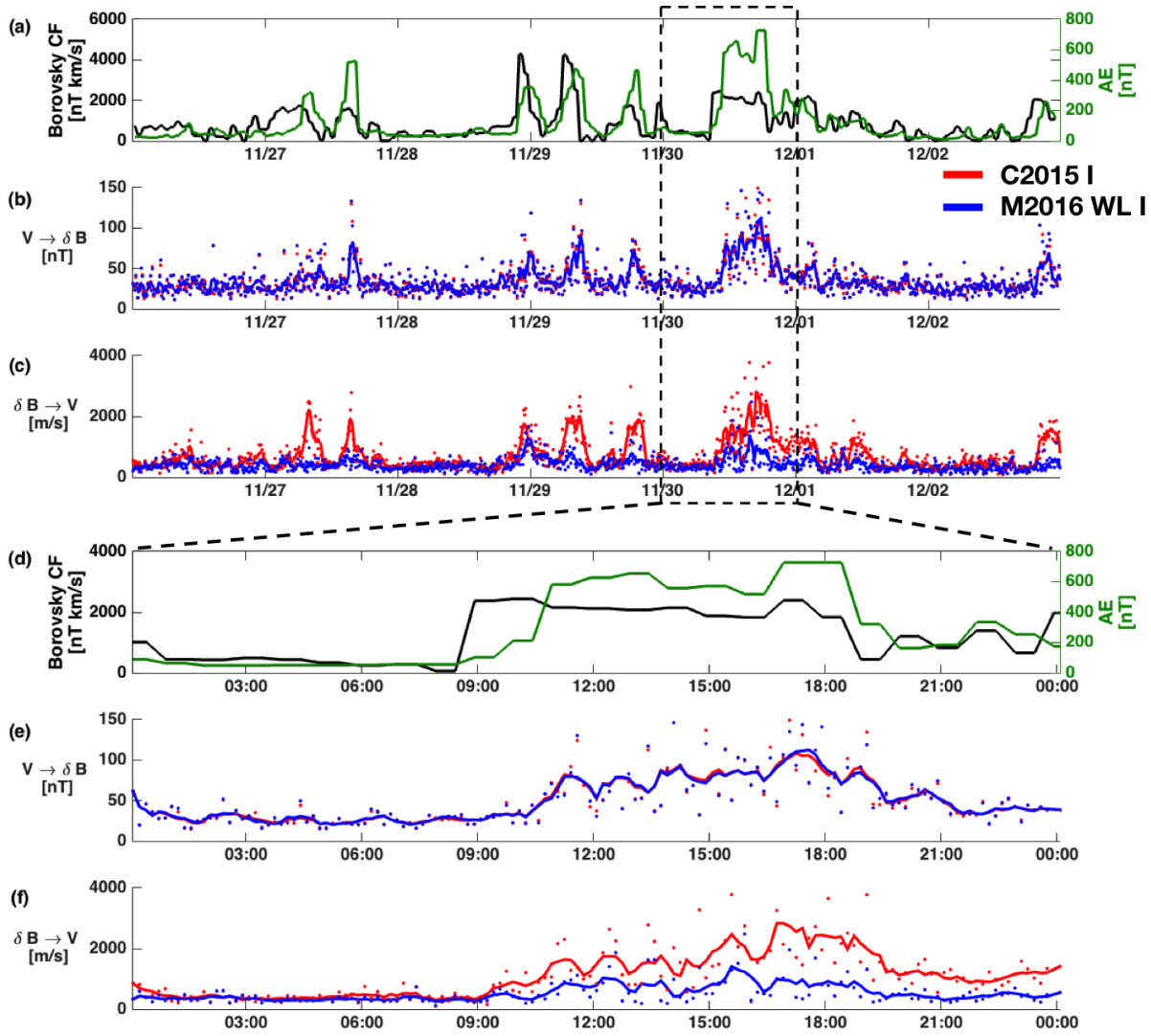

Figure 7.8: Temporal dependence of observation-prediction MADs using (b) SuperDARN to predict AMPERE ($V \rightarrow \delta B$) or (c) AMPERE to predict SuperDARN ($\delta B \rightarrow V$) over the November 26-December 2, 2011 analysis time period. (a) The Borovsky coupling function (black trace, left y-axis) and AE index (green trace, right y-axis) over the same period. (d-e) The same parameters magnified for November 30, 2011. MADs have been binned according to time (i.e. a single MAD value was calculated from all spatial locations at a given time).

SuperDARN ($\delta B \rightarrow V$). The $\delta B \rightarrow V$ cases are shown because of the sensitivity of the result to the conductance model as shown in Figure 7.8. The observation-prediction MADs for the M2016 WL I and C2015 I conductance models are shown in the top and middle rows, respectively, and the difference between these distributions ($M2016_{MADs}$ - $C2015_{MADs}$) are shown in the bottom row. The bottom row reflects the difference in the distributions after binning. Here, blue indicates the M2016 conductances yielded smaller observation-prediction MADs than the C2015 model (i.e. better predicted the observations). Because we found that the M2016 conductance models provide greater benefit during active conditions, we also organize these results according to the AE index (Figure 7.2c). The columns of Figure 7.9, therefore, are organized in quartile increments of the AE index reported during the week with the left-most column showing the results for the MADs calculated when AE is between the 1st and 25th percentiles, and the right-most column showing that when AE is between the 76th and 99th percentiles. Nearly 500,000 observation-prediction data points were used to compute these distributions. The values shown in blue at the bottom left of each polar plot give the average of all spatially-binned MADs in the high-latitude region. Blue areas show the prediction improvement from using the M2016 conductances compared with the C2015 conductances as the AE index increases. Though the average MADs for both models increases with AE, the M2016 trend is considerably smaller (better) than the C2015 trend. Therefore, while the C2015 model causes increasingly larger errors as activity increases, the M2016 model error level holds steady. Even during quiet times, the average MADs indicate that the M2016 model better predicts the observations.

7.4 Discussion

Statistical conductance models are no longer sufficient to be used in data assimilative procedures for specifying ionospheric electrodynamics. To evaluate the ability of our OI conductances to support assimilative ionospheric electrodynamics analyses we performed an extensive comparison against statistical models and the models and methodologies used in C2015.

In Section 7.3 we introduced a new optimal interpolation technique to produce complete

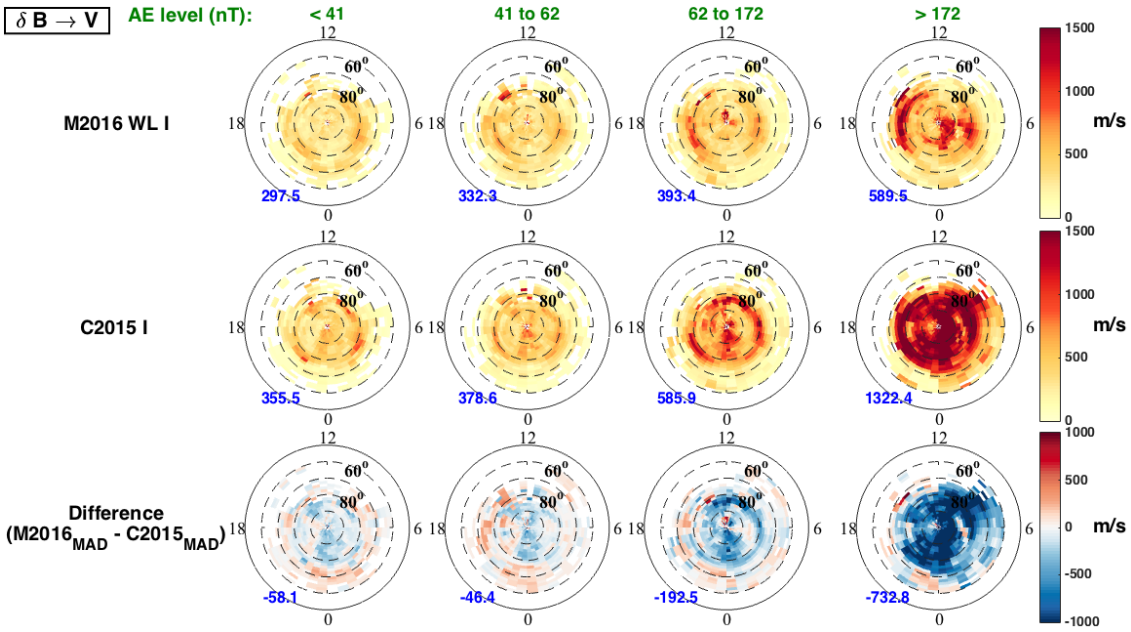

Figure 7.9: Spatial distributions of observation-prediction MADs using AMPERE to predict SuperDARN ($\delta B \rightarrow V$) over the November 26-December 2, 2011 analysis time period. MADs from the entire period have been binned according to spatial location using the AMIE grid (2° MLAT × 0.67 hr MLT) and then further by quartiles of the AE index (i.e. the left-most column are MADs distributions when the AE index was below the 25th percentile level and the right-most column are MADs distributions when AE was above the 75th percentile level.) The top row shows the distributions with the M2016 WL I conductance model applied, the middle row shows the distributions with the C2015 I model applied, and the bottom row shows the difference (M2016 - C2015). The blue values to the bottom left of each plot are the average MADs computed for the entire high-latitude distribution. The outermost dashed ring on all polar plots represents the 50° MLAT location and each ring moving inward is a 10° increment.

high-latitude conductance distributions. Figure 7.3 suggests that the peak conductances observed along a DMSP satellite trajectory are better specified by the OI model conductances. Further, the observation-prediction RMS values computed for the entire pass showed that the OI conductances better predicted the observed conductances as a whole. Such peak conductances are generally associated with more energetic particle precipitation that depart significantly from simple prescribed forms, such as a Maxwellian (*Newell et al.*, 1996d; *Hardy et al.*, 2008; *McIntosh and Anderson*, 2015). The conductance pseudo-observations used to produce the background model error covariance and the OI results in this chapter are free of any assumption about the spectral form of the incident electron precipitation such at those in FRE87 and R87; one reason for the improved specification.

Table 7.3 supports that the comparison in Figure 7.3 is representative of the more general picture, with reduced observation-prediction mean, median, standard deviation, and RMS values calculated over the entire week-long analysis period. In terms of the mean differences during this period the OI models predict the observations roughly 400% more accurately than the R87 model, and provide nearly an order of magnitude improvement over the FRE87 model. On average, the R87 and FRE87 models under- and over-predict the Hall conductance, respectively. These statistics corroborate the conclusions drawn from Figure 7.3 and indicate that this case is representative of the general situation.

The RMS values in Table 7.3 represent a more modest improvement, likely associated with the low percentage of overall conductance enhancements caused by discrete precipitation. Most of the conductance enhancement is due to diffuse precipitation that generally accounts for ∼75% of the overall precipitation into the ionosphere (*Winningham et al.*, 1975), and which is reasonably described by the FRE87 and R87 models. The spatial extent of the conductance enhancements also likely contributes to these results since diffuse precipitation is typically much more broadly distributed over the high-latitudes while discrete precipitation tends to be more confined (*Newell et al.*, 2009; *McIntosh and Anderson*, 2015). For these reasons, better characterization of the discrete precipitation will only provide a modest improvement in overall statistics. The largest percentage of

the improvements in Table 7.3 can be explained by the difference between statistical and OI treatments of the diffuse quasi-permanent conductances. The FRE87 model represents a statistically averaged model of the ionospheric conductances and is thus only capable of a "climatological" characterization of the polar ionosphere (*Ahn et al.*, 1998). Because we use the characteristic energy and energy flux data from the FRE87 model to produce complete distributions of the R87 model using Equations 7.14-7.15, the R87 model inherits the statistical nature of the FRE87 model. The extent to which OI models resolve conductance features that are smoothed in the statistical conductance models is likely the predominant contributor to the RMS improvement in Table 7.3.

As shown in Figure 7.5, the M2016 conductances yield much closer qualitative agreement with SSUSI auroral imagery data obtained during heightened geomagnetic activity than do the C2015 conductances. The agreement is pronounced in two regions: 1) the dusk-to-midnight sector and 2) the post-dawn MLT sector. Both sectors are locations of accelerated electron precipitation. In the dusk-to-midnight sector the accelerated component of precipitation is dominant during active conditions (see Figures 3 and 4 from *Newell et al.* (2009)). The C2015 I model misses the associated conductance enhancement completely. In the post-dawn sector the accelerated precipitation is accompanied by enhanced diffuse precipitation extending beyond dawn as well. Because the ionization in the post-dawn sector is likely due to a combination of discrete and diffuse precipitation, the C2015 I conductance only partially captures the enhancement whereas the M2016 WL I conductances appear to describe a larger extent of the enhancement (see Figures 7.5c and f in comparison with Figure 7.5g).

Figure 7.6 examined the field-aligned current patterns obtained using each of the conductance distributions shown in Figure 7.5 and revealed differences in the intensities of the large-scale R1/R2 currents and mesoscale differences poleward of the large-scale current systems. Examining Figure 7.6c, the upward component of the R1 current system on the duskside, shown by the blue crescent signature near 70° MLAT extending a few hours MLT on either side of dusk, is more than -0.1 μ A/m^2 more intense (more current directed upward) using the M2016 WL I conductances. Both maximum and minimum FAC differences occur at 18.67 MLT. The maximum positive difference is

0.87 μ A/m^2 at 74° MLAT and the maximum negative difference is -1.51 μ A/m^2 at 68° MLAT, revealing the largest difference in upward FACs occurs in the large-scale R1 currents. The enhanced intensity in the upward R1 currents extends through the midnight MLT meridian, consistent with the large-scale R1 current under large positive B_y conditions (*He et al.*, 2012). There are also mesoscale differences in the FAC distributions throughout the northern hemisphere at MLATs poleward of the R1/R2 currents as demonstrated by Figure 7.6c.

Differences in the large-scale currents are expected since the M2016 model includes discrete precipitation, whereas the C2015 model does not. Figure 7.6c verifies that the effect of these conductance differences on the FACs can be significant during geomagnetic activity. Such significant FAC differences would correspond to differences in the upper atmospheric behavior and magnetospheric composition and dynamics (*Iijima*, 2000). We also found that the upward FACs obtained using the M2016 conductances associated with the R1 system were more intense throughout the nightside, which is indicative of positive B_y IMF conditions (*He et al.*, 2012) and consistent with the fact that ionospheric conductances exert large influence over nightside upward FACs (*Nakano et al.*, 2002). In a broader sense, the FACs obtained from our new technique will likely provide a more accurate picture of magnetospheric dynamics.

The mesoscale (taken here to mean $\sim$ 10s - 100s km (*Fujiwara et al.*, 2007)) differences in MLATs poleward of the large-scale R1/R2 currents may also have significance due to relatively recent findings regarding the significance of polar cap energy deposition (*Huang et al.*, 2015). For example, *Deng et al.* (2015) identified a complex, but undetermined, relationship between Poynting flux and soft particle precipitation in the polar regions, that are not sufficiently described by current ionosphere/thermosphere models. Mesoscale polar cap FACs could be associated with this polar cap energy deposition (*Thayer et al.*, 1995; *Maeda et al.*, 2002; *Vogt*, 2002; *Streltsov and Lotko*, 2004; *Maeda et al.*, 2005; *Fujiwara et al.*, 2007; *Hasunuma et al.*, 2008; *Huang et al.*, 2016). Note that the analysis here does not resolve to 10's of km.

The M2016 conductance models were also evaluated quantitatively through the application to the assimilative and inverse procedure developed by *Cousins et al.* (2015a). Table 7.4 demonstrates

that they can reduce differences between AMPERE and SuperDARN data without artificially increasing the background conductances. Comparison of C2015 I, M2016 SL I, and M2016 WL I clearly shows that, when a realistic background conductance is applied, the M2016 models help AMPERE data to predict SuperDARN observations much more effectively, providing a nearly 50% improvement in the observation-prediction MADs. Additionally, the SSUSI covariance augmentation shows evidence of providing even further improvement. When the conductance background is artificially increased with background II, the table shows that the observation-prediction discrepancies are reduced no matter which conductance model is applied. This may be due to the fact that artificial increases reduce conductance gradients, likely making the average conductances closer to the true average, which would bring the observations into closer agreement in terms of magnitude, though not necessarily in specific features. *Sofko et al.* (1995) demonstrated that when conductance gradients are small FACs are expected to be more closely related to the vorticity of plasma convection. In the absence of conductance gradients, measurements related to FAC (AMPERE) will give more useful information about convection, and measurements related to convection (SuperDARN) will do the same for FACs, though not in a physically-meaningful manner. Alternatively, the artificial enhancement may compensate for inaccurate auroral oval conductance values in the C2015 I model. The M2016 and C2015 II models both increase conductances in the evening auroral oval with respect to C2015 I. Therefore, inaccurate auroral oval conductances may also cause C2015 I to perform poorly. Ultimately, the disagreements between AMPERE and SuperDARN are likely due to some combination of these effects, but we cannot identify the primary cause from our results. Regardless of the source of the discrepancies it is essential to specify conductances to correctly locate FACs with respect to plasma convection, and the approach of artificially enhancing the conductances will degrade the accuracy of the resultant electrodynamics analyses even if it does promote overall agreement between AMPERE and SuperDARN. In order to prevent such degradation, the conductance spatial distribution must be accurately specified by the conductance model, which is one of the key outstanding issues identified by C2015 and is the outcome of the present work. A comparison of the models with realistic backgrounds shows that the present OI approach

improves interdata set agreement. Our results suggest additional improvements are possible with further refinement of these methods or the inclusion of additional data, as we demonstrated in one instance by improving the background covariance with SSUSI data (conductance model M2016 WL I + SSUSI augment).

Despite the benefit recorded when using AMPERE to predict SuperDARN as summarized in Table 7.4, the conductance model seems to have little or no effect on the results when using SuperDARN to predict AMPERE. There are several plausible explanations. First, magnetic perturbations generated by high-latitude FACs are typically less than $\sim 1\%$ of the total magnetic field (e.g. *Knipp et al.* (2014)). Because of this and additional factors, including magnetometer sensitivity and attitude control of the IRIDIUM satellites (*Knipp et al.*, 2014), the AMPERE signal to noise ratio may be low, even with careful baseline removal and data processing (*Korth et al.*, 2010). In such a case the SuperDARN data will only be able to explain a percentage of the total signal, despite the application of an appropriate conductance model, with the unexplained portion being the noise. If the conductance models allow the estimation to approach this noise level, and the level is consistent, so, too, will be the $V \rightarrow \delta B$ observation-prediction results. An alternative explanation is that the SuperDARN data contain a magnitude bias that blurs the differences attributable to the conductance model in the $V \rightarrow \delta B$ results. Such issues with the SuperDARN data have been suggested before (*Drayton et al.*, 2005; *Gillies et al.*, 2009, 2011). Determining the actual cause(s) is beyond the scope of this chapter.

There may be additional factors contributing to discrepancies between the SuperDARN and AMPERE results. The reduction in discrepancies shown in Table 7.4 may be due in part to the applied conductance models compensating for measurement biases in each data set differently (*Cousins et al.*, 2015a). Similarly, neutral wind effects, ignored in these analyses, could contribute to the differences. However, given the additional support in Section 7.3, we believe the majority of the discrepancy reduction is due to improved estimation of the electrodynamics fields using the M2016 conductance models. This result suggests that in the future SuperDARN plasma drift observations can be used more effectively for magnetic potential solutions (path from V to A in Figure

7.7b) and AMPERE magnetic perturbation observations can be used more effectively for electric potential solutions (path from δB to Φ in Figure 7.7a). More importantly, the improved conductance distributions allow diverse observations to be used together more effectively for ionospheric electrodynamics specification. Facilitating the use of diverse observations together is extremely important given the emphasis on data assimilation for understanding the entire geospace environment (*Zhu et al.*, 2012; *Schunk et al.*, 2014).

Consistent with the finding that the M2016 conductances better specify enhancements due to discrete precipitation than C2015 I conductances, Figures 7.8 and 7.9 demonstrate the improvement is even more pronounced as geomagnetic activity increases. In terms of facilitating the prediction of SuperDARN plasma drift observations by AMPERE data the M2016 WL I model yielded a nearly 750 m/s improvement over the entire northern hemisphere when the AE index was in the top quartile during the week long study period. Further, it was not uncommon for the improvement to be well in excess of 1 km/s at times. Maintaining a level of accuracy invariant of activity level is an important development for ionospheric specification. Figure 7.10 details the M2016 WL I model result is significantly less dependent on activity level than the C2015 I model result.

To visualize the improvement yielded by the M2016 conductance model as a function of geomagnetic activity we provide Figure 7.10 which shows the average MADs of the spatially-binned data (equivalent to the blue values in Figure 7.9) as a function of deciles of the AE index and corresponding linear fits for the C2015 I model (in red) and the M2016 WL I model (in blue). A comparison of the two fits reveal that the observation-prediction MAD growth rate as a function of AE when using the C2015 I model is nearly five times that when using the M2016 WL I model. Moreover, the MAD growth rate is relatively flat when using the M2016 WL I model, indicating that accuracy is not significantly affected by geomagnetic activity.

Accurately characterizing the location, in addition to the magnitude, of conductance enhancement due to discrete precipitation is also critical to improving observation predictions. C2015 evaluated conductance models that included the discrete precipitation from OVATION Prime and found that, because the model misplaces the discrete precipitation, these conductance fields produced

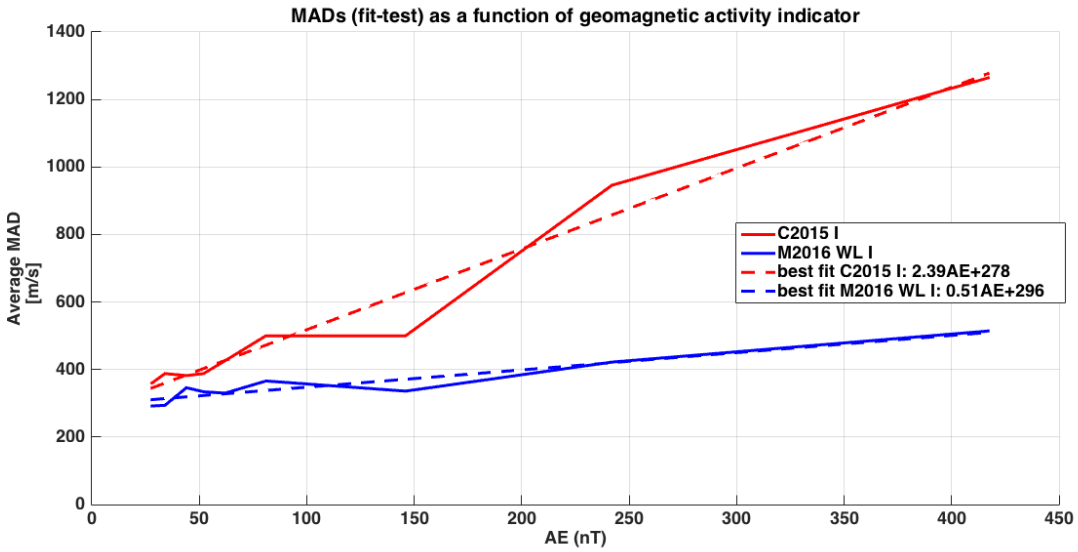

Figure 7.10: Spatially-binned average northern hemisphere MADs as a function of deciles of the AE index and corresponding linear fits when the C2015 I conductance model is applied (in red) and when the M2016 WL I model is applied (in blue).

less accurate observation predictions than when this type of precipitation was excluded altogether (*Cousins et al.*, 2015a). Because the OI conductance fields better predict the observations in the presence of discrete precipitation, we conclude that they more accurately characterize both the magnitude and location of discrete precipitation-induced enhancements.

7.4.1 Considerations for future work

There are a number of ways the work in this chapter can be extended in the future. In terms of pseudo-conductance calculations, a more sophisticated background neutral atmosphere could be used, though the benefit of such an improvement is believed to be relatively small (*Brekke et al.*, 1974). More significantly, additional data could be incorporated, including GPS-satellite occultation electron density profiles which provide much improved coverage in both space and time (*Yue et al.*, 2014).

Data quality, quality control, and the estimation of more robust uncertainty information for each data set at the level required for assimilation are extremely important for the procedure applied here. Further investigations into the DMSP, AMPERE, and SuperDARN data are continually improving the products provided to the community from each of these missions. Future work will benefit from these efforts.

Additional means of specifying conductances to agree with discrete precipitation have been suggested based on FACs (*Marklund et al.*, 1988; *Marsal et al.*, 2012; *Korth et al.*, 2014; *Marsal*, 2015). Incorporating such approaches will be an important direction for future study.

Finally, improvement of the background conductance model used for the OI may be an important future consideration. *Sotirelis and Newell* (2000) showed that using the median of their precipitation model electron energy spectra was more representative of commonly observed DMSP fluxes than the mean, and a similar dependence of model conductance results in this chapter may be found if the median, rather than mean, distributions found during the estimation of the conductance EOFs are used. We also suggest that creating a background model that varies with geomagnetic activity indicators, primarily Kp, auroral intensity, and dynamic auroral boundaries could improve

the OI estimation.

7.5 Conclusions

Our new optimal interpolation technique to estimate complete high-latitude ionospheric Hall and Pedersen conductances is capable of more accurately specifying conductances due to auroral electron precipitation. The improvement is especially pronounced for discrete precipitation and particularly during geomagnetically active periods. The improved capability eliminates an assumption on the incident electron energy spectra in calculating conductances and uses optimal interpolation rather than statistical averaging to estimate complete fields. We showed that conductance fields created in this manner, compared with the C2015 I conductance model, are better able to reduce discrepancies between SuperDARN and AMPERE in AMIE, resolving one of the outstanding issues with electrodynamics analyses identified by C2015 and addressing similar issues due to conductance limitations in previous AMIE analyses (*Lu et al.*, 2001; *Raeder et al.*, 2001; *Crowley and Hackert*, 2001; *Cosgrove et al.*, 2009). We compared conductance models with realistic background values (C2015 I, M2016 SL I, M2016 WL I, and M2016 WL I + SSUSI augment) and showed that the M2016 models reduced the discrepancy between the SuperDARN plasma drift observations and their prediction by AMPERE magnetic field data by over 25% over the November 26 through December 2, 2011 period, and over 40% for November 30, a period of relatively high activity, in comparison with C2015 I. Moreover, we found that during periods with enhanced geomagnetic activity the benefit of the M2016 models in terms of observation-prediction median absolute deviation was even greater. Comparing M2016 WL I with C2015 I, we improved SuperDARN plasma drift observation predictions by nearly 750 m/s for the northern hemisphere during the highest activity of the week-long period. In some cases the improvement was in excess of 1 km/s. The improved predictions are a result of more accurately specifying the location and magnitude of conductance enhancements due to discrete precipitation. These improvements suggest that the OI conductance fields allow diverse data to be used consistently for ionospheric data assimilative analyses. This is an important development given that the ionosphere is under-observed and no single observing

system can sample its state completely, such that merging information from various observing systems is necessary for better ionospheric electrodynamics specification. Our conductance modeling approach can be used beyond OI for SuperDARN and AMPERE, which was highlighted in this chapter, being applicable in stand-alone applications to study ionospheric conductances and in ionosphere-thermosphere general circulation models.

Chapter 8

Three-dimensional Conductivities

8.1 Introduction

Technological improvements and expansion of observational systems are enabling three-dimensional ionospheric (3-D) volumetric analyses. *Semeter et al.* (2009) presented the first results from a fully 3-D volumetric imaging of the ionosphere from the Poker Flat Incoherent Scatter Radar (PFISR). *Lynch et al.* (2015) studied the 3-D structure and dynamics of field-aligned currents in auroral arcs using data collected from the Magnetosphere-Ionosphere Coupling in the Alfvén Resonator (MICA) sounding rocket together with larger-scale, contextual measurements from several ground-based instruments. With increasing computational capability and more capable parameterizations, global models are able to specify the 3-D ionosphere at increasingly finer resolutions. Diverse data from the growing geospace observational system can be assimilated to address missing physics and representativeness error in the global models with increased effectiveness. *Amm et al.* (2008) identified global height profiles of ionospheric conductivities as the critical information needed to support auroral ionospheric electrodynamics analyses and data assimilation. We have shown in this dissertation that the ionospheric conductivity is the key piece to accurately bring diverse data from the growing geospace observational system together to study the ionospheric electrodynamics (*Cousins et al.*, 2015a; *McGranaghan et al.*, 2016, submitted and revised). Understanding the conductivity in 3-D is essential.

Figure 8.1 shows typical parallel (black trace), Pedersen (blue trace), and Hall (red trace) auroral region conductivity profiles (70°N and 0°E geographic coordinates; 68.6°N and 89.9°E in

AACGM coordinates at 120 km) on March 21, 2010 and 1200 UT for low solar activity (10.7 cm radio flux of 84.1 $\times$ 10^{-22} W m$-$2 Hz^{-1}) and low geomagnetic activity (A_p= 2 nT). Since conductivity profiles demonstrate significant variability and complicated behavior due to complex MI interactions 'typical' here means that climatological background features of conductivity profiles are represented. This figure illustrates the altitudinal variation that is characteristic of the Pedersen and Hall conductivities and also serves as a point of reference for later discussion.

Due to lack of observation, historically it has been impractical, if not impossible, to acquire the 3-D structures of the conductivity globally (see (*Lilensten et al.*, 1997, and references therein)). Here in this chapter we present the first characterization of the primary modes of variability of E Region, height-dependent conductivities over the polar region. These modes are in the form of Empirical Orthogonal Functions (EOFs) as developed in *McGranaghan et al.* (2015b) and Chapter 5 and applied here to the altitude range of 100-150 km.

The first three modes together account for >50% of the total ionospheric conductivity variability at altitudes throughout the E Region ionosphere (∼80-150 km). The first mode captures variability of the quasi-permanent auroral oval primarily driven by diffuse precipitation. The second mode is associated with the spatially delineated response of the conductivities to changes in the interplanetary magnetic field (IMF) B_Z component, revealing features with signs that change in tandem (i.e. as one increases the other decreases) depending on the sign of B_Z. The third mode of variability captures the effects of Alfvénic Poynting flux (*Thayer and Semeter*, 2004; *Chaston et al.*, 2007; *Newell et al.*, 2009) on the conductivities. Within this mode we find two distinctive features, and we label these 'first-order' and 'second-order' effects, according to their separate intensity variations. The first-order effect occurs in the premidnight LT sector while the second-order effect occurs in dayside locations flanking noon LT. Finally, we find that the distribution of the power among the EOFs are generally explained by the relative contribution of the primary electron precipitation types to the global electron energy precipitation budget as identified by *Newell et al.* (2009).

Comparing the primary modes presented herein with those for the height-integrated conduc-

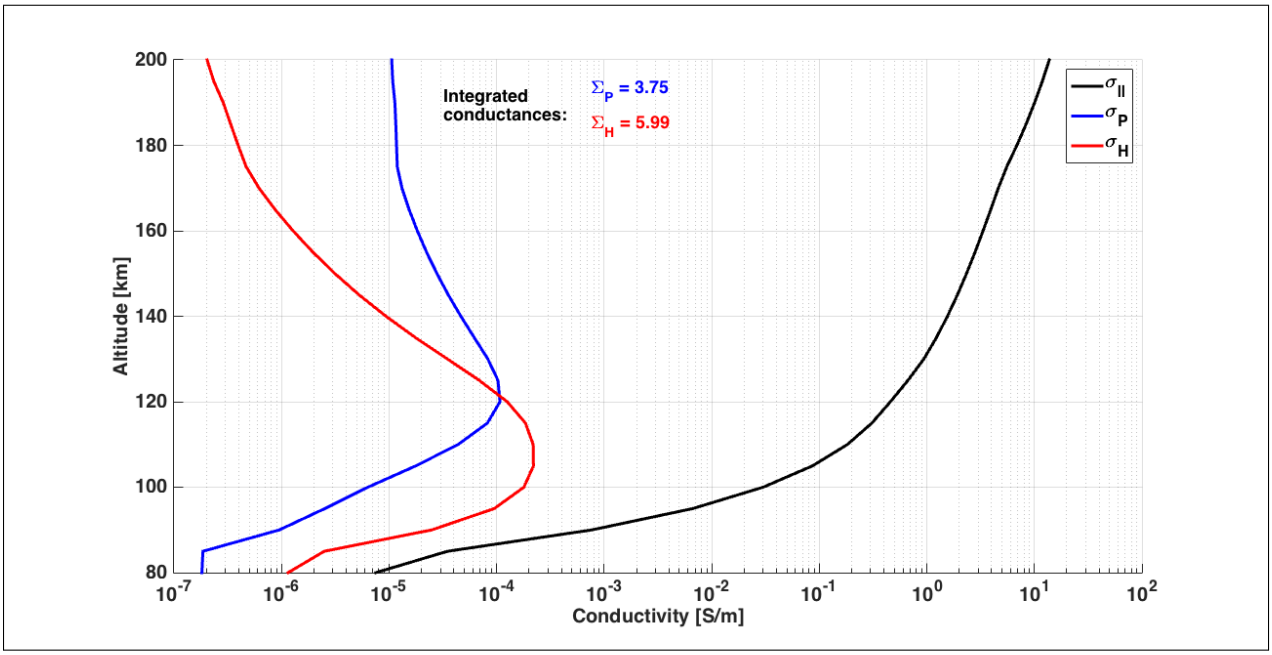

Figure 8.1: Conductivity profiles at 70°N and 0°E geographic coordinates (68.6°N and 89.9°E in altitude adjusted corrected geomagnetic coordinates (AACGM) at 120 km) on March 21, 2010 and 1200 UT for low solar activity (10.7 cm radio flux = 84.1 $\times$ 10^{-22} W m$-$2 Hz^{-1}) and low geomagnetic activity (A_p = 2 nT). Parallel, Pedersen, and Hall conductivities in S/m are shown in black, blue, and red, respectively. Profiles were obtained from the World Data Center (WDC) for geomagnetism in Kyoto, which used the International Reference Ionosphere 2012 (*Bilitza et al.*, 2014), NRLMSISE-00 neutral atmosphere model (*Picone et al.*, 2002), and collision frequencies from *Banks and Kockarts* (1973).

tances in (*McGranaghan et al.*, 2015b), we find distinct differences. This result suggests corresponding differences between height-integrated and height-dependent characterizations of the ionosphere and underscores the importance of analyzing the E Region ionosphere in 3-D.

Ultimately this improved understanding of the variability of ionospheric conductivities supports the characterization of a robust uncertainty for constraining 3-D ionospheric analyses in a manner similar to the two-dimensional (2-D) conductance EOF analysis of *McGranaghan et al.* (2015b) as applied in *McGranaghan et al.* (2016, submitted and revised).

8.2 Data and Methods

We process the same in-situ observations from the Special Sensor J version 5 (SSJ/5) instrument onboard the F6-F8 and F16-F18 Defense Meteorological Satellite Program (DMSP) satellites (*Hardy et al.*, 1984; *Kadinsky-Cade et al.*, 2004) used in Chapters 5 and 6 with the GLOW model to produce altitude profiles of the conductivities. However, the magnitudes of the height-dependent conductivities are much smaller than the height-integrated values and are more sensitive to outliers. Therefore, we use the median value over each 60-second interval, rather than the running average that was used in the height-integrated analyses, to yield 60-second resolved conductivity values. The conductivities are called pseudo-observations in this chapter as well.

We perform the EOF analysis on the pseudo-observations to determine the primary modes of variability of the ionospheric Hall and Pedersen conductivities. The EOF analysis follows that described in Chapter 5 and *McGranaghan et al.* (2015b), but is applied at distinct altitudes spanning 100 to 150 km at ten km steps. We define the conductivity variability as a residual field, which encompasses all perturbations from the mean conductivity ($\bar{\boldsymbol{\sigma}}$):

$$\begin{aligned} \boldsymbol{\sigma}'_{100\text{ km}} &= \boldsymbol{\sigma}_{100\text{ km}} - \bar{\boldsymbol{\sigma}}_{100\text{ km}} \\ &\vdots \\ \boldsymbol{\sigma}'_{150\text{ km}} &= \boldsymbol{\sigma}_{150\text{ km}} - \bar{\boldsymbol{\sigma}}_{150\text{ km}} \end{aligned} \tag{8.1}$$

We decompose the conductivity variability into dominant modes of variability represented by EOFs

(i.e. principal components):

$$\begin{aligned}
\sigma'_{100\text{ km}}(\mathbf{r},t) &= \sum_{\nu=1}^{3}\left[\alpha^{(\nu)}_{100\text{ km}}(t)\cdot\mathcal{EOF}^{(\nu)}_{100\text{ km}}(\mathbf{r})\right]+\mathbf{e}'_{100\text{ km}}(\mathbf{r},t)\\
&\vdots\\
\sigma'_{150\text{ km}}(\mathbf{r},t) &= \sum_{\nu=1}^{3}\left[\alpha^{(\nu)}_{150\text{ km}}(t)\cdot\mathcal{EOF}^{(\nu)}_{150\text{ km}}(\mathbf{r})\right]+\mathbf{e}'_{150\text{ km}}(\mathbf{r},t)
\end{aligned} \tag{8.2}$$

where $\mathbf{r}$ denotes spatial position (MLAT and MLT), $\alpha^{(\nu)}(t)$ are time-dependent coefficients of the vth EOF at a given altitude, and $\mathbf{e}'(\mathbf{r},t)$ is the residual after removing the mean and sum of weighted EOFs from $\boldsymbol{\sigma}$. Essentially, the EOFs represent 2-D time-invariant spatial modes of conductivity variability at a given altitude and $\alpha^{(\nu)}(t)$ represents the temporal variation that scales the spatial modes in time. Note that the temporal variation resolved in the analysis is one hour. Application of this process at discrete altitude levels allows us to investigate of the three-dimensional ionospheric conductivities.

The EOF estimation methodology is provided in Chapter 5 and *McGranaghan et al.* (2015b) and is not repeated here. However, in order to obtain a more robust estimate of the modes of variability, we perform this EOF analysis 25 times using 25 random subsets of the complete DMSP data set. Each random subset contains 2500 one-hour time periods, or ~20% of the total number, yielding roughly 200,000 data points per subset.

We follow the procedure outlined by *Cousins et al.* (2013a) to obtain a set of average EOFs from 25 independent sets of EOFs. There are three steps to this calculation:

(1) the covariance matrix from each set of EOFs (25 total for each altitude) is calculated from:

$$C_{lm}=\frac{1}{J-1}\sum_{j=1}^{J}\left[\sum_{\nu=1}^{N}\alpha_j^{(\nu)}\beta_l^{(\nu)}\right]\left[\sum_{\nu=1}^{N}\alpha_j^{(\nu)}\beta_m^{(\nu)}\right], \tag{8.3}$$

where β refers to the spatial coefficients as defined in Chapter 5;

(2) the 25 covariance matrices at each altitude are averaged; and

(3) the first three eigenvalues are calculated from the average covariance matrix at each altitude.

The covariance matrices in Equation 8.3 are calculated in terms of the 50 dominant principal components of the Assimilative Mapping of Ionospheric Electrodynamics (AMIE) basis functions (*Richmond and Kamide*, 1988). To average the 25 covariance matrices at each altitude we first calculate the 25 normalized correlation matrices and average them element-by-element. We then specify the diagonal elements as the medians of each diagonal element across all 25 samples. Finally, the average covariance matrix is reconstructed from the average correlation matrices and median value of the variances. We then compute the first three EOFs from the eigenvalue decomposition of the average covariance matrix. The result is a set of three EOFs for each altitude. The average EOFs are presented in this chapter.

8.3 Results: Fundamental ionospheric conductivity variability across the high-latitude E Region ionosphere

Figures 8.2a and b show the mean and first three EOFs for the Hall and Pedersen conductivities, respectively, as a function of altitude from 100 to 150 km in 10 km increments. The mean patterns are shown along the top row of Figures 8.2a and b with a linear color scale (yellow to red) and EOFs are shown along rows beneath the mean patterns with a diverging color scheme (blue to red) and scaled to a -0.5 to 0.5 range. The altitude increases from left to right and each polar plot is oriented with the sun off to the top of the figure, dawn to the right, and dusk to the left. The distributions are shown in altitude adjusted corrected geomagnetic coordinates (AACGM).

Comparing the mean fields in Figures 8.2a and 8.2b with the auroral profiles in Figure 8.1, we see the typical altitudinal structure represented in the complete high-latitude mean distributions. The Hall conductivity peaks between the altitudes of roughly 100-130 km with a relatively steep decrease above 130 km. The Pedersen conductivity, on the other hand, peaks at higher altitudes and over a broader range (~110-140 km). The vertical anisotropy in the Hall and Pedersen conductivities reflects the relative motions of ions and electrons in the upper atmosphere. At higher altitudes the ion-neutral collision frequency (ν_{in}) is relatively small such that the difference in ion and electron velocities is small, but directed along the electric field (i.e. a Pedersen current, see

Figure 2.7). At lower altitudes ion and neutral collisions are more frequent such that the ions are essentially tied to the neutral atmosphere and the current is carried largely by electrons, which move in the $\mathbf{E} \times \mathbf{B}$ direction (i.e. a Hall current). The point at which the Pedersen conductivity becomes the dominant term occurs between 120-130 km (*Richmond and Thayer*, 2000). The vertical anisotropies are relatively small above 150 km where both profiles decrease slowly with altitude.

The Hall conductivity reflects higher energy electrons with sufficient energy to penetrate into and ionize the lower altitude atmosphere. Higher energy electrons exhibit two primary characteristics evident in Hall conductivity profiles: 1) deeper penetration into the ionosphere and 2) ionization at earlier LTs due to a faster transit from the magnetosphere to the ionosphere and accordingly less time to undergo gradient curvature drift towards later LTs (eastward drift). Both characteristics are evident in the mean Hall fields between 100-120 km. The auroral zone enhancement of the mean Hall conductivity exhibits a counterclockwise rotation in LT with decreasing altitude. A similar LT dependency is not apparent in the mean Pedersen fields due to a rapid decrease in magnitude below 120 km.

After removal of the mean components, different for each altitude, the first EOFs identify the primary mode of variability in the residual data. We hereafter use HEOF and PEOF to refer to Hall and Pedersen EOFs, respectively. Both EOF1 altitude-specific patterns are similar in large-scale structure, and exhibit LT and localized intensity variations. HEOF1 and PEOF1 are consistent with a strengthening/weakening of the auroral oval signatures of the mean patterns as discussed by *McGranaghan et al.* (2015b). These patterns can be explained primarily by the variability of conductivity due to the predominance of diffuse precipitation (*Winningham et al.*, 1975; *Hardy et al.*, 1985; *Fuller-Rowell and Evans*, 1987; *Newell et al.*, 2009; *Milan et al.*, 2010; *Korth et al.*, 2014; *Carter et al.*, 2016). The patterns show distinct features as a function of altitude. At 150 km the EOF1 auroral region spans all nightside LTs and extends into dayside LTs with peak intensity at ~0100-0400 LT. At lower altitudes, the region expands slightly in latitude and exhibits variation in intensity as a function of MLAT and MLT, which we use synonymously with LT in the remainder of this work. The auroral zone variability in EOF1 is less continuous at lower altitudes, with a

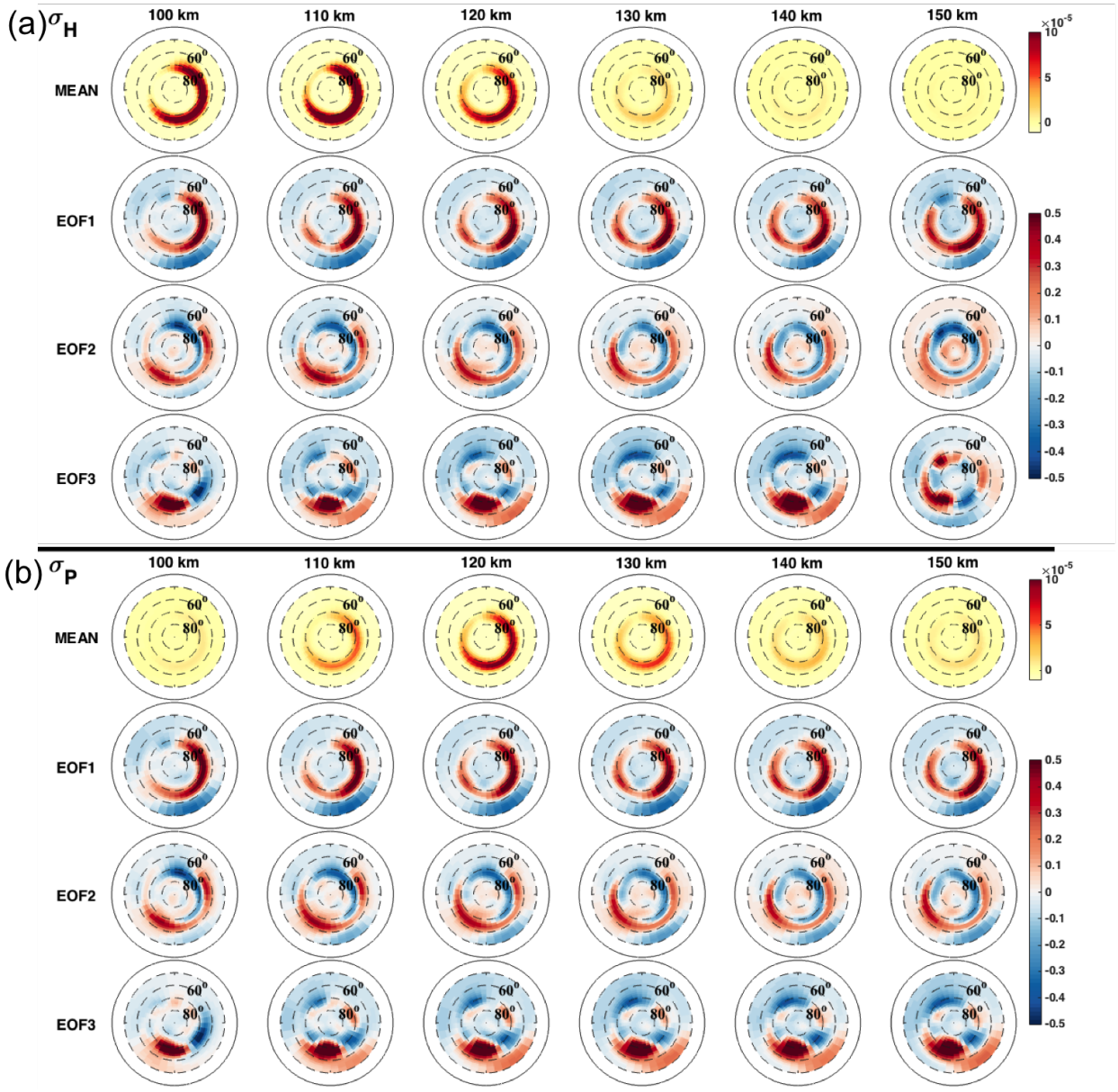

Figure 8.2: The mean and first three primary modes of variability (average EOFs) as a function of altitude over the E Region ionosphere for: (a) Hall conductivities (σ_H) and (b) Pedersen conductivities (σ_P). Mean patterns are shown along the top row of (a) and (b) with a linear color scale (yellow to red) and EOFs are shown along rows beneath the mean patterns with a diverging color scheme (blue to red) and scaled to a -0.5 to 0.5 range. The altitude increases from left to right. Each polar plot is oriented with the sun off to the top of the figure, dawn to the right, and dusk to the left and displays the distributions in altitude adjusted corrected geomagnetic coordinates (AACGM).

reduction in variability at midnight LT. The peak intensity in the postmidnight LT sector moves to early morning LTs (∼0200-0500) as altitude decreases between 130-110 km, and centers around dawn LT at 100 km. The premidnight variability is relatively constant in LT, but diminishes in intensity with decreasing altitude and disappears below 110 km. Differences between the Hall and Pedersen EOF1 fields are less pronounced than the differences between the two mean fields, suggesting that the variability about the mean patterns is similar for both conductivities.

As shown in Figure 8.2, between 110-140 km the Hall and Pedersen EOF2 fields show similar variations with altitude, consistent with the ionospheric conductivity response to enhanced magnetospheric convection (*Kamide et al.*, 1996; *Kamide and Kokubun*, 1996; *McGranaghan et al.*, 2015b). Whereas the height-integrated response shows a latitudinally expanded auroral zone with nearly uniform intensity centered around the morning LT sector (Figure 5.5 in this dissertation), HEOF2 (Figure 8.2a) and PEOF2 (Figure 8.2b) show distinct LT variation in the intensity.

HEOF2 at 150 km is uniform throughout the expanded auroral oval region. At 140 km, there are separate intensity peaks at the dawn and post dusk regions. The intensities of these local peaks increase with decreasing altitude, but the dawn intensity peak remains fixed in LT whereas the post dusk intensity peak moves toward midnight at lower altitudes. PEOF2 is similar, but the two local peaks are evident at all altitudes, including 150 km.

The EOF3 Hall and Pedersen conductivity fields are characterized by smaller-scale features and reduced correlations with solar wind parameters and geomagnetic activity indices (see Figure 8.3). Two responses appear most prominently: the first in the $\sim 2100 - 0100$ LT sector and spanning a wide MLAT band, and the second as a pair of features at MLAT $> 70°$ surrounding the noon LT meridian. These locations are consistent with broadband precipitation into the ionosphere (*Newell et al.*, 2009). The response in the $\sim 2100 - 0100$ LT sector that extends to earlier LTs in a comparatively thin latitudinal region between 60-70° is also apparent in the *Newell et al.* (2009) broadband energy precipitation (their Figure 4).

To explore the possible geophysical drivers of the dominant modes of variability represented by the EOFs in Figures 8.2, we correlated the amplitude of each EOF at a given time with the cor-

responding hourly time series of various solar wind parameters and solar and geomagnetic indices. The parameters and indices we chose include the IMF components in geocentric solar magnetospheric (GSM) coordinates (B_X, B_Y, and B_Z), geomagnetic indices (auroral electrojet indices (AE, AL, and AU), planetary index (Kp), polar cap index (PC), and disturbance storm time index (Dst)), and specialized coupling functions (the interplanetary electric field ($E_Y = -V_{SW} \times B_{Z,GSM}$), the Borovsky coupling function (CF) (*Borovsky*, 2013), and the Newell CF (*Newell et al.*, 2007)). For each of the 25 subsets used to construct the average EOFs in Figure 8.2, we calculate the correlation coefficient between each parameter/index and each EOF amplitude. This gives 25 correlation coefficients for each parameter/index-EOF combination (for instance, 25 correlation coefficients between IMF B_Z and HEOF1). We then calculate the median of these 25 correlations and display that value in Figure 8.3. This process is carried out separately for each altitude level. Figures 8.3a-c show these median correlations for HEOFs 1-3, respectively, and Figures 8.3d-f show the correlations for PEOFs 1-3. Each altitude is represented by a different color and dashed connecting lines are provided as a visual aid.

Figures 8.3a and d demonstrate that the amplitudes of the first EOFs correlate with geomagnetic activity drivers (B_Z, for instance) and indicators (the geomagnetic indices and CFs). These are consistent with the correlations of the ionospheric conductance EOF1 amplitudes in *McGranaghan et al.* (2015b). Examining the height-dependency, we find that there is distinct separation with altitude in the HEOF1 correlations, with lower altitudes being more strongly correlated with the parameters tested. The HEOF1 correlations at the top of the E Region (150 km) are smaller than those at lower altitudes. The PEOF1 correlations are more uniform with altitude.

Figures 8.3b and e show the HEOF2 and PEOF2 amplitude correlations, respectively. Again, HEOF2 correlations differ with altitude, showing largest correlations at 120-140 km and slightly reduced correlations at 110 and 150 km. There is a similar separation of PEOF2 correlations, except the largest correlations occur between 120-150 followed by smaller correlations at 110 km. The correlations are smallest at 100 km for both patterns.

EOF2 is anticorrelated with the IMF B_Z component, indicating that the magnetospheric

convection-driven conductivity variability increases with the strength of southward IMF. This follows the well-established correlation between the magnitude of southward IMF B_Z, the level of solar wind magnetospheric coupling, and enhanced magnetospheric convection and Region 1/2 FACs (*Iijima and Potemra*, 1978; *Cowley and Lockwood*, 1992; *Kamide et al.*, 1996; *Milan et al.*, 2007, 2012; *Coxon et al.*, 2014). These patterns also correlate strongly with both the Borovsky and Newell CFs.

A striking relationship is revealed when we consider that the signs of the EOFs are arbitrary, and any pattern can be equally replaced by its negative (*Cosgrove et al.*, 2014). If we switch the signs of EOF2 patterns, the high-latitude dayside region extending roughly from predawn until postnoon MLT and at MLATs almost exclusively greater than 70° (shown as negative (blue) in Figures 8.2a and b) becomes the positive feature while the magnetospheric convection-driven variability becomes negative. When the signs of the EOF patterns are reversed, so, too, are the signs of the correlations. Thus, the high-latitude feature is positively correlated with IMF B_Z, indicating conductivity variability driven by northward IMF. Therefore, EOF2 reveals a mode of ionospheric conductivity variability with two components that vary in tandem, but in opposite senses, depending on the direction of the IMF B_Z component. We explore this in Section 8.4.1.

The amplitude correlations of HEOF3 and PEOF3 are largest at 100 km, and small at higher altitudes. EOF3 suggests that broadband precipitation, and, therefore, Alfvénic Poynting flux, plays a role in the variability of ionospheric conductivity. EOF3 also indicates that two levels of different strengths exist in this variability. The variability associated with the first-order response is strongest. The second-order response is weaker, but significant. We explore this further in Section 8.4.2.

We note that, in general, the spread of correlation coefficients for each parameter/index-EOF across the 25 samples was small (not shown). The standard deviations were typically $\sim 0.02 - 0.05$ for all combinations of parameter/index-EOF below 140 km. At 140-150 km, the standard deviations of correlation coefficients were higher for EOF2 and EOF3. The increase was most noticeable for the index and CF correlations (~ 0.1 for EOF2 and ~ 0.2 for EOF3 at these

altitudes).

We also explore the distribution of the power among the EOFs. Figures 8.4a and b show the percentages of the overall variability in the pseudo-conductivity observations captured at each altitude by the HEOFs and PEOFs, respectively. We compute the percentage variability for each of the 25 subsets used to construct the average EOFs presented in Figure 8.2 and described in Section 8.2 and plot the upper and lower quartiles as green points and connecting lines and the median as blue points and connecting line for each altitude. There is very little spread in the percentage variability captured across the 25 subsets for both conductivities and at all altitudes.

Figure 8.4 shows that EOF1 captures between 30-40% of the variability in the observations at lower altitudes, and generally between 20-30% above 120 km altitude. The results for EOF2 and EOF3 are more uniform with altitude, representing $\sim 10\%$ and $\sim 5-8\%$ of the overall variability at all altitudes, respectively.

8.4 Discussion

In Section 8.3 we presented the primary modes of Hall and Pedersen conductivity variability throughout the E Region ionosphere. Here we expand on two findings that have been identified for the first time in our results: the relationship between EOF2 and the IMF B_Z component and the EOF3 association with Poynting flux-driving of the ionosphere. We conclude this section by relating the organization of our EOFs to the different types of electron precipitation and the global energy flux budget.

8.4.1 Relationship between EOF2 and IMF B_Z

EOF2 characterizes the conductivity variability due to IMF B_Z. These patterns identify two clear, spatially delineated conductivity responses, distinguished by the direction of the B_Z component: 1) under southward-directed B_Z, conductivities are enhanced in the latitudinally expanded auroral oval, consistent with the expanding/contracting polar cap (ECPC) paradigm (*Cowley and Lockwood*, 1992; *Milan et al.*, 2012) dictated by enhanced magnetospheric convection; and 2) under

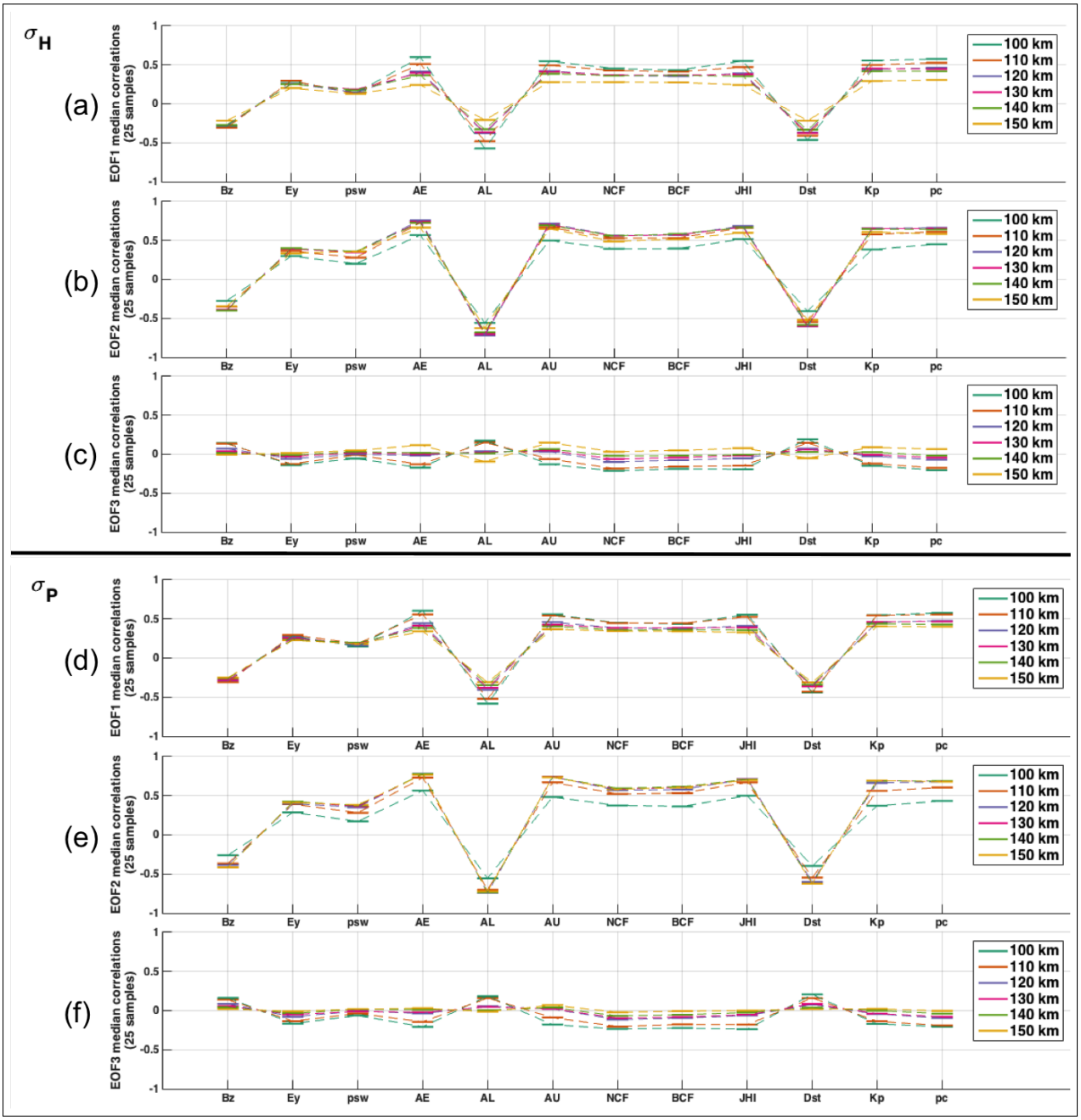

Figure 8.3: Correlations between EOF amplitudes over time and hourly averaged solar wind parameters and geomagnetic indices. The parameters and indices shown are the IMF components in geocentric solar magnetospheric (GSM) coordinates (B_X, B_Y, and B_Z), geomagnetic indices (auroral electrojet indices (AE, AL, and AU), planetary index (Kp), polar cap index (PC), and disturbance storm time index (Dst)), and specialized coupling functions (the interplanetary electric field ($E_Y = -V_{SW} \times B_{Z,GSM}$), the Borovsky coupling function (BCF) (*Borovsky*, 2013), and the Newell coupling function (NCF) (*Newell et al.*, 2007)). (a-c) HEOF1-3 correlations. (d-f) PEOF1-3 correlations. Altitudes are shown by different colors and dashed connecting lines are provided as a visual aid.

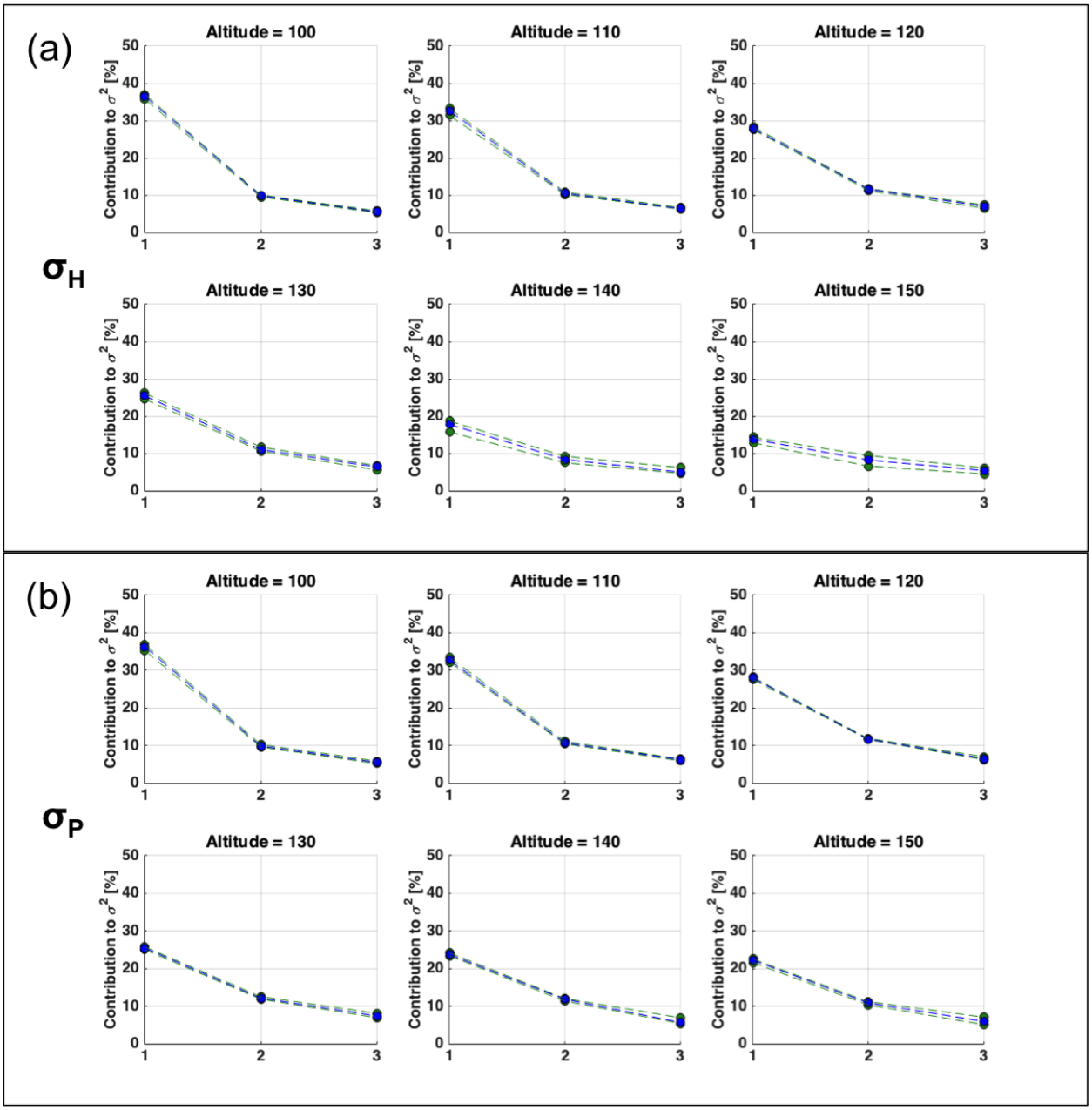

Figure 8.4: Percentage variability of the complete DMSP pseudo-observations captured by the first three EOFs of the (a) Hall and (b) Pedersen conductivities over each altitude analyzed. At each altitude the percentages were calculated for each of the 25 subsets and the quartiles are shown (green dots and dashed lines mark the upper and lower quartiles, and blue dots and dashed lines mark the medians).

northward-directed B_Z, conductivities are enhanced at MLATs $> 70^\circ$ and dayside LTs, consistent with precipitation from boundary plasma regions (*Vasyliunas*, 1979; *Rich et al.*, 1990; *Newell and Meng*, 1992; *Newell et al.*, 2009). We use the term boundary plasma region (BPR) to indicate the region at low altitude that maps to the prominent magnetospheric boundary layers (*Vasyliunas*, 1979; *Rich et al.*, 1990), including the boundary plasma sheet, low-latitude boundary layer, mantle, and cusp/cleft (see Figure 2.11 in the introduction of this dissertation).

As mentioned in the previous section, we have identified a two-component nature of the ionospheric conductivity variability in EOF2 that is organized by the IMF B_Z. The component due to $+B_Z$ (i.e. northward) has not been discussed. We address this component here.

Figure 8.5 shows the HEOF2 amplitudes and the hourly averaged IMF B_Z during a period of almost exclusively northward IMF from 28 October to 02 November 2010. Positive values are shown in blue and negative values in red to illustrate the relationship between $+B_Z$ and $-\alpha^{(2)}$. The figure shows that HEOF2 amplitudes are negative during periods of $+B_Z$ (northward), indicating that a switch in the sign of HEOF2 shown in Figure 8.2a occurs at these times. The relationship is more pronounced at and below an altitude of 130 km. At 140 km the correspondence is still high, while at 150 km the relationship is less pronounced. The strength of the relationship between the HEOF2 patterns and the IMF B_Z is also reflected in the magnitudes of the EOF amplitudes with increasing altitude (bottom to top in Figure 8.5). The amplitudes at 100-120 km are orders of magnitude larger than at higher altitudes. The PEOF2 amplitudes, not shown, exhibit the same relationships, however, the amplitudes are more uniform with altitude, increasing in a broader range between 110-140 km altitude.

We believe the two components of EOF2 can be associated with the magnetospheric source location of the precipitating electrons (not including the diffuse precipitation component, which was accounted for in EOF1). Under southward IMF the precipitation is dominated by accelerated electrons, both monoenergetic and broadband, mapping to the central plasma sheet (CPS) (*Newell et al.*, 2009). The CPS precipitation is correlated with the large-scale Region 1/Region 2 FACs and maps to the expanded auroral oval (*Iijima and Potemra*, 1978; *Kamide et al.*, 1996). As the IMF

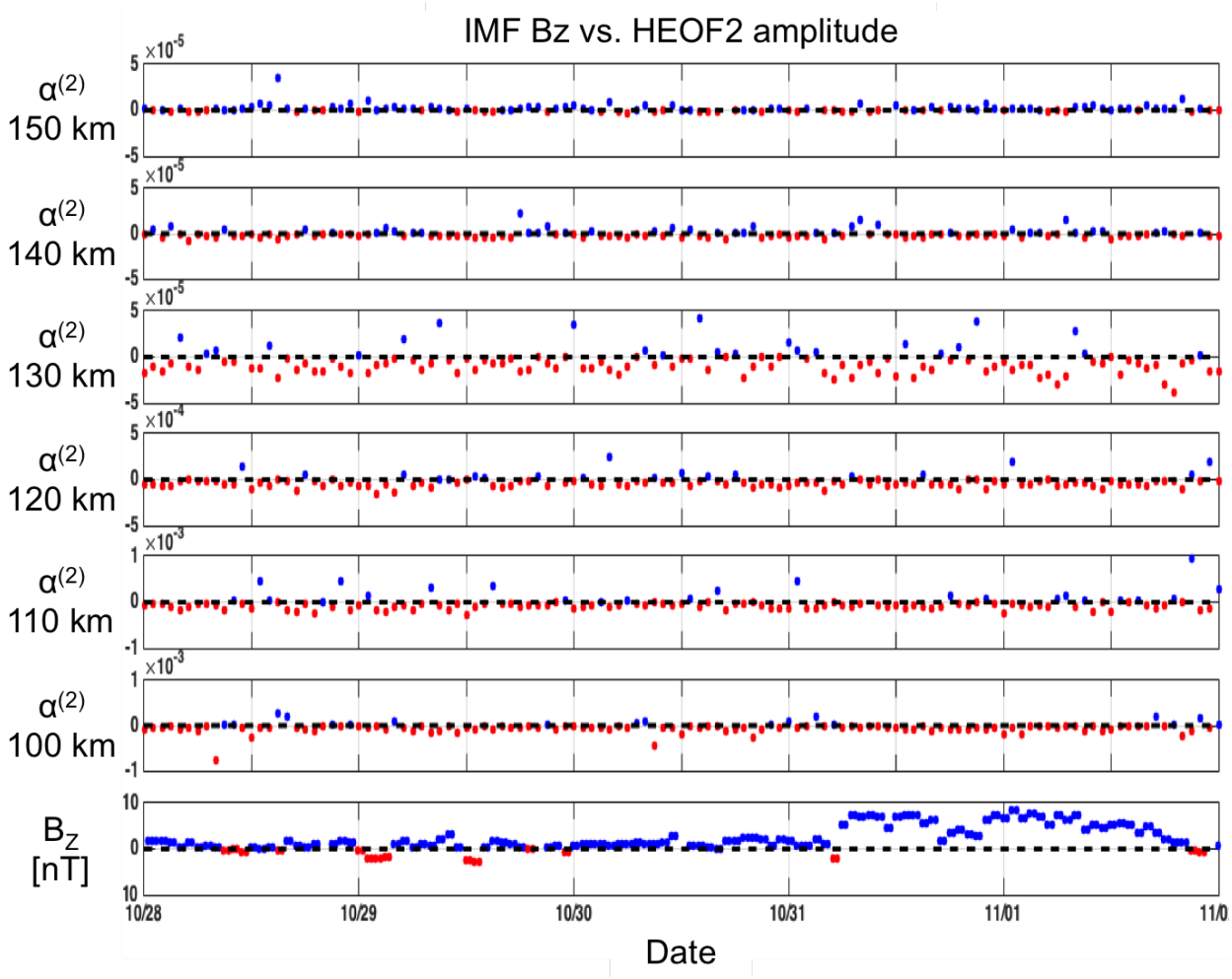

Figure 8.5: HEOF2 amplitudes for each altitude and hourly averaged IMF B_Z (bottom row) during a period of predominantly $+B_Z$ between 28 October and 02 November 2010. Positive values are shown in blue and negative values in red.

turns northward the precipitation changes and primarily originates in the BPR, which maps largely to the high-latitudes and dayside ionosphere along a configuration of FACs consisting of the NBZ and high-latitude Region 1 systems (*Iijima and Potemra*, 1976a,b; *Vasyliunas*, 1979; *Rich et al.*, 1990). Figure 2.2c in the introduction to this dissertation shows a schematic of magnetic merging under northward IMF, mapping to the high-latitude dayside region (*Maezawa*, 1976). *Iijima and Shibaji* (1987) identified that the transition between Region 1 + Region 2 + NBZ FAC systems is continuous and that the dayside and nightside parts of these systems are disconnected. *Rich et al.* (1990) then explored this relationship during a magnetic storm with well-defined southward and northward IMF B_Z periods and found that variations in the extent of particle precipitation from the BPR occur in tandem with changes in the large-scale Region 1/Region 2 FAC systems. They concluded: 'The shrinking of the latitudinal width of the CPS was coincident with the disappearing of the auroral zone Region 1/Region 2 currents. In addition, the expansion of the BPR to higher latitudes occurred simultaneously with the appearing of the NBZ current system...' These aspects of MI coupling due to IMF B_Z are reflected in our results for the ionospheric conductivity variabilities.

These connections indicate that EOF2 is related to conductivity variability driven in large part by monoenergetic precipitation. Figure 8.6 shows a comparison of our results with the hemispheric number and energy fluxes of monoenergetic electron precipitation from *Newell et al.* (2009). Figures 8.6a-b show the locations of 130283 monoenergetic electron precipitation spectra identified using the criteria of *Newell et al.* (2009) during January 2010, separated according to B_Z+ (Figure 8.6a, 60013 total spectra) and B_Z- (Figure 8.6b, 70270 total spectra) conditions. The January 2010 period is considered representative of the data used to generate the EOFs. These figures show that occurrence of monoenergetic precipitation is common in the dayside high-latitude regions flanking noon LT for B_Z+ conditions and occurrences increase in the dusk and nightside LT sectors for B_Z- conditions. Figures 8.6c-d reproduce the hemispheric monoenergetic number flux results of *Newell et al.* (2009) during low (Figure 8.6c) and high (Figure 8.6d) solar wind driving (their Figure 7). There is a close correspondence between the occurrence of monoenergetic precipitation during B_Z+ and low solar wind driving conditions and during B_Z- and high solar wind driving

conditions. Figures 8.6e-f show the HEOF2 patterns at 120 km during B_Z+ (Figure 8.6e) and B_Z- (Figure 8.6f) conditions. These are representative of the EOF2 patterns. Figures 8.6g-h show the same thing as Figures 8.6c-d, except for the monoenergetic precipitation hemispheric energy flux. The conductivity variability in EOF2 is a convolution of the monoenergetic number and energy flux. During low solar wind driving/B_Z+ conditions the EOF2 pattern in Figure 8.6e captures the high dayside occurrence frequency convolved with the relatively low-level energy flux that extends through the morning and dayside LTs between 75-80°. Under high solar wind driving/B_Z- conditions the EOF2 pattern in Figure 8.6f captures conductivity variability that reflects the latitudinally expanded regions of enhanced number and energy flux at LTs extending from dusk through midnight to morning. We note that the correspondences are not exact. Differences may be due to several factors, including: 1) representation of our EOFs by polar-cap spherical harmonics basis functions versus the straightforward binning that was used to create the Newell maps; 2) different analysis time periods (our EOFs were created from DMSP data in 1987 and 2010, Newell maps were created from DMSP data between 1988-1998); and 3) different separation of results (the level of solar wind driving used to separate results in *Newell et al.* (2009) (determined by the NCF (*Newell et al.*, 2009)) is not identical to our separation by B_Z direction). Even with these differences in analyses, the correspondences shown in Figure 8.6 are convincing.

We have identified a two-component nature in the pattern of variability represented by EOF2. These two components vary in tandem, and in opposite sense, and we have shown that the determining factor is the direction of the IMF B_Z component. We can, therefore, trace the connection of this mode of variability to well-established relationships between northward and southward IMF conditions. Figure 8.7 provides a schematic of the connection from the solar wind to the ionospheric conductivity.

8.4.2 Relationship between EOF3 and Alfvén Poynting flux

In Section 8.3 we suggested that broadband precipitation drives two types of conductivity variability and that both are represented in EOF3. The predominant driver of broadband precipi-

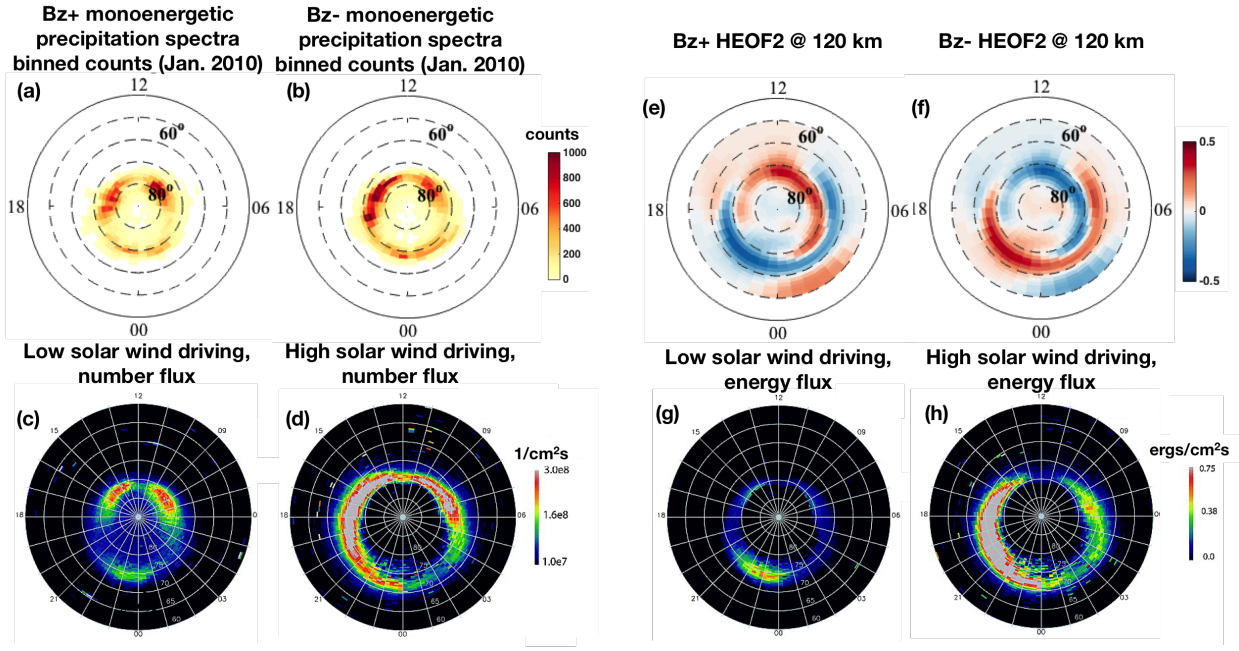

Figure 8.6: Monoenergetic precipitation characteristics for January 2010 compared to *Newell et al.* (2009) hemispheric monoenergetic number and energy flux distributions and characteristic EOF2 patterns. Counts of all monoenergetic precipitation spectra binned into the AMIE grid used to create the EOF patterns for (a) B_Z+ and (b) B_Z- conditions. The hemispheric precipitation number flux for monoenergetic precipitation events averaged over one solar cycle for (c) low and (d) high solar wind driving (based on the Newell coupling function *Newell et al.* (2007)), reproduced from Figure 7 of (*Newell et al.*, 2009). HEOF2 patterns for (e) B_Z+ and (f) B_Z- conditions. (g-h) Same as (c-d) except for the energy flux and reproduced from Figure 3 of (*Newell et al.*, 2009).

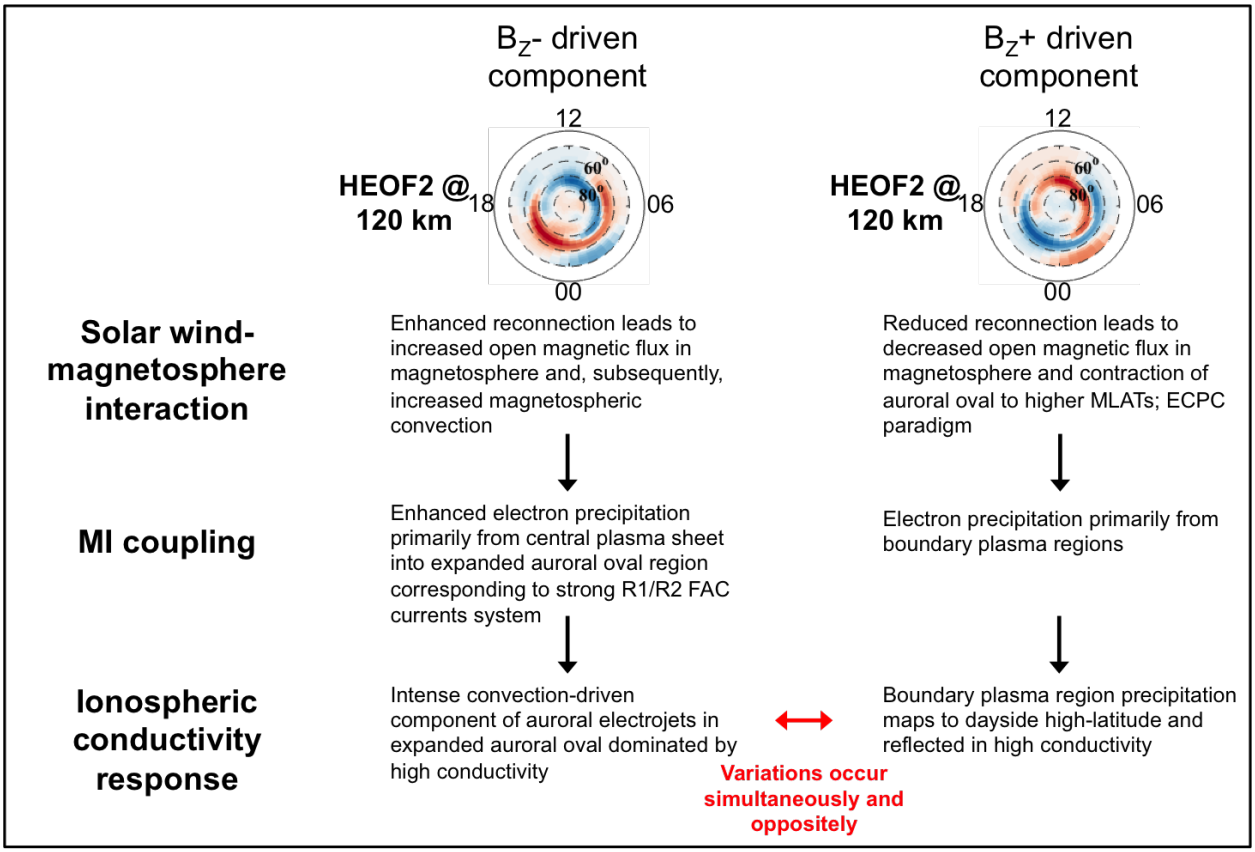

Figure 8.7: Schematic detailing the two components of EOF2. The connection between the solar wind and ionospheric conductivity effects is illustrated. The HEOF2 patterns at 120 km are used for the illustration.

tation is the convergence of Alfvén Poynting flux in the auroral acceleration region (AAR) causing a divergence of particle kinetic energy flux over a broad range of energies into the ionosphere (*Lotko*, 1986; *Thayer and Semeter*, 2004; *Newell et al.*, 2009). To investigate the connection between the variability of the ionospheric conductivities with Alfvénic Poynting flux it is important to distinguish the DC and Alvénic components of the Poynting flux: 1) the DC component is associated with large-scale perturbations in electric and magnetic fields and associated changes in FACs (spatial scales of >100 km and temporal scales of $\sim$ 5 minutes); and 2) the Alfvénic component is tied to smaller scale perturbations and currents. A convergence of either the DC or Alfvénic components in the AAR (located at altitudes between $\sim$0.2-2 Earth radii (*Forsyth et al.*, 2012)) drives a divergence of particle kinetic energy flux downward into the ionosphere. Kinetic energy divergence driven by the DC component results largely in monoenergetic electron precipitation, which has been discussed in relation to EOF2. Kinetic energy divergence driven by the Alfvénic component, on the other hand, has not previously been associated with ionospheric conductivity variability. Our EOF3 results suggest that the signature of the Alfvénic Poynting flux is a prominent component in the modification of ionospheric conductivities.

The component of EOF3 in the premidnight regime is consistent with the primary ionospheric mapping location of electrons that have been accelerated over a broad range of energies, or broadband precipitation (*Lotko*, 1986; *Newell et al.*, 2009). *Lotko* (1986) established that broadband precipitation is strongly correlated with the fluctuating component of the geomagnetic field-aligned electric field. A more direct connection was established between broadband electron precipitation and Alfvénic Poynting fluxes on the basis of in-situ satellite observations above and below the AAR, showing that broadband precipitation is largely driven by dispersive Alfvén waves (DAWs) (*Andersson et al.*, 2002; *Keiling et al.*, 2003; *Chaston et al.*, 2007). Convergence of the Alfvénic Poynting flux in the AAR drives a divergence of the particle kinetic energy flux (*Thayer and Semeter*, 2004). The particle kinetic energy divergence results in broadband precipitation directed downward into the ionosphere (*Chaston et al.*, 2007).

Chaston et al. (2007) and, more recently, *Zhang et al.* (2014) showed that Alfvénic Poynting

flux convergence in the premidnight regime is several times more energetic than on the dayside, and that this pattern is repeated in the energetic electron fluxes. The premidnight component is prominent in our EOF3 patterns. The dayside broadband component (*Chaston et al.*, 2005), separated into pre and postnoon LT locations, is also captured and is related to less intense conductivity variability. *Newell et al.* (2009) found that the broadband precipitation was extremely common in the prenoon LT location, and is accordingly more pronounced than the postnoon dayside feature in our results.

The dayside regions of enhanced conductivities due to broadband precipitation are highly variable with altitude. These locations of broadband precipitation are likely more directly controlled by the IMF B_Y direction, which our results are not sensitive to because we assume hemispheric conjugacy. This may contribute to the variability of the locations and intensities of these regions in our EOF3 patterns. Nevertheless, these regions indicate that broadband precipitation effectively modifies ionospheric conductivity in the dayside, as well as the nightside, high-latitude regions.

Figure 8.8a-b shows the broadband precipitation characteristics for January 2010. Figure 8.8a superimposes the locations of all 1383 broadband precipitation spectra identified using the criteria of *Newell et al.* (2009) over the month long period onto the HEOF3 pattern at 120 km, which is used as a characteristic pattern for this mode of variability. Figure 8.8b bins these broadband spectra onto the AMIE grid used to fit the EOFs. It is clear from these figures that the broadband precipitation occurs frequently in the dayside high-latitude regime during this period, and that there is also frequent broadband precipitation into the nightside LT sector associated with the premidnight conductivity variability. Figures 8.8c-d reproduce the high solar wind driven (specified by the NCF (*Newell et al.*, 2007)) broadband precipitation hemispheric energy and number fluxes, respectively, from the 1988-1998 time period created by *Newell et al.* (2009). The energy flux corresponds very closely with the HEOF3 pattern in Figure 8.8a, with the most intense precipitation and largest variability in the premidnight LT sector. It is also clear why we have termed the dayside features flanking noon LT of second-order importance from these figures. The dayside locations are associated with less energetic broadband precipitation and correspondingly reduced conductivity

variability. Figure 8.8d shows that the broadband precipitation number flux is more evenly divided between the dayside and premidnight features, and, in fact, the number flux peaks in the prenoon location, where broadband accelerated electron events are extremely common. Figure 8.8b also shows a large number of precipitation events in this region in the January 2010 data.

The difference of the HEOF3 pattern at 150 km is noteworthy. This pattern shows a strong signature of duskside variability at MLATs consistent with enhanced magnetospheric convection in addition to the broadband premidnight broadband precipitation feature. This suggests that the conductivity effects due to monoenergetic precipitation under enhanced magnetospheric convection are not fully accounted for in EOF2 for the Hall conductivity at 150 km (the HEOF2 variability is less intense in the duskside region than the HEOF2 patterns at lower altitudes). There is an accompanying dayside variability in HEOF3 at 150 km that is markedly different than the variability at lower altitudes. The correlations of the HEOF3 amplitudes at 150 km are small (see Figure 8.3c) and provide little information about the potential physical driver(s) at this altitude, though it is interesting to note that they have the opposite sign from the HEOF3 amplitude correlations at other altitudes and PEOF3 amplitude correlations at all altitudes. We do not comment further on the interesting case of HEOF3 at 150 km here, nor do we investigate the difference between HEOF3 and PEOF3 at 150 km. However, we suggest that those results warrant future consideration.

Figure 8.9 schematically illustrates the Alfvénic Poynting flux progression leading to variability of the ionospheric conductivities. The green circles on the inset polar plots explicitly identify the regions we interpret as the ionospheric locations of first- and second-order broadband electron precipitation.

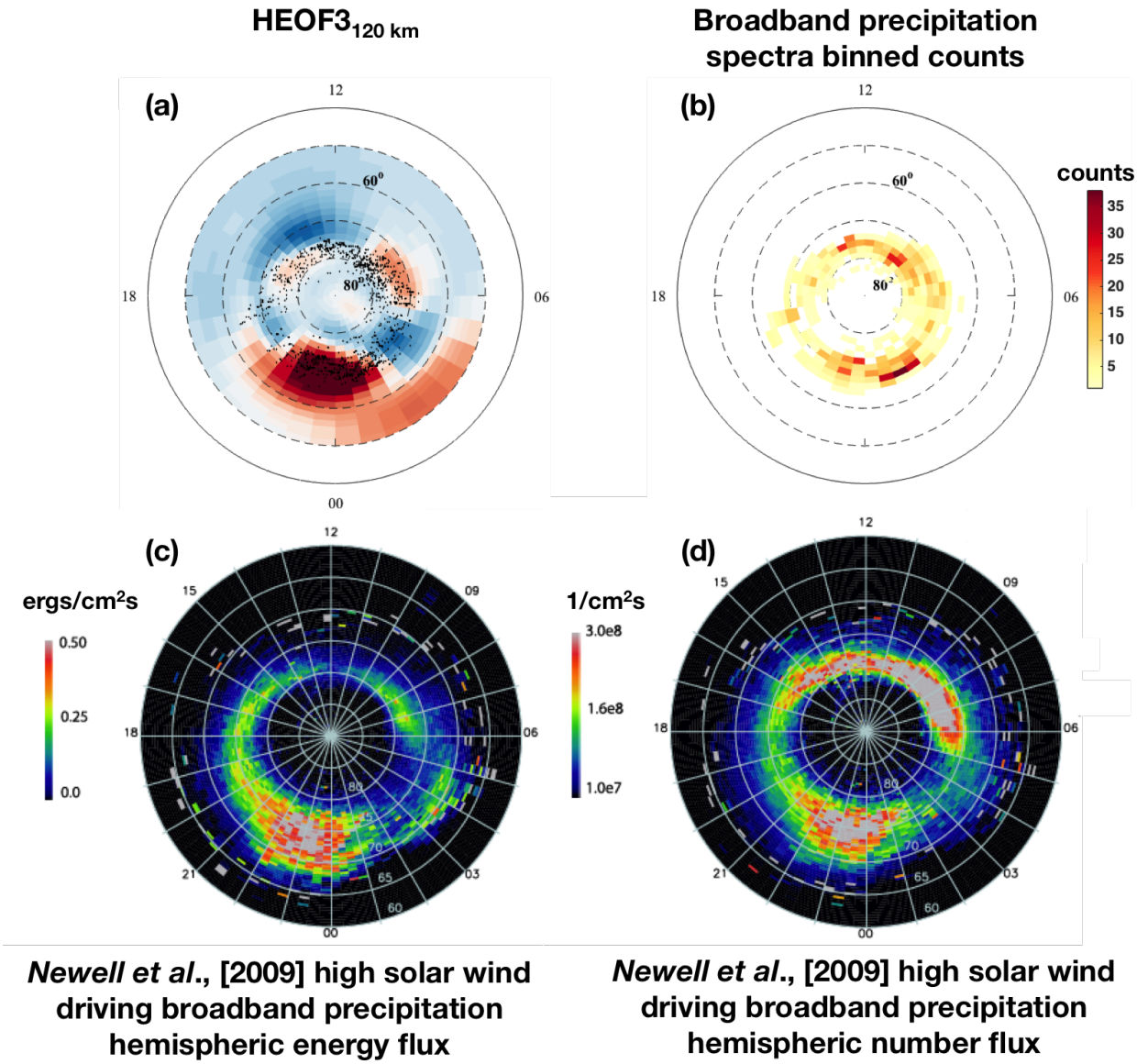

Figure 8.8: Broadband precipitation characteristics for January 2010. (a) Location of all broadband precipitation spectra from DMSP F16-F18 (black points) superimposed on the HEOF3 pattern at 120 km. (b) Counts of all broadband precipitation spectra binned into the AMIE grid used to create the EOF patterns. (c) The hemispheric precipitation energy flux for broadband precipitation events averaged over one solar cycle for high solar wind driving (based on the Newell coupling function *Newell et al.* (2007)), reproduced from Figure 4 of (*Newell et al.*, 2009). (d) Same as c except for the number flux and reproduced from Figure 8 of (*Newell et al.*, 2009).

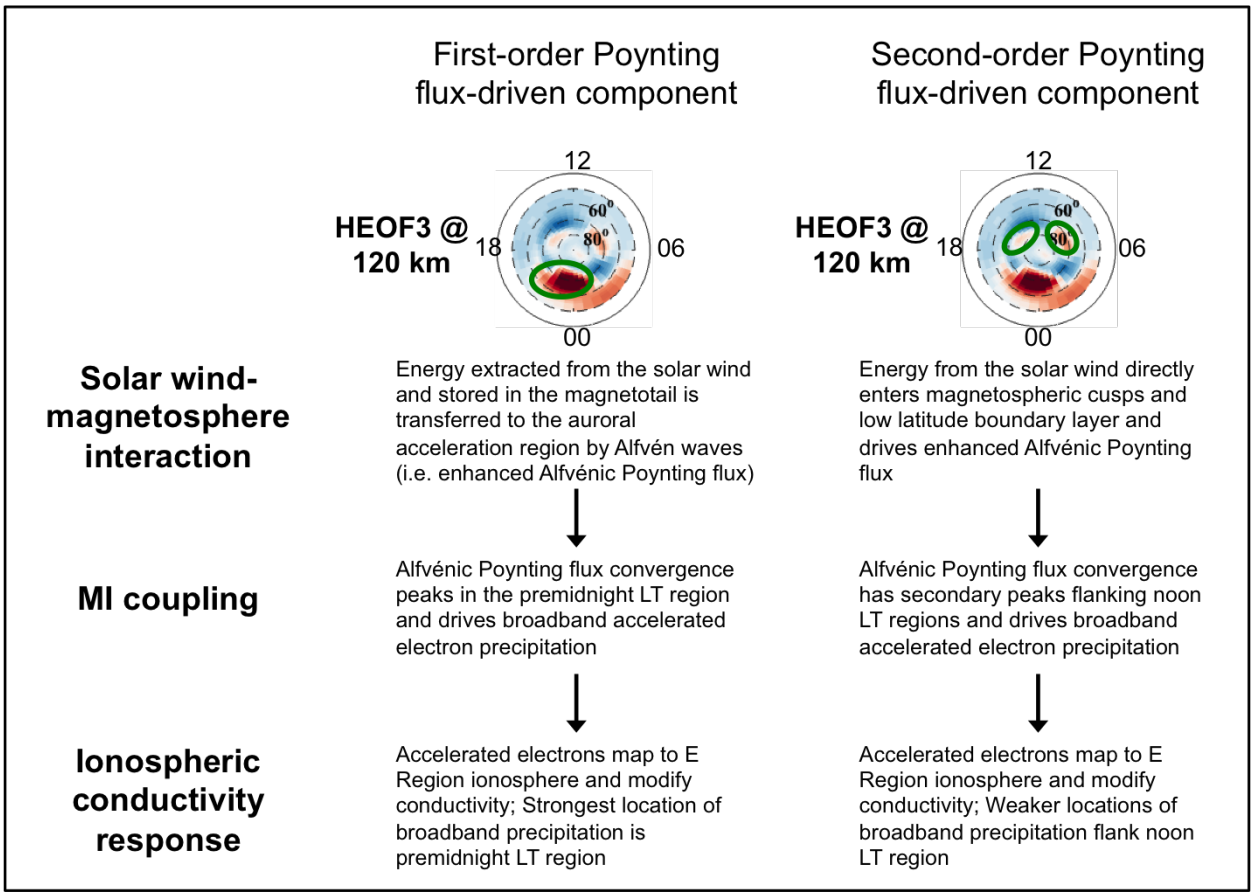

Figure 8.9: Schematic detailing the physical explanation for the broadband electron precipitation in EOF3: the strongest component at premidnight LT and weaker components flanking noon LT. The connection between the solar wind and ionospheric conductivity effects is illustrated. The HEOF3 patterns at 120 km are used for the illustration.

8.4.3 Correspondence between the distribution of power among the EOFs and the global electron energy precipitation budget

Table 8.1 reproduces the statistical electron energy precipitation budget results derived from DMSP satellite data between 1988-1998 by *Newell et al.* (2009). The relative contributions from the three primary electron energy precipitation types are provided for low and high solar wind driving conditions.

Table 8.1: Global electron energy flux hemispheric contributions by the three types of auroral electron precipitation identified by *Newell et al.* (2009).

	Low solar wind driving	High solar wind driving	All conditions	High/Low Ratio
Diffuse electrons	63%	57%	61%	3.0
Monoenergetic	10%	15%	16%	5.3
Broadband	6%	13%	6%	8.0

It is clear from a comparison of Table 8.1 and Table 8.2 and Figures 8.4a and b that the organization of our EOFs, in general, reflect the overall electron precipitation energy budget. The largest contributor is the diffuse component, the primary contributor to EOF1, followed by the monoenergetic and broadband accelerated electron precipitation. The conductivity variability due to monoenergetic precipitation showed prominently in EOF2. EOF3 then captured the variability due to the broadband precipitation component. Table 8.1 also shows that the broadband component is the most responsive to solar wind driving in terms of the global electron energy flux. It should not be surprising, then, that this becomes a mode of variability beyond the more steady modes represented by EOFs 1 and 2. Though we discuss the precipitation type primarily associated with each EOF pattern, it is important to note that none of the EOFs are driven solely by one type of precipitation. For instance, the ionospheric projections of monoenergetic and broadband precipitation overlap in certain areas and likely drive similar conductivity variabilities in those locations. The altitude dependencies of the conductivity variabilities shown here certainly provide more information with which to separate such ambiguities than the height-integrated conductance

variabilities.

We also recognize a correspondence between the percentage variabilities captured by each EOF and the contribution to the global electron energy flux budget by the three types of precipitation. Table 8.2 shows the average percentage variability captured by the Hall and Pedersen EOFs. The average values shown in the table are computed from the median percentages over all altitudes for each EOF (blue dots shown in Figure 8.4).

Table 8.2: Average percentage variability captured by the Hall and Pedersen EOFs[1].

EOF	Hall	Pedersen
1	26%	28%
2	10%	11%
3	6%	6%

[1] Values computed as the average of the median percentages shown in Figure 8.4 over all altitudes.

The diffuse precipitation and EOF1 are the dominant contributors to the global budget (∼65%) and variability captured (between 20%-40%, generally), respectively. The monoenergetic precipitation contributes roughly six times less to the global budget than the diffuse precipitation, while EOF2 captures between two and three times less of the overall variability than EOF1. It is likely that diffuse precipitation, subject to similar driving as the monoenergetic and broadband precipitation, also contributes to conductivity variabilities beyond EOF1. It is also likely that monoenergetic and broadband precipitation affect EOF2 and 3 patterns simultaneously in certain locations (see note at the end of the previous paragraph). This may explain why the ratios between the percentage variabilities captured by each EOF are reduced compared to the contributions of the various precipitation types to the global precipitation budget. For instance, the EOF1:EOF2 percentage variation captured ratio is roughly 3:1 while the diffuse to monoenergetic contribution to the global precipitation budget is roughly 6:1. Finally, the broadband electrons are between 6%-13% of the global electron energy flux, and EOF3 captures generally ∼6% of the total observational variability. The relationships in Figure 8.4 are less well-defined at higher altitudes, where the diffuse

component captures a smaller percentage of the variability.

8.5 Conclusions

We have conducted the first EOF analysis of height-dependent ionospheric conductivities based on in-situ energetic electron precipitation measurements from DMSP spacecraft. No assumption on the electron energy spectra was made, representing another significant first in the analysis of height-dependent conductivities. The EOFs showed distinct altitude-dependent behavior and differences from EOFs derived in the same manner for height-integrated conductivities in *McGranaghan et al.* (2015b). These differences suggest that height-integrated and height-dependent characterizations of the ionosphere may be distinctly different, and underscore the importance of analyzing the E Region ionosphere in three dimensions.

Our height-dependent EOFs reveal two previously unidentified characteristics of ionospheric conductivity variability: 1) a clear, spatially delineated relationship between conductivity variability and the direction of IMF B_Z in EOF2; and 2) the influence of broadband electron precipitation on the conductivity variability in EOF3, separated into a first-order effect in the premidnight LT sector and second-order effects flanking the noon LT sector. These relationships may be exploited in future ionospheric conductivity specification and forecasting efforts. Finally, we found that the distribution of the power among the primary modes of ionospheric conductivity variability are, in general, explained by the contributors to the global budget of precipitating electron energy flux: 1) EOF1/diffuse precipitation; 2) EOF2/monoenergetic precipitation; and 3) EOF3/broadband precipitation.

We suggest that 3-D ionospheric conductivities are a critical piece in unifying understanding of auroral particle precipitation, ionospheric electric fields, and field-aligned currents and the complex relationships between them. The EOFs we presented can be used to create a realistic conductivity model error covariance for application to ionospheric data assimilative techniques in the same manner that height-integrated conductivity EOFs were used to improve specification of ionospheric electrodynamics in two dimensions in *McGranaghan et al.* (2016, submitted and revised). Therefore,

these results enable 3-D specification of the ionospheric electrodynamics.

Chapter 9

Conclusion and outlook

The research in this dissertation was motivated primarily by the question: *how can the global modeling of ionospheric conductivity be improved to better study the coupled magnetosphere-ionosphere-thermosphere system?* To answer this question we first determined the current state of conductivity modeling and identified six outstanding issues:

- lack of direct observations of conductivity,
- assumption of an equivalent ionospheric current (2-D approximation),
- assumption of a Maxwellian distribution for the energy spectrum of precipitating particles,
- reliance on proxies and/or indices of geomagnetic activity and particle precipitation,
- sparse observations, and
- lack of resolution of fine-scale spatial and temporal structure.

Based on these outstanding issues, we formulated a number of detailed questions and addressed them through specific investigations. We list these questions and summarize the key findings of the corresponding investigations in the following section and provide an outlook to the future in Section 9.2.

9.1 Summary

How limited are analyses of the magnetosphere-ionosphere-thermosphere (MIT) system that rely on proxies and/or indices of geomagnetic activity and particle precipitation?

Chapter 3 summarized *McGranaghan et al.* (2014), which investigated the MIT system response to solar wind corotating interaction region high speed streams (CIR-HSS) in the absence of knowledge of direct geospace coupling via conductivity. In that study, indirect measures of the MIT system were used to understand the system connections and response. We established a new probabilistic forecasting paradigm based on these indirect measures. These forecasts rely on statistically observed responses and are valid only during specific periods, such as near equinox. We concluded that this forecasting paradigm, while useful, suffers from a lack of more direct understanding of system connections. We identified that the key to address these shortcomings is to improve modeling of the system connections and treat the coupled solar wind-MIT system, or geospace system, together. The ionospheric conductivity is a critical component of this objective.

How can indirect observations be used most effectively to study ionospheric conductivity?

Chapter 4 addressed the use of indirect observations to study conductivity. We introduced the GLobal AirglOW (GLOW) model, which takes an input particle energy spectrum and produces altitude profiles of the ionization and dissociation rates and ion and electron densities based on a robust two-stream electron transport code. We implemented a module that calculates the altitude profiles of ionospheric Hall and Pedersen conductivities. The updated GLOW model permits indirect in-situ satellite observations of the particle environment incident on the ionosphere to be used to study conductivities. We also created a new computationally-efficient version of the GLOW model, called GLOWfast, by replacing the computationally expensive electron transport algorithm with highly accurate parameterizations for solar photoionization (*Qian and Solomon*, 2012) and electron impact ionization (*Fang et al.*, 2008, 2010). GLOWfast is freely available to the community for scientific use and makes extensive evaluation of the GLOW model tractable. We anticipate

GLOWfast becoming a useful tool for the atmospheric modeling community.

Can we overcome assumptions on the energy spectrum of precipitating particles to analyze ionospheric conductivities?

Chapter 4 also addressed the use of prescribed functional forms to describe the electron energy spectra that determine the characteristics of electrons precipitating into the ionosphere, and, subsequently, conductivity changes. The most commonly assumed form is a Maxwellian distribution. However, we replaced this conventional approach by using electron energy spectra directly measured by the Defense Meteorological Satellite Program (DMSP) satellites, and, thus, free of assumption of the functional distribution. We created a modeling framework in which DMSP particle observations could be directly applied as input to the GLOW model. This enabled us to specify conductivity profiles at locations of DMSP observations without the limitations introduced by the Maxwellian assumption, a significant improvement and an important outcome of this dissertation.

How can we overcome the sparsity of indirect observations to study conductivity?

In Chapter 5 we compiled a database of more than 60 million one-second DMSP particle spectra to drive the estimation of global high-latitude patterns of variability for the Hall and Pedersen height-integrated conductivities, or conductances. We represented the variabilities as empirical orthogonal functions (EOFs). The work presented in Chapter 5 represented the first large-scale analysis of directly calculated ionospheric Hall and Pedersen conductances completely free of assumption of the incident electron energy spectra. It was also the first comprehensive EOF analysis of satellite particle precipitation data. We showed that this analysis, and an extension presented in Chapter 6, yielded a new fundamental picture of ionospheric conductance and revealed a number of new physical insights into the auroral processes.

Can we specify conductivities on finer spatial and temporal scales than current statistical models and, if so, what influence do these finer scales have on the specification of ionospheric electrodynamics?

In Chapter 7 we combined the improved modeling of conductivity and understanding of conductance variability from Chapters 4 and 5 to overcome observation sparsity and specify conductance on finer scales than past statistical models. We accomplished this by creating a new optimal interpolation (OI) technique that capably reconstructs the dynamically evolving global distribution of high-latitude Hall and Pedersen conductances from sparse instantaneous conductance observations available along satellite tracks. The sparse observational information is combined with a background conductance model and the uncertainty information associated with the background model and observations to yield estimated global conductance patterns. The OI technique can also yield an objective measure of the uncertainty associated with each estimated conductance pattern. This represented the first time a global assimilative analysis of the Hall and Pedersen conductances has been obtained from in-situ spectrally resolved particle precipitation observations. Based on a case study analysis of OI conductance distributions we found that this new technique quantitatively and qualitatively provides better ionospheric conductance specification than past statistical models, especially during heightened geomagnetic activity. We also showed that our OI conductance patterns allow Assimilative Mapping of Ionospheric Electrodynamics (AMIE) reconstructions driven separately by ground-based radar and satellite-based magnetometer observations to be in closer agreement than when other, commonly used, conductance models are applied. Finally, Chapter 7 illustrated that the OI conductance distributions better capture the dynamics and locations of discrete electron precipitation that modulate the coupling of the magnetosphere-ionosphere-thermosphere system and the behavior of each region.

What are the limitations of a two-dimensional representation of the ionosphere and what are the three-dimensional characteristics of the ionospheric conductivities?

Chapter 8 expanded the EOF analysis of Chapter 5 to three dimensions and compared the two-dimensional (2-D) and three-dimensional (3-D) variabilities of the Hall and Pedersen conductivities. We found distinct differences in the two representations. The modes of variability of height-integrated conductivities, often assumed to represent the entire ionosphere as a horizontal

slab at ∼120 km, and the modes for the 120 km altitude level in the 3-D analysis exhibited noticeable differences in spatial distribution and intensity. Additionally, the 3-D modes of variability revealed new understanding on the ionospheric conductivity variability: 1) conductivities exhibit fundamentally different, but simultaneously varying, responses to the direction of the interplanetary magnetic field (IMF) B_Z component; and 2) conductivities are significantly modified by Alfvénic Poynting flux-driven electron precipitation, which can be divided into first- and second-order responses. Our investigation emphasizes the importance of analyzing the E Region ionosphere in 3-D.

9.1.1 Importance of systems science approach

We motivated the work presented in this dissertation by the need to better understand the solar wind-magnetosphere-ionosphere-thermosphere system. We accomplished this objective by exploring the geospace environment as a closely coupled, complex system, rather than as separate components. The goal of geospace system science is to understand the energy pathways that permeate each region and create the connections between regions. The ionospheric conductivity largely determines the energy interactions in geospace, and is, therefore, a critical parameter for geospace system science. We addressed ionospheric conductivity through the application of advanced mathematical tools and cutting-edge computational techniques, leading to improved modeling and new understanding. Our findings provided new insight into the geospace environment. Therefore, this dissertation is strong evidence for the systems science approach.

9.2 Outlook

An important measure of the impact of a dissertation is through the new areas of research that it identifies and enables. In this final section, we provide a brief outlook to possible future directions for the continuation of this dissertation work.

9.2.1 Additional observations of the electron precipitation

The ability of the EOF and OI techniques presented in this dissertation depend in part on the data available to drive them. Space-based observations from the Fast Auroral Snapshot Explorer (FAST) spacecraft, electron density information from Global Positioning Services radio occultations (GPSRO), including profiles from the Constellation Observing System for Meteorology, Ionosphere, and Climate (COSMIC), and auroral imagery data can be used to complement DMSP observations to improve data coverage. To illustrate the potential for improved coverage Figures 9.1a and b show the distribution of electron precipitation observations from the FAST spacecraft in the northern hemisphere throughout 1997 and 1998, respectively.

Radio occultations from the COSMIC constellation provide unprecedented global coverage at short latency and high vertical resolution. Electron density profiles with these characteristics, properly coupled with atmospheric models to calculate conductivities, can help further constrain the OI technique presented in this dissertation. Given the large number of planned low Earth orbit (LEO) missions equipped with GPS receivers, LEO-GPS occultation data are important to the continuation of the work presented in this dissertation and to the future of geospace system science.

Auroral imagery data, such as those from the SSUSI instrument onboard the DMSP spacecraft that were used in Chapter 7, provide another means to improve spatial coverage of the polar ionosphere. Data products derived from the remotely sensed auroral optical emissions yield accurate information over large areas about the composition, energetics, and dynamics of the IT system. Incorporating these important, relatively untapped, data more fully into our conductivity and ionospheric electrodynamics analyses will be an important extension. Additionally, this will help pave the way to better utilize data from upcoming missions such as the Ionospheric CONnection Explorer (ICON) (*Immel*, 2012) and Global Observations of the Limb and Disk (GOLD) (*Eastes*, 2009).

Additional data coverage from FAST, COSMIC, and auroral imagery will permit generation of

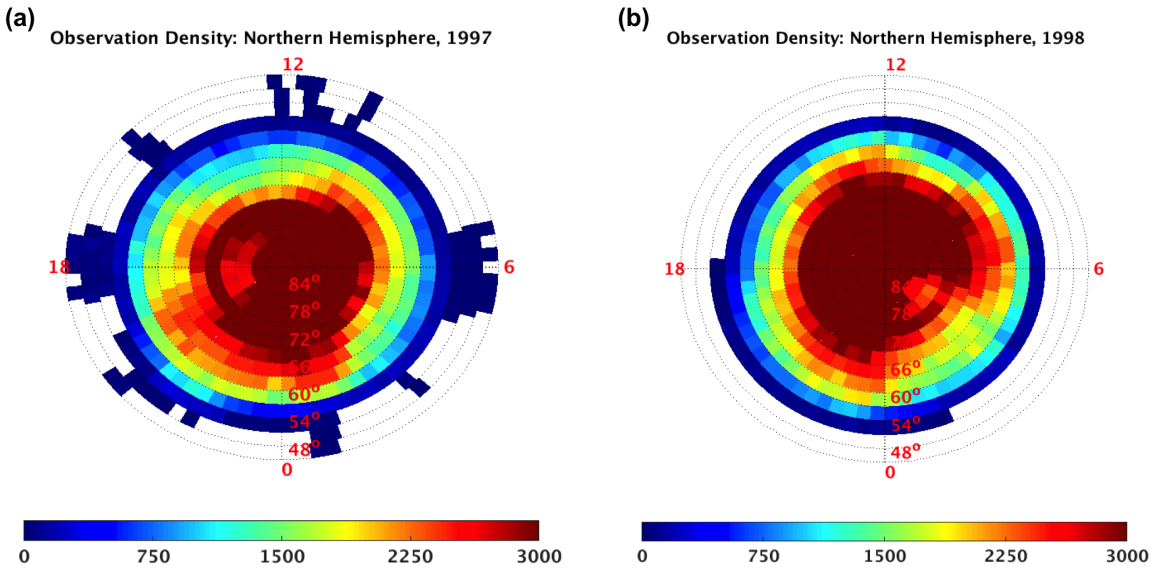

Figure 9.1: Distribution of FAST satellite observations in the northern hemisphere for two 12-month periods: (a) 1997 and (b) 1998. The data have been averaged over 60-seconds and resolved onto an equal-area grid for easy visual interpretation. Data are given in altitude adjusted corrected geomagnetic coordinates (AACGM).

separate EOFs for the northern and southern hemispheres. These may then be used to understand the asymmetries between the two hemispheres, an important area of current space science research (*Stenbaek-Nielsen et al.*, 1973; *Newell et al.*, 1996d; *Østgaard et al.*, 2003, 2005).

9.2.2 Ion precipitation influence on ionospheric conductivity

Ion (specifically proton) precipitation can be a significant perturbation to the auroral conductivities in specific locations and at certain times (*Galand and Richmond*, 2001b; *Galand et al.*, 2001). *Fang et al.* (2013) created a parameterization of proton impact ionization valid for incident proton energies between 100 eV and 1 MeV. To assess the role of proton precipitation on the MIT system, and particularly on the conductivities, their parameterization may be incorporated into an upper atmospheric model in the same manner that the *Fang et al.* (2008) and *Fang et al.* (2010) electron impact ionization parameterization was incorporated into the GLOW model in Chapter 4 of this dissertation.

9.2.3 OI technique improvement and extension

The OI technique can be improved in the future. The three primary components of the technique are: 1) conductance observations; 2) a background model; and 3) the error properties of each. Future improvement should focus on these components.

In Chapter 7 we provided initial evidence that auroral images from the Defense Meteorological Satellite Program Special Sensor Ultraviolet Spectrographic Imager instrument can be used to improve the OI conductance maps. Additional observations of the conductances (perhaps from the GLOW model with auroral input specified by FAST electron energy spectra) may provide similar benefit.

The background model error and observational error properties can also be further improved. Uncertainty quantification and propagation analyses for the background model and observations could lead to better knowledge of these error properties.

Finally, we are currently extending the OI technique to three dimensions using information

from the 3-D EOFs presented in Chapter 8. This technique will yield 3-D volumetric reconstructions of the global high-latitude ionospheric conductivities, and will be a critical piece for future ionospheric electrodynamics analyses, particular the next generation of the Assimilative Mapping of Ionospheric Electrodynamics (AMIE NextGen - http://ncwebserv.colorado.edu/∼matsuot/AMIEnextgen/index.html).

9.2.4 Impact on neutral density specification and satellite drag

It will be important to assess the impact of our new height-dependent conductivity modeling capabilities on specification of upper atmospheric neutral density. The conductivity mediates ion-neutral coupling (*Richmond*, 2011). In Chapter 7 we showed that the ionospheric conductances are highly structured both spatially and temporally, and, in Chapter 8, found that the variability of the conductivities are strongly functions of altitude as well. These strong 3-D spatial and temporal dependencies, therefore, affect the upper atmospheric neutral density and thermospheric dynamics.

The state of the thermosphere determines the atmospheric drag experienced by low altitude satellites and space debris, and is the dominant uncertainty in orbit determination for these objects (*Marcos et al.*, 2006; *Bowman et al.*, 2008). Collision prevention for the International Space Station, conjunction analysis, satellite lifetime estimates, space situational awareness, and reentry prediction are just a few of the critical applications for precise orbit determination and tracking. Because of it's importance to the critical engineering and operational concerns associated with satellite drag and collision avoidance, more accurate specification of 3-D neutral densities is a significant area of future research that is enabled by the new 3-D conductivity modeling capabilities provided by this dissertation.

Bibliography

A, E., D. Zhang, A. J. Ridley, Z. Xiao, and Y. Hao (2012), A global model: Empirical orthogonal function analysis of total electron content 1999-2009 data, *Journal of Geophysical Research: Space Physics*, *117*(A3), A03328, doi:10.1029/2011JA017238.

Ahn, B.-H., A. D. Richmond, Y. Kamide, H. W. Kroehl, B. A. Emery, O. de la Beaujardiére, and S.-I. Akasofu (1998), An ionospheric conductance model based on ground magnetic disturbance data, *Journal of Geophysical Research: Space Physics*, *103*(A7), 14,769–14,780, doi:10.1029/97JA03088.

Akasofu, S.-I., and J. Kan (1982), Importance of initial ionospheric conductivity on substorm onset, *Planetary and Space Science*, *30*(12), 1315 – 1316, doi:http://dx.doi.org/10.1016/0032-0633(82)90105-2.

Aksnes, A., J. Stadsnes, J. Bjordal, N. Østgaard, R. R. Vondrak, D. L. Detrick, T. J. Rosenberg, G. A. Germany, and D. Chenette (2002), Instantaneous ionospheric global conductance maps during an isolated substorm, *Annales Geophysicae*, *20*(8), 1181–1191, doi:10.5194/angeo-20-1181-2002.

Amm, O., and A. Viljanen (1999), Ionospheric disturbance magnetic field continuation from the ground to the ionosphere using spherical elementary current systems, *Earth, Planets and Space*, *51*(6), 431–440, doi:10.1186/BF03352247.

Amm, O., A. Aruliah, S. C. Buchert, R. Fujii, J. W. Gjerloev, A. Ieda, T. Matsuo, C. Stolle, H. Vanhamäki, and A. Yoshikawa (2008), Towards understanding the electrodynamics of the 3-dimensional high-latitude ionosphere: Present and future, *Annales Geophysicae*, *26*(12), 3913–3932, doi:10.5194/angeo-26-3913-2008.

Andersson, L., N. Ivchenko, J. Clemmons, A. A. Namgaladze, B. Gustavsson, J.-E. Wahlund, L. Eliasson, and R. Y. Yurik (2002), Electron signatures and Alfvén waves, *Journal of Geophysical Research: Space Physics*, *107*(A9), 1244, doi:10.1029/2001JA900096.

Bailey, S. M., C. A. Barth, and S. C. Solomon (2002), A model of nitric oxide in the lower thermosphere, *Journal of Geophysical Research: Space Physics*, *107*(A8), SIA 22–1–SIA 22–12, doi:10.1029/2001JA000258.

Baker, K. B., and S. Wing (1989), A new magnetic coordinate system for conjugate studies at high latitudes, *Journal of Geophysical Research: Space Physics*, *94*(A7), 9139–9143, doi:10.1029/JA094iA07p09139.

Banks, G., and P. Kockarts (1973), *Aeronomy*, Academic Press, doi: http://dx.doi.org/10.1016/B978-0-12-077802-7.50005-1.

Banks, P. (1966a), Collision frequencies and energy transfer electrons, *Planetary and Space Science*, *14*(11), 1085 – 1103, doi:http://dx.doi.org/10.1016/0032-0633(66)90024-9.

Banks, P. (1966b), Collision frequencies and energy transfer ions, *Planetary and Space Science*, *14*(11), 1105 – 1122, doi:http://dx.doi.org/10.1016/0032-0633(66)90025-0.

Banks, P. M., and A. F. Nagy (1970), Concerning the influence of elastic scattering upon photoelectron transport and escape, *Journal of Geophysical Research*, *75*(10), 1902–1910, doi: 10.1029/JA075i010p01902.

Banks, P. M., C. R. Chappell, and A. F. Nagy (1974), A new model for the interaction of auroral electrons with the atmosphere: Spectral degradation, backscatter, optical emission, and ionization, *Journal of Geophysical Research*, *79*(10), 1459–1470, doi:10.1029/JA079i010p01459.

Bartels, J., N. H. Heck, and H. F. Johnston (1939), The three-hour-range index measuring geomagnetic activity, *Terrestrial Magnetism and Atmospheric Electricity*, *44*(4), 411–454, doi: 10.1029/TE044i004p00411.

Baumjohann, W. (1982), Ionospheric and field-aligned current systems in the auroral zone: A concise review, *Advances in Space Research*, *2*(10), 55 – 62, doi:http://dx.doi.org/10.1016/0273-1177(82)90363-5, Proceedings of the Topical Meeting of the COSPAR Interdisciplinary Scientific Commission C of the COSPAR Twenty-fourth Plenary Meeting.

Berger, M., S. Seltzer, and K. Maeda (1974), Some new results on electron transport in the atmosphere, *Journal of Atmospheric and Terrestrial Physics*, *36*(4), 591 – 617, doi: http://dx.doi.org/10.1016/0021-9169(74)90085-3.

Berger, M. J., S. M. Seltzer, and K. Maeda (1970), Energy deposition by auroral electrons in the atmosphere, *Journal of Atmospheric and Terrestrial Physics*, *32*(6), 1015 – 1045, doi: http://dx.doi.org/10.1016/0021-9169(70)90115-7.

Bilitza, D. (1990), International reference ionosphere 1990, *Tech. Rep. NSSDC/WDC-A-R&S 90-22*, National Space Science Data Center, Lanham, Maryland.

Bilitza, D. (2001), International reference ionosphere 2000, *Radio Science*, *36*(2), 261–275, doi: 10.1029/2000RS002432.

Bilitza, D., D. Altadill, Y. Zhang, C. Mertens, V. Truhlik, P. Richards, L. McKinnell, and B. Reinisch (2014), The International Reference Ionosphere 2012: A model of international collaboration, *J. Space Weather Space Clim.*, *4*, A07, doi:10.1051/swsc/2014004.

Borovsky, J. E. (2013), Physical improvements to the solar wind reconnection control function for the Earth's magnetosphere, *Journal of Geophysical Research: Space Physics*, *118*(5), 2113–2121, doi:10.1002/jgra.50110.

Borovsky, J. E., and T. E. Cayton (2011), Entropy mapping of the outer electron radiation belt between the magnetotail and geosynchronous orbit, *Journal of Geophysical Research: Space Physics*, *116*(A6), A06216, doi:10.1029/2011JA016470.

Borovsky, J. E., and M. H. Denton (2013), The differences between storms driven by helmet streamer CIRs and storms driven by pseudostreamer CIRs, *Journal of Geophysical Research: Space Physics*, *118*, 1–16, doi:10.1002/jgra.50524.

Bowman, B., K. Tobiska, F. Marcos, C. Huang, C. Lin, and W. Burke (2008), A new empirical thermospheric density model, JB2008 using new solar and geomagnetic indices, in *Proceedings of the American Institute of Aerodynamics and Astronautics*, 2008-6438, Air Force Space Command, AIAA.

Brekke, A., and J. Moen (1993), Observations of high latitude ionospheric conductances, *Journal of Atmospheric and Terrestrial Physics*, *55*(1112), 1493 – 1512, doi:http://dx.doi.org/10.1016/0021-9169(93)90126-J, The XX IUGG General Assembly.

Brekke, A., J. R. Doupnik, and P. M. Banks (1974), Incoherent scatter measurements of E region conductivities and currents in the auroral zone, *Journal of Geophysical Research*, *79*(25), 3773–3790, doi:10.1029/JA079i025p03773.

Burke, W. J., C. Y. Huang, and F. J. Rich (2006), Energetics of the April 2000 magnetic superstorm observed by DMSP, *Advances in Space Research: [Special Issue] The Great Historical Geomagnetic Storm of 1859: A Modern Look*, *38*(2), 239 – 252, doi:10.1016/j.asr.2005.07.085.

Burke, W. J., C. S. Lin, M. P. Hagan, C. Y. Huang, D. R. Weimer, J. O. Wise, L. C. Gentile, and F. A. Marcos (2009), Storm time global thermosphere: A driven-dissipative thermodynamic system, *Journal of Geophysical Research: Space Physics*, *114*(A6), A06306, doi:10.1029/2008JA013848.

Burnside, R. G., C. A. Tepley, and V. B. Wickwar (1987), The O(+)-O collision cross-section - Can it be inferred from aeronomical measurements?, *Annales Geophysicae*, *5*, 343–349.

Carlson, C., J. McFadden, P. Turin, D. Curtis, and A. Magoncelli (2001), The electron and ion plasma experiment for fast, in *The FAST Mission*, edited by J. Pfaff, R.F., pp. 33–66, Springer Netherlands, doi:10.1007/978-94-010-0332-2_2.

Carter, J. A., S. E. Milan, J. C. Coxon, M.-T. Walach, and B. J. Anderson (2016), Average field-aligned current configuration parameterized by solar wind conditions, *Journal of Geophysical Research: Space Physics*, 2015JA021567, doi:10.1002/2015JA021567.

Cassak, P. A. (2016), Inside the black box: Magnetic reconnection and the Magnetospheric Multiscale Mission, *Space Weather*, 2015SW001313, doi:10.1002/2015SW001313.

Chapman, S. (1931a), The absorption and dissociative or ionizing effect of monochromatic radiation in an atmosphere on a rotating earth, *Proceedings of the Physical Society*, *43*(1), 26.

Chapman, S. (1931b), The absorption and dissociative or ionizing effect of monochromatic radiation in an atmosphere on a rotating earth part II. Grazing incidence, *Proceedings of the Physical Society*, *43*(5), 483.

Chappell, C. R. (1969), The Interaction of Auroral Electrons with the Atmosphere., Ph.D. thesis, Rice University.

Chaston, C. C., L. M. Peticolas, C. W. Carlson, J. P. McFadden, F. Mozer, M. Wilber, G. K. Parks, A. Hull, R. E. Ergun, R. J. Strangeway, M. Andre, Y. Khotyaintsev, M. L. Goldstein, M. Acua, E. J. Lund, H. Reme, I. Dandouras, A. N. Fazakerley, and A. Balogh (2005), Energy deposition by Alfvén waves into the dayside auroral oval: Cluster and FAST observations, *Journal of Geophysical Research: Space Physics*, *110*(A2), A02211, doi:10.1029/2004JA010483.

Chaston, C. C., C. W. Carlson, J. P. McFadden, R. E. Ergun, and R. J. Strangeway (2007), How important are dispersive Alfvén waves for auroral particle acceleration?, *Geophysical Research Letters*, *34*(7), L07101, doi:10.1029/2006GL029144.

Chen, G.-m., J. Xu, W. Wang, J. Lei, and A. G. Burns (2012), A comparison of the effects of CIR- and CME-induced geomagnetic activity on thermospheric densities and spacecraft orbits: Case studies, *Journal of Geophysical Research*, *117*(A08315), doi:10.1029/2012JA017782.

Christon, S. P., D. J. Williams, D. G. Mitchell, C. Y. Huang, and L. A. Frank (1991), Spectral characteristics of plasma sheet ion and electron populations during disturbed geomagnetic conditions, *Journal of Geophysical Research: Space Physics*, *96*(A1), 1–22, doi:10.1029/90JA01633.

Clauer, C. R., and Y. Kamide (1985), DP 1 and DP 2 current systems for the March 22, 1979 substorms, *Journal of Geophysical Research: Space Physics*, *90*(A2), 1343–1354, doi:10.1029/JA090iA02p01343.

Clausen, L. B. N., J. B. H. Baker, J. M. Ruohoniemi, S. E. Milan, J. C. Coxon, S. Wing, S. Ohtani, and B. J. Anderson (2013), Temporal and spatial dynamics of the regions 1 and 2 Birkeland currents during substorms, *Journal of Geophysical Research: Space Physics*, *118*(6), 3007–3016, doi:10.1002/jgra.50288.

Codrescu, M. V., T. J. Fuller-Rowell, and J. C. Foster (1995), On the importance of E-field variability for Joule heating in the high-latitude thermosphere, *Geophysical Research Letters*, *22*(17), 2393–2396, doi:10.1029/95GL01909.

Connors, M. (1998), Auroral current systems studied using automated forward modeling, Ph.D. thesis, Department of Physics, University of Alberta.

Cosgrove, R., M. McCready, R. Tsunoda, and A. Stromme (2011), The bias on the Joule heating estimate: Small-scale variability versus resolved-scale model uncertainty and the correlation of electric field and conductance, *Journal of Geophysical Research: Space Physics*, *116*(A9), A09320, doi:10.1029/2011JA016665.

Cosgrove, R. B., G. Lu, H. Bahcivan, T. Matsuo, C. J. Heinselman, and M. A. McCready (2009), Comparison of AMIE-modeled and Sondrestrom-measured Joule heating: A study in model resolution and electric field–conductivity correlation, *Journal of Geophysical Research: Space Physics*, *114*(A4), A04316, doi:10.1029/2008JA013508.

Cosgrove, R. B., H. Bahcivan, S. Chen, R. J. Strangeway, J. Ortega, M. Alhassan, Y. Xu, M. V. Welie, J. Rehberger, S. Musielak, and N. Cahill (2014), Empirical model of Poynting flux derived from FAST data and a cusp signature, *Journal of Geophysical Research: Space Physics*, *119*(1), 411–430, doi:10.1002/2013JA019105.

Coumans, V., J.-C. Gérard, B. Hubert, M. Meurant, and S. B. Mende (2004), Global auroral conductance distribution due to electron and proton precipitation from IMAGE-FUV observations, *Annales Geophysicae*, *22*(5), 1595–1611, doi:10.5194/angeo-22-1595-2004.

Cousins, E. D. P., and S. G. Shepherd (2012), Statistical maps of small-scale electric field variability in the high-latitude ionosphere, *Journal of Geophysical Research: Space Physics*, *117*(A12), A12304, doi:10.1029/2012JA017929.

Cousins, E. D. P., T. Matsuo, and A. D. Richmond (2013a), Mesoscale and large-scale variability in high-latitude ionospheric convection: Dominant modes and spatial/temporal coherence, *Journal of Geophysical Research: Space Physics*, *118*(12), 7895–7904, doi:10.1002/2013JA019319.

Cousins, E. D. P., T. Matsuo, and A. D. Richmond (2013b), SuperDARN assimilative mapping, *Journal of Geophysical Research: Space Physics*, *118*(12), 7954–7962, doi:10.1002/2013JA019321.

Cousins, E. D. P., T. Matsuo, and A. D. Richmond (2015a), Mapping high-latitude ionospheric electrodynamics with SuperDARN and AMPERE, *Journal of Geophysical Research: Space Physics*, 2014JA020463, doi:10.1002/2014JA020463.

Cousins, E. D. P., T. Matsuo, A. D. Richmond, and B. J. Anderson (2015b), Dominant modes of variability in large-scale Birkeland currents, *Journal of Geophysical Research: Space Physics*, *120*(8), 2014JA020462, doi:10.1002/2014JA020462.

Cowley, S. W. H. (1995), The Earth's magnetosphere: A brief beginner's guide, *Eos, Transactions American Geophysical Union*, *76*(51), 525–529, doi:10.1029/95EO00322.

Cowley, S. W. H. (2000), Magnetosphere-ionosphere interactions: A tutorial review, in *Magnetospheric Current Systems*, edited by S.-I. Ohtani, R. Fujii, M. Hesse, and R. L. Lysak, pp. 91–106, American Geophysical Union, Washington, D.C., doi:10.1029/GM118p0091.

Cowley, S. W. H., and M. Lockwood (1992), Excitation and decay of solar wind-driven flows in the magnetosphere-ionosphere system, *Annales Geophysicae*, *10*, 103–115.

Coxon, J. C., S. E. Milan, L. B. N. Clausen, B. J. Anderson, and H. Korth (2014), The magnitudes of the regions 1 and 2 Birkeland currents observed by AMPERE and their role in solar wind-magnetosphere-ionosphere coupling, *Journal of Geophysical Research: Space Physics*, *119*(12), 2014JA020138, doi:10.1002/2014JA020138.

Crooker, N. U. (1992), Reverse convection, *Journal of Geophysical Research: Space Physics*, *97*(A12), 19,363–19,372, doi:10.1029/92JA01532.

Crowley, G., and C. L. Hackert (2001), Quantification of high latitude electric field variability, *Geophysical Research Letters*, *28*(14), 2783–2786, doi:10.1029/2000GL012624.

Crowley, G., D. J. Knipp, K. A. Drake, J. Lei, E. Sutton, and H. Lhr (2010), Thermospheric density enhancements in the dayside cusp region during strong By conditions, *Geophysical Research Letters*, *37*(7), L07110, doi:10.1029/2009GL042143.

Dahlgren, H., G. Perry, J.-P. St Maurice, T. Sundberg, K. Hosokawa, J. L. Semeter, M. J. Nicolls, and K. Shiokawa (2014), 3D imaging reveals electrodynamics of polar cap aurora, *Astronomy and Geophysics*, *55*(5), 5.26–5.28, doi:10.1093/astrogeo/atu215.

Daley, R. (1993), *Atmospheric Data Analysis*, Cambridge Atmospheric and Space Science Series, Cambridge University Press.

Davies, J., and M. Lester (1998), The relationship between electric fields, conductances and currents in the high-latitude ionosphere: A statistical study using EISCAT data, *Annales Geophysicae*, *17*(1), 43–52, doi:10.1007/s00585-999-0043-3.

de Boer, J. D., J.-M. A. Noël, and J.-P. St.-Maurice (2010), The effects of mesoscale regions of precipitation on the ionospheric dynamics, electrodynamics and electron density in the presence of strong ambient electric fields, *Annales Geophysicae*, *28*(6), 1345–1360, doi:10.5194/angeo-28-1345-2010.

de la Beaujardiere, O., R. Vondrak, R. Heelis, W. Hanson, and R. Hoffman (1981), Auroral arc electrodynamic parameters measured by AE-C and the Chatanika radar, *Journal of Geophysical Research: Space Physics*, *86*(A6), 4671–4685, doi:10.1029/JA086iA06p04671.

Demmel, J. W. (1997), *Applied Numerical Linear Algebra*, Society for Industrial and Applied Mathematics, Philadelphia, PA, USA.

Deng, Y., T. J. Fuller-Rowell, A. J. Ridley, D. Knipp, and R. E. Lopez (2013), Theoretical study: Influence of different energy sources on the cusp neutral density enhancement, *Journal of Geophysical Research: Space Physics*, *118*(5), 2340–2349, doi:10.1002/jgra.50197.

Deng, Y., C. Sheng, Y.-J. Su, M. R. Hairston, D. Knipp, C. Y. Huang, D. Ober, R. J. Redmon, and R. Coley (2015), Correlation between Poynting flux and soft electron precipitation in the dayside polar cap boundary regions, *Journal of Geophysical Research: Space Physics*, *120*(10), 2015JA021075, doi:10.1002/2015JA021075.

Drayton, R. A., A. V. Koustov, M. R. Hairston, and J.-P. Villain (2005), Comparison of DMSP cross-track ion drifts and SuperDARN line-of-sight velocities, *Annales Geophysicae*, *23*(7), 2479–2486, doi:10.5194/angeo-23-2479-2005.

Dungey, J. W. (1961), Interplanetary magnetic field and the auroral zones, *Phys. Rev. Lett.*, *6*, 47–48, doi:10.1103/PhysRevLett.6.47.

Eastes, R. (2009), NASA mission to explore forcing of Earth's space environment, *Eos, Transactions American Geophysical Union*, *90*(18), 155–155, doi:10.1029/2009EO180002.

Eastwood, J. P., T. D. Phan, J. F. Drake, M. A. Shay, A. L. Borg, B. Lavraud, and M. G. G. T. Taylor (2013), Energy partition in magnetic reconnection in Earth's magnetotail, *Phys. Rev. Lett.*, *110*, 225,001, doi:10.1103/PhysRevLett.110.225001.

Ebihara, Y., M.-C. Fok, R. A. Wolf, T. J. Immel, and T. E. Moore (2004), Influence of ionosphere conductivity on the ring current, *Journal of Geophysical Research: Space Physics*, *109*(A8), A08205, doi:10.1029/2003JA010351.

Elphinstone, R. D., J. S. Murphree, and L. L. Cogger (1996), What is a global auroral substorm?, *Reviews of Geophysics*, *34*(2), 169–232, doi:10.1029/96RG00483.

Emery, B., D. Evans, M. Greer, E. Holeman, K. Kadinsky-Cade, F. Rich, and W. Xu (2006), Low energy auroral electron and ion hemispheric power after NOAA and DMSP intersatellite adjustments, *Tech. Rep. NCAR/TN-470+STR*, National Center for Atmospheric Research, High Altitude Observatory (HAO), Boulder, CO.

Evans, D. (1987), Global statistical patterns of auroral phenomena, in *Quantitative Modeling of Magnetospheric-Ionospheric Coupling Processes*, edited by Y. Kamide and R. Wolf, p. 325, Kyoto Sangyo Univ.

Evans, D. S., N. C. Maynard, J. Trøim, T. Jacobsen, and A. Egeland (1977), Auroral vector electric field and particle comparisons, 2: Electrodynamics of an arc, *Journal of Geophysical Research*, *82*(16), 2235–2249, doi:10.1029/JA082i016p02235.

Fang, X., M. W. Liemohn, J. U. Kozyra, D. S. Evans, A. D. DeJong, and B. A. Emery (2007a), Global 30-240 keV proton precipitation in the 17-18 April 2002 geomagnetic storms: 1. Patterns, *Journal of Geophysical Research: Space Physics*, *112*(A5), A05301, doi:10.1029/2006JA011867.

Fang, X., M. W. Liemohn, J. U. Kozyra, and D. S. Evans (2007b), Global 30-240 keV proton precipitation in the 17-18 April 2002 geomagnetic storms: 2. Conductances and beam spreading, *Journal of Geophysical Research: Space Physics*, *112*(A5), A05302, doi:10.1029/2006JA012113.

Fang, X., A. J. Ridley, M. W. Liemohn, J. U. Kozyra, and D. S. Evans (2007c), Global 30-240 keV proton precipitation in the 17-18 April 2002 geomagnetic storms: 3. Impact on the ionosphere and thermosphere, *Journal of Geophysical Research: Space Physics*, *112*(A7), A05302, doi:10.1029/2006JA012144.

Fang, X., C. E. Randall, D. Lummerzheim, S. C. Solomon, M. J. Mills, D. R. Marsh, C. H. Jackman, W. Wang, and G. Lu (2008), Electron impact ionization: A new parameterization for 100 eV to 1 MeV electrons, *Journal of Geophysical Research: Space Physics*, *113*(A9), A09311, doi:10.1029/2008JA013384.

Fang, X., C. E. Randall, D. Lummerzheim, W. Wang, G. Lu, S. C. Solomon, and R. A. Frahm (2010), Parameterization of monoenergetic electron impact ionization, *Geophysical Research Letters*, *37*(22), L22106, doi:10.1029/2010GL045406.

Fang, X., D. Lummerzheim, and C. H. Jackman (2013), Proton impact ionization and a fast calculation method, *Journal of Geophysical Research: Space Physics*, *118*(8), 5369–5378, doi:10.1002/jgra.50484.

Fear, R. C., M. Palmroth, and S. E. Milan (2012), Seasonal and clock angle control of the location of flux transfer event signatures at the magnetopause, *Journal of Geophysical Research: Space Physics*, *117*(A4), A04202, doi:10.1029/2011JA017235.

Fedder, J. A., and J. G. Lyon (1987), The solar wind-magnetosphere-ionosphere current-voltage relationship, *Geophysical Research Letters*, *14*(8), 880–883, doi:10.1029/GL014i008p00880.

Feldstein, Y. (1966), Peculiarities in the auroral distribution and magnetic disturbance distribution in high latitudes caused by the asymmetrical form of the magnetosphere, *Planetary and Space Science*, *14*(2), 121 – 130, doi:http://dx.doi.org/10.1016/0032-0633(66)90112-7.

Forbes, J. M., X. Zhang, E. R. Talaat, and W. Ward (2003), Nonmigrating diurnal tides in the thermosphere, *Journal of Geophysical Research: Space Physics*, *108*(A1), 1033, doi:10.1029/2002JA009262.

Forsyth, C., A. N. Fazakerley, A. P. Walsh, C. E. J. Watt, K. J. Garza, C. J. Owen, D. Constantinescu, I. Dandouras, K.-H. Fornaon, E. Lucek, G. T. Marklund, S. S. Sadeghi, Y. Khotyaintsev,

A. Masson, and N. Doss (2012), Temporal evolution and electric potential structure of the auroral acceleration region from multispacecraft measurements, *Journal of Geophysical Research: Space Physics*, *117*(A12), A12203, doi:10.1029/2012JA017655.

Foster, J. C., J. M. Holt, R. G. Musgrove, and D. S. Evans (1986), Ionospheric convection associated with discrete levels of particle precipitation, *Geophysical Research Letters*, *13*(7), 656–659, doi:10.1029/GL013i007p00656.

Frank, L. A., and K. L. Ackerson (1971), Observations of charged particle precipitation into the auroral zone, *Journal of Geophysical Research*, *76*(16), 3612–3643, doi:10.1029/JA076i016p03612.

Frey, H. U., S. B. Mende, V. Angelopoulos, and E. F. Donovan (2004), Substorm onset observations by IMAGE-FUV, *Journal of Geophysical Research: Space Physics*, *109*(A10), A10304, doi:10.1029/2004JA010607.

Fujii, R., R. A. Hoffman, P. C. Anderson, J. D. Craven, M. Sugiura, L. A. Frank, and N. C. Maynard (1994), Electrodynamic parameters in the nighttime sector during auroral substorms, *Journal of Geophysical Research: Space Physics*, *99*(A4), 6093–6112, doi:10.1029/93JA02210.

Fujiwara, H., R. Kataoka, M. Suzuki, S. Maeda, S. Nozawa, K. Hosokawa, H. Fukunishi, N. Sato, and M. Lester (2007), Electromagnetic energy deposition rate in the polar upper thermosphere derived from the EISCAT Svalbard radar and CUTLASS Finland radar observations, *Annales Geophysicae*, *25*(11), 2393–2403, doi:10.5194/angeo-25-2393-2007.

Fukushima, N. (1969), Equivalence in ground geomagnetic effect of Chapman-Vestine's and Birkeland-Alfvén's electric current-systems for polar magnetic storms, *Rep. Ionos. Space Res. Jpn*, *23*, 219–227.

Fukushima, N. (1976), Generalized theorem for no ground magnetic effect of vertical currents connected with Pedersen currents in the uniform-conductivity ionosphere, *Rep. Ionos. Space Res. Jpn*, *30*, 35–40.

Fuller-Rowell, T., M. Codrescu, and E. Araujo-Pradere (2001), Capturing the Storm-Time F-Region Ionospheric Response in an Empirical Model, in *Space Weather*, *Geophysical Monograph Series*, vol. 125, edited by P. Song, H. J. Singer, and G. L. Siscoe, pp. 393–401, American Geophysical Union, doi:10.1029/GM125p0393.

Fuller-Rowell, T. J., and D. S. Evans (1987), Height-integrated Pedersen and Hall conductivity patterns inferred from the TIROS-NOAA satellite data, *Journal of Geophysical Research: Space Physics*, *92*(A7), 7606–7618, doi:10.1029/JA092iA07p07606.

Galand, M., and A. D. Richmond (2001a), Ionospheric electrical conductances produced by auroral proton precipitation, *Journal of Geophysical Research: Space Physics*, *106*(A1), 117–125, doi:10.1029/1999JA002001.

Galand, M., and A. D. Richmond (2001b), Ionospheric electrical conductances produced by auroral proton precipitation, *Journal of Geophysical Research: Space Physics*, *106*(A1), 117–125, doi:10.1029/1999JA002001.

Galand, M., R. G. Roble, and D. Lummerzheim (1999), Ionization by energetic protons in Thermosphere-Ionosphere Electrodynamics General Circulation Model, *Journal of Geophysical Research: Space Physics*, *104*(A12), 27,973–27,989, doi:10.1029/1999JA900374.

Galand, M., T. J. Fuller-Rowell, and M. V. Codrescu (2001), Response of the upper atmosphere to auroral protons, *Journal of Geophysical Research: Space Physics*, *106*(A1), 127–139, doi: 10.1029/2000JA002009.

Gaspari, G., and S. E. Cohn (1999), Construction of correlation functions in two and three dimensions, *Quarterly Journal of the Royal Meteorological Society*, *125*(554), 723–757, doi: 10.1002/qj.49712555417.

Germany, G. A., M. R. Torr, P. G. Richards, and D. G. Torr (1990), The dependence of modeled OI 1356 and N2 Lyman Birge Hopfield auroral emissions on the neutral atmosphere, *Journal of Geophysical Research: Space Physics*, *95*(A6), 7725–7733, doi:10.1029/JA095iA06p07725.

Germany, G. A., D. G. Torr, P. G. Richards, M. R. Torr, and S. John (1994), Determination of ionospheric conductivities from FUV auroral emissions, *Journal of Geophysical Research: Space Physics*, *99*(A12), 23,297–23,305, doi:10.1029/94JA02038.

Germany, G. A., G. K. Parks, M. Brittnacher, J. Cumnock, D. Lummerzheim, J. F. Spann, L. Chen, P. G. Richards, and F. J. Rich (1997), Remote determination of auroral energy characteristics during substorm activity, *Geophysical Research Letters*, *24*(8), 995–998, doi:10.1029/97GL00864.

Gillies, R. G., G. C. Hussey, G. J. Sofko, K. A. McWilliams, R. A. D. Fiori, P. Ponomarenko, and J.-P. St.-Maurice (2009), Improvement of SuperDARN velocity measurements by estimating the index of refraction in the scattering region using interferometry, *Journal of Geophysical Research: Space Physics*, *114*(A7), A07305, doi:10.1029/2008JA013967.

Gillies, R. G., G. C. Hussey, G. J. Sofko, P. V. Ponomarenko, and K. A. McWilliams (2011), Improvement of HF coherent radar line-of-sight velocities by estimating the refractive index in the scattering volume using radar frequency shifting, *Journal of Geophysical Research: Space Physics*, *116*(A1), A01302, doi:10.1029/2010JA016043.

Gjerloev, J. W., and R. A. Hoffman (2000), Height-integrated conductivity in auroral substorms: 2. Modeling, *Journal of Geophysical Research: Space Physics*, *105*(A1), 227–235, doi: 10.1029/1999JA900353.

Gjerloev, J. W., and R. A. Hoffman (2002), Currents in auroral substorms, *Journal of Geophysical Research: Space Physics*, *107*(A8), SMP 5–1–SMP 5–13, doi:10.1029/2001JA000194.

Gjerloev, J. W., R. A. Hoffman, J. B. Sigwarth, and L. A. Frank (2007), Statistical description of the bulge-type auroral substorm in the far ultraviolet, *Journal of Geophysical Research: Space Physics*, *112*(A7), A07213, doi:10.1029/2006JA012189.

Gosling, J. T., M. F. Thomsen, S. J. Bame, R. C. Elphic, and C. T. Russell (1991), Observations of reconnection of interplanetary and lobe magnetic field lines at the high-latitude magnetopause, *Journal of Geophysical Research: Space Physics*, *96*(A8), 14,097–14,106, doi:10.1029/91JA01139.

Grocott, A., and S. E. Milan (2014), The influence of imf clock angle timescales on the morphology of ionospheric convection, *Journal of Geophysical Research: Space Physics*, *119*(7), 5861–5876, doi:10.1002/2014JA020136.

Gussenhoven, M. S. (1988), Low-altitude convection, precipitation, and current patterns in the baseline magnetosphere, *Reviews of Geophysics*, *26*(4), 792–808, doi:10.1029/RG026i004p00792.

Hagan, M. E., and J. M. Forbes (2002), Migrating and nonmigrating diurnal tides in the middle and upper atmosphere excited by tropospheric latent heat release, *Journal of Geophysical Research: Atmospheres*, *107*(D24), 4754, doi:10.1029/2001JD001236.

Hall, E. H. (1879), On a new action of the magnet on electric currents, *American Journal of Mathematics*, *11*(3), 287–292.

Hannachi, A., I. T. Jolliffe, and D. B. Stephenson (2007), Empirical orthogonal functions and related techniques in atmospheric science: A review, *International Journal of Climatology*, *27*(9), 1119–1152, doi:10.1002/joc.1499.

Hardy, D. A., L. K. Schmidt, M. S. Gussenhoven, F. J. Marshall, H. C. Yeh, T. L. Shumaker, A. Huber, and J. Pantazis (1984), Precipitating electron and ion detectors (SSJ/4) for the Block 5D/flights 6-10 DMSP satellites: Calibration and data presentation, *Tech. Rep. ADA157080*, Air Force Geophysics Laboratory, United States Air Force.

Hardy, D. A., M. S. Gussenhoven, and E. Holeman (1985), A statistical model of auroral electron precipitation, *Journal of Geophysical Research: Space Physics*, *90*(A5), 4229–4248, doi:10.1029/JA090iA05p04229.

Hardy, D. A., M. S. Gussenhoven, R. Raistrick, and W. J. McNeil (1987), Statistical and functional representations of the pattern of auroral energy flux, number flux, and conductivity, *Journal of Geophysical Research: Space Physics*, *92*(A11), 12,275–12,294, doi:10.1029/JA092iA11p12275.

Hardy, D. A., M. S. Gussenhoven, and D. Brautigam (1989), A statistical model of auroral ion precipitation, *Journal of Geophysical Research: Space Physics*, *94*(A1), 370–392, doi:10.1029/JA094iA01p00370.

Hardy, D. A., E. G. Holeman, W. J. Burke, L. C. Gentile, and K. H. Bounar (2008), Probability distributions of electron precipitation at high magnetic latitudes, *Journal of Geophysical Research: Space Physics*, *113*(A6), A06305, doi:10.1029/2007JA012746.

Hasunuma, T., T. Nagatsuma, R. Kataoka, Y. Takahashi, H. Fukunishi, A. Matsuoka, and A. Kumamoto (2008), Statistical study of polar distribution of mesoscale field-aligned currents, *Journal of Geophysical Research: Space Physics*, *113*(A12), A12214, doi:10.1029/2008JA013358.

He, M., J. Vogt, H. Lhr, E. Sorbalo, A. Blagau, G. Le, and G. Lu (2012), A high-resolution model of field-aligned currents through empirical orthogonal functions analysis (MFACE), *Geophysical Research Letters*, *39*(18), L18105, doi:10.1029/2012GL053168.

Heppner, J. P., M. C. Liebrecht, N. C. Maynard, and R. F. Pfaff (1993), High-latitude distributions of plasma waves and spatial irregularities from DE 2 alternating current electric field observations, *Journal of Geophysical Research: Space Physics*, *98*(A2), 1629–1652, doi:10.1029/92JA01836.

Heroux, L., and H. E. Hinteregger (1978), Aeronomical reference spectrum for solar UV below 2000 å, *Journal of Geophysical Research: Space Physics*, *83*(A11), 5305–5308, doi:10.1029/JA083iA11p05305.

Hinteregger, H. E., K. Fukui, and B. R. Gilson (1981), Observational, reference and model data on solar EUV, from measurements on AE-E, *Geophysical Research Letters*, *8*(11), 1147–1150, doi:10.1029/GL008i011p01147.

Hoffman, R. A., and J. L. Burch (1973), Electron precipitation patterns and substorm morphology, *Journal of Geophysical Research*, *78*(16), 2867–2884, doi:10.1029/JA078i016p02867.

Huang, C., Y. Huang, Y.-J. Su, E. Sutton, and M. Hairston (2015), Energy Flow in the Magnetosphere-Ionosphere-Thermosphere (MIT) System, *AGU Fall Meeting Abstracts*, (SM14A-06).

Huang, C. Y., and W. J. Burke (2004), Transient sheets of field-aligned current observed by DMSP during the main phase of a magnetic superstorm, *Journal of Geophysical Research: Space Physics*, *109*(A6), A06303, doi:10.1029/2003JA010067.

Huang, C. Y.-Y., Y. Huang, Y.-J. Su, E. K. Sutton, M. R. Hairston, and W. R. Coley (2016), Ionosphere-thermosphere (IT) response to solar wind forcing during magnetic storms, *J. Space Weather Space Clim.*, *6*, A4, doi:10.1051/swsc/2015041.

Iijima, T. (2000), Field-aligned currents in geospace: Substance and significance, in *Magnetospheric Current Systems*, edited by M. H. S.-I. Ohtani, R. Fujii and R. L. Lysak, pp. 107–129, American Geophysical Union, Washington, D. C., doi:10.1029/GM118p0107.

Iijima, T., and T. A. Potemra (1976a), The amplitude distribution of field-aligned currents at northern high latitudes observed by Triad, *Journal of Geophysical Research*, *81*(13), 2165–2174, doi:10.1029/JA081i013p02165.

Iijima, T., and T. A. Potemra (1976b), Field-aligned currents in the dayside cusp observed by Triad, *Journal of Geophysical Research*, *81*(34), 5971–5979, doi:10.1029/JA081i034p05971.

Iijima, T., and T. A. Potemra (1978), Large-scale characteristics of field-aligned currents associated with substorms, *Journal of Geophysical Research: Space Physics*, *83*(A2), 599–615, doi:10.1029/JA083iA02p00599.

Iijima, T., and T. Shibaji (1987), Global characteristics of northward IMF-associated (NBZ) field-aligned currents, *Journal of Geophysical Research: Space Physics*, *92*(A3), 2408–2424, doi:10.1029/JA092iA03p02408.

Immel, T. (2012), The Ionospheric Connection Explorer ICON: A pioneering research mission for space physics and aeronomy, *AGU Fall Meeting abstracts 2012*, (SA21C-06).

International Association of Geomagnetism and Aeronomy, Working Group V-MOD. Participating members, C. C. Finlay, S. Maus, C. D. Beggan, T. N. Bondar, A. Chambodut, T. A. Chernova, A. Chulliat, V. P. Golovkov, B. Hamilton, M. Hamoudi, R. Holme, G. Hulot, W. Kuang, B. Langlais, V. Lesur, F. J. Lowes, H. Lhr, S. Macmillan, M. Mandea, S. McLean, C. Manoj, M. Menvielle, I. Michaelis, N. Olsen, J. Rauberg, M. Rother, T. J. Sabaka, A. Tangborn, L. Tffner-Clausen, E. Thbault, A. W. P. Thomson, I. Wardinski, Z. Wei, and T. I. Zvereva (2010), International geomagnetic reference field: the eleventh generation, *Geophysical Journal International*, *183*(3), 1216–1230, doi:10.1111/j.1365-246X.2010.04804.x.

James, G. M., T. J. Hastie, and C. A. Sugar (2000), Principal component models for sparse functional data, *Biometrika*, *87*, 587–602.

Joliffe, I. (2002), *Principal Component Analysis*, 2 ed., Springer New York, New York, doi:10.1007/b98835.

Jones, R., and M. Rees (1973), Time dependent studies of the aurora I. Ion density and composition, *Planetary and Space Science*, *21*(4), 537 – 557, doi:http://dx.doi.org/10.1016/0032-0633(73)90069-X.

Kadinsky-Cade, K., E. G. Holeman, J. McGarrity, F. J. Rich, W. F. Denig, W. J. Burke, and D. A. Hardy (2004), First results from the SSJ/5 precipitating particle sensor on DMSP F16: Simultaneous observation of keV and MeV particles during the 2003 Halloween storms, *AGU Spring Meeting Abstracts*, (85(1), Jt. Assem. Suppl., Abstract SH53A-03).

Kalnay, E. (2003), *Atmospheric Modeling, Data Assimilation and Predictability*, Cambridge University Press.

Kamide, Y. (1988), *Electrodynamic Processes in the Earth's Ionosphere and Magnetosphere*, Kyoto Sangyo University Press.

Kamide, Y., and A. Brekke (1975), Auroral electrojet current density deduced from the Chatanika Radar and from the Alaska Meridian Chain of magnetic observatories, *Journal of Geophysical Research*, *80*(4), 587–594, doi:10.1029/JA080i004p00587.

Kamide, Y., and S. Kokubun (1996), Two-component auroral electrojet: Importance for substorm studies, *Journal of Geophysical Research: Space Physics*, *101*(A6), 13,027–13,046, doi:10.1029/96JA00142.

Kamide, Y., and A. D. Richmond (1982), Ionospheric conductivity dependence of electric fields and currents estimated from ground magnetic observations, *Journal of Geophysical Research: Space Physics*, *87*(A10), 8331–8337, doi:10.1029/JA087iA10p08331.

Kamide, Y., and G. Rostoker (1977), The spatial relationship of field-aligned currents and auroral electrojets to the distribution of nightside auroras, *Journal of Geophysical Research*, *82*(35), 5589–5608, doi:10.1029/JA082i035p05589.

Kamide, Y., A. D. Richmond, and S. Matsushita (1981), Estimation of ionospheric electric fields, ionospheric currents, and field-aligned currents from ground magnetic records, *Journal of Geophysical Research: Space Physics*, *86*(A2), 801–813, doi:10.1029/JA086iA02p00801.

Kamide, Y., W. Sun, and S.-I. Akasofu (1996), The average ionospheric electrodynamics for the different substorm phases, *Journal of Geophysical Research: Space Physics*, *101*(A1), 99–109, doi:10.1029/95JA02990.

Keiling, A., J. R. Wygant, C. A. Cattell, F. S. Mozer, and C. T. Russell (2003), The global morphology of wave Poynting flux: Powering the aurora, *Science*, *299*(5605), 383–386, doi:10.1126/science.1080073.

Kepko, L., R. McPherron, O. Amm, S. Apatenkov, W. Baumjohann, J. Birn, M. Lester, R. Nakamura, T. Pulkkinen, and V. Sergeev (2014), Substorm current wedge revisited, *Space Science Reviews*, pp. 1–46, doi:10.1007/s11214-014-0124-9.

Kihn, E. A., and A. J. Ridley (2005), A statistical analysis of the assimilative mapping of ionospheric electrodynamics auroral specification, *Journal of Geophysical Research: Space Physics*, *110*(A7), A07305, doi:10.1029/2003JA010371.

Kirkwood, S., H. Opgenoorth, and J. Murphree (1988), Ionospheric conductivities, electric fields and currents associated with auroral substorms measured by the EISCAT radar, *Planetary and Space Science*, *36*(12), 1359 – 1380, doi:http://dx.doi.org/10.1016/0032-0633(88)90005-0.

Kivelson, M. G., and C. T. Russell (1995), *Introduction to Space Physics*, Cambridge ; New York : Cambridge University Press.

Knipp, D., W. Tobiska, and B. Emery (2004), Direct and indirect thermospheric heating sources for solar cycles 21-23, *Solar Physics*, *224*(1-2), 495–505, doi:10.1007/s11207-005-6393-4.

Knipp, D. J. (1989), Quantifying and reducing uncertainty in the assimilative mapping of ionospheric electrodynamics, Ph.D. thesis, UCLA via Air Force Institute of Tech Wright-Patterson Air Force Base.

Knipp, D. J., A. D. Richmond, G. Crowley, O. de la Beaujardiére, E. Friis-Christensen, D. S. Evans, J. C. Foster, I. W. McCrea, F. J. Rich, and J. A. Waldock (1989), Electrodynamic patterns for September 19, 1984, *Journal of Geophysical Research: Space Physics*, *94*(A12), 16,913–16,923, doi:10.1029/JA094iA12p16913.

Knipp, D. J., B. A. Emery, and G. Lu (1994), Application of the assimilative mapping of ionospheric electrodynamics (AMIE) procedure to cusp identification, in *Physical Signatures of Magnetospheric Boundary Layer Processes*, vol. 425, edited by J. A. Holtet and A. Egeland, pp. 401–420, doi:10.1007/978-94-011-1052-5_28.

Knipp, D. J., T. Matsuo, L. Kilcommons, A. Richmond, B. Anderson, H. Korth, R. Redmon, B. Mero, and N. Parrish (2014), Comparison of magnetic perturbation data from LEO satellite constellations: Statistics of DMSP and AMPERE, *Space Weather*, *12*(1), 2–23, doi:10.1002/2013SW000987.

Korth, H., L. Dyrud, B. Anderson, C. L. Waters, and R. J. Barnes (2010), AMPERE Science Data Reduction and Processing, *AGU Fall Meeting Abstracts*, A1692.

Korth, H., Y. Zhang, B. J. Anderson, T. Sotirelis, and C. L. Waters (2014), Statistical relationship between large-scale upward field-aligned currents and electron precipitation, *Journal of Geophysical Research: Space Physics*, *119*(8), 2014JA019961, doi:10.1002/2014JA019961.

Kozelov, B. V., I. V. Golovchanskaya, A. A. Ostapenko, and Y. V. Fedorenko (2008), Wavelet analysis of high-latitude electric and magnetic fluctuations observed by the Dynamic Explorer 2 satellite, *Journal of Geophysical Research: Space Physics*, *113*(A3), A03308, doi:10.1029/2007JA012575.

Kutiev, I., I. Tsagouri, L. Perrone, D. Pancheva, P. Mukhtarov, A. Mikhailov, J. Lastovicka, N. Jakowski, D. Buresova, E. Blanch, B. Andonov, D. Altadill, S. Magdaleno, M. Parisi, and J. Miquel Torta (2013), Solar activity impact on the earth's upper atmosphere, *J. Space Weather Space Clim.*, *3*, A06, doi:10.1051/swsc/2013028.

Le, G., J. A. Slavin, and R. J. Strangeway (2010), Space Technology 5 observations of the imbalance of regions 1 and 2 field-aligned currents and its implication to the cross-polar cap Pedersen currents, *Journal of Geophysical Research: Space Physics*, *115*(A7), A07202, doi:10.1029/2009JA014979.

Lei, J., S. Syndergaard, A. G. Burns, S. C. Solomon, W. Wang, Z. Zeng, R. G. Roble, Q. Wu, Y.-H. Kuo, J. M. Holt, S.-R. Zhang, D. L. Hysell, F. S. Rodrigues, and C. H. Lin (2007), Comparison of COSMIC ionospheric measurements with ground-based observations and model predictions: Preliminary results, *Journal of Geophysical Research: Space Physics*, *112*(A7), A07308, doi: 10.1029/2006JA012240.

Lei, J., J. P. Thayer, W. Wang, and R. L. McPherron (2011), Impact of CIR storms on thermosphere density variability during the solar minimum of 2008, *Solar Physics*, *274*, 427–437, doi:10.1007/s11207-010-9563-y.

Lei, J., T. Matsuo, X. Dou, E. Sutton, and X. Luan (2012), Annual and semiannual variations of thermospheric density: EOF analysis of CHAMP and GRACE data, *Journal of Geophysical Research: Space Physics*, *117*(A1), A01310, doi:10.1029/2011JA017324.

Lester, M., J. A. Davies, and T. S. Virdi (1996), High-latitude Hall and Pedersen conductances during substorm activity in the SUNDIAL-ATLAS campaign, *Journal of Geophysical Research: Space Physics*, *101*(A12), 26,719–26,728, doi:10.1029/96JA00979.

Li, W., J. Bortnik, R. M. Thorne, Y. Nishimura, V. Angelopoulos, and L. Chen (2011), Modulation of whistler mode chorus waves: 2. Role of density variations, *Journal of Geophysical Research: Space Physics*, *116*(A6), A06206, doi:10.1029/2010JA016313.

Liemohn, M. W., A. J. Ridley, P. C. Brandt, D. L. Gallagher, J. U. Kozyra, D. M. Ober, D. G. Mitchell, E. C. Roelof, and R. DeMajistre (2005), Parametric analysis of nightside conductance effects on inner magnetospheric dynamics for the 17 April 2002 storm, *Journal of Geophysical Research: Space Physics*, *110*(A12), A12S22, doi:10.1029/2005JA011109.

Lilensten, J., P. L. Blelly, W. Kofman, and D. Alcaydé (1997), Auroral ionospheric conductivities: A comparison between experiment and modeling, and theoretical F10.7-dependent model for EISCAT and ESR, *Annales Geophysicae*, *14*(12), 1297–1304, doi:10.1007/s00585-996-1297-7.

Lin, C. S., and R. A. Hoffman (1982), Observations of inverted-V electron precipitation, *Space Science Reviews*, *33*(4), 415–457, doi:10.1007/BF00212420.

Lockwood, M. (2013), Reconstruction and prediction of variations in the open solar magnetic flux and interplanetary conditions, *Living Reviews in Solar Physics*, *10*(4), doi:10.1007/lrsp-2013-4.

Lorenc, A. C. (1986), Analysis methods for numerical weather prediction, *Quarterly Journal of the Royal Meteorological Society*, *112*(474), 1177–1194, doi:10.1002/qj.49711247414.

Lorenz, E. (1956), *Empirical Orthogonal Functions and Statistical Weather Prediction*, Massachusetts Institute of Technology. Statistical Forecasting Project, Massachusetts Institute of Technology, Department of Meteorology.

Lotko, W. (1986), Diffusive acceleration of auroral primaries, *Journal of Geophysical Research: Space Physics*, *91*(A1), 191–203, doi:10.1029/JA091iA01p00191.

Lotko, W. (2007), The magnetosphere–ionosphere system from the perspective of plasma circulation: A tutorial, *Journal of Atmospheric and Solar-Terrestrial Physics*, *69*(3), 191–211, doi: 10.1016/j.jastp.2006.08.011.

Lotko, W., R. H. Smith, B. Zhang, J. E. Ouellette, O. J. Brambles, and J. G. Lyon (2014), Ionospheric control of magnetotail reconnection, *Science*, *345*(6193), 184–187, doi: 10.1126/science.1252907.

Lu, G., G. L. Siscoe, A. D. Richmond, T. I. Pulkkinen, N. A. Tsyganenko, H. J. Singer, and B. A. Emery (1997), Mapping of the ionospheric field-aligned currents to the equatorial magnetosphere, *Journal of Geophysical Research: Space Physics*, *102*(A7), 14,467–14,476, doi: 10.1029/97JA00744.

Lu, G., A. D. Richmond, J. M. Ruohoniemi, R. A. Greenwald, M. Hairston, F. J. Rich, and D. S. Evans (2001), An investigation of the influence of data and model inputs on assimilative mapping of ionospheric electrodynamics, *Journal of Geophysical Research: Space Physics*, *106*(A1), 417–433, doi:10.1029/2000JA000606.

Lu, J. Y., R. Rankin, R. Marchand, I. J. Rae, W. Wang, S. C. Solomon, and J. Lei (2007), Electrodynamics of magnetosphere-ionosphere coupling and feedback on magnetospheric field line resonances, *Journal of Geophysical Research: Space Physics*, *112*(A10), A10219, doi: 10.1029/2006JA012195.

Lummerzheim, D. (1992), Comparison of energy dissipation functions for high energy auroral electrons and ion precipitation, *Tech. Rep. UAG-R 318*, Geophysical Institute, University of Alaska Fairbanks.

Lummerzheim, D., and J. Lilensten (1994), Electron transport and energy degradation in the ionosphere: Evaluation of the numerical solution, comparison with laboratory experiments and auroral observations, *Annales Geophysicae*, *12*(10-11), 1039–1051, doi:10.1007/s00585-994-1039-7.

Lummerzheim, D., M. Rees, and H. Anderson (1989), Angular dependent transport of auroral electrons in the upper atmosphere, *Planetary and Space Science*, *37*(1), 109 – 129, doi: http://dx.doi.org/10.1016/0032-0633(89)90074-3.

Lummerzheim, D., M. Rees, J. Craven, and L. Frank (1991), Ionospheric conductances derived from DE-1 auroral images, *Journal of Atmospheric and Terrestrial Physics*, *53*(34), 281 – 292, doi:http://dx.doi.org/10.1016/0021-9169(91)90112-K, ionospheric Signatures of Magnetospheric Phenomena.

Lummerzheim, D., M. Brittnacher, D. Evans, G. A. Germany, G. K. Parks, M. H. Rees, and J. F. Spann (1997), High time resolution study of the hemispheric power carried by energetic electrons into the ionosphere during the May 19/20, 1996 auroral activity, *Geophysical Research Letters*, *24*(8), 987–990, doi:10.1029/96GL03828.

Lynch, K. A., D. L. Hampton, M. Zettergren, T. A. Bekkeng, M. Conde, P. A. Fernandes, P. Horak, M. Lessard, R. Miceli, R. Michell, J. Moen, M. Nicolls, S. P. Powell, and M. Samara (2015), MICA sounding rocket observations of conductivity-gradient-generated auroral ionospheric responses: Small-scale structure with large-scale drivers, *Journal of Geophysical Research: Space Physics*, *120*(11), 2014JA020860, doi:10.1002/2014JA020860.

Maeda, S., S. Nozawa, M. Sugino, H. Fujiwara, and M. Suzuki (2002), Ion and neutral temperature distributions in the E-region observed by the EISCAT Tromsø and Svalbard radars, *Annales Geophysicae*, *20*(9), 1415–1427, doi:10.5194/angeo-20-1415-2002.

Maeda, S., S. Nozawa, Y. Ogawa, and H. Fujiwara (2005), Comparative study of the high-latitude E region ion and neutral temperatures in the polar cap and the auroral region derived from the EISCAT radar observations, *Journal of Geophysical Research: Space Physics*, *110*(A8), A08301, doi:10.1029/2004JA010893.

Maezawa, K. (1976), Magnetospheric convection induced by the positive and negative Z components of the interplanetary magnetic field: Quantitative analysis using polar cap magnetic records, *Journal of Geophysical Research*, *81*(13), 2289–2303, doi:10.1029/JA081i013p02289.

Marcos, F. A., B. Bowman, and R. E. Sheehan (2006), Accuracy of earth's thermospheric neutral density models, in *In Proceedings of the AIAA/AAS Astrodynamics Specialist Conference and Exhibit*, edited by AIAA, 2006-6167, Air Force Research Laboratory.

Marklund, G. T., L. G. Blomberg, K. Stasiewicz, J. S. Murphree, R. Pottelette, L. J. Zanetti, T. A. Potemra, D. A. Hardy, and F. J. Rich (1988), Snapshots of high-latitude electrodynamics using Viking and DMSP F7 observations, *Journal of Geophysical Research: Space Physics*, *93*(A12), 14,479–14,492, doi:10.1029/JA093iA12p14479.

Marsal, S. (2015), Conductivities consistent with Birkeland currents in the AMPERE-driven TIE-GCM, *Journal of Geophysical Research: Space Physics*, 2015JA021385, doi: 10.1002/2015JA021385.

Marsal, S., A. D. Richmond, A. Maute, and B. J. Anderson (2012), Forcing the TIEGCM model with Birkeland currents from the Active Magnetosphere and Planetary Electrodynamics Response Experiment, *Journal of Geophysical Research: Space Physics*, *117*(A6), A06308, doi: 10.1029/2011JA017416.

Marsh, D. R., S. C. Solomon, and A. E. Reynolds (2004), Empirical model of nitric oxide in the lower thermosphere, *Journal of Geophysical Research: Space Physics*, *109*(A7), A07301, doi: 10.1029/2003JA010199.

Matsuo, T., and J. M. Forbes (2010), Principal modes of thermospheric density variability: Empirical orthogonal function analysis of CHAMP 2001-2008 data, *Journal of Geophysical Research: Space Physics*, *115*(A7), A07309, doi:10.1029/2009JA015109.

Matsuo, T., and A. D. Richmond (2008), Effects of high-latitude ionospheric electric field variability on global thermospheric Joule heating and mechanical energy transfer rate, *Journal of Geophysical Research: Space Physics*, *113*(A7), A07309, doi:10.1029/2007JA012993.

Matsuo, T., A. D. Richmond, and D. W. Nychka (2002), Modes of high-latitude electric field variability derived from DE-2 measurements: Empirical orthogonal function (EOF) analysis, *Geophysical Research Letters*, *29*(7), 11–1–11–4, doi:10.1029/2001GL014077.

Matsuo, T., A. D. Richmond, and G. Lu (2005), Optimal interpolation analysis of high-latitude ionospheric electrodynamics using empirical orthogonal functions: Estimation of dominant modes of variability and temporal scales of large-scale electric fields, *Journal of Geophysical Research: Space Physics*, *110*(A6), A06301, doi:10.1029/2004JA010531.

Matsuo, T., M. Fedrizzi, T. J. Fuller-Rowell, and M. V. Codrescu (2012), Data assimilation of thermospheric mass density, *Space Weather*, *10*(5), S05002, doi:10.1029/2012SW000773.

Matsuo, T., D. J. Knipp, A. D. Richmond, L. Kilcommons, and B. J. Anderson (2015), Inverse procedure for high-latitude ionospheric electrodynamics: Analysis of satellite-borne magnetometer data, *Journal of Geophysical Research: Space Physics*, *120*(6), 2014JA020565, doi:10.1002/2014JA020565.

McDiarmid, I. B., J. R. Burrows, and E. E. Budzinski (1976), Particle properties in the day side cleft, *Journal of Geophysical Research*, *81*(1), 221–226, doi:10.1029/JA081i001p00221.

McGranaghan, R., H. Godinez, S. Morley, D. Knipp, and T. Matsuo (2014), Global high-latitude conductivity modeling: New data and improved methods, *Los Alamos Space Weather Summer School Research Reports, http://www.swx-school.lanl.gov/papers/report2014.pdf*, (LA-UR 15-20136).

McGranaghan, R., D. J. Knipp, S. C. Solomon, and X. Fang (2015a), A fast, parameterized model of upper atmospheric ionization rates, chemistry, and conductivity, *Journal of Geophysical Research: Space Physics*, 2015JA021146, doi:10.1002/2015JA021146.

McGranaghan, R., D. J. Knipp, T. Matsuo, H. Godinez, R. J. Redmon, S. C. Solomon, and S. K. Morley (2015b), Modes of high-latitude auroral conductance variability derived from DMSP energetic electron precipitation observations: Empirical orthogonal function analysis, *Journal of Geophysical Research: Space Physics*, 2015JA021828, doi:10.1002/2015JA021828.

McGranaghan, R. M., D. J. Knipp, T. Matsuo, and E. Cousins (2016, submitted and revised), Optimal interpolation analysis of high-latitude ionospheric Hall and Pedersen conductivities: Application to assimilative ionospheric electrodynamics reconstruction, *Journal of Geophysical Research: Space Physics*, *121*.

McIntosh, R. C., and P. C. Anderson (2015), Maps of precipitating electron spectra characterized by Maxwellian and kappa distributions, *Journal of Geophysical Research: Space Physics*, *119*, 10,116–10,132, doi:10.1002/2014JA020080.

McPherron, R. L., C. T. Russell, and M. P. Aubry (1973), Satellite studies of magnetospheric substorms on August 15, 1968: 9. Phenomenological model for substorms, *Journal of Geophysical Research*, *78*(16), 3131–3149, doi:10.1029/JA078i016p03131.

McPherron, R. L., D. M. Baker, T. Pulkkinen, J. Kissinger, and X. Chu (2013), Changes in solar wind-magnetosphere coupling with solar cycle, season, and time relative to stream interfaces, *Journal of Atmospheric and Solar-Terrestrial Physics*, *99*, 1–13, doi:10.1016/j.jastp.2012.09.003.

Meng, C.-I. (1981), The auroral electron precipitation during extremely quiet geomagnetic conditions, *Journal of Geophysical Research: Space Physics*, *86*(A6), 4607–4627, doi:10.1029/JA086iA06p04607.

Merkine, V. G., K. Papadopoulos, G. Milikh, A. S. Sharma, X. Shao, J. Lyon, and C. Goodrich (2003), Effects of the solar wind electric field and ionospheric conductance on the cross polar cap potential: Results of global MHD modeling, *Geophysical Research Letters*, *30*(23), 2180, doi:10.1029/2003GL017903.

Milan, S. E., G. Provan, and B. Hubert (2007), Magnetic flux transport in the Dungey cycle: A survey of dayside and nightside reconnection rates, *Journal of Geophysical Research: Space Physics*, *112*(A1), A01209, doi:10.1029/2006JA011642.

Milan, S. E., T. A. Evans, and B. Hubert (2010), Average auroral configuration parameterized by geomagnetic activity and solar wind conditions, *Annales Geophysicae*, *28*(4), 1003–1012, doi: 10.5194/angeo-28-1003-2010.

Milan, S. E., J. S. Gosling, and B. Hubert (2012), Relationship between interplanetary parameters and the magnetopause reconnection rate quantified from observations of the expanding polar cap, *Journal of Geophysical Research: Space Physics*, *117*(A3), A03226, doi:10.1029/2011JA017082.

Millward, G. H., I. C. F. Mller-Wodarg, A. D. Aylward, T. J. Fuller-Rowell, A. D. Richmond, and R. J. Moffett (2001), An investigation into the influence of tidal forcing on F region equatorial vertical ion drift using a global ionosphere-thermosphere model with coupled electrodynamics, *Journal of Geophysical Research: Space Physics*, *106*(A11), 24,733–24,744, doi: 10.1029/2000JA000342.

Moen, J., and A. Brekke (1993), The solar flux influence on quiet time conductances in the auroral ionosphere, *Geophysical Research Letters*, *20*(10), 971–974, doi:10.1029/92GL02109.

Murphree, J., S. Ismail, L. Cogger, D. Wallis, G. Shepherd, R. Link, and D. Klumpar (1983), Characteristics of optical emissions and particle precipitation in polar cap arcs, *Planetary and Space Science*, *31*(2), 161–172, doi:http://dx.doi.org/10.1016/0032-0633(83)90051-X.

Nagy, A. F., and P. M. Banks (1970), Photoelectron fluxes in the ionosphere, *Journal of Geophysical Research*, *75*(31), 6260–6270, doi:10.1029/JA075i031p06260.

Nakano, S., T. Iyemori, and S. Yamashita (2002), Net field-aligned currents controlled by the polar ionospheric conductivity, *Journal of Geophysical Research: Space Physics*, *107*(A5), SMP 4–1–SMP 4–6, doi:10.1029/2001JA900177.

Newell, P. T., and J. W. Gjerloev (2011a), Evaluation of SuperMAG auroral electrojet indices as indicators of substorms and auroral power, *Journal of Geophysical Research: Space Physics*, *116*(A12), A12211, doi:10.1029/2011JA016779.

Newell, P. T., and J. W. Gjerloev (2011b), Substorm and magnetosphere characteristic scales inferred from the SuperMAG auroral electrojet indices, *Journal of Geophysical Research: Space Physics*, *116*(A12), A12232, doi:10.1029/2011JA016936.

Newell, P. T., and J. W. Gjerloev (2012), SuperMAG-based partial ring current indices, *Journal of Geophysical Research: Space Physics*, *117*(A5), A05215, doi:10.1029/2012JA017586.

Newell, P. T., and C.-I. Meng (1992), Mapping the dayside ionosphere to the magnetosphere according to particle precipitation characteristics, *Geophysical Research Letters*, *19*(6), 609–612, doi:10.1029/92GL00404.

Newell, P. T., W. J. Burke, E. R. Snchez, C.-I. Meng, M. E. Greenspan, and C. R. Clauer (1991), The low-latitude boundary layer and the boundary plasma sheet at low altitude: Prenoon precipitation regions and convection reversal boundaries, *Journal of Geophysical Research: Space Physics*, *96*(A12), 21,013–21,023, doi:10.1029/91JA01818.

Newell, P. T., K. M. Lyons, and C.-I. Meng (1996a), A large survey of electron acceleration events, *Journal of Geophysical Research: Space Physics*, *101*(A2), 2599–2614, doi:10.1029/95JA03147.

Newell, P. T., Y. I. Feldstein, Y. I. Galperin, and C.-I. Meng (1996b), Morphology of nightside precipitation, *Journal of Geophysical Research: Space Physics*, *101*(A5), 10,737–10,748, doi: 10.1029/95JA03516.

Newell, P. T., C.-I. Meng, and K. M. Lyons (1996c), Suppression of discrete aurorae by sunlight, *Nature*, *381*, 766 – 767, doi:10.1038/381766a0.

Newell, P. T., K. M. Lyons, and C.-I. Meng (1996d), A large survey of electron acceleration events, *Journal of Geophysical Research: Space Physics*, *101*(A2), 2599–2614, doi:10.1029/95JA03147.

Newell, P. T., T. Sotirelis, J. M. Ruohoniemi, J. F. Carbary, K. Liou, J. P. Skura, C.-I. Meng, C. Deehr, D. Wilkinson, and F. J. Rich (2002), OVATION: Oval variation, assessment, tracking, intensity, and online nowcasting, *Annales Geophysicae*, *20*(7), 1039–1047, doi:10.5194/angeo-20-1039-2002.

Newell, P. T., T. Sotirelis, K. Liou, C.-I. Meng, and F. J. Rich (2007), A nearly universal solar wind-magnetosphere coupling function inferred from 10 magnetospheric state variables, *Journal of Geophysical Research: Space Physics*, *112*(A1), A01206, doi:10.1029/2006JA012015.

Newell, P. T., T. Sotirelis, and S. Wing (2009), Diffuse, monoenergetic, and broadband aurora: The global precipitation budget, *Journal of Geophysical Research: Space Physics*, *114*(A9), A09207, doi:10.1029/2009JA014326.

Newell, P. T., T. Sotirelis, and S. Wing (2010), Seasonal variations in diffuse, monoenergetic, and broadband aurora, *Journal of Geophysical Research: Space Physics*, *115*(A3), A03216, doi: 10.1029/2009JA014805.

Newell, P. T., K. Liou, Y. Zhang, T. Sotirelis, L. J. Paxton, and E. J. Mitchell (2014), OVATION Prime-2013: Extension of auroral precipitation model to higher disturbance levels, *Space Weather*, *12*(6), 368–379, doi:10.1002/2014SW001056.

Nicolls, M. J., N. Aponte, S. A. Gonzlez, M. P. Sulzer, and W. L. Oliver (2006), Daytime F region ion energy balance at Arecibo for moderate to high solar flux conditions, *Journal of Geophysical Research: Space Physics*, *111*(A10), A10307, doi:10.1029/2006JA011664.

Nicolls, M. J., R. Cosgrove, and H. Bahcivan (2014), Estimating the vector electric field using monostatic, multibeam incoherent scatter radar measurements, *Radio Science*, *49*(11), 1124–1139, doi:10.1002/2014RS005519.

Opgenoorth, H. J., M. A. L. Persson, T. I. Pulkkinen, and R. J. Pellinen (1994), Recovery phase of magnetospheric substorms and its association with morning-sector aurora, *Journal of Geophysical Research: Space Physics*, *99*(A3), 4115–4129, doi:10.1029/93JA01502.

Østgaard, N., S. B. Mende, H. U. Frey, L. A. Frank, and J. B. Sigwarth (2003), Observations of non-conjugate theta aurora, *Geophysical Research Letters*, *30*(21), 2125, doi:10.1029/2003GL017914.

Østgaard, N., S. B. Mende, H. U. Frey, and J. B. Sigwarth (2005), Simultaneous imaging of the reconnection spot in the opposite hemispheres during northward IMF, *Geophysical Research Letters*, *32*(21), L21104, doi:10.1029/2005GL024491.

Paxton, L. J., C.-I. Meng, G. H. Fountain, B. S. Ogorzalek, E. H. Darlington, S. A. Gary, J. O. Goldsten, D. Y. Kusnierkiewicz, S. C. Lee, L. A. Linstrom, J. J. Maynard, K. Peacock, D. F. Persons, and B. E. Smith (1992), Special sensor ultraviolet spectrographic imager: An instrument description, in *Proc. SPIE*, vol. 1745, pp. 2–15, doi:10.1117/12.60595.

Paxton, L. J., C.-I. Meng, G. H. Fountain, B. S. Ogorzalek, E. H. Darlington, S. A. Gary, J. O. Goldsten, D. Y. Kusnierkiewicz, S. C. Lee, L. A. Linstrom, J. J. Maynard, K. Peacock, D. F. Persons, B. E. Smith, D. J. Strickland, and R. E. Daniell, Jr. (1993), SSUSI - Horizon-to-horizon and limb-viewing spectrographic imager for remote sensing of environmental parameters, in *Proc. SPIE*, vol. 1764, pp. 161–176, doi:10.1117/12.140846.

Paxton, L. J., D. Morrison, Y. Zhang, H. Kil, B. Wolven, B. S. Ogorzalek, D. C. Humm, and C.-I. Meng (2002), Validation of remote sensing products produced by the Special Sensor Ultraviolet Scanning Imager (SSUSI): a far UV-imaging spectrograph on DMSP F-16, in *Proc. SPIE*, vol. 4485, pp. 338–348, doi:10.1117/12.454268.

Pearson, K. (1901), On lines and planes of closest fit to systems of points in space, *Philos. Mag.*, *2*(6), 559–572.

Pedersen, P. O. (1927), The propagation of radio waves along the surface of the Earth and in the atmosphere, Ph.D. thesis, Danmarks Naturvidenskabelige Samfund, Copenhagen.

Pellinen, R., T. Pulkkinen, and K. Kauristie (1994), Have we learned enough about auroral substorm morphology during the past 30 years?, in *Proceedings of the Second International Conference on Substorms*, edited by J. Kan and J. D. Craven and S.-I. Akasofu, 2006-6167, Geophysical Institute, Geophysical Institute, University of Alaska Fairbanks.

Pettigrew, E. D., S. G. Shepherd, and J. M. Ruohoniemi (2010), Climatological patterns of high-latitude convection in the Northern and Southern hemispheres: Dipole tilt dependencies and interhemispheric comparisons, *Journal of Geophysical Research: Space Physics*, *115*(A7), A07305, doi:10.1029/2009JA014956.

Picone, J. M., A. E. Hedin, D. P. Drob, and A. C. Aikin (2002), NRLMSISE-00 empirical model of the atmosphere: Statistical comparisons and scientific issues, *Journal of Geophysical Research: Space Physics*, *107*(A12), 1468, doi:10.1029/2002JA009430.

Preisendorfer, R., and C. Mobley (1988), *Principal component analysis in meteorology and oceanography*, Developments in atmospheric science, Elsevier.

Provan, G., M. Lester, S. B. Mende, and S. E. Milan (2004), Statistical study of high-latitude plasma flow during magnetospheric substorms, *Annales Geophysicae*, *22*(10), 3607–3624, doi:10.5194/angeo-22-3607-2004.

Pytte, T., R. Mcpherron, and S. Kokubun (1976), The ground signatures of the expansion phase during multiple onset substorms, *Planetary and Space Science*, *24*(12), 1115 – IN4, doi:http://dx.doi.org/10.1016/0032-0633(76)90149-5.

Qian, L., and S. C. Solomon (2012), Thermospheric density: An overview of temporal and spatial variations, *Space Sci. Rev.*, *168*, 147–173, doi:10.1007s112140119810z.

Qian, L., S. Solomon, and T. Kane (2009), Seasonal variation of thermospheric density and composition, *Journal of Geophysical Research*, *114*(A01312), doi:10.1029/2008JA013643.

Raeder, J., R. J. Walker, and M. Ashour-Abdalla (1995), The structure of the distant geomagnetic tail during long periods of northward IMF, *Geophysical Research Letters*, *22*(4), 349–352, doi: 10.1029/94GL03380.

Raeder, J., R. L. McPherron, L. A. Frank, S. Kokubun, G. Lu, T. Mukai, W. R. Paterson, J. B. Sigwarth, H. J. Singer, and J. A. Slavin (2001), Global simulation of the Geospace Environment Modeling substorm challenge event, *Journal of Geophysical Research: Space Physics*, *106*(A1), 381–395, doi:10.1029/2000JA000605.

Redmon, R. J., J. V. Rodriguez, J. C. Green, D. Ober, G. Wilson, D. Knipp, L. Kilcommons, and R. McGuire (2015a), Improved polar and geosynchronous satellite data sets available in common data format at the coordinated data analysis web, *Space Weather*, *13*(5), 2015SW001176, doi: 10.1002/2015SW001176.

Redmon, R. J., D. Ober, F. Rich, J. Rodriguez, D. Knipp, and L. Kilcommons (2015b), *DMSP Space Wx SSJ, SSM, SSIES ATBD and User's Manual*, National Geophysical Data Center.

Rees, M. H. (1963), Auroral ionization and excitation by incident energetic electrons, *Planetary and Space Science*, *11*(10), 1209 – 1218, doi:http://dx.doi.org/10.1016/0032-0633(63)90252-6.

Rees, M. H. (1989), *Physics and Chemistry of the Upper Atmosphere*, Cambridge University Press, cambridge Books Online.

Reiff, P. H. (1984), Models of auroral-zone conductances, in *Magnetospheric Currents*, edited by T. A. Potemra, pp. 180–191, American Geophysical Union, Washington, D.C, doi: 10.1029/GM028p0180.

Rich, F. J., D. D. Hardy, and M. S. Gussenhoven (1985), Enhanced ionosphere-magnetosphere data from the DMSP satellites, *Eos, Transactions American Geophysical Union*, *66*(26), 513–514, doi: 10.1029/EO066i026p00513.

Rich, F. J., D. A. Hardy, R. H. Redus, and M. S. Gussenhoven (1990), Northward IMF and patterns of high-latitude precipitation and field-aligned currents: The February 1986 storm, *Journal of Geophysical Research: Space Physics*, *95*(A6), 7893–7913, doi:10.1029/JA095iA06p07893.

Richards, P. G., and D. G. Torr (1986), Thermal coupling of conjugate ionospheres and the tilt of the Earth's magnetic field, *Journal of Geophysical Research: Space Physics*, *91*(A8), 9017–9021, doi:10.1029/JA091iA08p09017.

Richards, P. G., J. A. Fennelly, and D. G. Torr (1994), EUVAC: A solar EUV Flux Model for aeronomic calculations, *Journal of Geophysical Research: Space Physics*, *99*(A5), 8981–8992, doi:10.1029/94JA00518.

Richards, P. G., D. Bilitza, and D. Voglozin (2010), Ion density calculator (IDC): A new efficient model of ionospheric ion densities, *Radio Science*, *45*(5), RS5007, doi:10.1029/2009RS004332.

Richmond, A. (1992), Assimilative mapping of ionospheric electrodynamics, *Advances in Space Research*, *12*(6), 59 – 68, doi:http://dx.doi.org/10.1016/0273-1177(92)90040-5.

Richmond, A. (1995), Ionospheric electrodynamics, in *Handbook of Atmospheric Electrodynamics*, vol. 2, edited by H. Volland, CRC Press, Boca Raton, Fla.

Richmond, A. D. (2011), Electrodynamics of ionosphere–thermosphere coupling, in *Aeronomy of the Earth's Atmosphere and Ionosphere*, *IAGA Special Sopron Book Series*, vol. 2, edited by A. M. Abdu and D. Pancheva, pp. 191–201, Springer Netherlands, Dordrecht, doi:10.1007/978-94-007-0326-1_13.

Richmond, A. D., and W. Baumjohann (1984), Three-dimensional analysis of magnetometer array data, *Journal of Geophysics Zeitschrift Geophysik*, *54*, 138–156, doi:19840042230.

Richmond, A. D., and Y. Kamide (1988), Mapping electrodynamic features of the high-latitude ionosphere from localized observations: Technique, *Journal of Geophysical Research: Space Physics*, *93*(A6), 5741–5759, doi:10.1029/JA093iA06p05741.

Richmond, A. D., and J. P. Thayer (2000), Ionospheric electrodynamics: A tutorial, in *Magnetospheric Current Systems*, edited by S.-I. Ohtani, R. Fujii, M. Hesse, and R. L. Lysak, pp. 131–146, American Geophysical Union, Washington, D. C., doi:10.1029/GM118p0131.

Richmond, A. D., Y. Kamide, B. H. Ahn, S. I. Akasofu, D. Alcaydé, M. Blanc, O. de la Beaujardiére, D. S. Evans, J. C. Foster, E. Friis Christensen, T. J. Fuller Rowell, J. M. Holt, D. Knipp, H. W. Kroehl, R. P. Lepping, R. J. Pellinen, C. Senior, and A. N. Zaitzev (1988), Mapping electrodynamic features of the high-latitude ionosphere from localized observations: Combined incoherent-scatter radar and magnetometer measurements for january 18-19, 1984, *Journal of Geophysical Research: Space Physics*, *93*(A6), 5760–5776, doi:10.1029/JA093iA06p05760.

Richmond, A. D., E. C. Ridley, and R. G. Roble (1992), A thermosphere/ionosphere general circulation model with coupled electrodynamics, *Geophysical Research Letters*, *19*(6), 601–604, doi:10.1029/92GL00401.

Ridley, A., Y. Deng, and G. Tòth (2006), The global ionosphere thermosphere model, *Journal of Atmospheric and Solar-Terrestrial Physics* , *68*(8), 839 – 864, doi: http://dx.doi.org/10.1016/j.jastp.2006.01.008.

Ridley, A. J., T. I. Gombosi, and D. L. DeZeeuw (2004), Ionospheric control of the magnetosphere: Conductance, *Annales Geophysicae*, *22*(2), 567–584, doi:10.5194/angeo-22-567-2004.

Robinson, R. M., and R. R. Vondrak (1984), Measurements of E region ionization and conductivity produced by solar illumination at high latitudes, *Journal of Geophysical Research: Space Physics*, *89*(A6), 3951–3956, doi:10.1029/JA089iA06p03951.

Robinson, R. M., E. A. Bering, R. R. Vondrak, H. R. Anderson, and P. A. Cloutier (1981), Simultaneous rocket and radar measurements of currents in an auroral arc, *Journal of Geophysical Research: Space Physics*, *86*(A9), 7703–7717, doi:10.1029/JA086iA09p07703.

Robinson, R. M., R. R. Vondrak, K. Miller, T. Dabbs, and D. Hardy (1987), On calculating ionospheric conductances from the flux and energy of precipitating electrons, *Journal of Geophysical Research: Space Physics*, *92*(A3), 2565–2569, doi:10.1029/JA092iA03p02565.

Roble, R. G., and E. C. Ridley (1987), An auroral model for the NCAR thermospheric general circulation model (TGCM), *Annales Geophysicae*, *5*, 369–382.

Roble, R. G., E. C. Ridley, A. D. Richmond, and R. E. Dickinson (1988), A coupled thermosphere/ionosphere general circulation model, *Geophysical Research Letters*, *15*(12), 1325–1328, doi:10.1029/GL015i012p01325.

Russell, C. (2000), The solar wind interaction with the Earth's magnetosphere: A tutorial, *IEEE Transactions on Plasma Science*, *28*(6), 1818–1830, doi:10.1109/27.902211.

Sandford, P. (1968), Variations of auroral emissions with time, magnetic activity and the solar cycle, *Journal of Atmospheric and Terrestrial Physics*, *30*(12), 1921 – 1942, doi: http://dx.doi.org/10.1016/0021-9169(68)90001-9.

Scherliess, L., R. W. Schunk, J. J. Sojka, and D. C. Thompson (2004), Development of a physics-based reduced state Kalman filter for the ionosphere, *Radio Science*, *39*(1), RS1S04, doi: 10.1029/2002RS002797.

Scherliess, L., R. W. Schunk, J. J. Sojka, D. C. Thompson, and L. Zhu (2006), Utah State University Global Assimilation of Ionospheric Measurements Gauss-Markov Kalman filter model of the ionosphere: Model description and validation, *Journal of Geophysical Research: Space Physics*, *111*(A11), A11315, doi:10.1029/2006JA011712.

Schlegel, K. (1988), Auroral zone E-region conductivities during solar minimum derived from EISCAT data, *Annales Geophysicae*, *6*, 129–138.

Schreiner, W., C. Rocken, S. Sokolovskiy, S. Syndergaard, and D. Hunt (2007), Estimates of the precision of GPS radio occultations from the COSMIC/FORMOSAT-3 mission, *Geophysical Research Letters*, *34*(4), L04808, doi:10.1029/2006GL027557.

Schunk, R., and A. Nagy (2009), *Ionospheres: Physics, Plasma Physics, and Chemistry*, Cambridge Atmospheric and Space Science Series, Cambridge University Press.

Schunk, R. W., L. Scherliess, J. J. Sojka, D. C. Thompson, D. N. Anderson, M. Codrescu, C. Minter, T. J. Fuller-Rowell, R. A. Heelis, M. Hairston, and B. M. Howe (2004), Global Assimilation of Ionospheric Measurements (GAIM), *Radio Science*, *39*(1), RS1S02, doi:10.1029/2002RS002794.

Schunk, R. W., L. Scherliess, V. Eccles, L. C. Gardner, J. J. Sojka, L. Zhu, X. Pi, A. J. Mannucci, B. D. Wilson, A. Komjathy, C. Wang, and G. Rosen (2014), Ensemble modeling with data assimilation models: A new strategy for space weather specifications, forecasts, and science, *Space Weather*, *12*(3), 2014SW001050, doi:10.1002/2014SW001050.

Semeter, J., T. Butler, C. Heinselman, M. Nicolls, J. Kelly, and D. Hampton (2009), Volumetric imaging of the auroral ionosphere: Initial results from PFISR, *Journal of Atmospheric and Solar-Terrestrial Physics: [Special Issue] Advances in high latitude upper atmospheric science with the Poker Flat Incoherent Scatter Radar (PFISR)*, *71*(6-7), 738 – 743, doi: http://dx.doi.org/10.1016/j.jastp.2008.08.014.

Sergeev, V. A., L. I. Vagina, R. D. Elphinstone, J. S. Murphree, D. J. Hearn, L. L. Cogger, and M. L. Johnson (1996), Comparison of UV optical signatures with the substorm current wedge as predicted by an inversion algorithm, *Journal of Geophysical Research: Space Physics*, *101*(A2), 2615–2627, doi:10.1029/95JA00537.

Sheng, C., Y. Deng, X. Yue, and Y. Huang (2014), Height-integrated Pedersen conductivity in both E and F regions from COSMIC observations, *Journal of Atmospheric and Solar-Terrestrial Physics*, *115-116*(0), 79 – 86, doi:http://dx.doi.org/10.1016/j.jastp.2013.12.013, sun-Earth System Exploration: Moderate and Extreme Disturbances.

Siscoe, G., J. Raeder, and A. J. Ridley (2004), Transpolar potential saturation models compared, *Journal of Geophysical Research: Space Physics*, *109*(A9), A09203, doi:10.1029/2003JA010318.

Slinker, S. P., J. A. Fedder, B. A. Emery, K. B. Baker, D. Lummerzheim, J. G. Lyon, and F. J. Rich (1999), Comparison of global MHD simulations with AMIE simulations for the events of May19-20, 1996, *Journal of Geophysical Research: Space Physics*, *104*(A12), 28,379–28,395, doi: 10.1029/1999JA900403.

Sofko, G. J., R. Greenwald, and W. Bristow (1995), Direct determination of large-scale magnetospheric field-aligned currents with SuperDARN, *Geophysical Research Letters*, *22*(15), 2041–2044, doi:10.1029/95GL01317.

Solomon, S. C. (1993), Auroral electron transport using the Monte Carlo method, *Geophysical Research Letters*, *20*(3), 185–188, doi:10.1029/93GL00081.

Solomon, S. C. (2001), Auroral particle transport using Monte Carlo and hybrid methods, *Journal of Geophysical Research: Space Physics*, *106*(A1), 107–116, doi:10.1029/2000JA002011.

Solomon, S. C. (2006), Numerical models of the E-region ionosphere, *Advances in Space Research: [Special Issue] Advances in Specifying Plasma Temperatures and Ion Composition in the Ionosphere*, *37*(5), 1031 – 1037, doi:http://dx.doi.org/10.1016/j.asr.2005.09.040.

Solomon, S. C., and V. J. Abreu (1989), The 630 nm dayglow, *Journal of Geophysical Research: Space Physics*, *94*(A6), 6817–6824, doi:10.1029/JA094iA06p06817.

Solomon, S. C., and L. Qian (2005), Solar extreme-ultraviolet irradiance for general circulation models, *Journal of Geophysical Research: Space Physics*, *110*(A10), A10306, doi: 10.1029/2005JA011160.

Solomon, S. C., P. B. Hays, and V. J. Abreu (1988), The auroral 6300 å emission: Observations and modeling, *Journal of Geophysical Research: Space Physics*, *93*(A9), 9867–9882, doi: 10.1029/JA093iA09p09867.

Solomon, S. C., C. A. Barth, P. Axelrad, S. M. Bailey, R. Brown, R. L. Davis, T. E. Holden, R. A. Kohnert, F. W. Lacy, M. T. McGrath, D. C. O'Connor, J. P. Perich, H. L. Reed, M. A. Salada, J. Simpson, J. M. Srinivasan, G. A. Stafford, S. R. Steg, G. A. Tate, J. C. Westfall, N. R. White, P. R. Withnell, and T. N. Woods (1996), Student nitric oxide explorer, in *Proc. SPIE*, vol. 2810, pp. 121–132, doi:10.1117/12.255131.

Sotirelis, T., and P. T. Newell (2000), Boundary-oriented electron precipitation model, *Journal of Geophysical Research: Space Physics*, *105*(A8), 18,655–18,673, doi:10.1029/1999JA000269.

Sotirelis, T., H. Korth, S.-Y. Hsieh, Y. Zhang, D. Morrison, and L. Paxton (2013), Empirical relationship between electron precipitation and far-ultraviolet auroral emissions from DMSP observations, *Journal of Geophysical Research: Space Physics*, *118*(3), 1203–1209, doi: 10.1002/jgra.50157.

Spencer, L. (1959), Energy dissipation by fast electrons, *Tech. rep.*, UNT Llibraries, Government Archives Department.

Spiro, R. W., P. H. Reiff, and L. J. Maher (1982), Precipitating electron energy flux and auroral zone conductances-an empirical model, *Journal of Geophysical Research: Space Physics*, *87*(A10), 8215–8227, doi:10.1029/JA087iA10p08215.

Stamnes, K. (1980), Analytic approach to auroral electron transport and energy degradation, *Planetary and Space Science*, *28*(4), 427 – 441, doi:http://dx.doi.org/10.1016/0032-0633(80)90046-X.

Stamnes, K. (1981), On the two-stream approach to electron transport and thermalization, *Journal of Geophysical Research: Space Physics*, *86*(A4), 2405–2410, doi:10.1029/JA086iA04p02405.

Stenbaek-Nielsen, H. C., E. M. Wescott, T. N. Davis, and R. W. Peterson (1973), Differences in auroral intensity at conjugate points, *Journal of Geophysical Research*, *78*(4), 659–671, doi:10.1029/JA078i004p00659.

Streltsov, A. V., and W. Lotko (2004), Multiscale electrodynamics of the ionosphere-magnetosphere system, *Journal of Geophysical Research: Space Physics*, *109*(A9), A09214, doi:10.1029/2004JA010457.

Strickland, D., J. Bishop, J. Evans, T. Majeed, P. Shen, R. Cox, R. Link, and R. Huffman (1999), Atmospheric ultraviolet radiance integrated code (AURIC): Theory, software architecture, inputs, and selected results, *Journal of Quantitative Spectroscopy and Radiative Transfer*, *62*(6), 689 – 742, doi:http://dx.doi.org/10.1016/S0022-4073(98)00098-3.

Strickland, D. J., D. L. Book, T. P. Coffey, and J. A. Fedder (1976), Transport equation techniques for the deposition of auroral electrons, *Journal of Geophysical Research*, *81*(16), 2755–2764, doi:10.1029/JA081i016p02755.

Strobel, D., C. Opal, and R. Meier (1980), Photoionization rates in the night-time E- and F-region ionosphere, *Planetary and Space Science*, *28*(11), 1027 – 1033, doi:http://dx.doi.org/10.1016/0032-0633(80)90050-1.

Sutton, E. K., J. M. Forbes, and D. J. Knipp (2009), Rapid response of the thermosphere to variations in Joule heating, *Journal of Geophysical Research: Space Physics*, *114*(A4), doi:10.1029/2008JA013667.

Thayer, J. P., and J. Semeter (2004), The convergence of magnetospheric energy flux in the polar atmosphere, *Journal of Atmospheric and Solar-Terrestrial Physics: [Special Issue] Upper Atmosphere Tutorials from the 2001 Joint CEDAR SCOSTEP Meeting*, *66*(10), 807 – 824, doi:http://dx.doi.org/10.1016/j.jastp.2004.01.035.

Thayer, J. P., J. F. Vickrey, R. A. Heelis, and J. B. Gary (1995), Interpretation and modeling of the high-latitude electromagnetic energy flux, *Journal of Geophysical Research: Space Physics*, *100*(A10), 19,715–19,728, doi:10.1029/95JA01159.

Thomsen, M. F. (2004), Why Kp is such a good measure of magnetospheric convection, *Space Weather*, *2*(11), S11004, doi:10.1029/2004SW000089.

Thorne, R. M., B. Ni, X. Tao, R. B. Horne, and N. P. Meredith (2010), Scattering by chorus waves as the dominant cause of diffuse auroral precipitation, *Nature*, *467*(7318), 943–946, doi:10.1038/nature09467.

Tibshirani, R. (1996), Regression shrinkage and selection via the Lasso, *Journal of the Royal Statistical Society (Series B)*, *58*, 267–288, doi:10.2307/41262671.

Tobiska, W. (1991), Revised solar extreme ultraviolet flux model, *Journal of Atmospheric and Terrestrial Physics: [Special Issue] The 7th International Scostep symposium on Solar-Terrestrial Physics*, *53*(11-12), 1005 – 1018, doi:http://dx.doi.org/10.1016/0021-9169(91)90046-A.

Tobiska, W., and F. Eparvier (1998), EUV97: Improvements to EUV irradiance modeling in the soft X-rays and FUV, *Solar Physics*, *177*(1-2), 147–159, doi:10.1023/A:1004931416167.

Tobiska, W., T. Woods, F. Eparvier, R. Viereck, L. Floyd, D. Bouwer, G. Rottman, and O. White (2000), The SOLAR2000 empirical solar irradiance model and forecast tool, *Journal of Atmospheric and Solar-Terrestrial Physics*, *62*(14), 1233 – 1250, doi:http://dx.doi.org/10.1016/S1364-6826(00)00070-5, space Weather Week.

Tobiska, W. K. (1993), Recent solar extreme ultraviolet irradiance observations and modeling: A review, *Journal of Geophysical Research: Space Physics*, *98*(A11), 18,879–18,893, doi:10.1029/93JA01943.

Tobiska, W. K., and C. A. Barth (1990), A solar EUV flux model, *Journal of Geophysical Research: Space Physics*, *95*(A6), 8243–8251, doi:10.1029/JA095iA06p08243.

Vanhamäki, H., and O. Amm (2007), A new method to estimate ionospheric electric fields and currents using data from a local ground magnetometer network, *Annales Geophysicae*, *25*(5), 1141–1156, doi:10.5194/angeo-25-1141-2007.

Vassiliadis, D. (2006), Systems theory for geospace plasma dynamics, *Reviews of Geophysics*, *44*(2), RG2002, doi:10.1029/2004RG000161.

Vasyliunas, V. (1972), The interrelationship of magnetospheric processes, in *Earth's Magnetospheric Processes*, *Astrophysics and Space Science Library*, vol. 32, edited by B. McCormac, pp. 29–38, Springer Netherlands, doi:10.1007/978-94-010-2896-7_3.

Vasyliunas, V. M. (1970), Mathematical models of magnetospheric convection and its coupling to the ionosphere, in *Particles and Fields in the Magnetosphere*, *Astrophysics and Space Science Library*, vol. 17, edited by B. McCormac, pp. 60–71, Springer Netherlands, doi:10.1007/978-94-01032841_6.

Vasyliunas, V. M. (1979), Interaction between the magnetospheric boundary layers and the ionosphere, in *Proceedings of the Magnetospheric Boundary Layers Conference*, *ESA Special Publication*, vol. 148, edited by B. Battrick, J. Mort, G. Haerendel, and J. Ortner.

Vickrey, J. F., R. R. Vondrak, and S. J. Matthews (1981), The diurnal and latitudinal variation of auroral zone ionospheric conductivity, *Journal of Geophysical Research: Space Physics*, *86*(A1), 65–75, doi:10.1029/JA086iA01p00065.

Vogt, J. (2002), Alfvén wave coupling in the auroral current circuit, *Surveys in Geophysics*, *23*(4), 335–377, doi:10.1023/A:1015597724324.

Vondrak, R. R., and F. J. Rich (1982), Simultaneous Chatanika radar and S3-2 satellite measurements of ionospheric electrodynamics in the diffuse aurora, *Journal of Geophysical Research: Space Physics*, *87*(A8), 6173–6185, doi:10.1029/JA087iA08p06173.

Vorobjev, V., O. Yagodkina, and Y. Katkalov (2013), Auroral Precipitation Model and its applications to ionospheric and magnetospheric studies, *Journal of Atmospheric and Solar-Terrestrial Physics*, *102*, 157 – 171, doi:http://dx.doi.org/10.1016/j.jastp.2013.05.007.

Wallis, D. D., and E. E. Budzinski (1981), Empirical models of height integrated conductivities, *Journal of Geophysical Research: Space Physics*, *86*(A1), 125–137, doi:10.1029/JA086iA01p00125.

Wallis, D. D., C. D. Anger, and G. Rostoker (1976), The spatial relationship of auroral electrojets and visible aurora in the evening sector, *Journal of Geophysical Research*, *81*(16), 2857–2869, doi:10.1029/JA081i016p02857.

Wallis, D. D., J. R. Burrows, M. C. Moshupi, C. D. Anger, and J. S. Murphree (1979), Observations of particles precipitating into detached arcs and patches equatorward of the auroral oval, *Journal of Geophysical Research: Space Physics*, *84*(A4), 1347–1360, doi:10.1029/JA084iA04p01347.

Walt, M., W. M. MacDonald, and W. E. Francis (1968), Penetration of auroral electrons into the atmosphere, in *Physics of the Magnetosphere*, *Astrophysics and Space Science Library*, vol. 10, edited by R. L. Carovillano, J. F. McClay, and H. R. Radoski, pp. 534–555, Springer Netherlands, doi:10.1007/978-94-010-3467-8_17.

Watermann, J., O. de La Beaujardiere, and F. J. Rich (1993), Comparison of ionospheric electrical conductances inferred from coincident radar and spacecraft measurements and photoionization models, *Journal of Atmospheric and Terrestrial Physics*, *55*, 1513–1520, doi:10.1016/0021-9169(93)90127-K.

Waters, C. L., B. J. Anderson, and K. Liou (2001), Estimation of global field aligned currents using the iridium system magnetometer data, *Geophysical Research Letters*, *28*(11), 2165–2168, doi:10.1029/2000GL012725.

Weimer, D. R. (2001), An improved model of ionospheric electric potentials including substorm perturbations and application to the Geospace Environment Modeling November 24, 1996, event, *Journal of Geophysical Research: Space Physics*, *106*(A1), 407–416, doi:10.1029/2000JA000604.

Wilkinson, P. J., E. Nielsen, and H. Luhr (1986), Ionospheric conductances: Associations between ionospheric E region electric fields and ground magnetometer variations, *Journal of Geophysical Research: Space Physics*, *91*(A5), 5839–5849, doi:10.1029/JA091iA05p05839.

Wilks, D. (2011), *Statistical Methods in the Atmospheric Sciences*, vol. 100, 2 ed., Academic Press, doi:http://dx.doi.org/10.1016/B978-0-12-385022-5.00022-1.

Wilson, G. R., D. R. Weimer, J. O. Wise, and F. A. Marcos (2006), Response of the thermosphere to Joule heating and particle precipitation, *Journal of Geophysical Research: Space Physics*, *111*(A10), A10314, doi:10.1029/2005JA011274.

Wiltberger, M., R. S. Weigel, W. Lotko, and J. A. Fedder (2009), Modeling seasonal variations of auroral particle precipitation in a global-scale magnetosphere-ionosphere simulation, *Journal of Geophysical Research: Space Physics*, *114*(A1), A01204, doi:10.1029/2008JA013108.

Wing, S., M. Gkioulidou, J. R. Johnson, P. T. Newell, and C.-P. Wang (2013), Auroral particle precipitation characterized by the substorm cycle, *Journal of Geophysical Research: Space Physics*, *118*(3), 1022–1039, doi:10.1002/jgra.50160.

Winningham, J. D., F. Yasuhara, S. I. Akasofu, and W. J. Heikkila (1975), The latitudinal morphology of 10-eV to 10-keV electron fluxes during magnetically quiet and disturbed times in the 2100-0300 MLT sector, *Journal of Geophysical Research*, *80*(22), 3148–3171, doi:10.1029/JA080i022p03148.

Wolf, R. A. (1970), Effects of ionospheric conductivity on convective flow of plasma in the magnetosphere, *Journal of Geophysical Research*, *75*(25), 4677–4698, doi:10.1029/JA075i025p04677.

Wu, Q., D. A. Ortland, T. L. Killeen, R. G. Roble, M. E. Hagan, H.-L. Liu, S. C. Solomon, J. Xu, W. R. Skinner, and R. J. Niciejewski (2008a), Global distribution and interannual variations of mesospheric and lower thermospheric neutral wind diurnal tide: 1. Migrating tide, *Journal of Geophysical Research: Space Physics*, *113*(A5), A05308, doi:10.1029/2007JA012542.

Wu, Q., D. A. Ortland, T. L. Killeen, R. G. Roble, M. E. Hagan, H.-L. Liu, S. C. Solomon, J. Xu, W. R. Skinner, and R. J. Niciejewski (2008b), Global distribution and interannual variations of mesospheric and lower thermospheric neutral wind diurnal tide: 2. Nonmigrating tide, *Journal of Geophysical Research: Space Physics*, *113*(A5), A05309, doi:10.1029/2007JA012543.

Yue, X., W. S. Schreiner, D. C. Hunt, C. Rocken, and Y.-H. Kuo (2011), Quantitative evaluation of the low earth orbit satellite based slant total electron content determination, *Space Weather*, *9*(9), S09001, doi:10.1029/2011SW000687.

Yue, X., W. S. Schreiner, Y.-H. Kuo, D. C. Hunt, W. Wang, S. C. Solomon, A. G. Burns, D. Bilitza, J.-Y. Liu, W. Wan, and J. Wickert (2012), Global 3-D ionospheric electron density reanalysis based on multisource data assimilation, *Journal of Geophysical Research: Space Physics*, *117*(A9), A09325, doi:10.1029/2012JA017968.

Yue, X., W. S. Schreiner, N. Pedatella, R. A. Anthes, A. J. Mannucci, P. R. Straus, and J.-Y. Liu (2014), Space weather observations by GNSS radio occultation: From FORMOSAT-3/COSMIC to FORMOSAT-7/COSMIC-2, *Space Weather*, *12*(11), 616–621, doi:10.1002/2014SW001133.

Zhang, B., W. Lotko, O. Brambles, S. Xi, M. Wiltberger, and J. Lyon (2014), Solar wind control of auroral Alfvénic power generated in the magnetotail, *Journal of Geophysical Research: Space Physics*, *119*(3), 1734–1748, doi:10.1002/2013JA019178.

Zhang, B., W. Lotko, O. Brambles, M. Wiltberger, and J. Lyon (2015), Electron precipitation models in global magnetosphere simulations, *Journal of Geophysical Research: Space Physics*, *120*(2), 2014JA020615, doi:10.1002/2014JA020615.

Zhang, B.-C., Y. Kamide, R.-Y. Liu, H. Shinagawa, and K. Iwamasa (2004), A modeling study of ionospheric conductivities in the high-latitude electrojet regions, *Journal of Geophysical Research: Space Physics*, *109*(A4), A04310, doi:10.1029/2003JA010181.

Zhang, Y., and L. Paxton (2008), An empirical Kp-dependent global auroral model based on TIMED/GUVI FUV data, *Journal of Atmospheric and Solar-Terrestrial Physics*, *70*(89), 1231 – 1242, doi:http://dx.doi.org/10.1016/j.jastp.2008.03.008.

Zhou, X. W., C. T. Russell, G. Le, S. A. Fuselier, and J. D. Scudder (2000), Solar wind control of the polar cusp at high altitude, *Journal of Geophysical Research: Space Physics*, *105*(A1), 245–251, doi:10.1029/1999JA900412.

Zhu, L., J. Sojka, and R. Schunk (2005), Active ionospheric role in small-scale aurora structuring, *Journal of Atmospheric and Solar-Terrestrial Physics*, *67*(7), 687 – 700, doi: http://dx.doi.org/10.1016/j.jastp.2004.12.004.

Zhu, L., R. Schunk, L. Scherliess, and V. Eccles (2012), Importance of data assimilation technique in defining the model drivers for the space weather specification of the high-latitude ionosphere, *Radio Science*, *47*(4), RS0L24, doi:10.1029/2011RS004936.

Appendix A

Acronyms

Active Magnetosphere and Planetary Electrodynamics Response Experiment	(**AMPERE**)
Advance Modular Incoherent Scatter	(**AMISR**)
Altitude Adjusted Corrected Geomagnetic coordinates	(**AACGM**)
Active Magnetosphere and Planetary Electrodynamic Response Experiment	(**AMPERE**)
Assimilative Mapping of Ionospheric Electrodynamics	(**AMIE**)
Atmospheric Explorer	(**AE**)
Auroral Electrojet	(**AE**)
Auroral Acceleration Region	(**AAR**)
Boundary Plasma Region	(**BPR**)
Boundary Plasma Sheet	(**BPS**)
Central Plasma Sheet	(**CPS**)
Challenging Minisatellite Payload	(**CHAMP**)
Constellation Observing System for Meteorology, Ionosphere, and Climate	(**COSMIC**)
Coronal Mass Ejection	(**CME**)
Corotating Interaction Region	(**CIR**)
Coupling Function	(**CF**)
Defense Meteorological Satellite Program	(**DMSP**)
Dispersive Alfvén Wave	(**DAW**)
Disturbance Storm Time index	(**Dst**)

Electrojet (**EJ**)

Electromagnetic (**EM**)

Empirical Orthogonal Functions (**EOFs**)

Expanding/Contracting Polar Cap (**ECPC**)

Extreme Ultraviolet (**EUV**)

Extreme Ultraviolet flux model for Aeronomic Calculations (**EUVAC**)

Fast Auroral SnapshoT Explorer (**FAST**)

Field-Aligned Current (**FAC**)

Field Line Interhemispheric Plasma model (**FLIP**)

General Circulation Model (**GCM**)

Geocentric Solar Ecliptic (**GSE**)

Geocentric Solar Equatorial (**GSEQ**)

Geocentric Solar Magnetic (**GSM**)

Geospace Environment Modeling (**GEM**)

GLobal AirglOW (**GLOW**)

GLobal AirglOW + conductivity (**GLOWcon**)

GLobal AirglOW + conductivity parameterized (**GLOWfast**)

Global Positioning Services Radio Occultation (**GPSRO**)

Global-scale Observations of the Limb and Disk (**GOLD**)

Gravity Recovery and Climate Experiment (**GRACE**)

Hemispheric Power Index (**HPI**)

Heliospheric Current Sheet (**HCS**)

High Accuracy Satellite Drag Model (**HASDM**)

High Speed Stream (**HSS**)

International Reference Ionosphere (**IRI**)

Incoherent Scatter Radar (**ISR**)

Infrared (**IR**)

Interplanetary Magnetic Field (**IMF**)

Ionospheric CONnection Explorer (**ICON**)

Ionosphere-Thermosphere (**IT**)

Joule Heating Proxy (**JHP**)

Kamide-Richmond-Matsushita (**KRM**)

Least Absolute Shrinkage and Selection Operator (**LASSO**)

Local Time (**LT**)

Low Earth Orbit (**LEO**)

Low Latitude Boundary Layer (**LLBL**)

Lyman Birge Hopfield Long (**LBHL**)

Lyman Birge Hopfield Short (**LBHS**)

Magnetosphere-Ionosphere-Thermosphere (**MIT**)

Maximum Likelihood (**ML**)

Magnetic Local Time (**MLT**)

Magnetic Latitude (**MLAT**)

Median Absolute Deviation (**MAD**)

Monte Carlo (**MC**)

National Oceanic and Atmospheric Administration (**NOAA**)

National Research Laboratory Mass Spectrometer and Incoherent Scatter Radar Extended 2000 model (**NRLMSISE-00**)

Nitric Oxide Empirical Model (**NOEM**)

Optimal Interpolation (**OI**)

Oval Variation, Assessment, Tracking, Intensity, and Online Nowcasting (**OVATION**)

Polar Cap (**PC**)

Polar Orbiting Meteorological Satellites (**MetOp**)

Principal Component Analysis (**PCA**)

Probability Distribution Function (**pdf**)

Polar Orbiting Environmental Satellites	(**POES**)
Root Mean Square	(**RMS**)
Root Sum Square	(**RSS**)
Solar Electromagnetic Radiation Flux model	(**SERF**)
Solar Zenith Angle	(**SZA**)
Special Sensor J	(**SSJ**)
Special Sensor Ultraviolet Spectrographic Imager	(**SSUSI**)
Strong Localization	(**SL**)
Substorm Current Wedge	(**SCW**)
Super Dual Auroral Radar Network	(**SuperDARN**)
Thermosphere General Circulation Model	(**TGCM**)
Ultraviolet	(**UV**)
Ultraviolet Imager	(**UVI**)
Weak Localization	(**WL**)

Appendix B

Mathematical derivation of the GLOW electron transport algorithm

Here we provide a complete mathematical derivation and description of the two-stream electron transport approximation used in the GLOW model. We will follow the derivation given by *Stamnes* (1980) and *Stamnes* (1981). Following *Stamnes* (1980), the equation characterizing the behavior of an incident electron beam along a magnetic field line entering the atmosphere is given by:

$$\begin{aligned}\mu\frac{dI\left(l,\mathcal{E},\mu\right)}{dl} = &-\sum_s n_s(l)\sigma^s_{\rm tot}(\mathcal{E})I\left(l,\mathcal{E},\mu\right)\\ &+\sum_s n_s(l)\sigma^s_e(\mathcal{E})\frac{1}{2}\int_{-1}^{1}p^s_e\left(\mu,\mu'\right)I\left(l,\mathcal{E},\mu'\right)d\mu'\\ &+\int_{\mathcal{E}'>\mathcal{E}}^{\infty}d\mathcal{E}'\sum_s n_s(l)\sigma^s_{\rm inel}\left(\mathcal{E},\mathcal{E}'\right)\\ &\times\frac{1}{2}\int_{-1}^{1}p^s_{\rm inel}\left(\mu,\mu'\right)I\left(l,\mathcal{E}',\mu'\right)d\mu',\end{aligned} \tag{B.1}$$

where:

$\mathcal{E}$ = electron energy

$\mu = \cos\mu$ = pitch angle of electron

l = position along magnetic field line

$n_s(l)$ = density of atmospheric species s, cm^{-3}

$\sigma^s_{\text{tot}}(\mathcal{E})$ = total cross-section per particle for electron collision with species s, cm^2

$\sigma^s_e(\mathcal{E})$ = total elastic cross-section per particle for electron collision with species s, cm^2

$p^s_e\left(\mu,\mu'\right)$ = phase function; one half of this term is the probability that an electron will elastically scatter from pitch angle $\theta' = arccos(\mu')$ into pitch angle $\theta = arccos(\mu)$

$p^s_{\text{inel}}\left(\mu,\mu'\right)$ = phase function for inelastic scattering

$\sigma^s_{\text{inel}}\left(\mathcal{E},\mathcal{E}'\right)$ = differential inelastic cross-section per particle for production of electrons at energy $\mathcal{E}$ (either degraded primary electrons or secondary electrons) due to electrons with energy $\mathcal{E}'$ colliding with species s, cm^2eV

$I\left(l,\mathcal{E},\mu\right)$ = intensity of electrons at energy $\mathcal{E}$, position l, and pitch angle $arccos(\mu)$, $cm^{-2}sec^{-1}sr^{-1}eV^{-1}$.

Equation B.1 represents the change in electron intensity due to three classes of effects: 1) inelastic or elastic scattering of electrons out of the beam; 2) elastic scattering into the beam; and 3) sources (degraded primary electrons and secondary electrons).

Equation B.1 can be expressed in terms of the collision depth, $\tilde{\tau}$, which is analogous to optical depth, by dividing through by $\sum_s n_s(l)\sigma^s_{\text{tot}}(\mathcal{E})$:

$$\mu\frac{dI\left(\tilde{\tau},\mathcal{E},\mu\right)}{d\tilde{\tau}} = I\left(\tilde{\tau},\mathcal{E},\mu\right) - \frac{\tilde{\omega}_e\left(\tilde{\tau},\mathcal{E}\right)}{2} \times \int_{-1}^{1} p_e(\mu,\mu')I\left(\tilde{\tau},\mathcal{E},\mu'\right)d\mu - \tilde{Q}\left(\tilde{\tau},\mathcal{E},\mu\right), \tag{B.2}$$

where

$$d\tilde{\tau}(l,\mathcal{E}) = -\sum_s n_s(l)\sigma^s_{\rm tot}(\mathcal{E})ds.$$
$$\tilde{\omega}_e(\tilde{\tau},\mathcal{E}) = \frac{\sum_s n_s(l)\sigma^s_e(\mathcal{E}p^s_e(\mu,\mu')}{\sum_s n_s(l)\sigma^s_{\rm tot}(\mathcal{E})}$$
$$= \text{'single scattering albedo'}.$$

The single scattering albedo reduces to the elastic to total scattering cross-section in a single constituent atmosphere. Note that the *tilde* (i.e. $\tilde{x}$), on the variables in *Stamnes* (1980) refers to a variable prior to the application of a forward scattering peak approximation, which assumes the scattering can be described by a screened Rutherford cross-section *Berger et al.* (1970, 1974); *Strickland et al.* (1976). That aspect of the derivation is not presented here, but the reader is referred to Section 2.1 of *Stamnes* (1980) for the derivation. $\tilde{Q}$ is an electron source (i.e. production) term encompassing contributions from degraded primaries and secondaries cascading from higher energies due to excitation and ionization:

$$\begin{aligned}\tilde{Q}\left(\tilde{\tau},\mathcal{E},\mu\right) &= \int_{\mathcal{E}'>\mathcal{E}} d\mathcal{E}'\tilde{R}\left(\tilde{\tau},\mathcal{E},\mathcal{E}'\right) \\ &= \qquad \times\frac{1}{2}\int_{-1}^{1} p_{\rm inel}(\mu,\mu')I\left(\tilde{\tau},\mathcal{E},\mu'\right)d\mu'.\end{aligned} \tag{B.3}$$

The phase function for inelastic scattering, $p_{\rm inel}$, can be written as:

$$p_{\rm inel}(\mu,\mu')\tilde{R}(\tilde{\tau},\mathcal{E},\mathcal{E}') = \frac{\sum_s n_s(l)\sigma^s_{\rm inel}(\mathcal{E},\mathcal{E}')p^s(\mu,\mu')}{\sum_s n_s(l)\sigma_{\rm tot}(\mathcal{E},\mathcal{E}')},$$

where $\tilde{R}(\tilde{\tau},\mathcal{E},\mathcal{E}')$ is the redistribution function for inelastic scattering. Following the Rutherford forward scattering peak approximation and an appropriate recasting the problem onto a discrete energy grid because electrons lose energy in discrete amounts, the transport equation becomes (Equation 8 in *Stamnes* (1980) and Equation 1 in *Stamnes* (1981)):

$$\mu \frac{I_m(\tau,\mu)}{d\tau} = I_m(\tau,\mu) - \frac{1}{2}\sum_{L=0}^{2n-1} \omega_{mL} P_L(\mu) \int_{-1}^{1} P_L(\mu') I_m(\tau,\mu')\, d\mu' - Q_m(\tau,\mu) \tag{B.4}$$

where m represents the center of the m^{th} energy bin and:

ω_{mL} = proportional to the single scattering albedo,

$P_L(\mu)$ = Legendre polynomial,

$I_m(\tau,\mu)$ = intensity of electrons at energy $\mathcal{E} = \mathcal{E}_m$, scattering depth τ, and pitch angle $\theta = arccos(\mu)$.

The electron source term, Q_m, in this formulation is:

$$Q_m(\tau,\mu) = \sum_{i=1}^{N} \Delta\mathcal{E}_i R(\mathcal{E}_m,\mathcal{E}_i) \frac{1}{2} \int_{-1}^{1} p_{\text{inel}}(\mu,\mu') I_i(\tau,\mu') d\mu', \tag{B.5}$$

where $R(\mathcal{E}_m,\mathcal{E}_i)$ is the redistribution function that defines the efficiency by which electrons at energy $\mathcal{E}_i$ scatter into $\mathcal{E}_m$.

In the two stream approximation Equation B.4 reduces to a system of two coupled differential equations. *Stamnes* (1980) solves the differential equations using a discrete ordinate method, which can be solved explicitly. Numerical algorithms that address electron transport must include appropriate definitions of the source, redistribution, and scattering terms.

The GLOW model uses the *Banks et al.* (1974) electron transport algorithm, hereafter the Banks and Nagy two-stream code. The Banks and Nagy two-stream code solves for the upward and downward electron flux along a magnetic field line as a function of energy, assuming continuous energy losses at large electron particle energies (E>500 eV) and discrete losses at low energies (E<500 eV). At energies greater than 500 eV a Fokker-Planck diffusion approach *Walt et al.* (1968) with revised Born approximation *Chappell* (1969) is used to model electron energy losses. At

energies below 500 eV, the Banks and Nagy two-stream code uses the approach of *Banks and Nagy* (1970) and *Nagy and Banks* (1970) which takes into account the incident low-energy particles, the energy-degraded primaries particles, and secondary electrons created in impact ionization.

The algorithm produces complete electron energy spectra of auroral electrons as a function of altitude in terms of upward and downward electron fluxes. From these spectra it is possible to compute ionization rates, optical emission rates, and numerous other important quantities, such as conductivities.

Appendix C

Empirical orthogonal functions

Principal Component Analysis (PCA) is a multivariate statistical technique that attempts to reduce the dimensionality of a data set (*Wilks*, 2011). This is accomplished by identifying significant spatio-temporal patterns that dominate the variability in the data set. *Lorenz* (1956) applied this technique to the atmospheric sciences and called it Empirical Orthogonal Function (EOF) analysis. The names PCA and EOF analysis are each used to describe the same technique. We use the term EOF analysis throughout the dissertation and will continue to do so in this appendix.

This appendix provides details of EOF analysis and specifically identifies the distinction between the classical approach and the methods used in this dissertation. Comprehensive treatments of the EOF technique can be found in *Preisendorfer and Mobley* (1988); *Joliffe* (2002); *Hannachi et al.* (2007); *Wilks* (2011).

C.1 Objective of EOF analysis

EOF analysis attempts to reduce the dimensionality of a data set by representing the data with new variables. The new variables are linear combinations of the original variables and are chosen to represent the maximum possible variance in the original data. When the original data contain significant correlations, which is often the case with geophysical fields, the new variables may be far fewer in number than the original set, yielding a compact representation. Beyond the benefit of a compact representation of the variance of a data set, EOF analysis also yields new insight into the spatial and temporal variations of the data.

C.2 Classical EOF analysis

Classical EOF analysis generally concerns data collected at regular intervals and on a spatial grid. Suppose we have a space-time field $x(t, s)$, given on a spatial grid, representing the value of a field $\mathbf{x}$ at time t and spatial position s. We define the climatology, or background mean, of the field as the temporal average of each grid point in the spatial domain:

$$\bar{x}(s) = \frac{1}{n} \sum_{t=1}^{n} x(t, s), \tag{C.1}$$

where the field climatology is given by:

$$\bar{\mathbf{x}} = (\bar{x}(1), ..., \bar{x}(p)), \tag{C.2}$$

and p is the number of spatial locations. We then define the *anomaly field* or *perturbation field* as the observations minus the climatology:

$$\mathbf{x}' = \mathbf{x} - \bar{\mathbf{x}}. \tag{C.3}$$

EOF analysis aims to find the linear combination of all the variables, i.e. the grid points, that explains the maximum variance. To do so, we represent the field by the data matrix X:

$$X = \begin{bmatrix} x_{11} & x_{12} & \cdots & x_{1p} \\ x_{21} & x_{22} & \cdots & x_{2p} \\ \vdots & \vdots & \ddots & \vdots \\ x_{n1} & x_{n2} & \cdots & x_{np} \end{bmatrix}, \tag{C.4}$$

where n is the number of time points and p is the number of spatial grid points, transformed into a row vector for each time that data are collected. From the perturbation field representation of X we can form the covariance matrix:

$$\mathbf{COV} = X'^{\mathrm{T}} X'. \tag{C.5}$$

EOF analysis finds the direction $\mathbf{a} = (a_1, ..., a_p)^{\mathrm{T}}$ such that $X'a$ has maximum variability. Observing that the variance of the time series $X'a$ is:

$$\mathrm{var}(X'a) = \mathbf{a}^{\mathrm{T}}\mathbf{COV}\mathbf{a}, \tag{C.6}$$

and subjecting $\mathbf{a}$ to the bounding constraint $\mathbf{a}^{\mathrm{T}}\mathbf{a} = 1$, the solution to $\mathbf{max}_a \left(\mathbf{a}^{\mathrm{T}}\mathbf{COV}\mathbf{a}\right)$ is an eigenvalue problem:

$$\mathbf{COV}\mathbf{a} = \lambda\mathbf{a}. \tag{C.7}$$

The kth EOF is, therefore, just the kth eigenvector after sorting according to descending eigenvalue. The kth principal component (PC), c_k, is the projection of the perturbation field X' onto the kth EOF:

$$c_k(t) = \sum_{s=1}^{p} x'(t,s)a_k(s). \tag{C.8}$$

By definition, EOFs are orthogonal and the PCs are uncorrelated. The property of orthogonality provides a complete basis by which the time-varying perturbation field can be represented by:

$$X'(t,s) = \sum_{k=1}^{M} c_k(t)a_k(s), \tag{C.9}$$

where M is the number of EOFs chosen to represent the field. In other words the EOFs define a new coordinate system in which the EOFs are the unit vectors and the principal components are the coordinates (*Wilks*, 2011). These can be understood in the context of the more familiar concept of cartesian coordinates. In a cartesian coordinate system a spatial location is defined using orthogonal unit vectors, $[\hat{x}, \hat{y}, \hat{z}]$, and an associated magnitude in each direction, which can depend on time, $[X(t)\hat{x}, Y(t)\hat{y}, Z(t)\hat{z}]$. In this comparison, EOFs are comparable to the unit vectors, representing spatial structure (time independent), and PCs are comparable to the magnitudes of each direction, scaling the EOFs in time.

One drawback of EOFs is that M must be a finite value, resulting in representativeness error due to truncation.

C.2.1 Simple two-dimensional example

EOFs can be most easily visualized in two-dimensions as a coordinate rotation that maximizes the variance explained. Figure C.1 shows a scatter of data in two dimensions (x_1, x_2). The EOFs are shown as line plots superimposed on the data. The first EOF points in the direction of most variability in the data and the second EOF is orthogonal to it.

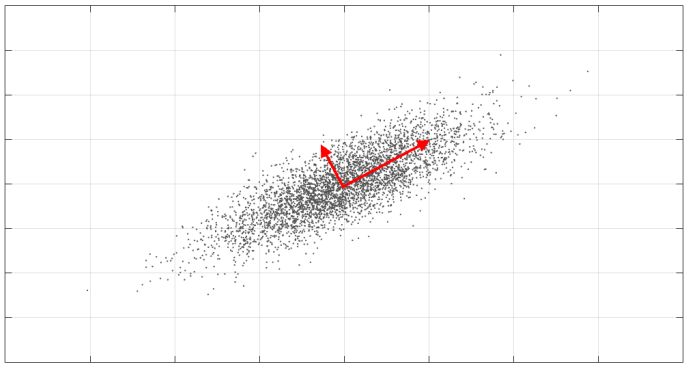

Figure C.1: Example of two-dimensional data and the associated primary directions of variability identified by EOF analysis. The scatter points are the original data and the EOFs are the superimposed red lines, identifying the directions of most variability. EOF2 is constrained to be orthogonal by EOF1, such that in two dimensions its direction is completely defined by EOF1.

C.3 EOF analysis for irregular and sparse data: Reduced rank, mixed effects framework

When dealing with sparse data collected on an irregular grid, it is difficult to estimate the sample covariance matrix **COV** necessary for conventional EOF analysis. In this case, smoothness constraints can be imposed to stabilize the estimation. One common way to accomplish this is by representing the EOFs and PCs as smooth basis functions, which means one projects each row of the data matrix onto the basis and performs EOF analysis on the basis function coefficients (*James*

et al., 2000). This is called the *direct method*. The direct method has two primary shortcomings: 1) if few data are collected at a given time, a unique representation of the data may not be possible; and 2) the available information is not completely utilized because the method treats estimated data as observed data and thereby gives equal weight to all observed data despite their irregular spacing.

Alternatively, one can model the data using basis functions, sample on a fine grid, and perform EOF analysis of the resulting data (*James et al.*, 2000). This approach is called a *mixed effects method* because the data $\mathbf{Y}$ are represented as the combination of a fixed effects term that captures the sample mean and a random effects term that captures individual variation. EOF analysis can then be performed on the variation about the mean. In order to fit the mixed effects model we must estimate the fixed coefficients of the basis functions corresponding to the sample mean and the population covariance matrix calculated from the random vectors of basis function coefficients for each time sample of data. Expectation maximization algorithms that yield a best linear unbiased estimation of the random coefficients are commonly used to fit mixed effects models. In the body of this dissertation we have referred to the fixed coefficients as β and the random coefficients as α. In the EOF framework, each EOF has a unique set of β and α coefficients such that the fit is performed for each EOF in a sequential manner with the contribution from each prior EOF removed from the data at each step.

The mixed effects method overcomes irregularly spaced data, however, in situations where the data are also sparse, estimation of the complete population covariance matrix is problematic due to the number of parameters that must be estimated. A *reduced rank* approach in which the EOFs and PCs are estimated directly, rather than first estimating the covariance matrix and then solving the eigenvalue problem, results in fewer required estimated parameters and is thus advantageous for sparse data. *James et al.* (2000) gives a more extensive development and explanation of the reduced rank, mixed effects method, including an outline of the algorithm in their Appendix A. *Matsuo et al.* (2002) addresses the application of this method to irregular and sparse data from a polar-orbiting satellite, which is comparable to the manner in which the method is used in this

dissertation.

Appendix D

Optimal Interpolation

Optimal interpolation (OI) is a method of data assimilation in which a spatial field $\mathbf{x}$ is estimated for a specified time given: 1) knowledge of the background field $\mathbf{x}_b$ and 2) irregularly spaced, often sparse, observations $\mathbf{y}_o$ at observation locations $\mathbf{r}_i$ (*Kalnay*, 2003). The observations $\mathbf{y}_o$ are different from the model variables by either being located at difference points than the model grid points and/or being *indirect* measurements of the model variables. Therefore, we define the observation operator $\mathbf{H}(\mathbf{x})$ that maps between observation space and model space. $\mathbf{H}(\mathbf{x})$ interpolates the background field to the locations of the observations, and, if necessary, transforms the background field into observational space. In other words, $\mathbf{H}(\mathbf{x})$ maps the background field into *first guess* observations.

In OI we cast the analysis as the sum of the background field and the optimally weighted innovation vector $\mathbf{d}$, defined as the difference between the observations and the background field:

$$\mathbf{x}_t = \mathbf{x}_b + \mathbf{W}\left(\mathbf{y}_o - \mathbf{H}(\mathbf{x})\right) + \epsilon_a = \mathbf{x}_b + \mathbf{W}\mathbf{d} + \epsilon_a, \tag{D.1}$$

where $\mathbf{x}_t$ is the unknown true field and ϵ_a is the analysis error:

$$\epsilon_a = \mathbf{x}_a - \mathbf{x}_t. \tag{D.2}$$

It is useful to discuss the dimensions of the variables. The unknown analysis $\mathbf{x}_a$ can be a two-dimensional field of a single variable, or a three-dimensional field of several parameters. In any case, $\mathbf{x}_a$ is organized into a vector of length n, where n is the product of the number of grid points

and the number of model variables. The truth and background fields are also vectors of length n. The number of observations available for a given estimation cycle is p, which makes the optimal weights $\mathbf{W}$ a $n \times p$ matrix and the observation operator $\mathbf{H}$ a $p \times n$ matrix. The innovation vector $\mathbf{d}$ is a vector of length p. The weights matrix is also called the gain matrix, or the Kalman gain in a Kalman filter process, and will be denoted my $\mathbf{K}$ below to be consistent with the notation of this dissertation and the majority of the literature.

If we assume that the prior distribution of the true field $\mathbf{x}$ is given by:

$$\mathbf{x} \sim \mathcal{N}\left[\mathbf{x}_b, \mathbf{P}_b\right], \tag{D.3}$$

where $\mathcal{N}$ denotes a normal distribution, $\mathbf{x}_b$ is the prior mean field, and $\mathbf{P}_b$ is the background error covariance defined by:

$$\mathbf{P}_b = E\left[\epsilon_b \cdot \epsilon_b\right], \tag{D.4}$$

where ϵ_b is the error in the prior mean field $\epsilon_b = \mathbf{x} - \mathbf{x}_b$. Therefore:

$$\epsilon_b \sim \mathcal{N}\left[0, \mathbf{P}_b\right]. \tag{D.5}$$

We relate the observation vector to the state variable using the observation operator such that:

$$\mathbf{y}_o = \mathbf{H}(\mathbf{x}) + \epsilon_r, \tag{D.6}$$

where ϵ_r is the error in the observation and it's distribution is given by:

$$\epsilon_r \sim \mathcal{N}\left[0, \mathbf{R}\right], \tag{D.7}$$

and $\mathbf{R}$ denotes the observation error covariance matrix. The OI technique is a best linear unbiased estimator (BLUE) for the analysis field $\mathbf{x}_a$:

$$\mathbf{x}_a = \mathbf{x}_b + \mathbf{K}\mathbf{d}, \tag{D.8}$$

where the Kalman gain is given by:

$$\mathbf{K} = \left[\mathbf{H}^{\mathrm{T}}\mathbf{R}^{-1}\mathbf{H} + \mathbf{P}_b^{-1}\right]^{-1}\mathbf{H}^{\mathrm{T}}\mathbf{R}^{-1} \tag{D.9}$$

$$= \mathbf{P}_b\mathbf{H}^{\mathrm{T}}\left[\mathbf{H}\mathbf{P}_b\mathbf{H}^{\mathrm{T}} + \mathbf{R}\right]^{-1}. \tag{D.10}$$

The Kalman gain matrix distributes in space the discrepancy between the background field $\mathbf{x}_b$ and the observations $\mathbf{y}_o$ as an update to the background field. The gain is determined by minimizing $\epsilon_a^{\mathrm{T}}\epsilon_a$, which is equivalent to solving:

$$\left.\frac{\partial J(\mathbf{x})}{\partial \mathbf{x}}\right|_{\mathbf{x}=\mathbf{x}_b} = 0, \tag{D.11}$$

where:

$$J(\mathbf{x}) = \frac{1}{2}\left[\mathbf{x} - \mathbf{x}_b\right]^{\mathrm{T}}\mathbf{P}_b^{-1}\left[\mathbf{x} - \mathbf{x}_b\right] \tag{D.12}$$

$$+ \frac{1}{2}\left[\mathbf{y}_o - \mathbf{H}(\mathbf{x})\right]^{\mathrm{T}}\mathbf{R}_b^{-1}\left[\mathbf{y}_o - \mathbf{H}(\mathbf{x})\right]. \tag{D.13}$$

Equation D.12 qualitatively states that: 1) the analysis field is allowed to depart further from the background field as the background error variance (diagonal elements of $\mathbf{P}_b$ that represent uncertainty in the background field) increases; and 2) the difference between the analysis transformed to observation space $\mathbf{H}(\mathbf{x}_a)$ is allowed to depart further from the observations as the diagonal elements of the observation error variance (diagonal elements of $\mathbf{R}$ that represents the uncertainty in the observations) increases.

If we assume that the observation and model errors are normally distributed and uncorrelated with each other, Equation D.8 is equivalent to the maximum likelihood estimation of $\mathbf{x}$ (*Daley*, 1993). The OI procedure outlined above assumes that the background model error covariance $\mathbf{P}_b$ and observation error covariance $\mathbf{R}$ are known *a priori*, and their determination is a critical part of the OI estimation process.

There are many good resources on the optimal interpolation technique and interested readers are specifically referred to *Lorenc* (1986); *Daley* (1993); *Kalnay* (2003) for further information. *Richmond and Kamide* (1988); *Matsuo et al.* (2005); *Cousins et al.* (2015a) provide specific information about the application of OI for mapping high-latitude ionospheric electrodynamics.

Appendix E

Electrodynamics relationships and associated assumptions used in Assimilative Mapping of Ionospheric Electrodynamics (AMIE) and *Cousins et al.* (2015a) procedures

Solutions to the ionospheric electrodynamics can be defined in terms of the electrostatic potential, Φ, or the vector magnetic potential, A. The electrostatic potential representation was developed for the AMIE procedure by *Richmond and Kamide* (1988) and the magnetic potential representation is provided in C2015, but reproduced here. In the following, the two-dimensional magnetic perturbation vectors are assumed to be purely toroidal, which, together with the assumption of vertical magnetic field lines, allows the electrodynamic relationships to be represented in terms of the radial component of the vector magnetic potential, A_r:

$$\delta\vec{B} = \nabla \times (\hat{r}A_r), \tag{E.1}$$

$$\mu_0 J_r = \hat{r} \cdot \nabla \times \delta\vec{B} = -\nabla^2 A_r, \tag{E.2}$$

$$J_r = \nabla \cdot \vec{I}, \tag{E.3}$$

$$\vec{I} = \Sigma \cdot \vec{E}, \tag{E.4}$$

$$\vec{E} = -\nabla\Phi, \tag{E.5}$$

$$\vec{v} = \frac{\vec{E} \times \vec{B}}{B^2}, \tag{E.6}$$

$$\frac{\nabla^2 A_r}{\mu_0} = \Sigma_P \nabla^2 \Phi + \nabla\Phi \cdot \nabla\Sigma_P \pm \hat{r} \cdot (\nabla\Sigma_H \times \nabla\Phi), \tag{E.7}$$

where μ_0 is the permeability of free space, $\hat{r}$ is the unit radial vector, J_r is the radial current density above the ionosphere (which is assumed to be equivalent to FAC density), $\vec{I}$ is the height-integrated horizontal current density flowing in the ionospheric layer, $\vec{E}$ is the horizontal electric field in the ionosphere, Σ is the conductance in the ionosphere and is a tensor (we choose to model the conductance as the electrical conductivity integrated over 80-200 km altitude), $\vec{B}$ is the geomagnetic field (given by the International Geomagnetic Reference Field (IGRF)), and Σ_P and Σ_H are the Pedersen and Hall conductances, respectively. The $\pm$ sign in Equation E.7 represents the northern and southern hemispheres, respectively.

Equations E.4 - E.6 represent the electrostatic potential relationships. Equation E.7 is obtained by combining these three equations with Equation E.3. Assuming the conductance is known, each of these relationships are linear in terms of either the electrostatic or magnetic potential.